UNDERSTANDING SUSTAINED SPIRAL CHAOS USING NON-CHAOTIC SOLUTIONS OF A SIMPLE MODEL OF ATRIAL EXCITATION

A Thesis
Presented to
The Academic Faculty

by

Christopher D. Marcotte

In Partial Fulfillment
of the Requirements for the Degree
Doctor of Philosophy in the
School of Physics

Georgia Institute of Technology
December 2016

UNDERSTANDING SUSTAINED SPIRAL CHAOS USING NON-CHAOTIC SOLUTIONS OF A SIMPLE MODEL OF ATRIAL EXCITATION

Approved by:

Professor Roman Grigoriev, Advisor
School of Physics
Georgia Institute of Technology

Professor Kurt Weisenfeld
School of Physics
Georgia Institute of Technology

Professor Predrag Cvitanović
School of Physics
Georgia Institute of Technology

Professor Rafael de la Llave
School of Mathematics
Georgia Institute of Technology

Professor Flavio Fenton
School of Physics
Georgia Institute of Technology

Date Approved: 2 November 2016

Hail Satan,

the most reliable man I know.

ACKNOWLEDGEMENTS

I must begin by expressing overwhelming gratitude to my advisor, Prof. Roman Grigoriev. I have learned a great deal under his direction, and I owe a great deal of my success to his insight and patience. That this thesis punctuates our time together is bittersweet.

I must also thank the members of my thesis committee, not only for agreeing to volunteer their time and expertise, but for their suggestions to improve the presentation of the results contained herein. The clarity of this thesis is due in no small part to their considerable insight and patience.

I would like to acknowledge my fellow graduate students for, in equal measure, their assistance and their folly. In particular I would like to thank Bradford Taylor for stimulating discussions of our respective focuses, and for often confusing my experience with expertise. I would also like to thank Radford Mitchell, for spurring numerous discussions of the subtleties of Newton-Krylov methods and offering illustrative codes; his guidance was foundational in any success I have found.

I must extend special appreciation to those who have opened their homes to me in the last few months, including my mother, Prof. Flavio Fenton, Raenell Soller, and Kimberly Short. I can not express how instrumental your generosity has been to the completion of this work. I would finally like to extend my thankfulness for their moral support to Prof. Flavio Fenton and Prof. Elizabeth Cherry; your encouragement was essential when my stubbornness faltered.

TABLE OF CONTENTS

LIST OF TABLES

LIST OF FIGURES

SUMMARY

The research presented in this thesis was motivated by a desire to understand the dynamics of spiral chaos featuring multiple interacting spiral waves in two spatial dimensions.Additionally, we wished to study how simple non-chaotic solutions of these model equations develop into considerably more complicated regimes and how the instabilities of simple solutions can inform our understanding of multi-spiral dynamics typical of sustained spiral chaos. This thesis presents a numerical and theoretical investigation of a simplified model of cardiac tissue dynamics and the unstable solutions representative of nontrivial dynamics.

Sustained spiral chaos can be understood in terms of the constituent features – the coherent spiral waves which make up the state. This regime is dominated by slow recurrent evolution intermittently punctuated by fast transitions between distinct multi-spiral configurations through the creation or annihilation of spiral cores. For recurrent dynamics, the domain can be split into slowly evolving and interacting tiles, each of which supports a single spiral wave corresponding to a periodic or relative periodic solution. The fast transitions between topologically distinct solutions can similarly be understood as the local approach of the state to a small set of unstable critical solutions. Both the tiling decomposition and the approach to critical solutions reflect the persistence of local Euclidean symmetry resulting from weak spatial correlations in reaction-diffusion models of cardiac tissue excitation.

The description of sustained spiral chaos using the persistence of local Euclidean symmetry is conceptually simple but it is not merely qualitative. Single-spiral instabilities not only predict the development of spiral chaos from a single spiral wave –

in analogy to the transition from atrial tachycardia to atrial fibrillation – but the development of these instabilities in the presence of boundaries predicts the sustaining mechanism for the spatiotemporally chaotic state. Similarly, the adjoint eigenfunctions of a single-spiral solution predicts the organization of multi-spiral states in sustained spiral chaos, and the interaction between neighboring spirals on distinct tiles. Transitions between distinct multi-spiral configurations can also be understood in terms of local symmetries and the proximity of the state to exact saddle solutions, whose effect can be observed in the dominant directions of the tangent space.

Using a simple model of atrial tissue excitation developed to reproduce the qualitative instabilities expected to underly the onset of fibrillation, we found it necessary to extend the canonical sets of non-chaotic solutions to include drifting solutions on bounded domains (i.e. generalized relative periodic orbits) and apply novel numerical tools to compute them from nearby orbit fragments. Exact solutions of this numerical model were computed using a Newton-Krylov solver with a preconditioning method aimed at manipulating persistent local Euclidean symmetries on bounded domains. Additionally, we developed iterative factorization techniques, direct numerical simulation solvers, and bespoke interpolation methods for adjoint calculations to further characterize the dynamics in the linear neighborhood of the state. These tools enabled a number of investigations regarding the stability and symmetry properties of, in particular, single-spiral instances of generalized relative periodic orbits.

CHAPTER I

INTRODUCTION

1.1 Cardiac excitation

Heart muscle contractions are essential for pumping blood through the circulatory system and are controlled by the electrical stimulation of the tissue. The atria, followed by the ventricles, relax, filling with blood, and then contract coherently, pushing the blood out of the organ and to the rest of the body. This coordinated relaxation and contraction, referred to as normal rhythm, can be disrupted by various mechanisms leading to a range of arrhythmic behaviors. These arrhythmias can drastically reduce the efficiency of the pumping of the heart, contributing to the cardiac related disease as the leading cause of death in the developed world [99]. Fibrillation is one such arrhythmia characterized by turbulent dynamics featuring multiple interacting spiral waves where both the spatial and temporal coherence of the muscular contraction is destroyed, and the propagation of excitation is disrupted by conduction block [48, 79]. Ventricular fibrillation [49, 89] is particularly dangerous and, if not treated within minutes, can lead to death.

Numerous models of cardiac cell dynamics exist – as well as multiple models to combine them into a continuous medium (i.e., cardiac tissue) e.g., the monodomain and bidomain formulations. The majority of so-called monodomain models fall in the general class of reaction-diffusion systems [53, 54, 14, 108, 43, 158, 135, 47]. Besides cardiac tissue, reaction-diffusion systems are also used to model diverse phenomena such as chemical reactions [133, 110], bacterial chemotaxis [157, 166], and disease propagation [134]. All of these systems display turbulent solutions dominated by multiple interacting spiral waves, though the terminology to describe this regime varies:

e.g., defect-mediated turbulence [136], spiral chaos [91], spiral breakup [137], or spiral defect chaos [129]. This lack of consistency reflects the mostly empirical approach to the study of multi-spiral patterns and the lack of a fundamental understanding of the associated dynamics.

Cardiac arrhythmias, such as atrial and ventricular fibrillation, are characterized by spatially complex, high-dimensional dynamics that are generated as multiple excitation waves propagate through cardiac tissue, merging and breaking up. These processes involve multiple temporal and spatial scales, ranging from $O(1)$ ms for the excitation time to $200 - 400$ ms for the duration of an action potential, and $O(1)$ mm for the width of a wavefront to 20 mm for the action potential width in the epicardium [43]. Despite substantial advances in computing power and the development of detailed ionic models of cardiac cells, quantitatively accurate direct numerical simulation of cardiac tissue remains computationally expensive and provides limited dynamical insight into mechanisms that initiate and sustain the spatiotemporal chaos that underpins these arrhythmias.

During fibrillation, individual spiral waves possess rotational frequencies in excess of the normal rhythm pacing [71] and as a result are typically *strongly unstable*, often encountering refractory regions of tissue and breaking up within a few rotations [12, 72, 20]. However, at present our understanding of the properties and dynamics of unstable spirals, especially in the context of cardiac dynamics, is limited. Dynamical descriptions of fibrillation (and more generally, sustained spiral chaos) rely predominantly on the intuition gleaned from the studies of *stable* solitary spirals. In particular, Barkley *et al.* [18] showed that even very simple reaction-diffusion models can produce qualitatively different types of spirals.

1.2 Symmetry and wave-particle duality

Spiral and scroll waves are robust solutions of excitable and oscillatory media in, respectively, two and three spatial dimensions. The stability of these solutions is described by the spectra of the tangent evolution operators obtained by linearizing the governing equations. Although the governing equations describing homogeneous and isotropic media respect Euclidean symmetry (on the $\mathbb{R}^2$ plane), the particular wave solutions are not invariant under the action of this group. As a result, the respective evolution operators are generically non-self-adjoint, so that their right (conventional) eigenfunctions are not mutually orthogonal and do not coincide with the left (adjoint) eigenfunctions.

Although non-trivial wave solutions do not respect the underlying Euclidean symmetry of the evolution equation, the symmetry manifests itself in the emergence of marginal modes (with zero growth-rate) in the spectrum of the tangent evolution. In two dimensions the spectrum ideally contains three marginal modes which correspond to the three continuous Euclidean symmetries: translation in the two directions spanning the plane and in-plane rotation [16]. The corresponding modes are known as Goldstone modes in Quantum Field Theory and Pattern Formation. The corresponding adjoint eigenfunctions have been termed response functions [35]. For stable spiral waves the Goldstone modes represent the dominant degrees of freedom and, in the presence of weak interactions, their evolution is naturally described in terms of the response functions.

The earliest work illustrating the role of response functions in the context of reaction-diffusion systems is due to Keener [112] who investigated the dynamics of scroll wave filaments. Scroll waves with a straight untwisted filament can be unstable even if the corresponding two-dimensional spiral wave solution is stable: the bend or twist of the filament leads to self-interaction which causes transverse motion of the filament that, for small curvature and torsion, can be described with the help of the

response functions.

The weak interaction picture also motivated investigations which aimed to describe the drift of stable spirals in two dimensions. Biktashev and Holden [28] showed that experimental and numerical results describing the dynamics of a spiral wave in the presence of resonant forcing, perturbations of parameters, or interaction with the boundary can be understood using an empirical model containing three coupled ordinary differential equations (ODE) for the position of the wave core and the phase of the wave. In a subsequent paper the same authors [26] showed that the ODEs can be derived with the help of the three response functions.

Barkley [16] and Barkley and Kevrekidis [17] showed that the tip dynamics for both pinned and meandering spirals can be reproduced using a system of five weakly nonlinear ordinary differential equations (ODE) derived by assuming the dynamics are equivariant under the Euclidean symmetry group. These ODEs describe the evolution of the spiral tip in two spatial dimensions, the velocity of the tip, and the instantaneous rotational velocity of the wave about the tip. As neither the position nor the phase enter into the right hand side due to the equivariance of the evolution equations, the ODEs can be reduced identically to a two-dimensional system, with the understanding that the position and phase dynamics are essentially reconstruction equations and set the origin of the group manifold. Fiedler *et al.* [75, 76] showed that, more generally, equivariance with respect to non-compact, finite-dimensional Lie groups (such as the Euclidean group $E(d)$) allows description of the dynamics near relative equilibria (such as rigidly rotating spirals) in terms of a skew-product flow, where the motion transverse to the group manifold is decoupled from the motion on the group manifold.

Generally, stable spiral waves may rotate rigidly about a fixed position, or it may deform in time and the origin of the spiral will be time-dependent. By using a reference frame rotating with the spiral, the tip dynamics can be simplified: in the first

case the tip becomes stationary while in the second it executes a periodic motion. These spirals are referred to as pinned or meandering spiral waves, respectively. Typically, pinned spiral waves are attached to macroscopic heterogeneities of the tissue or medium, e.g. blood vessels, but this is a superficial distinction of scale and describes spirals pinned to microscopic features just as well. Barkley [15] subsequently showed that Newton-Krylov methods can be used to efficiently compute pinned spiral waves in a rotating reference frame in which they become stationary (i.e., are described by relative equilibria). He also computed their leading eigenvalues using Arnoldi iteration [87] and verified that transition from pinned to meandering spirals (relative equilibria to relative periodic orbits) is described by a Hopf bifurcation. The same approach was later applied to unstable spiral waves in a model of cardiac tissue by Allexandre and Otani [2].

Locally, the group manifold represents all symmetry transformations of a particular solution. For instance, in two dimensions, the skew decomposition separates the evolution of the shape of the spiral from the changes in the position or phase of the spiral. Sandstede *et al.* performed a center manifold reduction of the dynamics near relative equilibria [150] and near relative periodic orbits [151], formalizing and extending the reduced description of Barkley and Kevrekidis [16, 17] to physical spaces of arbitrary dimensionality. Further discussion of symmetries and equivariant dynamics in particular is available in Chossat and Lauterbach [51].

Periodic orbit theory attempts to quantitatively understand the dynamics of chaotic systems, such as (most relevantly for the present discussion) turbulence. This formalism explores the dynamics of turbulence as the transitions between several unstable exact solutions, following the stable and unstable manifolds of these solutions. The method has found significant success in plane-Couette fluid flow [167, 86, 85, 93]. In principle, similar techniques should apply to other kinds of spatiotemporal chaos,

such as the sustained spiral chaos of reaction-diffusion models of cardiac tissue excitation.

Reaction-diffusion systems often respect continuous Euclidean symmetries – constrained primarily by the homogeneity of the medium – which complicates a dynamical description based on periodic orbit theory [90, 63]. In particular, continuous symmetries give rise to several other dynamically relevant classes of non-chaotic unstable solutions, such as relative equilibria and relative periodic orbits, which reduce to equilibria and time-periodic orbits in a co-moving reference frame. Notably, the numerical methods for computing such solutions in co-moving frames were developed in the context of excitable/oscillatory systems such as the Barkley model [15, 96], FitzHugh-Nagumo [77], $\lambda - \omega$, and complex Ginzburg-Landau model [56]. In two (or three) dimensions, however, rotational symmetry requires that the computation be performed on a circular (or cylindrical) domain, using a polar grid, which severely limits the usefulness of this approach.

Beyn and Thümmler [23] developed a numerical method for computing the dynamics near relative equilibria on unbounded domains which used the skew-product representation of the dynamics to eliminate or "freeze" the dynamics along the group manifold. The freezing approach was later used by Beyn and Lorentz [22] to numerically compute the entire stability spectra for pinned spiral waves. They also found good agreement between the numerically computed eigenvectors associated with marginal eigenvalues and the Goldstone modes associated with infinitesimal translations and rotations of the spiral wave. The same approach was later used by Hermann and Gottwald [98] to investigate the dynamics of spiral waves in the large-core limit and by Foulkes and Biktashev [78] to characterize drift and meandering of spiral waves.

The response functions, unlike the Goldstone modes, were not computed for any reaction-diffusion systems until much later. Biktasheva *et al.* [35] computed them for

the spiral waves in the complex Ginzburg-Landau equation (CGLE), which describes the generic dynamics of a broad class of spatially extended systems close to the onset of the oscillatory instability, and Henry and Hakim [95, 96] computed response functions for scroll waves in the Barkley model of excitable media. In both instances the calculations were performed in a co-rotating reference frame which transforms the originally time-dependent formulated solutions (relative equilibria) into steady states (absolute equilibria). This reduction based on the equivalence of the temporal evolution and rotation has been employed for computing the adjoint eigenfunctions in nearly all subsequent studies.

With the help of the computed response functions it was possible to check that there is not just qualitative, but also quantitative agreement between numerical simulations and the ODE-based model for the resonant drift of spiral waves in CGLE [37] in the Eckhaus-stable parameter regime. All three response functions (adjoint to translational and rotational Goldstone modes) were found to decay exponentially with the distance to the spiral core for the CGLE, in agreement with the analytical prediction [35]. Exponential localization was later found even in the Eckhaus-unstable parameter regime [31].

Response functions can be used to describe the interaction of spiral waves not only with boundaries, but also with other spiral waves. Indeed, exponentially decaying interaction for spiral wave solutions of CGLE was predicted previously using the amplitude-phase equation formalism [7, 141, 142]. The analytical results obtained for CGLE, however, cannot be extended to strongly nonlinear waves in excitable media. The response function formalism, in the absence of a simplified solution description, is the only tractable means of predicting the evolution of spiral waves in response to internal or external perturbations.

Quite interestingly, the response functions were found to be exponentially localized

also for the Barkley [96], FitzHugh-Nagumo [36], Oregonator [34], and Beeler-Reuter-Pumir [25] models, suggesting that, as a rule, the spiral core acts as the organizing center for the wave, although there are rare counter-examples [27] such as the Mornev model [128].

The exponential localization of the response functions enables quantitative description of the dynamics of the spiral core as a singular forced object. As Ref. [32] put it, "spiral waves look like essentially nonlocalized objects but behave as effectively localized particles." As a result, despite the dissipative nature of excitable media, one finds a wave-particle duality that is more akin to that found in Hamiltonian-governed quantum systems. For example, Langham and Barkley [115, 116] used the response function formalism to show that core of a resonantly driven spiral in a bounded domain moves almost like a classical particle, although reflections from the "walls" are characterized by a strongly nonlinear relation between the incident and reflected angle.

1.3 Spiral wave chaos

When the spiral or scroll wave is unstable, its dynamics can not be described solely in terms of the marginal degrees of freedom (i.e., Goldstone modes and response functions). Instead, one must also consider the evolution of all the unstable modes. The only relevant study that we are aware of is due to Allexandre and Otani [2] who considered the problem of feedback control of unstable spiral wave solutions of the Fenton-Karma [69] model. In addition to the response functions, the eigenfunctions adjoint to all of the unstable modes were computed. The structure of the unstable adjoint eigenfunctions is especially important in the context of control of these dynamical patterns as it allows significant optimization of the controller input voltage [82, 83].

The simplest type of spiral wave solution considered – those described by relative

equilibria – can be reduced to a steady state in a rotating reference frame. However, typical single-spiral states involve more complex types of solutions. For instance, the simplest type of a spiral wave on a bounded domain of generic shape is described by a periodic solution. The simplest meandering spirals are described by relative periodic solutions that are reducible to periodic solutions in a translating and rotating reference frame. The generalization of even the most basic results obtained for relative equilibria to more complex types of solutions is far from straightforward. Furthermore, it is not understood what kind of effects are introduced by the intrinsic time-dependence of the shape of a spiral wave. Most importantly, multi-spiral dynamics are generally not reducible by global symmetry transformations, and thus the technique of global symmetry reduction is of limited relevance for spatiotemporal chaos – or more specifically, sustained spiral chaos.

Substantial progress in understanding some types of spatiotemporal chaos has been made over the past two decades using an idea that is now over a century old. In developing celestial mechanics, Poincaré [143] realized that unstable equilibria and periodic orbits provide a skeletal structure which organizes chaotic dynamics. His idea was later developed in the context of quantum chaos by Gutzwiller [90] and subsequently applied to high-dimensional chaos generated by nonlinear partial differential equations such as the Kuramoto-Sivashinski equation [52, 114] and Ginzburg-Landau equation [118].

Although in one spatial dimension unstable periodic solutions could be computed using brute-force Newton iteration, this numerical approach becomes intractable for two- and three-dimensional PDEs whose discretization routinely involve millions of degrees of freedom. In this case both non-chaotic solutions and their spectra can be computed efficiently [167] using a combination of Newton descent, Krylov subspace or GMRES solution of the Newton equations, and "trust-region" heuristic for the magnitude of the Newton steps. Newton-Krylov methods facilitated recent studies of

various fluid flows at intermediate Reynolds numbers [86, 125, 60, 46], which produced valuable new insight into the mechanisms that generate and sustain fluid turbulence – arguably the most challenging unsolved problems of classical physics. Although periodic orbit theory has never been used to analyze spatiotemporally chaotic dynamics in excitable systems, its success in uncovering the mysteries of fluid turbulence gives us hope that it can also generate new insights into the problem of fibrillation and thereby help develop new and improved methods of defibrillation [101, 168, 121].

Despite the progress that has already been made in using unstable non-chaotic solutions to understand chaotic dynamics, many open problems remain. In particular, it is not always clear what types of unstable non-chaotic solutions play a dominant role in spatiotemporal chaos. For spatially extended systems, non-chaotic solutions are characterized not only by their temporal properties (e.g. equilibria, periodic orbits), but also by their spatial structure. In fact, the spatial structure received far more attention in the studies of fluid flows, which motivated the recent development and application of periodic orbit theory to fluid turbulence. As a result, non-chaotic solutions of nonlinear partial differential equations embedded in the chaotic set on which the dynamics take place have become known as exact coherent structures, reflecting their connection with the empirically observed coherent structures within fluid flows. A similar conceptual approach can be applied to sustained spiral chaos and the features which dominate this regime – spiral waves – through a consideration of local symmetry. For recurrent multi-spiral states the persistence of Euclidean symmetries in the presence of boundaries generates slow relative drift and relative rotation of the spiral waves.

1.4 Objectives and outline

To date, quantitative descriptions of cardiac arrhythmias are predominantly informed by numerical simulation of ever-more-detailed cellular models. These models describe

the excitability of different tissues, both within the same organ and across species – and involve markedly distinct numbers of variables and parameters. However, as tachycardia and fibrillation occur in many distinct tissues and species, the underlying dynamical mechanisms are in some sense universal, and minimal models should effectively provide insight into their development. Similarly, the relative cost of investigating detailed ionic models numerically means that the use of minimal models which qualitatively reproduce the patterns of fibrillation instead can be effectively investigated in different ways, such as those based on the machinery of dynamical systems – in particular a description of the dynamical patterns typical of fibrillation in terms of exact solutions. From this perspective, a central open question is what the relevant set of solutions for fibrillation-like sustained spiral chaos?

These, and other questions, will be addressed throughout this text. We will attempt to quantitatively explain the development of fibrillation-like dynamics from simpler unstable exact solutions, i.e., (relative) periodic orbits, using just such a minimal model of cardiac excitation. In particular, we shall describe simple unstable exact solutions and their role in organizing the spatiotemporally chaotic state. Then we shall investigate how to combine these exact solutions into more complex states which do not correspond to exactly periodic structures, and their role in sustained spiral chaos. Finally, we attempt to describe a universal mechanism for topological changes in the underlying state using conduction block and the implications of this description for a geometrical picture of extensive spatiotemporal chaos.

In Ch. 3 we investigate the properties of unstable single-spiral waves and their Floquet spectra, especially as they relate to the interaction with no-flux boundaries. In Ch. 4 we expand on the single-spiral results and show that the non-perturbative imposition of boundaries can be explained using the response function formalism. In Ch. 5 we discuss the segmentation of a multi-spiral state into single-spirals using tiling. We consider topological transitions of fully-developed spiral wave chaos in

Ch. 6 and characterize the tangent space for these types of solutions, relating some to unstable solutions in one spatial dimension. Finally, we conclude in Ch. 7.

CHAPTER II

BACKGROUND

In this chapter we begin with a simple description of excitable dynamics and cardiac cellular dynamics in particular. We then relate the dynamics of excitable cells to spatially-extended excitable dynamics, i.e. cardiac tissue, and briefly motivate the derivation of the idealized monodomain equations from the physiologically detailed bidomain formulation. We introduce the governing dynamical system for the particular cardiac cellular dynamics. We then begin the exploration of invariant solutions of the reaction-diffusion system with uniform equilibria and traveling waves and specifically their linear stability. In the next two chapters we consider the central results concerning single-spiral solutions on bounded domains – (relative) periodic orbits – and their stability. For these kinds of solutions, both the left (adjoint) and right (canonical) eigenfunctions inform the dynamics of the spiral wave, with the former indicating, e.g. the dynamics of the spiral core, and the latter controlling the dynamics of the far-field. This leads to a consideration of multi-spiral solutions, including relative periodic orbits which control the dynamics between core collisions and conduction block. Finally, we discuss some many-spiral dynamics and in particular, the dynamically preferred inter-core spacing and its relation to the adjoint eigenfunctions on no-flux bounded domain.

2.1 Cardiac tissue and excitable dynamics

Passively excitable heart tissue is comprised of specially adapted muscle cells called cardiomyocytes arranged in an irregular grid with orientation and anisotropy, otherwise known as striated muscle tissue. The cardiomyocytes are roughly elongated

rectangular prisms, and their coordination in tissue aligns locally to form a quasi-rectilinear lattice. The conductivity of this tissue is anisotropic, reflecting the anisotropy of the cardiomyocytes, and preferentially conducting along the longest dimension of the cells, i.e., "along the fiber". Each cardiomyocyte contains within it stores of calcium, sodium, potassium, and other biochemically important ions [74]. The ions pass through large numbers of pores in the membrane, the ionic channels. These ionic currents generate a net de- or repolarization of the cellular membrane, or action potential. The depolarization relaxes back toward the pre-excitation value over a relatively long time-scale compared to the excitation time of the action potential. A more detailed description of the action potential involves four canonical segments distinguished by the dominant features of the waveform, (see Fig. 1). The rapid depolarization corresponds to an influx of sodium ions, and concomitant increase in the sodium density. Then a short decay which is due to the sodium-channel inactivation and a repolarizing efflux of potassium. The action potential then plateaus, resulting from the opening of voltage-sensitive calcium channels, for a time-span which depends on previous excitations. Finally, the action potential relaxes to the rest state due to the cumulative effects of the sodium-channel inactivation. Broadly, we have introduced the basic features of cardiac excitation modeling. After stimulation, the tissue action potential goes through a very fast depolarization, followed by repolarization on a much longer time-scale. Several ionic concentrations and the transmembrane potentials interact, forming a excitation-relaxation cycle, or in the presence of external forcing, an excitation-relaxation oscillator.

There exist a plethora of numerical models of cellular excitation, ranging from discrete models, to simplified two-variable models, to detailed ionic models representing detailed evolution for $O(100)$ state variables. A long, but still not exhaustive, list of cellular models associated with cardiac dynamics and other idealized excitable systems is given in Ref. [70]. In Sec. 2.2, we describe in detail the specific excitation

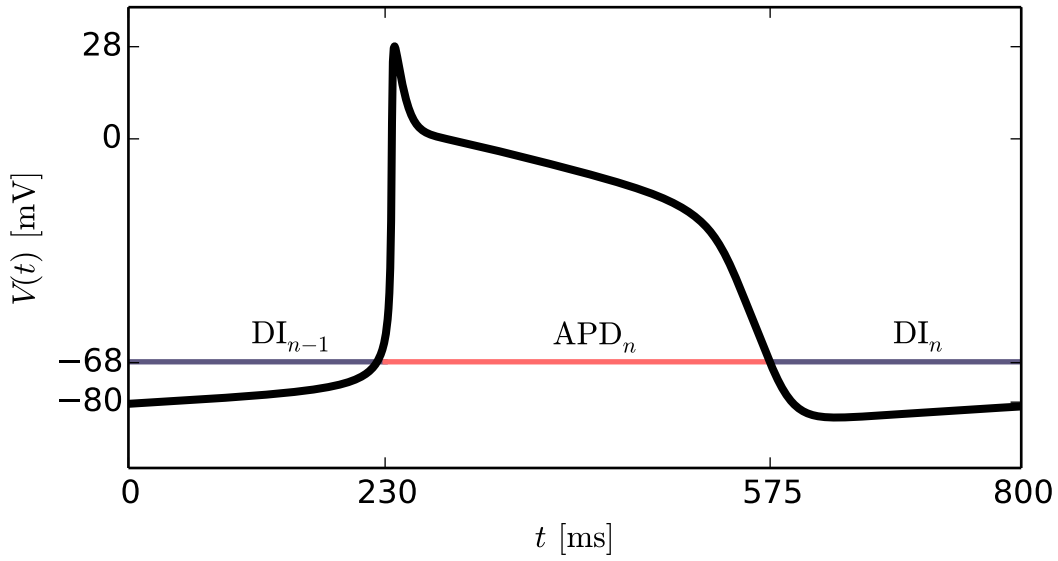

Figure 1: Representative action potential excitation voltage over time $V(t)$ for a full depolarization-relaxation cycle for the Noble model [135] of cellular kinetics.

model used for the present work.

In addition to the subtleties of the cellular dynamics, the spatial configuration of the dynamics of the voltage across the tissue requires its own discussion. Nominally, this deals with the distinction between the bidomain and monodomain models of cardiac tissue, the coupling between cells within the tissue, and issues of heterogeneity in the tissue structure [145, 74]. Bidomain models of cardiac tissue concern not only transmembrane potential φ_t but the intracellular φ_i and extracellular φ_e potentials. The bidomain model was formulated in the late 1970s [126, 140, 139, 65, 130, 132, 131, 165] and generalizes the results of the theory of voltage propagation along a cable. We begin with a heuristic construction of the bidomain formulation of action potential dynamics to establish nomenclature and scale. From Ohm's law, the current $\mathbf{J}$, potential φ, and conductivity G are related through the electric field $\mathbf{E}$,

$$\mathbf{J} = G\mathbf{E} \equiv -G\nabla\varphi, \tag{1}$$

which extends to the extracellular and intracellular domains in particular: $\mathbf{J}_e =$

$-G_e\nabla\varphi_e$ and $\mathbf{J}_i = -G_i\nabla\varphi_i$. Assuming only membrane sources,

$$\nabla\cdot\mathbf{J}_i = -I_m, \quad \nabla\cdot\mathbf{J}_e = +I_m, \tag{2}$$

where I_m is the transmembrane current density, defined in terms of the ion flow and the transmembrane potential, $\varphi_t \equiv \varphi_i - \varphi_e$. The divergence of the intracellular current $\mathbf{J}_i$ and the conservation of intra- and extracellular sources yields,

$$I_m = \nabla\cdot(G_i\nabla(\varphi_e+\varphi_t)), \quad \text{and} \quad 0 = \nabla\cdot(G_e+G_i)\nabla\varphi_e + \nabla\cdot G_i\nabla\varphi_t, \tag{3}$$

respectively. Identifying the transmembrane current in terms of the ionic contributions i_{ion} and the time-variation of the transmembrane potential, $I_m = \beta_m(C_m\mathrm{d}\varphi_t/\mathrm{d}t + i_{\text{ion}})$, where C_m is the cell-membrane capacitance and β_m is the ratio of the surface area to the volume of the cardiac cell, a closed set of partial differential equations for the extracellular and transmembrane potentials is found,

$$0 = \nabla\cdot(G_e+G_i)\nabla\varphi_e + \nabla\cdot G_i\nabla\varphi_t, \tag{4}$$

$$\beta_m\left(C_m\frac{\mathrm{d}\varphi_t}{\mathrm{d}t} + i_{\text{ion}}\right) = \nabla\cdot(G_i\nabla(\varphi_e+\varphi_t)). \tag{5}$$

When the intra- and extra-cellular conductivity tensors are similar, $G_e = \alpha G_i$, $\alpha\in\mathbb{R}$, the bidomain description simplifies to the monodomain formulation. The hyperbolic PDE, which relates the extra-cellular and transmembrane potentials, is rewritten to eliminate the non-diffusive differential term in the evolution equation:

$$\beta_m\left(C_m\frac{\mathrm{d}\varphi_t}{\mathrm{d}t} + i_{\text{ion}}\right) = \frac{\alpha}{1+\alpha}\nabla\cdot(G_i\nabla\varphi_t). \tag{6}$$

Equation (6) represents the physical form of the monodomain model approximation for the transmembrane potential. This is a parabolic nonlinear PDE for the temporal evolution of the transmembrane potential, involving an unspecified number of intercellular dynamical variables through the ionic term, i_{ion}. We shall expand on the specific form of the monodomain model used throughout this work in the next section.

Provided some conservative assumptions on the form of the boundary conditions and the form of φ_e, it is possible to construct an integro-differential equation for the transmembrane potential by inverting the constraint equation (4). I discuss preliminary results concerning this simplified formulation for bidomain systems in A.5.

2.2 Model description

Rather than a detailed ionic model of cardiac tissue excitation, throughout this work we use a variant of the Karma [107, 108] model. This model presents a simplified set of variables which generate the patterns typical of fibrillation and tachycardia through reproduction of the dominant instability associated with spiral wave breakup in tissue. We have made several modifications to the original system, with the goal to make the resulting set of coupled PDEs better conditioned, numerically. The original system presented in Ref. [108],

$$\partial_t E = \gamma \Delta E + \tau_E^{-1} f(E, n), \tag{7}$$

$$\partial_t n = \tau_n^{-1} g(E, n), \tag{8}$$

$$f(E, n) = -E + [E^* - n^M][1 - \tanh(E - E_h)]\frac{E^2}{2}, \tag{9}$$

$$g(E, n) = \frac{1 - [1 - \mathrm{e}^{-Re}]n}{1 - \mathrm{e}^{-Re}}\,\Theta(E - E_n) - [1 - \Theta(E - E_n)]n, \tag{10}$$

describes the temporal evolution of the dimensionless transmembrane potential $E = E(t, \mathbf{x})$ and a variable $n = n(t, \mathbf{x})$ which represents the essential interactions of a slow non-specific current gate. The parameter Re controls the restitution properties of the tissue, and in particular increasing Re makes the tissue recover faster, such that the action potential more quickly approaches its maximal value with increasing diastolic interval. Practically, Re can destabilize certain patterns by enhancing the restitution, making such patterns for susceptible to dynamical instability. The parameters τ_E and τ_n are characteristic time scales which control the relative time-scales of the cellular kinetics. Dispersion is partially controlled by the parameter M, whereby increasing M

lead to weaker dispersion. The diffusion coefficient γ describes the electrical coupling between adjacent cells in the tissue.

Equation (7) features discontinuous switching functions of the transmembrane potential $\Theta(E - E_n)$ which imply that the derivatives of $g(E, n)$ are similarly discontinuous. This naturally suggests a modification to Equation (7), whereby each discontinuous switching function is replaced by a continuous analogue, $\Theta(x) \to \Theta_s(x)$, where the switching is a sigmoidal function of the argument,

$$\Theta_s(x) \equiv \frac{1}{2}\left(1 + \tanh(sx)\right). \tag{11}$$

It is easy to see that $\lim_{s\to\infty} \Theta_s(x) \to \Theta(x)$ and all derivatives $\partial_x^n \Theta_s(x)$ are non-singular for finite s, thus the derivatives of the cellular dynamics are well-defined for this modification. Additionally, we modified the form of the kinetics function $g(E, n)$ specifically, through the introduction of new terms. In particular, we added terms based on numerical experience simulating Equation (7),

$$G(E, n) = g(E, n) + \Theta_s(n - n^*)(n - n^*), \tag{12}$$

The addition to $g(E, n)$ is designed to suppress the growth of a singular spike in the gating variable n observed near spiral wave cores in two spatial dimensions. This is a narrow region in which the values of n vary rapidly, and which introduce very sensitive dependence of the solution on the mesh spacing. This spike can not be adequately resolved on physiologically relevant mesh spacings Ch. 3 and is unphysical. Finally, we added diffusive coupling in the slow ionic channel between the cells, with diffusion coefficient $\nu\gamma$, where $0 \leq \nu \ll 1$, to further regularize the shape of solutions in the core region. Although diffusion is almost universally ignored in the equations describing the dynamics of gating variables, all relevant ions and even most secondary messengers such as IP3, cAMP, and cGMP can pass through the gap junctions between cells [21, 80], so the addition of a diffusive coupling for the gating variables is justified from the physiological properties of the ions and molecules this variable is intended to

represent. However, experimentally measuring the diffusive scale for these molecules in tissue is very difficult, so we merely keep the values small (via the control parameter $\nu \ll 1$).

Both the transmembrane potential variable E and the slow ionic current gate n are dimensionless, however the parameters γ, τ_E, and τ_n, as well as the spatial $\mathbf{x}$ and temporal t variables are dimensional. We non-dimensionalize the spatial scales using the cardiomyocyte size $\xi = 0.0262\,\mathrm{cm}$, and the temporal scale using the shorter of the two time-scales, $\tau_E = 2.5\,\mathrm{ms}$. After re-assigning t to the dimensionless time and $\mathbf{x}$ to dimensionless space, we arrive at a reaction-diffusion evolution equation,

$$\partial_t \mathbf{u} = D\nabla^2 \mathbf{u} + \mathbf{f}(\mathbf{u}), \tag{13}$$

wherein the cellular kinetics $\mathbf{f}(\mathbf{u})$ are determined by the functional form,

$$\mathbf{f}(\mathbf{u}) = \begin{bmatrix} (u^* - u_2^M)\{1 - \tanh(u_1 - 3)\}u_1^2/2 - u_1 \\ \epsilon\{\beta\Theta_s(u_1 - 1) + \Theta_s(u_2 - 1)(u_2 - 1) - u_2\} \end{bmatrix}, \tag{14}$$

$\mathbf{u} = [u_1, u_2](t, \mathbf{x})$, and t, $\mathbf{x}$ are the non-dimensional time and space variables respectively. The term $\partial_t \mathbf{u}$ is the non-dimensional time derivative, $\nabla \mathbf{u}$ is the non-dimensional gradient, and $E^* \to u^*$, $E_h \to 3$, $E_n \to 1$, and $n^* \to 1$. Additionally, we have defined $\beta = (1 - \exp(-Re))^{-1}$, and $\epsilon = \tau_E/\tau_n$. The diffusion tensor is diagonal in the variable indices, $D = \mathrm{diag}(D_{11}, D_{22})$, where $D_{11} = \gamma\tau_n/\xi^2$ and $D_{22} = \nu D_{11}$, i.e., $D_{12} = D_{21} = 0$. The structure of the diffusion tensor D assumes that there is no induced transport in the ionic gating currents from the transmembrane potential, and vice-versa. The numerical values used throughout this work are summarized in Table 1, unless otherwise specified. In Figure 2(a-c), we demonstrate the effects of varying s values on the cellular kinetics via the nullclines of (14).

To fully define the evolution of the initial value problem, (13) must be amended with boundary conditions. Throughout this work we shall assert the specific form as necessary, but we shall deal with "no-flux" and periodic boundary conditions in turn.

Table 1: Values of the parameters used in Equation (14) throughout this work, with the interval denoted for s.

parameter	u_1^*	M	ϵ	β	s	D_{11}	ν
value	1.5415	4	0.01	1.389	$[1.2571, 32]$	4.0062	0.05

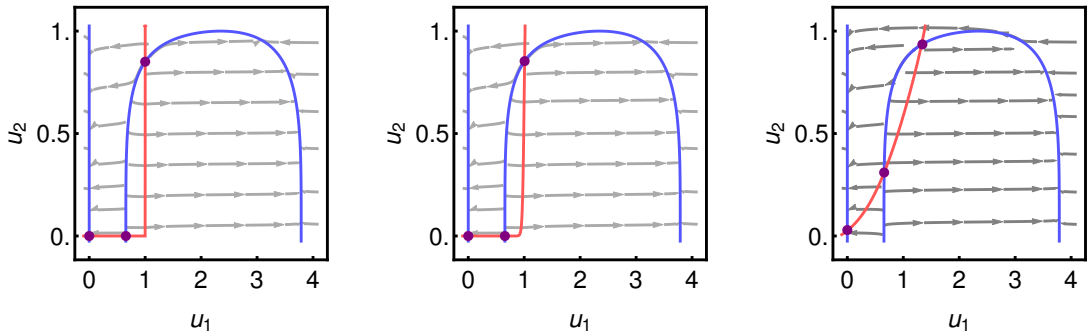

(a) (b) (c)

Figure 2: Nullclines (blue $f_1(\mathbf{u}) = 0$, red $f_2(\mathbf{u}) = 0$), flow field (grey arrows), and equilibria (purple dots) of $\mathbf{f}(\mathbf{u})$ for the original (non-dimensionalized) system (a), the large-s ($s = 32$) limit (b), and the low-s limit ($s = 1.2571$) (c).

No-flux boundary conditions follow from considering the form of the linear operator as the divergence of a current, as in (6). The no-flux condition requires that the net current through the boundary of the domain vanish instantaneously, such that

$$\hat{\mathbf{n}}(t, \mathbf{x}) \cdot \nabla \mathbf{u}(t, \mathbf{x})|_{\partial\Omega} = \mathbf{0}, \tag{15}$$

where $\hat{\mathbf{n}}(t, \mathbf{x})$ is the outward-oriented normal to the boundary of the domain at time t and position $\mathbf{x} \in \partial\Omega$ on the boundary. The no-flux condition reflects the most basic structure of the underlying tissue, which has boundaries through which current does not flow readily and may be considered, to a very good approximation, as non-conductive.

Alternatively, the domain may be compact, or represent a small portion of the tissue embedded within a larger tissue. In this case, it is justifiable to consider a small periodic domain as representative of the dynamics of the physical system. The periodic boundary conditions can be written as

$$\mathbf{u}(t, x) = \mathbf{u}(t, x + L), \quad \nabla \mathbf{u}(t, x) = \nabla \mathbf{u}(t, x + L), \tag{16}$$

on a one-dimensional domain of length L. The choice of boundary condition impacts several aspects of the nonlinear system which we shall introduce when appropriate.

We can describe the time evolution of the fully nonlinear flow (13) with cellular kinetics (14) and associated boundary conditions (15)-(16) by the shorthand map

$$\mathbf{u}(t + t', \mathbf{x}) = \mathcal{U}_t \mathbf{u}(t', \mathbf{x}), \tag{17}$$

for specified initial condition $\mathbf{u}(t', \mathbf{x})$ at time t'. The evolution operator $\mathcal{U}_t$ maps an initial condition to the state time-t later. The nonlinear map operator is simply connected to the identity, $\mathcal{U}_0 \equiv \mathbf{1}$, and composes in the expected way,

$$\mathbf{u}(t + t' + t'', \mathbf{x}) = \mathcal{U}_{t''} \mathbf{u}(t + t', \mathbf{x}) = \mathcal{U}_{t''} \mathcal{U}_{t'} \mathbf{u}(t, \mathbf{x}), \tag{18}$$

indicating that the nonlinear flow satisfies the properties of a semi-group. The main thrust of this work deals with non-trivial solutions of (17) and symmetric variations thereof, but before those we shall discuss simpler structures.

The evaluation of (13) and generally (17) is handled numerically, using a second-order $O(\Delta x^2)$ finite-difference discretization of the Laplacian in two spatial dimensions, a ghost-point method for the boundary conditions, and a fourth-order $O(\Delta t^4)$ explicit Runge-Kutta time-stepping scheme, where Δx and Δt are the spatial and temporal discretization scales. These numerical procedures are detailed in Sec. A.1 and Sec. A.2, respectively.

When the normal rhythm of the is disrupted and the symmetry of the propagation is broken, the propagation of excitation becomes qualitatively different. In atrial tissue, which is too thin to support variations along its depth and thus considered two-dimensional, the excitation wave develops into a spiral wave. This transition is identified as the development of tachycardia in medicine [138], and is characterized by a single dominant frequency of excitation corresponding to the rotational period of the spiral wave. Unlike the normal rhythm, tachycardia is only a transient behavior typical of functional reentry of the excitation [71]. Typically, tachycardia develops into fibrillation – a regime featuring multiple spiral waves – which is fatal.

Fig. 3 shows several snapshots of the u_1-variable from a long trajectory exhibiting sustained spiral chaos. This dynamical regime features multiple spiral waves continually interacting with each other. These states qualitatively represent the dynamics typical of atrial fibrillation.

2.3 Zero- and one-dimensional solutions

The nonlinear PDE model (13) possesses three uniform steady states (equilibria) in the region $(u_1, u_2) \geq 0$, which depend on the parameters of the underlying kinetics,

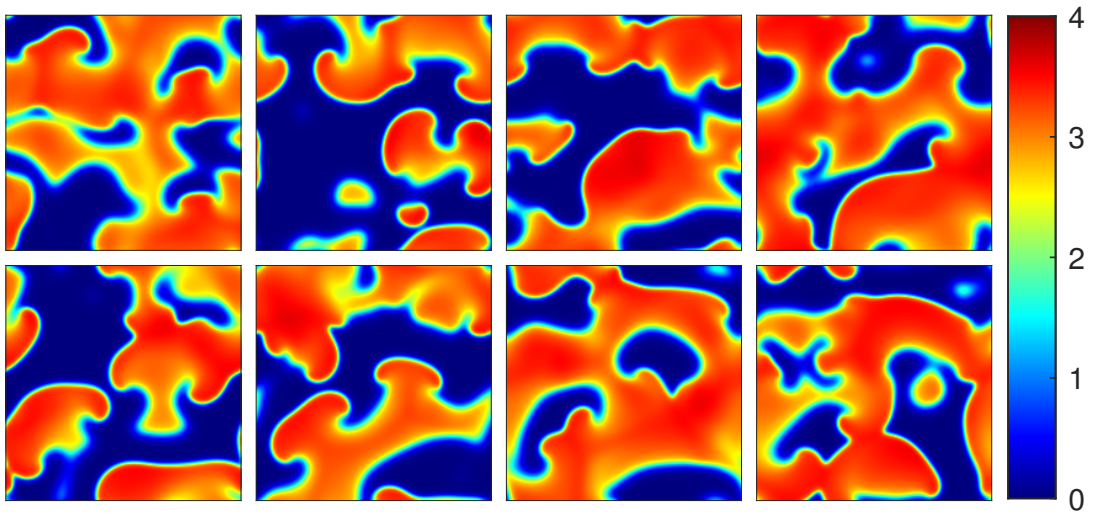

Figure 3: Snapshots of $u_1(t, \mathbf{x})$ from a long trajectory exhibiting sustained spiral chaos in two-dimensions with periodic boundary conditions and domain side-length $L = 192$.

and in particular on the value of the stiffness parameter s. These states satisfy

$$\partial_t \mathbf{u}(t, \mathbf{x}) = \mathbf{0}, \quad \nabla \mathbf{u}(t, \mathbf{x}) = \mathbf{0}, \tag{19}$$

that is, they are spatially extended, have no spatial variation, and do not evolve in time. It behooves us to discuss, first, the properties of these uniform steady states in the absence of any spatial information – as equilibria of the uncoupled cellular kinetics, (14).

There is always a uniform steady state which corresponds to quiescence, or no excitation in the tissue, as $\mathrm{EQ}_1 \approx \mathbf{0}$. The equilibrium EQ_1 is always stable for the cellular dynamics, as it defines the rest state, or absence of excitations. The generic case for excitable systems possesses only this equilibrium value [106]. Additionally, there is a steady state solution EQ_2 which delineates uniform perturbations which initially grow from those which immediately decay – as it sits on the nullcline which triggers excitability – and is a hyperbolic equilibrium. Finally, the steady state which corresponds to large transmembrane potential and large ionic current EQ_3 is an unstable focus equilibrium.These steady states are denoted by dots $(\cdot)$ at the intersections

of the nullclines in Figure 2.

For the spatially-extended PDE model (13), the stability of each steady-state solution is not merely described by the in- and out-flow of trajectories in a two-dimensional plane spanned by u_1 and u_2. Instead, we must consider the growth and decay of perturbations with spatial structure. We consider the dynamics nearby uniform steady states $\mathbf{u}_i \in \{\mathrm{EQ}_1, \mathrm{EQ}_2, \mathrm{EQ}_3\}$ and consider small perturbations to the state $\mathbf{u}(t, \mathbf{x}) = \mathbf{u}_i(t, \mathbf{x}) + \varepsilon \mathbf{v}(t, \mathbf{x})$. Substituting the linear variation into (13), the dynamics of the perturbation follow

$$\partial_t \mathbf{v}(t, \mathbf{x}) = D\nabla^2 \mathbf{v}(t, \mathbf{x}) + \mathbf{f}'(\mathbf{u}_i) \cdot \mathbf{v}(t, \mathbf{x}) + O(\varepsilon). \tag{20}$$

Here, $\mathbf{f}'(\mathbf{u}_i) = \partial \mathbf{f}(\mathbf{u})/\partial \mathbf{u}$ evaluated at the equilibrium point $\mathbf{u}_i$.

In an effort to not artificially restrict the symmetry of the solution, we shall assume bi-periodic boundary conditions on an infinite domain. The eigenfunctions of the differential operator consistent with these boundary conditions are Fourier modes, $\exp(\mathrm{i}\mathbf{q}\cdot\mathbf{x})$. The perturbation is, formally, an integral over the continuous set of modes

$$\mathbf{v}(t, \mathbf{x}) = \int \mathrm{d}\mathbf{q}\, \mathrm{e}^{\sigma_\mathbf{q} t}\, \mathrm{e}^{\mathrm{i}\mathbf{q}\cdot\mathbf{x}}\, \mathbf{V}(\mathbf{q}), \tag{21}$$

where the wavevector $\mathbf{q}$ is continuous, and we have absorbed the normalization of the field $\mathbf{v}(t, \mathbf{x})$ into the mode amplitudes $\mathbf{V}(\mathbf{q})$. On bounded domains, the periodic boundary conditions restrict the wavevectors to a discrete set: $\mathbf{q} = 2\pi[k_1, \ldots, k_d]/L$, where now k_i are integers. This discretization is essential and occurs for the modal bases of other domains and boundary conditions as well. Similarly, we have assumed linear growth of each mode, distinguished by continuous index, q: σ_q. Substituting this expansion into the evolution equation for $\mathbf{v}(t, \mathbf{x})$, (20), and considering a single value of the wavevector,

$$\sigma_\mathbf{q} \mathbf{V}(\mathbf{q}) = -Dq^2 \mathbf{V}(\mathbf{q}) + \mathbf{f}'(\mathbf{u}_i) \cdot \mathbf{V}(\mathbf{q}) + O(\varepsilon). \tag{22}$$

Thus the stability of these uniform states is, plainly, determined not only by the local cellular kinetics through $\mathbf{f}'(\mathbf{u}_i)$ but by the interaction of these kinetics with the spatial

variation. As $\mathbf{V}(\mathbf{q})$ is a two-dimensional vector of the variable $\mathbf{q}$, we pose the system as a simple eigenvalue equation for the growth rate $\sigma_{\mathbf{q}}$,

$$\sigma_{\mathbf{q}} \begin{pmatrix} V_1(\mathbf{q}) \\ V_2(\mathbf{q}) \end{pmatrix} = \begin{pmatrix} -D_{11}q^2 + \mathbf{f}'_{11}(\mathbf{u}_i) & -D_{12}q^2 + \mathbf{f}'_{12}(\mathbf{u}_i) \\ -D_{21}q^2 + \mathbf{f}'_{21}(\mathbf{u}_i) & -D_{22}q^2 + \mathbf{f}'_{22}(\mathbf{u}_i) \end{pmatrix} \begin{pmatrix} V_1(\mathbf{q}) \\ V_2(\mathbf{q}) \end{pmatrix}. \tag{23}$$

As this is only a two-dimensional system, it is possible to solve it analytically, which gives some insight on the properties of the fully realized partial differential equation in the vicinity of uniform steady state $\mathbf{u}_i$. The growth rates (asserting $D_{12} = D_{21} = 0$) for steady state $\mathbf{u}_i$ are

$$\sigma_{\mathbf{q}}^{(\pm)} = \frac{1}{2}\left(-q^2 \mathrm{tr} D + \mathrm{tr}\, \mathbf{f}'(\mathbf{u}_i) \pm \sqrt{4\mathbf{f}'_{12}(\mathbf{u}_i)\mathbf{f}'_{21}(\mathbf{u}_i) - B(\mathbf{q})^2}\right), \tag{24}$$

where we have written $B(\mathbf{q}) = -(D_{11} - D_{22})q^2 + (\mathbf{f}'_{11}(\mathbf{u}_i) - \mathbf{f}'_{22}(\mathbf{u}_i))$, with corresponding eigenvectors

$$\mathbf{V}^{(\pm)}(\mathbf{q}) = \begin{pmatrix} -B(\mathbf{q}) \mp \sqrt{4\mathbf{f}'_{12}(\mathbf{u}_i)\, \mathbf{f}'_{21}(\mathbf{u}_i) - B(\mathbf{q})^2} \\ -2\mathbf{f}'_{21}(\mathbf{u}_i) \end{pmatrix}. \tag{25}$$

Computing the equilibria of Equation (14) in general is a numerical undertaking given a particular set of parameters. For the equilibria defined near the beginning of this section, EQ_1, EQ_2, and EQ_3, their positions in the (u_1, u_2)-plane are given in Table 2, and their maximal growth rates are shown in Figure 4 for a one-dimensional solution, where $\mathbf{q} = q\hat{\mathbf{q}}$.

Clearly the uniform steady state solution EQ_1 is stable ($\mathrm{Re}\,\sigma_q \leq 0$) for the chosen parameter sets. This agrees with the physiological intuition afforded by the rest state, that which dies stays dead without persistent forcing. The uniform steady state EQ_2 is unstable ($\mathrm{Re}\,\sigma_q > 0$) to perturbations with long wavelengths, $|q| \lesssim 0.3$, categorizing this instability as Type IIIs, as $\mathrm{Im}\,\sigma_q = 0$ [55]. The unstable spiral solution EQ_3 is, of course, unstable with respect to uniform perturbations, $\mathrm{Re}\,\sigma_q > 0$ for $q = 0$, and for $s = 32$ is oscillatory Type IIIo [55] ($\mathrm{Im}\,\sigma_q = 0.55$) while it is instead Type IIIs

Table 2: Uniform steady-state solutions EQ_1, EQ_2, and EQ_3, for the parameter set shown in Table 1 with $s = 1.2571$, $s = 32$, and $s = 10^3$ (representative of the asymptotic values).

$s = 1.2571$	EQ_1	EQ_2	EQ_3
u_1	0.0	0.658535	1.34189
u_2	0.029048	0.309842	0.935026
$s = 32$	EQ_1	EQ_2	EQ_3
u_1	0.0	0.654674	1.00728
u_2	0.0	3.5×10^{-10}	0.853347
$s = 10^3$	EQ_1	EQ_2	EQ_3
u_1	0.0	0.654674	1.00022
u_2	0.0	0.0	0.850568

for $s = 1.2571$. Briefly, while the stability of both EQ_1 and EQ_2 are controlled predominantly by the dynamics of the transmembrane potential variable (which does not vary with s) the dynamics near EQ_3 more effected by the switching terms of the slow variable dynamics, and thus with s. Thus we see somewhat stronger instability for small-s values near EQ_3 and we should expect the spatially-varying dynamics to reflect a similar instability in relatively flat regions.

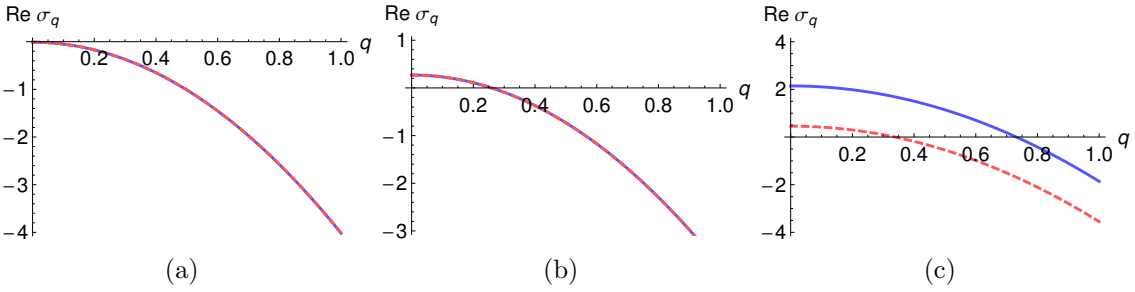

(a) (b) (c)

Figure 4: Maximal growth rates $\max(\mathrm{Re}\,\sigma_q)$ for the uniform steady states EQ_1 (a), EQ_2 (b), and EQ_3 (c), with $s = 1.2571$ (blue, solid) and with $s = 32$ (red, dashed).

The introduction of spatial variation beyond the linear neighborhood of uniform

states enables significantly more interesting dynamics for this system. In addition to the uniform states discussed in the first part of this section, there are non-evolving non-uniform solutions under particular circumstances; both of these types of solutions correspond to equlibria. This system also supports (in one-, two-, and three-dimensional spaces) traveling waves. These are solutions for which the temporal evolution aligns with the action of a continuous group symmetry, rigid translations. The evolution equations (13) are equivariant under translations in time and spatial transformations, $\mathcal{G}_a : (t, \mathbf{x}) \to (t', \mathbf{x}')$ from the Euclidean symmetry group $\mathcal{G}_a \in G = E(1) \times E(d)$, for a d-dimensional space, parametrized by the group angles $a \in \mathbb{R}^d$. The relevant group transformations in one spatial dimension take the form of rigid translations, concisely expressed as $x' = x + h$, for some translation h. This amounts to solutions $\mathbf{u}(t, x)$ which satisfy,

$$\partial_t \mathbf{u}(t, x) = c\, \partial_x \mathbf{u}(t, x), \tag{26}$$

for velocity $c \in \mathbb{R}^1$ which corresponds to temporal evolution along the translational symmetry directions. Generically, for a continuous group transformation $\mathcal{G}_a$ parametrized by group angles a, relative equilibria satisfy

$$\partial_t \mathbf{u}(t, \mathbf{x}) = \dot{\mathcal{G}}_0 \mathbf{u}(t, \mathbf{x}), \tag{27}$$

where $\dot{\mathcal{G}}_a = \dot{a}\, \mathcal{G}'_a$ is tangent to the group manifold spanned by the action of $\mathcal{G}_a$ for all group angle inputs, and $\mathcal{G}'_0$ is evaluated at the origin $a \equiv 0$. In the case of rigid spatial translation, $\mathcal{G}_a \equiv \mathcal{T}_{\mathbf{h}} = \exp(\mathbf{h} \cdot \nabla)$, and $\dot{\mathcal{G}}_0 \equiv \mathbf{c} \cdot \nabla$. Equation (26) describes the evolution of a traveling wave (for $d \geq 1$). Rotating waves are essentially two-dimensional solutions and feature prominently in the remainder of this thesis, so for the remainder of this Section we focus on traveling waves.

Computing traveling wave solutions in general is a numerical affair, as it requires not only the resolution of the field(s) $\mathbf{u}$ but the speed of the solution, c, simultaneously. Figure 5(a) depicts a traveling wave solution to equation (26), with the

transmembrane potential variable u_1 depicted as the solid line, and u_2 depicted as the dashed line. The solution to equation (26) is static in the co-moving frame, i.e. for $\mathbf{x} = x\hat{\mathbf{x}}$ and $\mathbf{c} = c\hat{\mathbf{x}}$ the solution simplifies to a system of coupled nonlinear ODEs parametrized by the (undetermined) speed of the wave, c, using the co-moving coordinate $\xi \equiv x - ct$,

$$\mathbf{0} = D\mathbf{u}'' + c\mathbf{u}' + \mathbf{f}(\mathbf{u}), \tag{28}$$

with periodic boundary conditions $\mathbf{u}(0) = \mathbf{u}(L)$, $\mathbf{u}'(0) = \mathbf{u}'(L)$, and the speed c determined by a phase condition.

One can alternatively interpret the traveling wave solutions in a fixed frame, with temporal periodicity $T \equiv L/c$. This identifies the solution as a periodic orbit in the fixed frame, satisfying

$$\mathbf{u}(T, \mathbf{x}) - \mathbf{u}(0, \mathbf{x}) = \mathcal{U}_T \mathbf{u}(0, \mathbf{x}) - \mathbf{u}(0, \mathbf{x}) = \mathbf{0}, \tag{29}$$

where $c = L/T$ is the (constant) speed of the pulse. For traveling wave solutions the diastolic interval (DI), action potential duration (APD), wavelength (λ), and speed (c) are related simply DI $= \lambda/c -$ APD. This is most trivially understood from the segmentation of the wave into action potential and diastolic behaviors, cf. Fig. 1. Provided the nonlinear flow defining $\mathcal{U}_t$, we may consider the dynamics of linear perturbations to the original state, just as in (20). This defines the forward tangent flow for the field $\mathbf{v}(t, \mathbf{x})$ which inherits the boundary conditions from the original nonlinear flow evolution,

$$\partial_t \mathbf{v}(t, \mathbf{x}) = \mathcal{L}[\mathbf{u}(t, \mathbf{x})] \cdot \mathbf{v}(t, \mathbf{x}) = D\nabla^2 \mathbf{v}(t, \mathbf{x}) + \mathbf{f}'(\mathbf{u}(t, \mathbf{x})) \cdot \mathbf{v}(t, \mathbf{x}), \tag{30}$$

and $\mathcal{L}[\mathbf{u}]$ is the instantaneous Jacobian of (13) evaluated at $\mathbf{u} = \mathbf{u}(t, \mathbf{x})$. This construction is distinguished from (20) in that we can consider the full generality of the tangent evolution – there is no assumption that the shape of the underlying nonlinear solution is fixed, i.e., $\partial_t \mathbf{u}(t, \mathbf{x}) \neq \mathbf{0}$. Similarly to the definition of (17), we may

construct a shorthand form for the forward tangent evolution propagator,

$$\mathcal{V}_t = \exp\left\{\int_0^t \mathrm{d}t'\, \mathcal{L}[\mathbf{u}(t', \mathbf{x})]\right\}, \tag{31}$$

which maps an infinitesimal perturbation $\mathbf{v}(0, \mathbf{x})$ in the tangent space to a later time $t \geq 0$, $\mathbf{v}(t, \mathbf{x}) = \mathcal{V}_t \mathbf{v}(0, \mathbf{x})$, where the operator is formally a time-ordered exponential product. Similarly, in an appropriate norm, the formal adjoint operator can be constructed. The action of the adjoint tangent evolution propagator $\mathcal{V}_t^\dagger$ maps an infinitesimal perturbation in the adjoint tangent space $\mathbf{w}(T, \mathbf{x})$ to a perturbation at an earlier time $\mathbf{w}(T-t, \mathbf{x}) = \mathcal{V}_t^\dagger \mathbf{w}(T, \mathbf{x})$, where the operator is formally the time-ordered exponential product,

$$\mathcal{V}_t^\dagger = \exp\left\{\int_0^t \mathrm{d}t'\, \mathcal{L}^\dagger[\mathbf{u}(T - t', \mathbf{x})]\right\}, \tag{32}$$

with $\mathcal{L}^\dagger[\mathbf{u}]$ the adjoint of the instantaneous Jacobian operator. The adjoint tangent evolution is defined by the time-reversed PDE,

$$-\partial_t \mathbf{w}(t, \mathbf{x}) = \mathcal{L}^\dagger[\mathbf{u}(t, \mathbf{x})]\, \mathbf{w}(t, \mathbf{x}) = D^\dagger \nabla^2 \mathbf{w}(t, \mathbf{x}) + [\mathbf{f}'(\mathbf{u}(t, \mathbf{x}))]^\dagger \cdot \mathbf{w}(t, \mathbf{x}). \tag{33}$$

Both (30) and (33) are evaluated by time-stepping using an explicit fourth-order $O(\Delta t^4)$ Runge-Kutta method, where Δt is the temporal discretization. While (30) inherits this numerical scheme from the numerical evaluation of (13), the numerical time-stepping of (33) is run in backwards time compared to the nonlinear solution and thus requires the development of additional techniques to solve accurately. The details of this computation are explored in Sec. A.2.1.

For a temporally periodic solution of period T, the spectral decomposition of $\mathcal{V}_T$ takes on special significance. The tangent space at time $t = 0$ and $t = T$ coincide identically, thus the eigenfunctions of $\mathcal{V}_T$ are elements of the same tangent space for the whole duration they are defined. The eigenfunctions $\mathbf{v}^i(t, \mathbf{x})$ and eigenvalues Λ_i of $\mathcal{V}_T$ satisfy

$$\mathbf{v}^i(T, \mathbf{x}) = \mathcal{V}_T \mathbf{v}^i(0, \mathbf{x}) = \Lambda_i \mathbf{v}^i(0, \mathbf{x}), \tag{34}$$

where $\Lambda_i \in \mathbb{C}^1$, generally. Similarly, the adjoint eigenfunctions $\mathbf{w}^j(t,\mathbf{x})$ and eigenvalues Λ_j satisfy

$$\mathbf{w}^j(0,\mathbf{x}) = \Lambda_j^* \mathbf{w}^j(T,\mathbf{x}) = \mathcal{V}_T^\dagger \mathbf{w}^j(T,\mathbf{x}), \tag{35}$$

where Λ_j^* is the complex-conjugate of Λ_j. As $\mathcal{V}_T$ is generally non-self-adjoint, the left and right eigenfunctions are not equivalent for the same eigenvalue: $\mathbf{w}^i(T-t,\mathbf{x}) \neq \mathbf{v}^i(t,\mathbf{x})$, though the two sets of eigenfunctions are mutually orthogonal. The orthogonality relation can be written in the general form

$$\langle \mathbf{w}^j(t) | \mathcal{Q} | \mathbf{v}^i(t) \rangle = \int_\Omega \mathrm{d}^2\mathbf{x}\, [\mathbf{w}^j(t,\mathbf{x})]^\dagger\, \mathcal{Q}(\mathbf{x})\, \mathbf{v}^i(t,\mathbf{x}) = \delta_{ij} \tag{36}$$

for $0 \leq t \leq T$, where $\mathbf{v}^i(t,\mathbf{x})$ is defined as the solution of (30) that coincides with the right eigenfunction $\mathbf{v}^i(0,\mathbf{x})$ at $t=0$ and $\mathbf{w}^j(t,\mathbf{x})$ as the solution of (33) that coincides with the left eigenfunction $\mathbf{w}^j(T,\mathbf{x})$ at $t=T$. For a time-periodic solution $\mathbf{u}(t,\mathbf{x})$ with period T, $\mathbf{v}^i(t,\mathbf{x})$ and $\mathbf{w}^i(t,\mathbf{x})$ correspond to the right and left Floquet modes with Floquet multiplier Λ_i. The choice of inner product defined by (36) is not unique. In principle, forms of $\mathcal{Q}(\mathbf{x})$ may be used to better emphasize regions of the domain, though this changes the interpretation of the adjoint eigenfunctions. For the present work we have chosen a uniform weighting, $\mathcal{Q}(\mathbf{x}) = \mathbf{1}$, which is the simplest choice and consistent with uniform conductivity, the symmetry of the evolution equations, and various boundary conditions.

Although the vast majority of studies of infinite-dimensional systems focus exclusively on the right (conventional) eigenfunctions, the importance of the left (adjoint) eigenfunctions is hard to overstate. In particular, an accurate estimate of the evolution operator $\mathcal{V}_T$ is crucial for a number of applications such as computing unstable solutions cf. Ch. 3, feedback control [2, 82, 83], and adjoint-based optimization [144, 67]. For infinite-dimensional systems, explicit evaluation of $\mathcal{V}_T$ is prohibitively expensive

(or simply impossible). Such estimates are often constructed by using Arnoldi iterations [8] leading to the k-dimensional factorization,

$$\mathcal{V}_T V_k = V_{k+1} \tilde{H}_{k+1}, \tag{37}$$

where $\tilde{H}_{k+1} = [H_k, h_{k+1,k}\mathbf{e}_{k+1}^\top]^\top$ is a partial reduction of $\mathcal{V}_T$ to upper-Hessenberg form, and $V_k = [\hat{\mathbf{v}}_1, \ldots, \hat{\mathbf{v}}_k]$ is a k-dimensional orthonormal basis for the action of $\mathcal{V}_T$, the Arnoldi basis for the Krylov space generated by $\mathcal{V}_T$. The eigenvalues and eigenvectors of H_k generate approximations of the leading eigenvalues and right eigenfunctions of the operator $\mathcal{V}_T$, but generally do not approximate the left eigenfunctions, as the construction usesonly the canonical application of the tangent propagator, i.e., $\mathcal{V}_T$ not $\mathcal{V}_T^\dagger$, and generically the propagator is not self-adjoint.

An optimal estimate of the propagator based on the truncated spectral decomposition

$$\mathcal{V}_T = \sum_{i=1}^{N} |\mathbf{v}^i\rangle \Lambda_i \langle \mathbf{w}^i| + O(\Lambda_{N+1}) \tag{38}$$

requires both sets of eigenfunctions. In comparison, an Arnoldi-based approximation

$$\mathcal{V}_T = \sum_{i=1}^{M} |\mathbf{v}^i\rangle \Lambda_i \langle \bar{\mathbf{w}}^i| + O\left(\sum_{i=1}^{M+1} \langle \mathbf{v}^i | \Lambda_i | \bar{\mathbf{w}}^{M+1} \rangle \right), \tag{39}$$

e.g., used in GMRES methods [148], uses synthetic adjoints $\bar{\mathbf{w}}^i$ which satisfy (36) only in the M-dimensional Krylov subspace spanned by $V_M = [\hat{\mathbf{v}}_1, \ldots, \hat{\mathbf{v}}_M]$. That is, $\langle \bar{\mathbf{w}}^j | \mathbf{v}^i \rangle \neq \delta_{ij}$ if either $i > M$ or $j > M$ and requires $M \gg N$ to achieve a similar level of accuracy to the spectral truncation (38). In fact, this relationship can be used to construct a set of pseudo-adjoints explicitly,

$$\bar{\mathbf{w}}^i = \left(\mathbf{v}^\dagger \mathbf{v}\right)^{-1} \mathbf{v}^i, \tag{40}$$

where $(\mathbf{v}^\dagger \mathbf{v})_{ij} = (\mathbf{v}^i)^\dagger \mathbf{v}^j$ is the auto-projection of the right eigenfunctions, which determines $\bar{\mathbf{w}}^i$ up to normalization. Trivially, $\langle \bar{\mathbf{w}}^i | \mathbf{v}^j \rangle = \delta_{ij}$ in the Krylov subspace. It should be clear that the construction of the pseudo-adjoints is numerically ill-conditioned for non-self-adjoint operators, as the set of right eigenfunctions are not orthogonal, which makes the set of pseudo-adjoints mostly useless.

The adjoints are required to compute the coordinates a_i of disturbances in the tangent space:

$$\delta\mathbf{u} = \sum_i a_i \mathbf{v}^i, \qquad a_i = \langle \mathbf{w}^i | \delta\mathbf{u} \rangle. \tag{41}$$

With the introduction of the tangent evolution propagators (31) and (32) and their eigenfunctions defined by (34) and (35), we are prepared to discuss the linear stability of traveling wave solutions in detail.

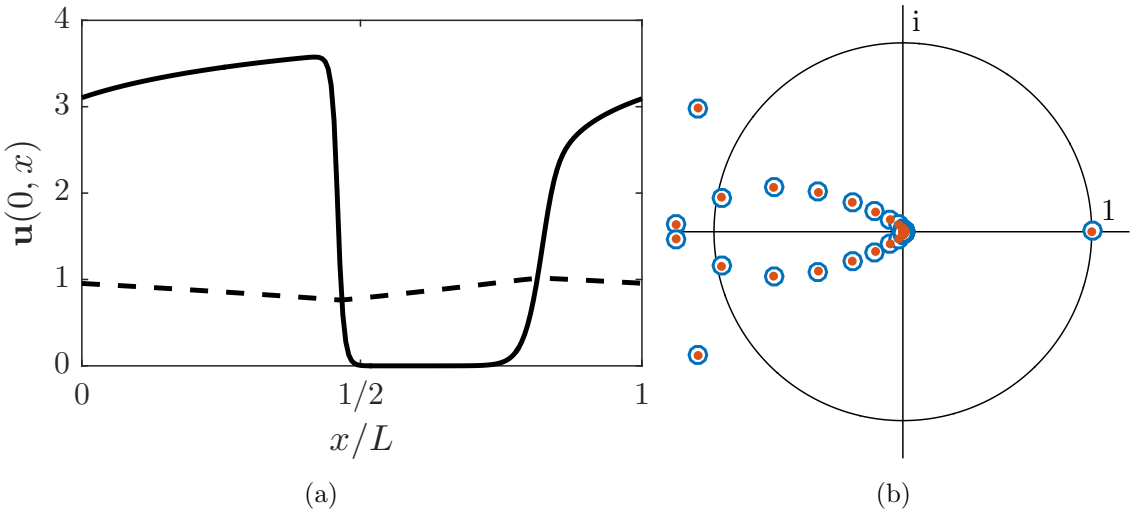

Figure 5: (a) Traveling wave solution $\mathbf{u}(0,x)$ on a periodic domain ($L = 192$), with u_1 denoted by the solid line and u_2 denoted by the dashed line ($s = 1.2571$). (b) Symmetric (y-invariant) Floquet spectrum (Λ_i) in the complex plane.

Figure 5 shows a symmetric (y-invariant) traveling wave solution and the Floquet spectra of the traveling wave solution in the symmetric subspace. The eigenspectrum exhibits a single unit multiplier, $\Lambda_i = 1$, for all s investigated ($1.2571 \leq s \leq 32.0$). The associated eigenfunction corresponds to the generator of translations applied to the state, such that for $\Lambda_i = 1$, $\mathbf{v}^i(t,\mathbf{x}) \propto \partial_x \mathbf{u}(t,\mathbf{x})$. The eigenspectrum possesses a dominant (complex-conjugate) pair of unstable modes, $|\Lambda_i| > 1$, where the associated eigenfunctions describe the development of an alternans instability which modulates the width of the excitation in both space and time. Additionally, there are a set of real-valued multipliers just outside the unit circle ($|\Lambda_i| > 1$, $\Lambda_i \approx -1$) indicating that

the associated modes are (weakly) linearly unstable. This is the extremal value of the 'continuous' spectrum of the solution, the remainder belonging to the set which are non-mixing [161, 172], and whose corresponding eigenfunctions are predominantly Fourier-mode dominated, having little to do with the shape of the underlying traveling wave.

The real parts of the three leading eigenfunctions of the pulse solution are shown in Fig. 6(a,c,e). We also show their exaggerated effect (b,d,f) on the state (black), against the original pulse (gray). The alternans instability mode ($\Lambda_{\pm} = -1.20 \pm 0.038$i, a-b) alternatively lengthens or shortens the width of the excited region after time T, depending on initial perturbation construction, leading to a deformation of the shape of the wave in the co-moving frame. The mode primarily effects the waveback, leaving the wavefront mostly unaltered and slightly modifies the decay rate within the excited region. Similarly, the unstable mode from the continuous spectrum ($\Lambda_{\pm} = -1.08 \pm 0.655$i, c-d) shifts the wavefront forward while simultaneously pulling the waveback backward. The marginal ($\Lambda = 1$, e-f) mode does not deform the wave, it merely shifts it relative to the original position when considered in the limit of infinitesimal amplitude. Furthermore, within each eigenfunction, these modes reveal that one component is much larger than the other i.e. $\sup_{\mathbf{x}} v_1(t, \mathbf{x}) \gg \sup_{\mathbf{x}} v_2(t, \mathbf{x})$. This is similarly true for the adjoint eigenfunctions, $\sup_{\mathbf{x}} w_1(t, \mathbf{x}) \ll \sup_{\mathbf{x}} w_2(t, \mathbf{x})$, so we will frequently show only the dominant component.

In general, the traveling wave solution can be computed from the boundary value problem (BVP) defined by (28). Figure 7(a) shows the u_1 component of the solution of the BVP on smaller domains with periodic boundary conditions, in particular for $L = 192$, 96, 48, 24, and the domain size on which the solution contracts to the unstable spiral equilibrium EQ_3, losing all spatial variation, $L = 13$. Additionally, as the speed of the pulse is implicitly dependent on the shape of the solution, it can be parametrized by the size of the domain, $c = c(L)$, for a particular solution

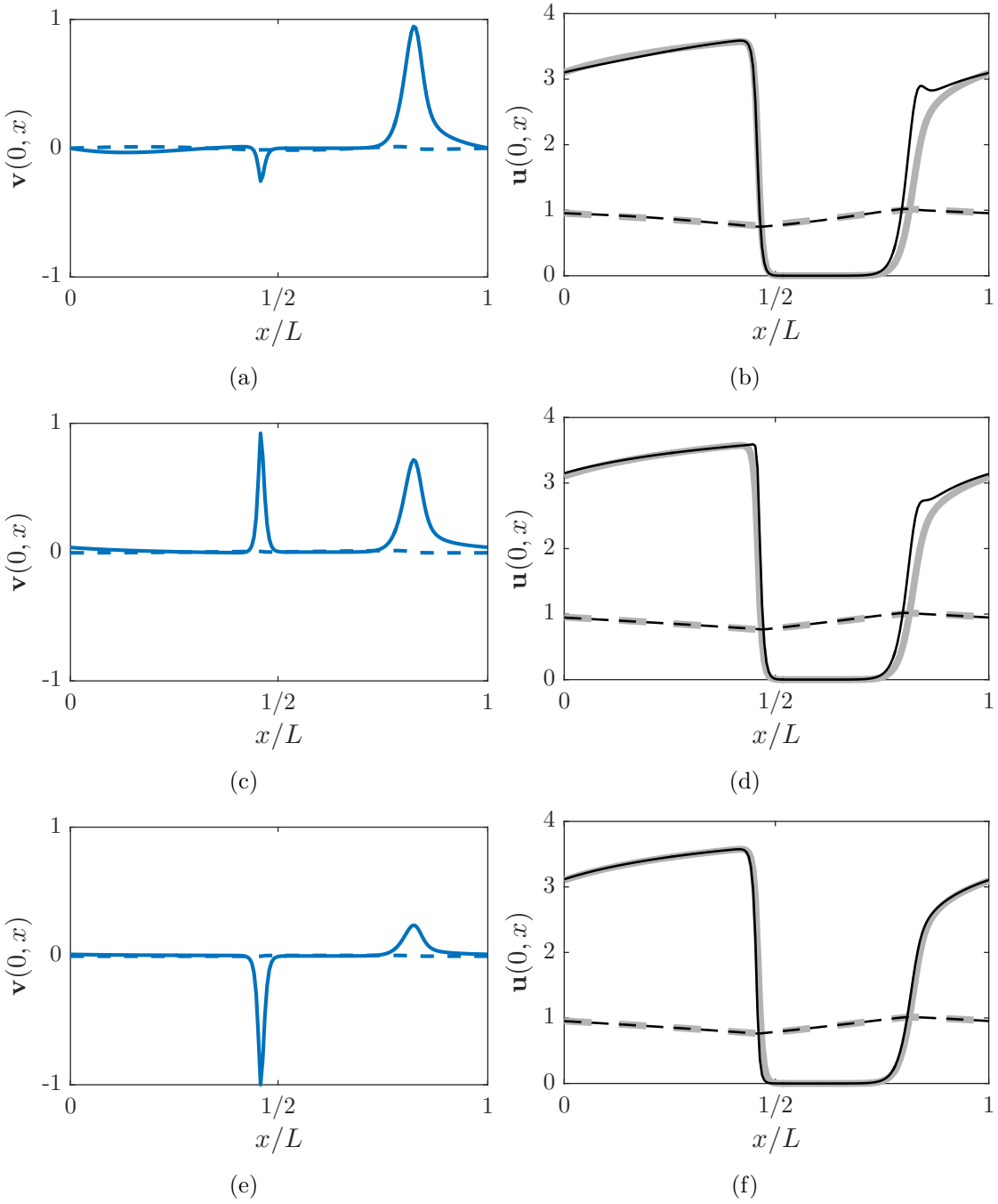

Figure 6: Real part of the eigenfunctions of $\mathcal{V}_T$ and their (exaggerated) effect on the $s = 1.2571$ pulse associated with $\Lambda_\pm = -1.20 \pm 0.038\mathrm{i}$ (first row), as well as $\Lambda_\pm = -1.08 \pm 0.655\mathrm{i}$ (second row), and the eigenfunction associated with translational symmetry $\Lambda = 1$ (third row). The solid and dashed curves denote the first and second components, respectively.

branch. This functional dependence is shown in Fig. 7(b) over the range of domain sizes investigated, $13 \leq L \leq 200$.

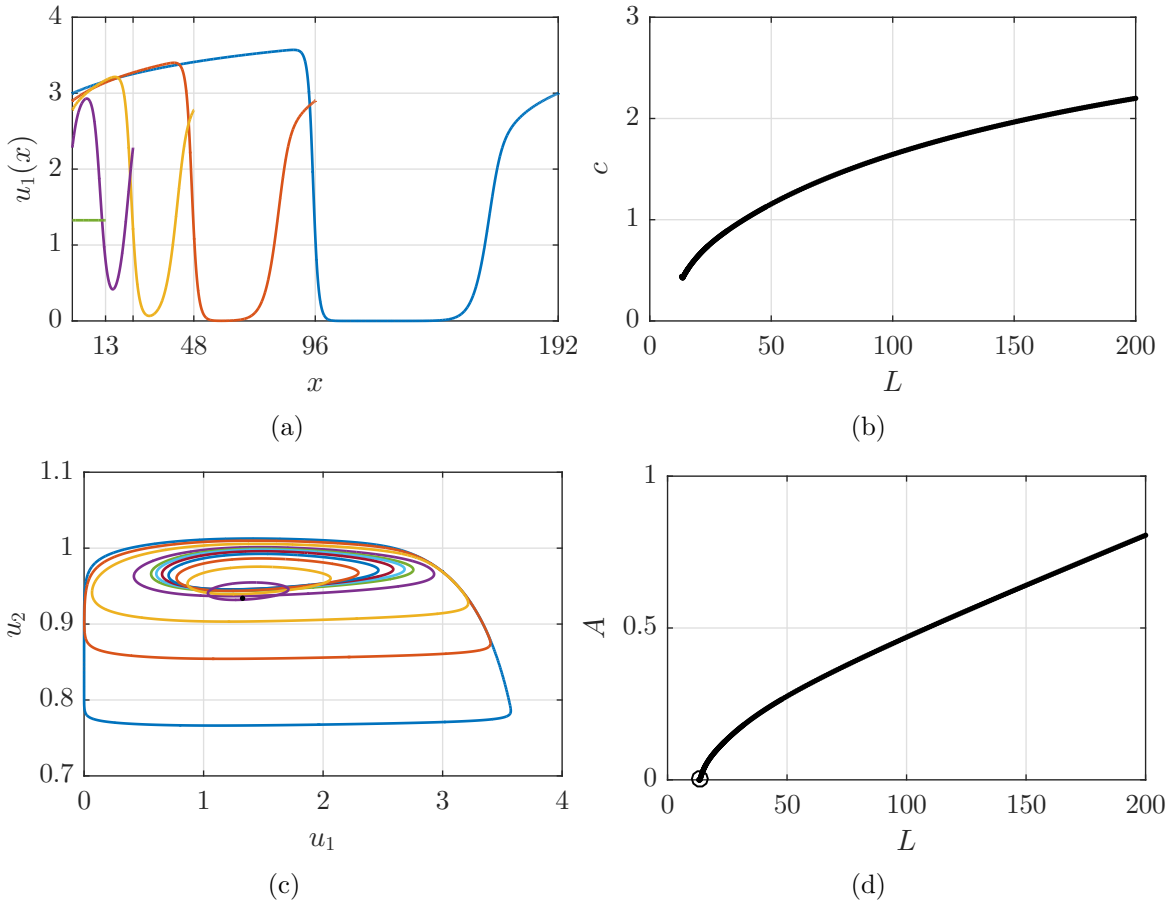

Figure 7: First component of the solution of (28) for $13 \leq L \leq 192$ (a), and the speed of the co-moving frame as a function of the domain size (b), several traveling wave solutions in the $\mathbf{u}$ plane (c), and the area A encircled by each traveling wave loop in the $\mathbf{u}$ plane (d).

Additionally, the area $A = |\oint \mathrm{d}\xi\, u_2(\xi) u_1'(\xi)|$ in the $\mathbf{u}$ plane encircled by the traveling wave solution decreases monotonically for smaller L, cf. Fig. 7(c-d). While (c) shows the loops in the $\mathbf{u}$ plane, (d) shows the dependence of the loop area on domain size explicitly. It should be noted that the relationship $A(L)$ is asymptotically linear ($A'(L \to \infty) \to$ const.), with monotonically decaying area for small L.

All the traveling wave solutions computed on domains of size $L \leq 200$ are unstable; though for larger domain sizes the isolated pulse solution stabilizes, $L \gtrsim 238$

(6.23 cm). This has precedence in the physiologically relevant dynamics of cardiac excitation – the normal rhythm of the heart corresponds to the coherent propagation of excitation through the tissue. The pulse solution in particular is qualitatively similar to the propagating excitation within the Purkinje fibers – effectively one-dimensional regions of tissue which enforce the global synchrony of the contraction of the muscle through electrical pathways connecting disparate regions of the ventricles [10, 62]. This regime is stable and persists in the presence of small structural perturbations (e.g., blood vessels) [47] and the associated small variations in the timing of the excitation [50].

2.4 Two-dimensional solutions

In two spatial dimensions a family of relative equilibria corresponding to extrusions of the one-dimensional pulse trains are supported, the traveling waves satisfying (26). The only remarkable modification of these solutions in two spatial dimensions is the addition of transverse wave instabilities, such that while $\mathbf{u}(t, \mathbf{x}) = \mathbf{u}(x - ct)$, appropriately oriented, perturbations about this solution are in general more complicated involving both spatial coordinates $\mathbf{v}(t, \mathbf{x}) = \mathbf{v}(x - ct, y)$. While these sorts of instabilities are relevant for some excitable systems [123, 127], they are not expected to be uniquely relevant to traveling wave solutions related to cardiac dynamics in the present model. We shall not discuss this instability in detail, and merely show the associated Floquet spectrum for asymmetric (i.e., not y-invariant) perturbations in Fig. 8. Generically, the symmetric (y-invariant) subspace appears as the extremal realization of the asymmetric spectrum. Qualitatively, this can be understood for perturbations written as a separable product of perturbations along the wave and transversely: $\mathbf{v}(\xi, y) = \tilde{\mathbf{v}}(\xi) \exp(\mathrm{i}ky)$. These perturbations likewise decouple under evolution in the co-moving frame – the transverse modulation decays in time, approaching the symmetric mode behavior.

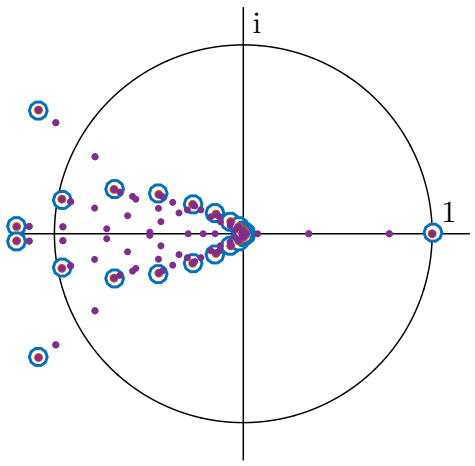

Figure 8: Floquet spectrum for the pulse solution shown in Fig. 5(a) with symmetric perturbations (blue) and asymmetric perturbations (purple) against the unit circle.

As explained in the previous section, the reaction-diffusion model in d dimensions is equivariant with respect to the $E(d)$ Euclidean group. The most relevant group transformations from this group in two spatial dimensions take the form of spatial translations or rigid rotations, concisely expressed as $\mathbf{x}' = \mathcal{R}_\phi \mathbf{x} + \mathbf{h}$, for some translation vector $\mathbf{h}$ and rotation angle ϕ. Due to the non-abelian nature of $E(2)$ – $[\mathcal{T}_\mathbf{h}, \mathcal{R}_\phi] \neq 0$ – for any non-trivial transformation involving shifts and rotations the specific values of $\mathbf{h}$ and ϕ are subject to convention and not unique, i.e., $\mathbf{x}' = \mathcal{R}_{\phi'}(\mathbf{x} + \mathbf{h}')$. In practice, we split these distinguishable transformations and their effects on the solution. We have already discussed traveling waves in some detail, their relationship to the propagation of excitation in normal cardiac rhythm, and their extension to two spatial dimensions. With $d \geq 2$, additional solutions are now accessible – e.g., relative equilibria for which the evolution is equivalent to rigid rotations about a fixed position, i.e., rotating waves.

Rotating waves are relative equilibria $\mathbf{u}(t, \mathbf{x})$ for which temporal evolution is equivalent to rigid rotations. As was the case for traveling waves, we can write the action of the group operator explicitly in terms of rigid spatial rotation, $\mathcal{G}_a \equiv \mathcal{R}_\phi = \exp(\phi \partial_\theta)$,

and $\dot{\mathcal{G}}_0 \equiv \omega\partial_\theta$. This gives an explicit equivalence for the temporal evolution,

$$\partial_t \mathbf{u}(t,\mathbf{x}) = \omega\partial_\theta \mathbf{u}(t,\mathbf{x}) = \omega\hat{\mathbf{z}} \cdot \left[(\mathbf{x}-\mathbf{x}_o) \times \nabla\mathbf{u}(t,\mathbf{x})\right], \tag{42}$$

when the axis of rotation $\mathbf{x}_o$ is specified. Rotating waves are examples of spiral waves, distinguished by their temporal invariance in the co-rotating frame. Thus, as with the relative equilibria corresponding to traveling waves, rotating waves require domains and boundary conditions consistent with the continuous symmetry of the evolution. On bounded domains rotating waves exist only when the domain is a disk, the axis of rotation is at the origin of the system, and the boundary conditions are independent of the angular coordinate. In the absence of these properties, a more general formulation of the significance of these approximately rotational dynamics is needed. Spiral wave solutions on finite, bounded, non-circular domains are investigated in the following Chapter (Ch. 3).

CHAPTER III

SINGLE-SPIRAL SOLUTIONS

The development of tachycardia into fibrillation requires the dynamical breakup of the spiral wave – from one spiral to several. Generically, these spiral waves will not correspond to rotating waves as the structure of the atria is not consistent with the symmetry of these relative equilibria. To describe the structure of more generic spiral wave solutions – in particular those which can not be made static in a rotating frame – we treat the temporal evolution explicitly. In this Chapter we present unstable spiral wave solutions of the modified Karma model computed using the weighted Newton-Krylov method described in Sec. A.4 and investigate their properties.

3.1 Unstable spiral waves

The spiral wave solution shown in Fig. 9(a) was found using continuation of a stable single-spiral solution on a square domain of side-length $L = 192$ (5.03 cm) with an approximately centered tip $\mathbf{x}_o = [74.43, 96.04]$ (i.e., slightly to the left of the center), achieved by decreasing β (which corresponds to increasing the restitution parameter Re, cf. Sec. 2.2). The periodic orbit has a period $T = 50.8273$ (127 ms) and wavelength $\lambda = 74$ (1.94 cm), and is resolved to $\|\mathbf{F}(\mathbf{u}, T)\| < \varepsilon_{\text{tol}}$ in Euclidean norm, where $\varepsilon_{\text{tol}} = 10^{-10}$ throughout this work. Fig. 9(b) shows the leading Floquet multipliers (Λ) of the periodic orbit, and it shows the solution has one Goldstone mode ($\Lambda = 1$) and three absolutely unstable modes ($|\Lambda| > 1$).

The periodic orbit function (29) may be generalized for solutions in the presence of symmetry to apply to relative periodic orbits,

$$\mathbf{F}(\mathbf{u}, a, T) = \mathcal{G}_a \mathcal{U}_T \mathbf{u} - \mathbf{u} = \mathbf{0}, \tag{43}$$

which denotes equivalence of a state after time T, up to a symmetry transformation $\mathcal{G}_a$. Equation (43) is general in the sense that any transformation from the Euclidean symmetry group is, in principle, permissible. Depending on the specific solution, $\mathcal{G}_a = \mathcal{T}_{\mathbf{h}}$ corresponding to translations or $\mathcal{G}_a = \mathcal{R}_\phi$ for rotations may be appropriate.

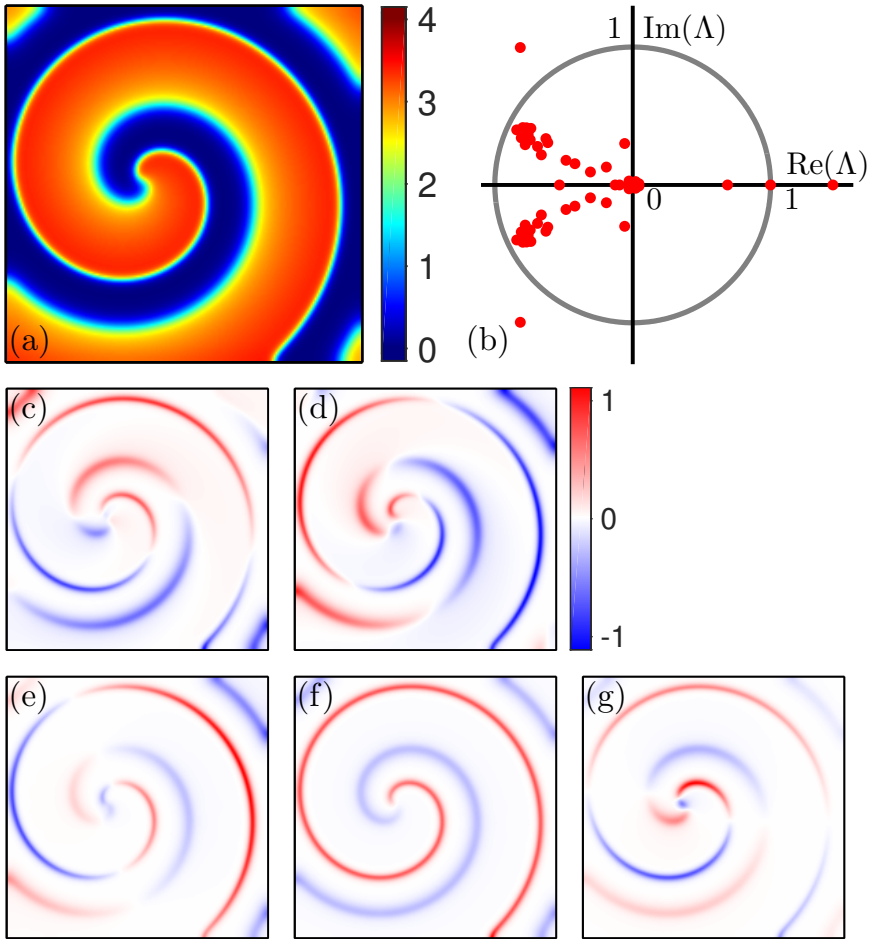

Figure 9: A pinned single-spiral solution $u_1(0, \mathbf{x})$ (a) and the spectrum of its Floquet multipliers Λ (b) for $s = 32$. The real and imaginary parts of the complex-conjugate unstable pair are shown in panels (c) and (d), respectively. The modes corresponding to the real eigenvalues $\Lambda = 0.69$, $\Lambda = 1.00$, and $\Lambda = 1.45$ are shown in panel (e), (f) and (g), respectively. The voltage component u_1 is shown in all the panels. The domain size is $L = 192 \approx 2.6\lambda$.

The Goldstone mode presented in Fig. 9f corresponds to the temporal derivative of the solution $\partial_t \mathbf{u}$, as expected for a periodic orbit. The real unstable mode (Fig. 9g) corresponds to an almost rigid shift of the spiral wave in the y direction and can be

identified with a frustrated translational Goldstone mode $\partial_y \mathbf{u}$ (its amplitude varies in space). The stable eigenvalue $\Lambda = 0.6882$ also corresponds to a frustrated Goldstone mode (Fig. 9e), which can be identified as linear combination of translations in the x and y directions, $\hat{\mathbf{n}} \cdot \nabla \mathbf{u}$, where $\hat{\mathbf{n}}$ is the direction of translation. The two complex conjugate unstable modes (Figs. 9c and 9d) correspond to the variation in the width of the excitation wave (i.e., alternation of the action potential duration), which is to be expected for $Re > 1$. Since the Goldstone modes associated with spatial translations are frustrated for $s = 32$ (continuous translational symmetry is broken), no additional constraints beyond orthogonality with respect to $\partial_t \mathbf{u}$ are needed. The residual $\|\mathbf{F}(\mathbf{u}, \mathbf{h}, T)\|$ – defined by the non-vanishing right-hand-side of (43) with $\mathcal{G}_a = \mathcal{T}_{-\mathbf{h}}$ – is minimized for $\mathbf{h} = \mathbf{0}$ (i.e., $\mathcal{G}_a = \mathbf{1}$), so this spiral wave is pinned and corresponds to an absolute (non-relative) periodic orbit.

Our results should be contrasted with those obtained by Allexandre and Otani [2] for the modified version of the 3-variable Fenton-Karma (3V-FK) model [69] (they also replaced the Heaviside step functions with smoothed versions $\Theta_s(u)$). The unstable spiral waves of 3V-FK (described by relative equilibria) were found to possess two near-Goldstone modes corresponding to spatial translations with $\Lambda \approx 1$ and one Goldstone mode corresponding to temporal translation (or spatial rotation) with $\Lambda = 1$. This suggests that translational symmetry is weakly broken due to the presence of boundaries (the calculations were performed on a circular domain of radius equal to just about half the wavelength λ). In addition, the spectrum included a pair of complex conjugate modes corresponding to meandering instability and a number of unstable modes corresponding to alternans, all laying on the negative real axis (i.e., corresponding to period-doubling, rather than Hopf, bifurcation). We can therefore expect that the alternans instability may lead to substantially different dynamics in the two models.

The origin of symmetry breaking in the Karma model can be understood by

considering the temporal evolution of the group tangents $\partial_x \mathbf{u}$, $\partial_y \mathbf{u}$, and $\partial_t \mathbf{u}$, which become Goldstone modes in the presence of global continuous symmetries. For the Goldstone modes we should have $(\mathcal{V}_T - \mathbf{1})\mathbf{e}_i = \mathbf{0}$ (up to the level of precision defined by ε_{tol}). We checked this by evolving the group tangents using the linearization of (13) about the periodic solution shown in Fig. 9(a). As Fig. 10 illustrates, the temporal tangent is a Goldstone mode: $|(\mathcal{V}_T - \mathbf{1})\partial_t \mathbf{u}| = O(10^{-11})$ while the spatial tangents are not. Both $(\mathcal{V}_T - \mathbf{1})\partial_y \mathbf{u}$ and $(\mathcal{V}_T - \mathbf{1})\partial_x \mathbf{u}$ achieve their $O(10^{-2})$ maxima on the boundary of Ω (Figs. 10d & e), which confirms the role of boundaries in breaking the global translational symmetry of the state. However, this symmetry-breaking is in some sense weak, as it scales inversely with the domain size, and there is another mechanism that also breaks translational symmetry. To isolate the contribution from the interior of the domain from the boundary contribution, we can construct a windowing function

$$W_d(\mathbf{x}) = \frac{1}{2}\left[1 - \tanh\left(\sigma \frac{2|\mathbf{x} - \mathbf{x}_c| - dL}{2L}\right)\right], \tag{44}$$

where $\mathbf{x}_c$ denotes the center of the domain and d determines the diameter of the (circular) "window" in units of L (we set $d = 0.7$ and $\sigma = 32$, unless specified otherwise). Applying windowing $W_d(\mathbf{x})$ to suppress the boundary effects, we discover that $\partial_y \mathbf{u}$ and $\partial_x \mathbf{u}$ behave like Goldstone modes everywhere except near the core of the spiral wave (Figs. 10g and 10h), suggesting that translational symmetry is also broken locally. We investigate this local mechanism next.

3.1.1 Effect of discretization

Spatial discretization can be a local source of symmetry breaking in addition to the global symmetry breaking due to the boundaries of the domain. The latter context is universally relevant to all numerical simulations of spatially bounded dynamics, as mentioned in Ch. 2. The former context is relevant in more specific circumstances; in order for local features to break the symmetry of the system, the solution should

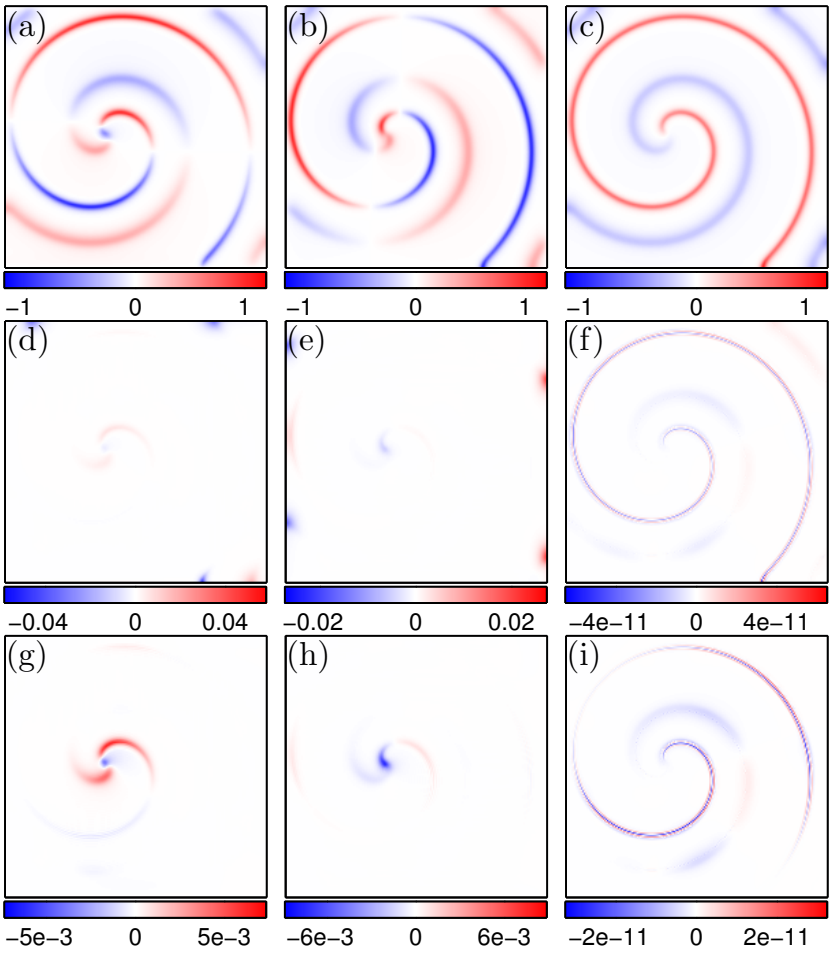

Figure 10: Group tangents of the pinned spiral wave solution, $\partial_y u_1$ (a), $\partial_x u_1$ (b), and $\partial_t u_1$ (c). The difference between the group tangents and their images under evolution, $(\mathcal{V}_T - \mathbf{1})\partial_y u_1$ (d), $(\mathcal{V}_T - \mathbf{1})\partial_x u_1$ (e), and $(\mathcal{V}_T - \mathbf{1})\partial_t u_1$ (f). The windowed difference $W_d(\mathcal{V}_T - \mathbf{1})\partial_y u_1$ (g), $W_d(\mathcal{V}_T - \mathbf{1})\partial_x u_1$ (h), and $W_d(\mathcal{V}_T - \mathbf{1})\partial_t u_1$ (i), where $d = 0.9$.

possess a length scale comparable to the scale of spatial discreteness, in this instance $\Delta x = \Delta y = 1$. Monodomain models of are an absolutely continuous model of an intrinsically discrete physical medium: cardiac tissue – comprised of cardiac cells, which are electrically and biochemically coupled in an irregular lattice structure. The spiral wave solution is characterized by several scales: the wavelength $\lambda = 74$, the length scale $\ell_1 = \sqrt{D_{11}} \approx 2$ of the fast (voltage) variable, which defines the width of the sharp leading front of the excitation wave, and the length scale ℓ_2 over which the dynamics of the slow variable u_2 switches from excitable to refractory. The latter length scale is controlled by the term $\beta\Theta_s(u_1 - 1)$ in (14) and, to leading order in ϵ, is given by $\ell_2 = 2\ell_1/(s\beta)$. Setting $\ell_2 = 1$ gives $s = 2\ell_1/\beta \approx 3$. Hence, for $\ell_2 \lesssim 1$ ($s \gtrsim 3$) the solution is spatially ill-resolved, and continuous translational symmetry is broken by regions where the gating dynamics switches between excitable and refractory – i.e. near the tip – pinning the spiral. On the other hand, for $\ell_2 \gtrsim 1$ ($s \lesssim 3$) the solution is well-resolved and continuous translational symmetry should be preserved, so the spiral can drift.

Indeed, this is exactly what we find for $s = 1.2571$. The spiral wave solution at this low value of s is similar to that shown in Fig. 9(a), but corresponds to a generalized relative periodic orbit with period $T = 54.7447$ and wavelength $\lambda = 78$. The displacement of the wave over one period is small, but non-zero ($|\mathbf{h}| = O(10^{-9}\lambda)$), and its direction depends on both the position and the phase of the spiral wave. The corresponding spectrum (Fig. 11a) contains two complex conjugate unstable eigenvalues which correspond to the alternans instability (the corresponding modes are similar to those shown in Figs. 9e and 9f) and three eigenvalues with $|\Lambda - 1| = O(10^{-6})$. The corresponding Goldstone modes, predictably, coincide with the three group tangents $\partial_t \mathbf{u}$ (Fig. 11d), $\partial_y \mathbf{u}$ (Fig. 11c), and $\partial_x \mathbf{u}$ (Fig. 11b). This indicates that although *global* Euclidean symmetry is broken on the finite domain, *local* Euclidean symmetry (i.e., symmetry with respect to small translations or rotations) remains

essentially exact provided that (i) the domain is sufficiently large and (ii) the length scale of heterogeneities is sufficiently small.

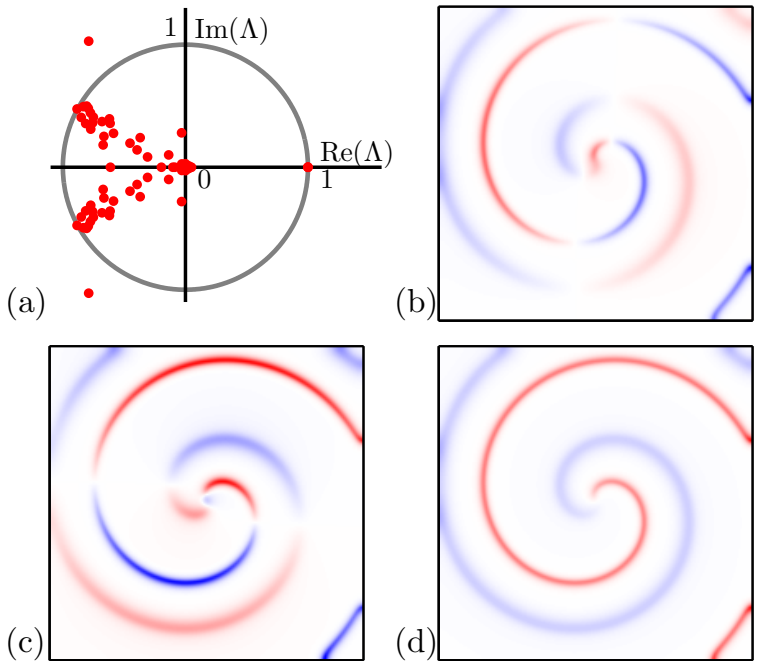

Figure 11: The eigenvalues of the drifting single-spiral solution for $s = 1.2571$ (a). The complex-conjugate pair of unstable modes are similar to those shown in Figs. 9e and 9f and thus omitted. The Goldstone modes are shown in panels (b)-(d). The domain size is $L = 192$.

The transition between the small-s regime where local Euclidean symmetry is preserved and the large-s regime where it is broken is continuous. This continuity further justifies our identification of the frustrated Goldstone modes for a solution which explicitly does not possess translation symmetry (i.e., for $s = 32$). The s-dependence of the leading eigenvalues is shown in Fig. 12(a). As the value of s is increased, two of the three unit eigenvalues split off around $s = 3$ and separate along the real axis. For this particular solution, Goldstone mode $\partial_y \mathbf{u}$ becomes unstable (and frustrated), while the Goldstone mode $\partial_x \mathbf{u}$ becomes stable (and frustrated) at large s. The exact symmetry of the problem with respect to rotations by $\phi = \pi/2$ means that there is a rotated copy of the solution we found for which the stability of these two modes is interchanged. In either case, however, we find that the x and y

directions play a special role: discretization breaks the rotational symmetry despite the use of the "best case scenario" Laplacian stencil (at this minimal width) which aims to preserve the equivalence of the x and y coordinates, cf. Sec. A.1 and (97) specifically.

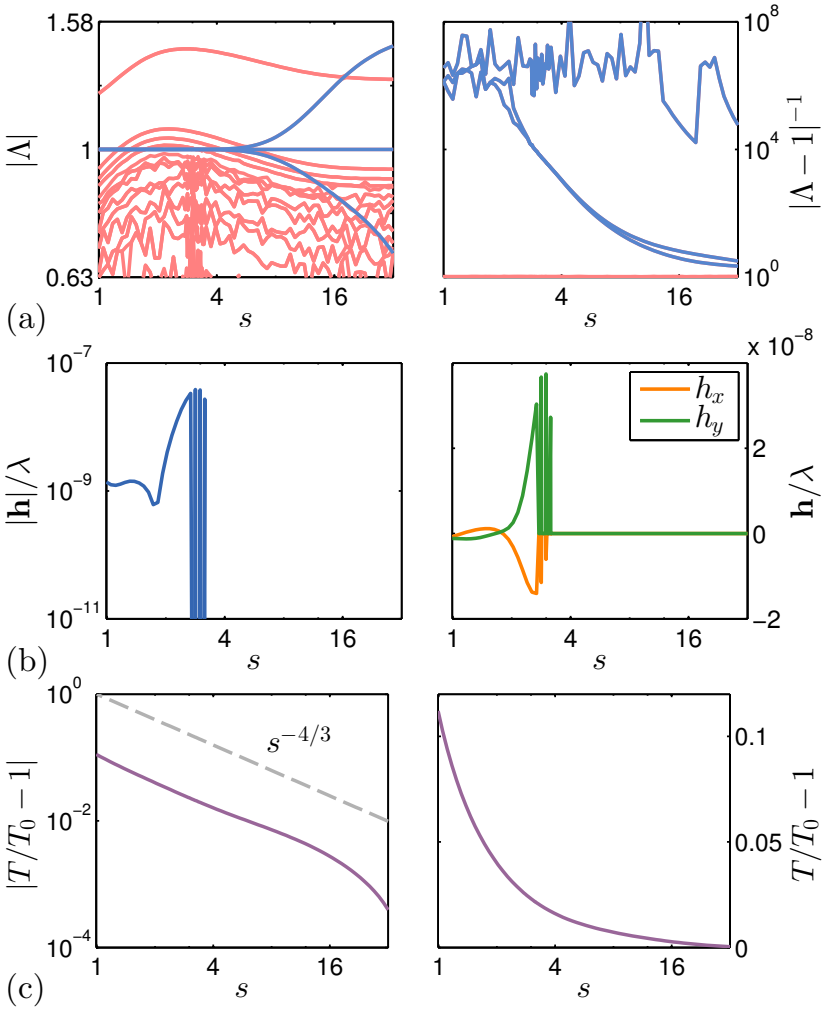

Figure 12: Dependence of various properties of the unstable spiral wave solution on the stiffness parameter over the range $1 \le s \le 32$. (a) Eigenvalues Λ_i of unstable and leading stable modes (red) and near-Goldstone modes (blue). (b) The spatial shift $\mathbf{h}$, normalized by the wavelength λ. (c) The deviation of the period T from the asymptotic value $T_0 = 50.8273$.

It is also worth pointing out that for $1.2 \lesssim s \lesssim 6$, several other modes become unstable. Unlike the modes shown in Figs. 9 and 11 which are isolated (belong to the

discrete spectrum), these new modes are not isolated (i.e, belong to the continuous spectrum). Hence, we should expect a continuum of unstable alternans-like modes to appear for single-spiral solutions in unbounded domains for intermediate values of s.

The variation of $\mathbf{h}$, which defines the net spatial displacement of the wave over one period of rotation, is shown in Fig. 12(b) as a function of s. Consistent with our dimensional analysis, we find that $\mathbf{h}$ vanishes for $s \gtrsim 3$, but does not vanish for $s \lesssim 3$. Even though the spirals drift for small s, when their tip is far from domain boundaries, the displacement over one period is too small to be resolved in DNS and can only be computed using extremely precise calculations based on Newton-Krylov method. However, we will see below that the drift can become quite significant for spirals whose tip is close to a boundary.

The period of the spiral was found to be a monotonically decreasing function of s, as Fig. 12c illustrates. The deviation from the limiting value T_0, which corresponds to $s \to \infty$, was found to be well-approximated by a power law, $T - T_0 \propto s^{-4/3}$. The overall variation, however, was not large, with the period being just 12% larger at $s = 1$ than at $s = 32$.

To further verify our dimensional analysis we also computed the single-spiral solution on progressively finer grids with fixed stiffness parameter $s = 32$ and physical domain size $L = 192$ and determined that the solution recovers the Goldstone modes associated with translational symmetry on sufficiently fine grids. The unit eigenvalues are recovered for the translational modes with precision $|\Lambda - 1| = O(10^{-4})$ when $\Delta x = \Delta y = 0.16$, whereas the dimensional analysis predicts a similar critical length scale $\ell_2 = 0.09$ for this value of s.

3.1.2 Boundary effects

Global translational symmetry implies that there are infinitely many copies of the solution on an unbounded domain that differ in their position but are otherwise

equivalent. On bounded domains characterized by local translational symmetry we can also find multiple solutions related to each other by a translation, but they are not, strictly speaking, equivalent. To quantify this relation more precisely we performed a continuation of the domain-centered solutions discussed previously by gradually shifting the tip towards one of the boundaries on a reasonably large domain. The choice of the boundary is arbitrary due to the 4-fold rotational symmetry of the problem.

For the present purposes it is convenient to place the origin of coordinates at the lower left corner of the domain. If the tip of the spiral (identified as the point at which $\partial_t \mathbf{u} = \mathbf{0}$) has coordinates $[x, y]$, then x and y define the distance of the tip of the spiral, respectively, from the left and bottom boundary. The continuation sequence involves shifting the converged spiral wave solution toward the left or right boundary (decreasing or increasing x) to generate an initial condition, which is refined into a new spiral wave solution using the Newton-Krylov solver A.4. This cycle repeats until the Newton-Krylov solver either fails to converge or converges to a previously found solution.

In the large-s regime local *continuous* symmetry is broken, so we only find solutions shifted by an integer multiple of the grid spacing Δx. Regardless of the direction (towards the left or right wall) the spiral wave solution with $y \approx L/2$ shown in Fig. 9(a) could only be continued for $|x - L/2| \lesssim 0.70\lambda$, i.e., no closer than 0.60λ to either wall (cf. Fig. 13c). We will denote this solution branch $\mathbf{u}_+$. When x was decreased below about 0.60λ, Newton-Krylov solver converged to a nearby spiral wave with $y \approx L/2 - \Delta y/2$. This new spiral wave solution can be continued until $x \approx 0.33\lambda$. We will denote this solution branch $\mathbf{u}_0$. If continued in the opposite direction, $\mathbf{u}_0$ can be extended symmetrically to $x \approx L - 0.33\lambda$.

An example of a spiral wave corresponding to the branch $\mathbf{u}_0$ with the tip near $[x, y] = [96.5, 95.5]$ along with its spectrum is shown in Fig. 14. Its shape is essentially

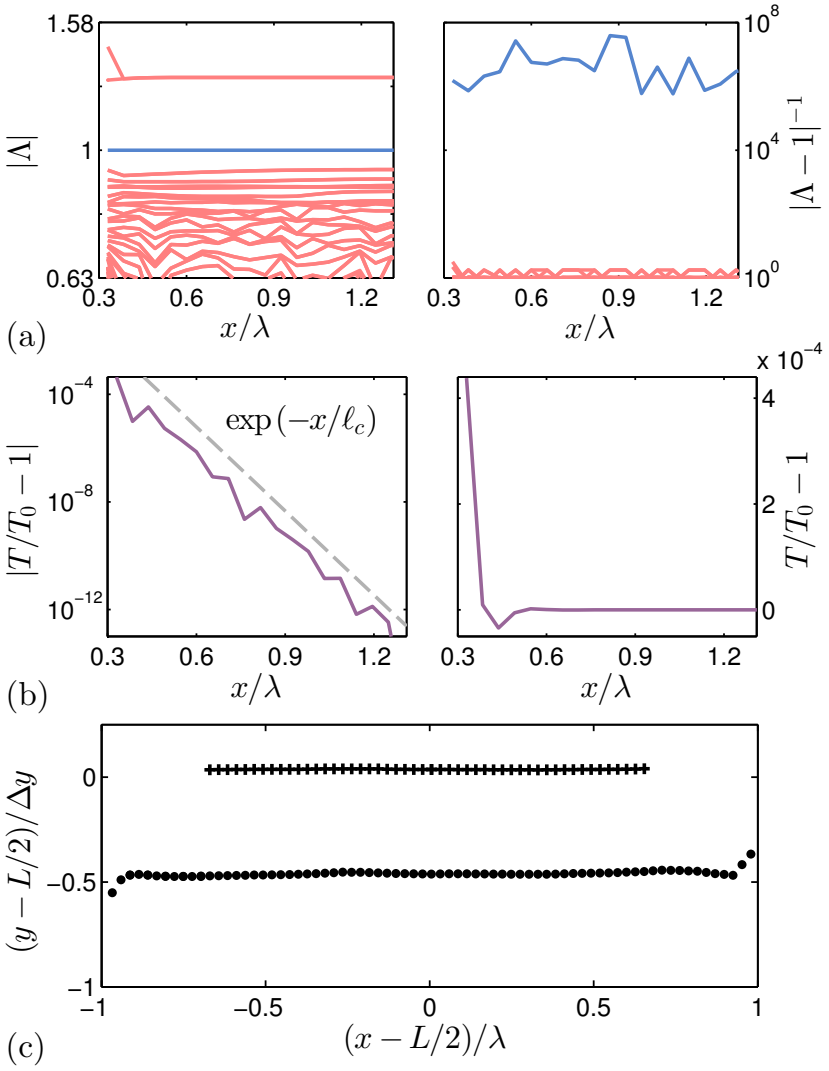

Figure 13: Dependence of the properties of pinned spiral waves on the distance to the boundary for $s = 32$. (a) The eigenvalues Λ of unstable and leading stable modes (red) and near-Goldstone modes (blue) of $\mathbf{u}_0$. (b) The deviation of the period T of $\mathbf{u}_0$ from the period of the domain-centered solution, $T_0 = 50.8321$. (c) The position of the tip of the spiral wave for the $\mathbf{u}_+$ (+) and for the $\mathbf{u}_0$ branch (•). Only every other position is shown.

indistinguishable from that of $\mathbf{u}_+$ (cf. Fig. 9a). Its spectrum is also similar to that of $\mathbf{u}_+$ (cf. Fig. 9b), except for the eigenvalues with positive real part: unlike $\mathbf{u}_+$ which has a pair of eigenvalues, one unstable and one stable, on the real axis, $\mathbf{u}_0$ has two stable complex conjugate eigenvalues $\Lambda_\pm = 0.4662 \pm 0.1735\mathrm{i}$. The real and imaginary part of the corresponding modes are shown in Figs. 14e and 14f and can be identified as a linear combination of frustrated translational Goldstone modes (their amplitude varies with distance from the tip). The real and imaginary part of the complex conjugate pair of unstable modes are shown in Figs. 14c and 14d and correspond to the alternans instability.

Counting $\mathbf{u}_0$, $\mathbf{u}_+$, and $\mathbf{u}_- = \mathcal{R}_{\pi/2}\mathbf{u}_+$, there are at least three distinct pinned spiral wave solutions in the large-s limit. Their tips are located, modulo Δx, approximately at $[0.5, 0.5]$ for $\mathbf{u}_0$, $[0.5, 0]$ for $\mathbf{u}_+$, and $[0, 0.5]$ for $\mathbf{u}_-$. Even though these three solutions are distinct, their shapes, temporal periods, and the unstable eigenvalues and eigenmodes corresponding to alternans are virtually indistinguishable, provided they are centered at roughly the same position. Since they can be shifted in either coordinate direction by an integer multiple of Δx, there are $O(N^2)$ "copies" of each of these three solutions.

Most of these "copies" are nearly identical. Consider, for instance the solution $\mathbf{u}_0$. Its leading eigenvalues (cf. Fig. 13a) are effectively independent of the position of the spiral wave and only begin to vary noticeably for $x \lesssim 0.4\lambda$. Similarly, the period of this solution (cf. Fig. 13b) is essentially independent of the position of the tip over almost the entire range of x. The deviation of the period from the reference value T_0 at $x \approx L/2$ decreases exponentially fast with x: $|T - T_0| \propto \exp(-x/\ell_c)$, where $\ell_c \approx \lambda/24$ is the characteristic length scale that describes the interaction of this spiral with the boundary.

In the small-s regime the continuous translational symmetries are recovered, so there is a continuum of drifting spiral wave solutions parametrized by the coordinates

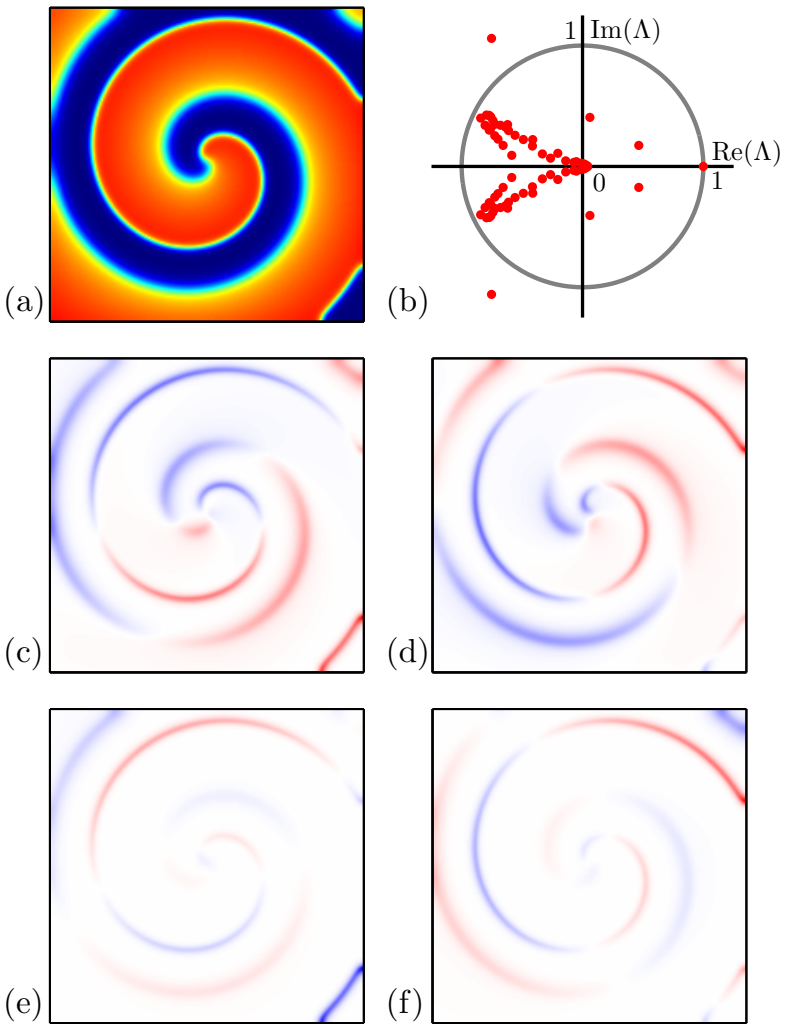

Figure 14: A sample solution from the branch $\mathbf{u}_0$ (a) and the spectrum of its eigenvalues (b). (c) Real and (d) imaginary part of the unstable complex conjugate pair of modes. (e) Real and (f) imaginary part of the stable complex conjugate pair of modes with eigenvalues $\Lambda_\pm = 0.4662 \pm 0.1735\mathrm{i}$.

$\mathbf{x}_o = [x, y]$ of the tip. Unlike the large-s limit, there is only one type of solution. Its leading eigenvalues Λ, the spatial shift $\mathbf{h}$ over one period, and the period T as a function of x (with $y = L/2$) are shown in Fig. 15. Just like in the large-s limit, we find all the basic properties of the spiral wave solution to be effectively independent of the position of the tip, provided $x \gtrsim 0.5\lambda$. The differences between distinct spiral wave solutions are exponentially small. For instance, Figs. 15(b) and 15c show that $|\mathbf{h}| \propto \exp(-x/\ell_c)$ and $|T - T_0| \propto \exp(-x/\ell_c)$, where T_0 is the period of the centered solution and now $\ell_c \approx \lambda/20$. The largest differences ($|\mathbf{h}| \approx 0.05\lambda$ and $|T - T_0| \approx 0.02T_0$) correspond to the distance of the closest approach $x \approx 0.14\lambda = O(\ell_c)$.

Our findings can be used to make the concept of local Euclidean symmetry more precise. As long as the tip of the spiral wave is not too close to the boundary of the domain, that solution can be shifted (discretely for large s or continuously for small s) without changing any of its properties up to some level of resolution ε_{res}. This level can be made arbitrarily small by increasing the separation between the tip of the spiral waves and the boundary and is only limited (from below) by the numerical tolerance ε_{tol}. Hence, for all practical purposes, distinct spiral wave solutions with their tips sufficiently separated from the boundary are completely equivalent, although their spatial shape is affected by the boundaries.

The symmetry breaking in the proximity of the boundary is reflected in the eigenvalues associated with Goldstone modes in the small-s limit. As Fig. 15(a) illustrates, the eigenvalue associated with the x-translation deviates from unity for $x \lesssim 0.6\lambda$. The vertical boundary does not break the y-translation symmetry for spiral waves (and hence does not cause a significant deviation of the corresponding eigenvalue from unity), unless they drift in the x direction. This symmetry is eventually broken for $x \lesssim 0.3\lambda$ when displacement h_x becomes significant. Comparison with Fig. 15(a) shows that for the corresponding eigenvalue $|\Lambda - 1| = O(|h_x|/\lambda)$.

It is worth noting that $h_x > 0$ for $x \lesssim 0.27\lambda$, and $h_x < 0$ for $0.27\lambda \lesssim x \lesssim 0.40\lambda$,

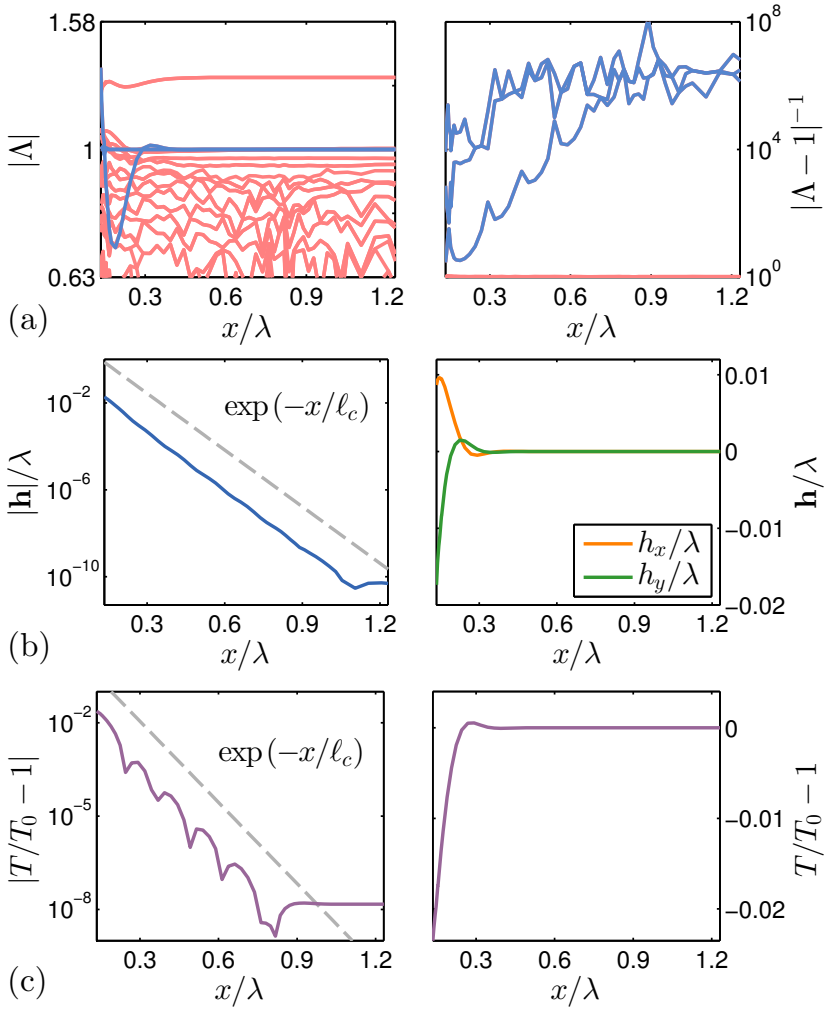

Figure 15: Dependence of the properties of drifting spiral waves on the distance to the boundary for $s = 1.2571$. (a) Eigenvalues Λ_i of unstable and leading stable modes (red) and near-Goldstone modes (blue). (b) The spatial shift $\mathbf{h}$, normalized by the wavelength λ. (c) The deviation of the period T from the period of the domain-centered solution, $T_0 = 54.7446$.

so that the interaction is repulsive (the drift is away from the boundary) at small distances and attractive (the drift is towards the boundary) at slightly larger distances. In a related work Langham and Barkley [115, 116] investigated the interaction with the boundaries for resonantly driven (and hence drifting) *stable* spiral waves in the Barkley model [14] of excitable media. They also found that the interaction is repulsive at close range and showed that the interaction length scale ℓ_c is determined by the spatial extent of the response functions (adjoints of the Goldstone modes) which are localized to the core region [36, 30, 33]. We have confirmed by direct calculation that both the spatial and temporal response functions in the Karma model (cf. Ch. 4) decay as e^{-r/ℓ_c}, where r is the distance to the tip.

Finally, the period of rotation shows opposite trends for pinned (large s) and drifting (small s) spirals. As a pinned spiral approaches a boundary it rotates more slowly (T increases), whereas a drifting spiral rotates more quickly (T decreases). A quantitative explanation of these different behaviors relies on the details of the spatial structure of the temporal response function, and is explored in Chapter 4.

3.1.3 Domain size effects

We already have some qualitative intuition about the effect the size of the domain has on the structure and properties of spiral wave solutions. As the size of the domain increases, the solution should approach an unbounded spiral and all its properties should become size-independent. In particular, global Euclidean symmetry (whether continuous for small s or discrete for large s) should be restored. On the other hand, as the size of the domain is reduced, the structure of the solution and its properties are expected to change significantly, and, on sufficiently small domains the spiral wave solution might not even exist.

To quantify the differences between single-spiral waves on domains of different size, we computed a sequence of unstable solutions on domains with fixed grid spacing Δx

and varying physical size L. The sequence was initiated from a large spiral wave with an approximately centered core, which was then truncated on all sides by trimming small regions in a symmetric fashion, which generated the initial condition for the next solution. The process continued until the Newton-Krylov solver failed to find a nontrivial solution.

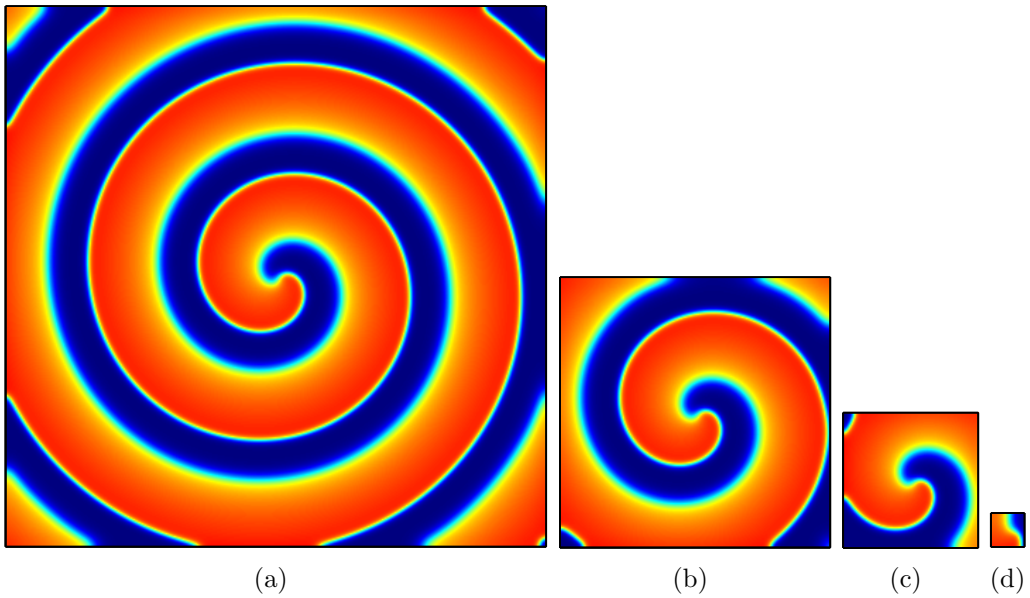

Figure 16: Domain-centered spiral wave described by a generalized relative periodic solution for $s = 1.2571$. Domains size is $L = 384 = 4.92\lambda$ (a), $L = 192 = 2.46\lambda$ (b), $L = 96 = 1.23\lambda$ (c), and $L = L_0 = 24 = 0.31\lambda$ (d), the minimal domain size in the small-s regime.

Local symmetry suggests that sufficiently far from the boundaries the solution should not depend on the boundary condition. Hence, solutions computed on domains of different size, e.g., $\Omega_2 \subset \Omega_1$, should be virtually indistinguishable away from the boundaries of Ω_2. This is exactly what we find by comparing two solutions $\mathbf{u}_1$ and $\mathbf{u}_2$ computed on domains of size $L_1 = 448$ and $L_2 = 432$, respectively. The difference $\delta\mathbf{u} = \mathbf{u}_1 - \mathbf{u}_2$ inside Ω_2 is found to be concentrated in a narrow boundary layer of width $O(\ell_c)$ (cf. Fig. 17b), where $\ell_c \approx \lambda/20$ for $s = 1.2571$, as we determined previously. Furthermore, Fig. 17(a) shows that the difference becomes exponentially small away from the boundaries, $|\delta\mathbf{u}| \propto \exp(-r/\ell_c)$, where r denotes the distance

from the boundary of the smaller domain. Inside the boundary layer the solution on the smaller domain adjusts to the no-flux condition and can have a large curvature κ comparable to that at the spiral wave core. Hence, it should not be surprising to see the same length scale describe both the width of the core and the width of the boundary layer.

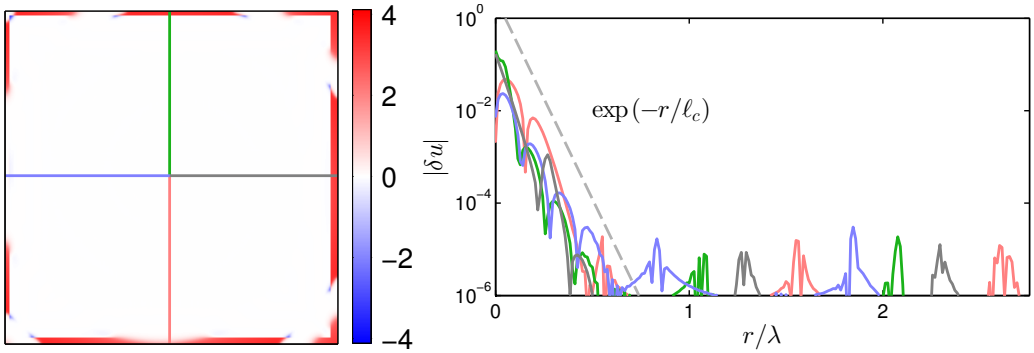

(a) (b)

Figure 17: The difference $\delta\mathbf{u}$ between centered spiral wave solutions computed on domains of different size ($L_1 = 448$ and $L_2 = 432$) for $s = 1.2571$. Only the u variable is shown. The results for the u_2 variable are qualitatively similar. (a) The magnitude of the difference in the interior of the smaller domain. (b) The difference along the four rays passing though the tip of the spirals shown in panel (a) as a function of the distance r from the boundary.

For $s = 32$, the spiral waves are pinned, and we find a minimal domain size, $L_0 = 17 \approx 0.23\lambda$, approximately 0.45 cm in dimensional units, below which spiral wave solutions cannot be found. This domain size corresponds to the distance between the tip of the spiral and the boundary equal to $L_0/2 = 0.115\lambda \approx 2\ell_c \approx \lambda/12$. Since ℓ_c determines both the radius of the spiral wave core and the width of the boundary layer, $L = L_0$ corresponds to the collision of the spiral core with the boundary layer. If this criterion applies more generally, we should expect to find spiral wave solutions only on domains of size $L \gtrsim 4\ell_c$.

Pinned spiral waves remain unstable in the entire range of system sizes. The dominant eigenvalues of the solution $\mathbf{u}_0$ are shown in Fig. 18(a). As L increases,

the eigenvalues from the discrete part of the spectrum approach a constant value, but new eigenvalues also appear which correspond to the continuous part of the spectrum. For $L_0 \leq L \leq 0.36\lambda$, there are between three and five unstable modes. As $L \to L_0$, the dominant eigenvalues quickly grow in magnitude, approaching $\Lambda_\pm = 2.0 \pm 2.77\mathrm{i}$ (these are outside of the range of Fig. 18a).

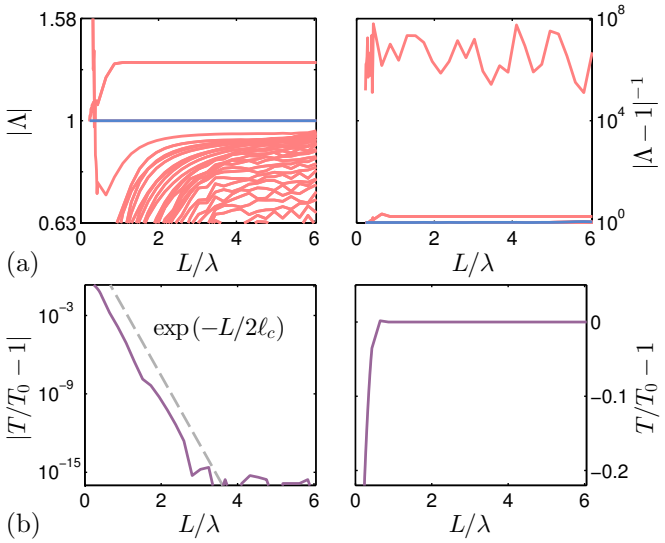

Figure 18: Dependence of the properties of the domain-centered pinned spiral wave $\mathbf{u}_0$ on the size of the domain for $s = 32$. (a) The eigenvalues Λ of unstable and leading stable modes (red) and Goldstone modes (blue). (b) The deviation of the period T from the period $T_0 = 50.8321$ at $L = 6\lambda$.

Interestingly, the character of the instability changes for $L < L_b \approx \lambda$. Consider, for instance, the solution at $L = 48 \approx 0.65\lambda$ shown in Fig. 19(a). The magnitude of its unstable eigenvalues (cf. Fig. 19b) is comparable to that in much larger systems, but the corresponding eigenmodes (Fig. 19c and 19d) correspond to the meandering instability, rather than alternans. Initial conditions close to this unstable solution produce spiral waves which persist for up to 10^3 rotations without breaking up, which is consistent with numerical results of Karma [108] for domains smaller than 2.1 cm (which corresponds to $L_b = 80 = 1.08\lambda$ in nondimensional units). As. Fig. 20 illustrates, the amplitude of meandering slowly grows, until the tip runs

into a boundary and the wave eventually collapses. The minimal domain size L_b that supports spiral wave breakup via alternans defines another important dynamical length scale.

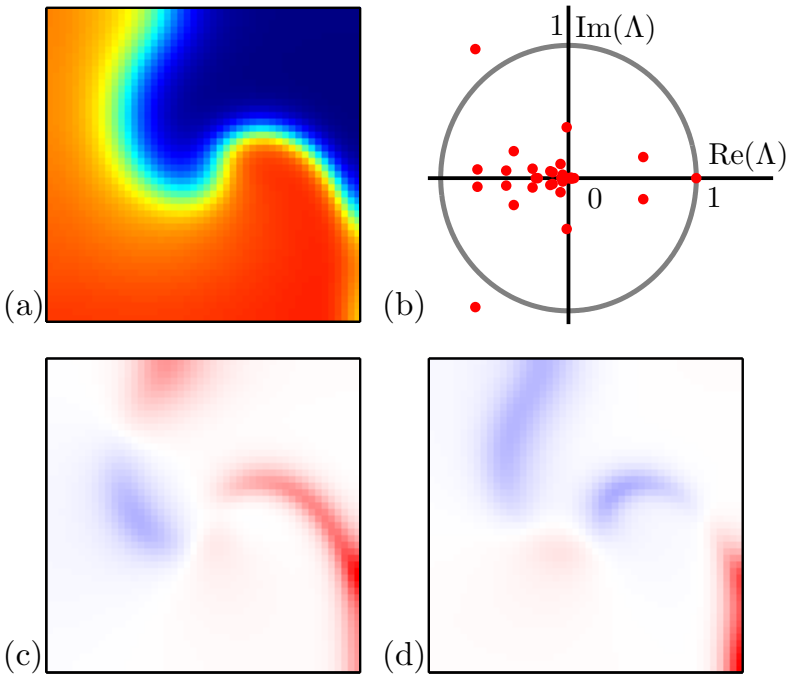

Figure 19: Pinned spiral wave solution on the domain of linear size $L = 48 \approx 0.65\lambda$ for $s = 32$ (a) and its spectrum (b). The real and imaginary parts of the complex conjugate modes corresponding to the unstable eigenvalue pair are shown in panels (c) and (d).

The period of the solution approaches the asymptotic value T_0 exponentially fast as L increases (cf. Fig. 18b). For $L \lesssim 3\lambda$ we find $|T - T_0| \propto \exp(-L/2\ell_c)$, which is consistent with the scaling we found previously. Indeed, for a domain-centered spiral wave $x = L/2$, or $L = 2x$, which means that scaling with x and L follows from the same general scaling law. For $L \gtrsim \lambda$, the period can be considered essentially independent of L.

Most of the results for small s are qualitatively similar, so we will only focus on what is new or different. This regime is characterized by continuous local symmetries, with drifting spiral waves possessing three Goldstone modes. The magnitude of the

spatial displacement of the spiral wave over one period decreases exponentially with L, $|\mathbf{h}| \propto \exp(-L/2\ell_c)$ (cf. Fig. 21b). As the domain is truncated, the eigenvalues associated with Goldstone modes begin to deviate from unity (cf. Fig. 21a). Eigenvalues corresponding to translational modes deviate first, at $L \approx 1.3\lambda$. This agrees well with the distance $x \approx 0.6\lambda$ to the boundaries at which translational symmetry is broken, as we found in the previous subsection. Somewhat unexpectedly, for even smaller domains ($L \lesssim 0.6\lambda$), the eigenvalue associated with temporal translation also deviates from unity. The critical domain size matches the distance of the tip to the boundary ($x \approx 0.3\lambda$) beyond which the spiral solution loses translational symmetry, as noted in the previous section. Hence deviation of the "temporal" eigenvalue from unity can be understood as a result of the non-perturbative nature of *finite* spatial shifts on small domains and the subsequent loss of temporal periodicity. For $L \lesssim 0.6\lambda$ the displacement of the spiral is significant enough to affect its temporal dynamics. The solutions in this limit do not describe relative periodic orbits. For instance, both the "period" and the spatial shift of $\mathbf{u}(0)$ and $\mathbf{u}(T)$ becomes noticeably different.

The decrease in the temporal period at small separations between the tip of the spiral and the boundaries observed in Figs. 15c, 18(b), and 21c is due to the negative curvature of the wave front near the boundary due to the no-flux boundary condition. It is well-known [111] that the speed of propagation of an excitation wave is related to the curvature κ of its front by a linear relationship, with convex ($\kappa > 0$) wave fronts traveling more slowly than flat ($\kappa = 0$) ones, and flat wave fronts traveling more slowly than concave ($\kappa < 0$) ones [176, 68]. The magnitude of this effect on the rotation period is controlled by the spatial structure of the temporal response function, which decays exponentially fast with the distance from the tip of the spiral, with the decay rate equal to the length scale ℓ_c. The local curvature deviation can be understood as the essential mechanism for speeding up the wave near the boundary in order for the whole state to be periodic with fixed period T.

The exponential dependence of the shift madnitude $|\mathbf{h}|$ and the period T of the drifting spiral waves found for the modified Karma model are in contradiction with the analytical results obtained by Aranson *et. al.* [5] for a similar model in the $\nu \to 0$ limit, which predict a super-exponential dependence of the drift speed $|\mathbf{h}|/T$ and rotational frequency $\omega = 2\pi/T$ of spiral waves on the domain size L. Davydov and Zykov [59] predict the frequency of spirals in a generic reaction-diffusion model with $\nu = 0$ to vary as the inverse of the domain size (for circular domains of radius comparable to λ). Hartmann *et. al.* [94] claim that their simulations confirm this prediction, but a quick inspection of their numerical results, as well as those of Davydov and Zykov, shows that their data is in excellent agreement with the exponential dependence.

3.2 Summary and discussion

We performed the first systematic investigation of unstable spiral wave solutions of a simple spatially discretized model of cardiac tissue with physiologically and dynamically relevant no-flux boundary conditions. We also characterized how the basic properties of these solutions, such as their temporal period, spatial drift, and stability, depend on the size of the domain, the proximity of the spiral core to the nearest domain boundary, and the microscopic heterogeneity associated with spatial discretization. We found that, although both the boundary conditions and the discretization break the global Euclidean symmetry of the model, unstable spiral wave solutions tend to respect a local – continuous or discrete – version of Euclidean symmetry.

Existing tools, such as Newton-Krylov solvers, developed for computing unstable solutions in the presence of global continuous symmetries (e.g., in unbounded domains or domains with periodic boundary conditions) break down on bounded domains with generic boundary conditions that are not consistent with the global symmetries. However, for reaction-diffusion systems in general, and monodomain models of cardiac tissue in particular, which lack long-range correlations, the effect of

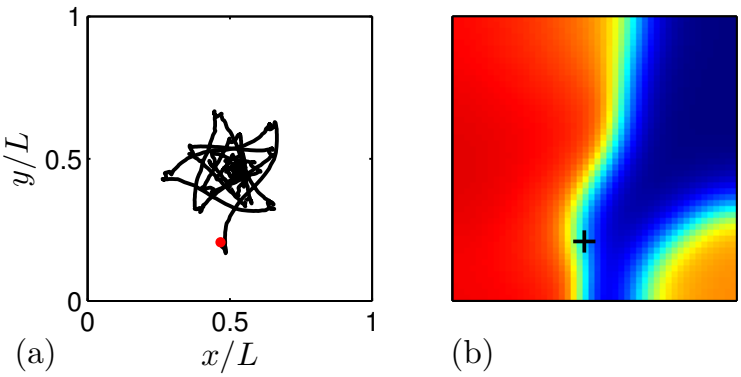

Figure 20: Meandering spiral wave solution on the domain of linear size $L = 48 \approx 0.65\lambda$ for $s = 32$. (a) The tip trajectory. (b) The state just before the wave collapse, with tip marked by the black +, which corresponds to the red dot in (a).

boundaries is localized, which enables computation of solutions satisfying local continuous symmetries using a generalization of Newton-Krylov solvers. The generalization involves weighting, or windowing, of the residual to suppress the symmetry-breaking effect of the boundaries. The generalized solvers permit the computation of unstable solutions describing, e.g., pinned and drifting spiral waves in a model of cardiac tissue in the regime characterized by spontaneous breakup of spiral waves leading to fibrillation-like dynamics.

The inherent spatial heterogeneity associated with the cellular structure of cardiac tissue, and the associated discreteness of the numerical model, was found to have an interesting effect which is usually overlooked in the studies of stable solutions. Cardiac tissue models typically involve discontinuous functions which describe switching of the state of various ionic pumps and channels. Although they simplify the formulation, these discontinuities are unphysical and lead to the emergence of short time scales and corresponding short length scales that can impact the properties of unstable solutions. When these short length scales are small compared to the size of cardiomyocytes, the spatial heterogeneity associated with cellular structure breaks the continuous translational symmetry, leading to pinning of unstable spiral waves. In the particular cardiac model considered here, at least three different branches of such pinned spiral

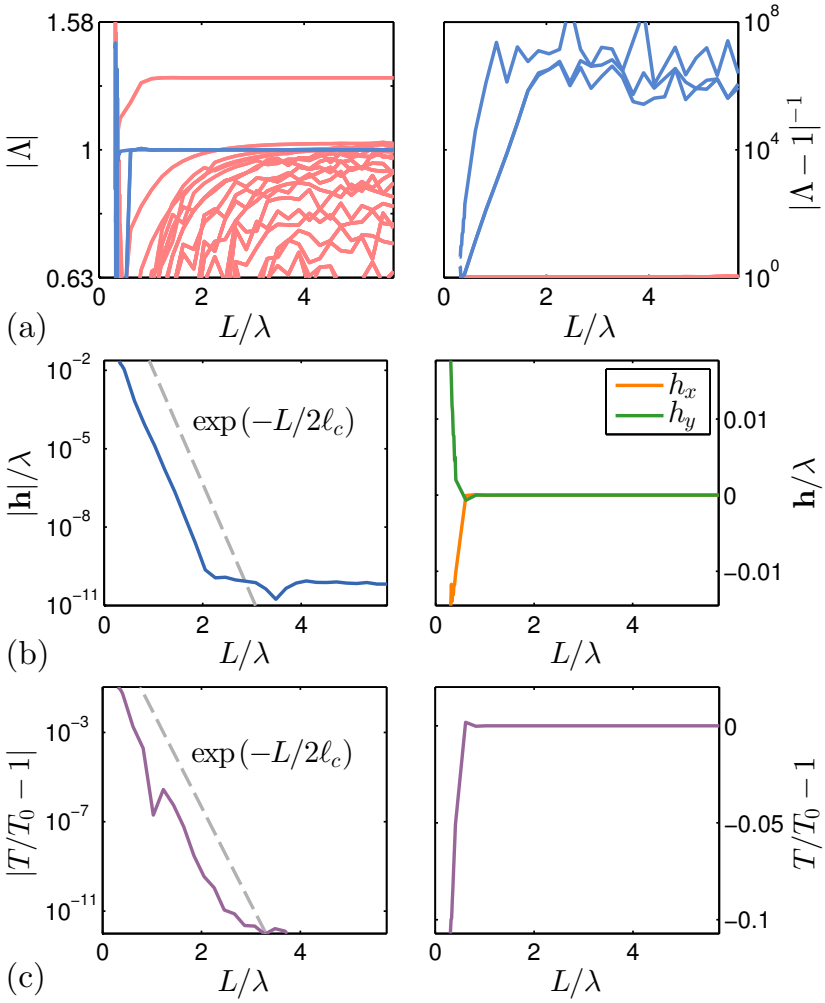

Figure 21: Dependence of the properties of a domain-centered drifting spiral wave on the domain size. For $s = 1.2571$ the minimal domain size is $L_0 = 24 \approx 0.31\lambda$. (a) The eigenvalues Λ of unstable and leading stable modes (red) and near-Goldstone modes (blue). (b) The spatial shift $\mathbf{h}$, normalized by the wavelength λ. (c) The deviation of the period T from the period $T_0 = 54.7447$ at $L = 5.74\lambda$.

waves exist, parametrized by the position of their tip relative to the computational grid and characterized by distinct stability properties. Notably, the "alternans-stable" meandering spiral waves found in the same parameter regime do not display pinning. However, even there discreteness manifests itself as arbitrarily large curvature of the tip trajectory under the development of the meander instability.

Even though microscopic spatial heterogeneity breaks the continuous translational symmetry, discrete translation symmetry survives on sufficiently large domains. We find that each unstable solution can be shifted by a discrete number of grid points (or cells) along or transversely to the direction of the fibers without changing, to numerical precision, either its stability properties or its period. Hence, for all practical purposes these solutions can be considered equivalent under discrete translations. This translation symmetry is local in the sense that the properties of different solutions from the same branch are only invariant (to numerical precision) for finite translations such that the tip of the spiral wave remains outside of the boundary layer of width $O(\ell_c)$, but they begin to vary as the tip approaches any of the boundaries. For each branch, the translation symmetry is reflected in the stability spectrum in the form of slightly frustrated analogues of translational Goldstone modes characterized by a pair of real or complex conjugate Floquet multipliers with positive real part.

Continuous translational symmetry can be restored by replacing the discontinuous switching functions in the ionic model with smooth ones. In the absence of small intrinsic length scales, spiral wave solutions become well-resolved even on a discrete grid. As a result, three discrete branches of pinned spiral wave solutions are merged into a single branch which comprises a continuum of symmetry-related drifting spiral waves parametrized by the position of their tip. Here too, the continuous translational symmetry is manifested in the stability spectra of the solutions, which possess three Goldstone modes corresponding to the three continuous translation symmetries,

one with respect to time and two with respect to spatial position. Again, the spatial symmetry is local: the properties of spiral wave solutions remain invariant (to numerical precision) with respect to finite translations, provided the tip of the spiral wave remains outside of the boundary layer of width $O(\ell_c)$.

Global Euclidean symmetry can, of course, be gradually restored by increasing the size L of the computational domain. However, even on finite domains one finds that the solutions approach their asymptotic shape in the interior of the domain exponentially fast as L increases. The difference between solutions with different L is again found to be confined to the boundary layer of width $O(\ell_c)$. Similarly, the properties of solutions approach the asymptotic values exponentially fast as L increases, with the same length scale ℓ_c. This length scale (ℓ_c) was found to control the effect of the boundaries rather generally. Effectively, ℓ_c controls the strength of interaction between a spiral wave and a (locally) straight boundary (and by extension, interaction between two identical counter-rotating spiral waves). With few exceptions (notably, the eigenvalues from the continuous part of the stability spectrum), the deviation from asymptotic values for all properties of spiral wave solutions (e.g., their shapes, temporal periods, spatial displacement over one rotation) were found to scale exponentially, i.e., as $\exp(-r/\ell_c)$, with the distance r to the boundary.

CHAPTER IV

ADJOINT EIGENFUNCTIONS

In the previous chapter we have utilized a numerical method which employs a Newton-Krylov solver for computing both the unstable generalized relative periodic orbits of (13) and their right eigenfunctions on bounded domains of arbitrary shape that break all the continuous symmetries of the underlying evolution equations. In this Chapter, we seek a better understanding of the structure of the left eigenfunctions of unstable single-spiral states, especially as relates to the marginal set – the response functions. A snapshot of a single-spiral solution described by a generalized relative periodic orbit is presented in Fig. 22(a), using the parameters laid out in Tab. 1 with $s = 1.2571$. This spiral wave solution has wavelength $\lambda = 78$ (2.04 cm) and period $T = 54.74$ (136.9 ms) on a domain of size $L = 192$ (5.03 cm). When the tip $\mathbf{x}_o(0)$ of the spiral (defined by $\partial_t \mathbf{u}(t, \mathbf{x}_o(t)) = \mathbf{0}$) is placed within 10 μm of the center of the domain, it drifts by just $|\mathbf{h}| = O(10^{-11}\lambda)$ over the course of the rotation, reflecting the discrete rotational symmetry of the problem associated with this particular initial condition. Hence, although it is a member of a class of relative periodic orbits, this particular solution is, to numerical precision, simply a periodic orbit. For other choices of $\mathbf{x}_o$, we found that $|\mathbf{h}| \propto e^{-\zeta/\ell_c}$, where ζ is the distance from $\mathbf{x}_o$ to the nearest boundary and ℓ_c is a numerically determined critical length scale.

4.1 Stability and sensitivity

This thesis introduces a method (detailed in A.2.1) of computing the adjoint eigenfunctions of time-dependent solutions that does not rely on a transformation to the co-moving frame, thus permitting computation of adjoint eigenfunctions for spiral wave solutions with arbitrary symmetry properties and temporal dependence. The

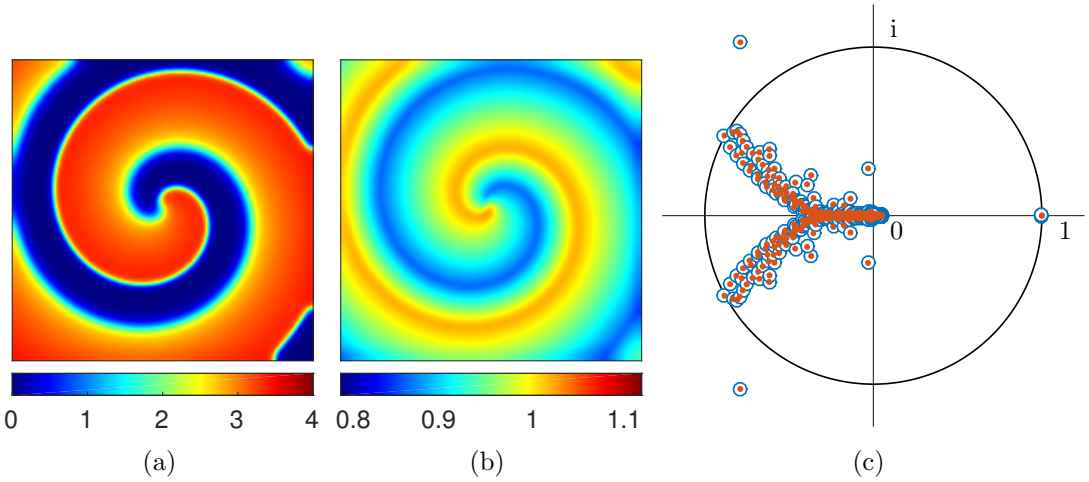

Figure 22: (a,b) Snapshot $\mathbf{u}(0, \mathbf{x})$ of the unstable generalized relative periodic solution with period $T = 54.74$ and wavelength $\lambda = 78$ (the first and second component are shown above, and below, respectively). (c) Floquet spectrum of the solution from the right (blue circles) and left (red dots) eigenfunction calculations.

method relies on the numerical time-stepping of the solution, the accurate evaluation of the forward tangent evolution, and similarly accurate computation of the adjoint tangent evolution. While the nonlinear and forward tangent models can be stepped in unison, using the relatively simple method stated in Ch. 2 and detailed in A.2, the computation of the adjoint evolution required special consideration due to the complications inherent to the formulation of the adjoint flow. In particular, this required traversing the nonlinear solution backwards in time, using a bespoke interpolant designed to uniformly accurately approximate the state with the same truncation order as the original time-stepping scheme. Due to the essentially discrete nature of a time-stepped solution, only states at times $t_n = n\Delta t$ are known, which makes evaluation between the time-steps non-trivial. This numerical technique is detailed in A.2.1, including the interpolant defined for the fourth-order time-stepping scheme used for the nonlinear model.

The spectrum of Floquet multipliers Λ_i for the spiral wave solution is shown in

Fig. 22(b). The Floquet multipliers correspond to the eigenvalues of $\mathcal{V}_T$; the corresponding Floquet exponents σ_i can be computed using the relation $\Lambda_i = e^{\sigma_i T}$. The spectrum is seen to include both a discrete and a continuous part. There are four unstable eigenvalues (two from the discrete and two from the continuous part) as well as a triply-degenerate marginal eigenvalue ($\Lambda = 1$) associated with infinitesimal spatial and temporal translations, just like for relative equilibria [16]. The two Goldstone modes associated with infinitesimal spatial translations persist on bounded domains [16] due to the *local* translational invariance of (13) even though the *global* translational symmetry is broken by the boundary conditions (15), cf. Ch. 3.

We have computed the leading 130 left and right eigenmodes with high accuracy (cf., Fig. 55 and the associated discussion). The movies of $\mathbf{v}^i(t, \mathbf{x})$ and $\mathbf{w}^j(t, \mathbf{x})$ for several dominant modes are included in the supplemental material of Ch. 4. As Fig. 22(b) shows, the eigenvalues associated with the left eigenfunctions are just as accurate as those associated with the right eigenfunctions. In particular, the eigenvalues associated with the marginal modes deviate from unity less than $O(10^{-7})$ for both the Goldstone modes and the response functions.

The Goldstone modes associated with translational symmetries are shown in Fig. 23(a-b) and (d-e). These correspond to the spatial derivatives of the initial condition $\mathbf{n} \cdot \nabla \mathbf{u}$ along two orthogonal directions $\mathbf{n}$. Figures 23(c) and (f) shows the Goldstone mode associated with temporal translation which corresponds to the temporal derivative $\partial_t \mathbf{u}$. Figures 23(g-l) show the corresponding response functions. The orthogonality condition (36) does not completely fix the normalization of the two sets of eigenfunctions. As the eigenfunctions represent solutions to a linear problem (and are thus scale-independent), we are free to choose the absolute scale of each set, provided (36) is satisfied. Hence, we added an additional constraint $\langle \mathbf{v}^i | \mathbf{v}^i \rangle = \langle \mathbf{w}^i | \mathbf{w}^i \rangle$, so that the scales of the dominant components of $\mathbf{v}^i$ and $\mathbf{w}^i$ are comparable.

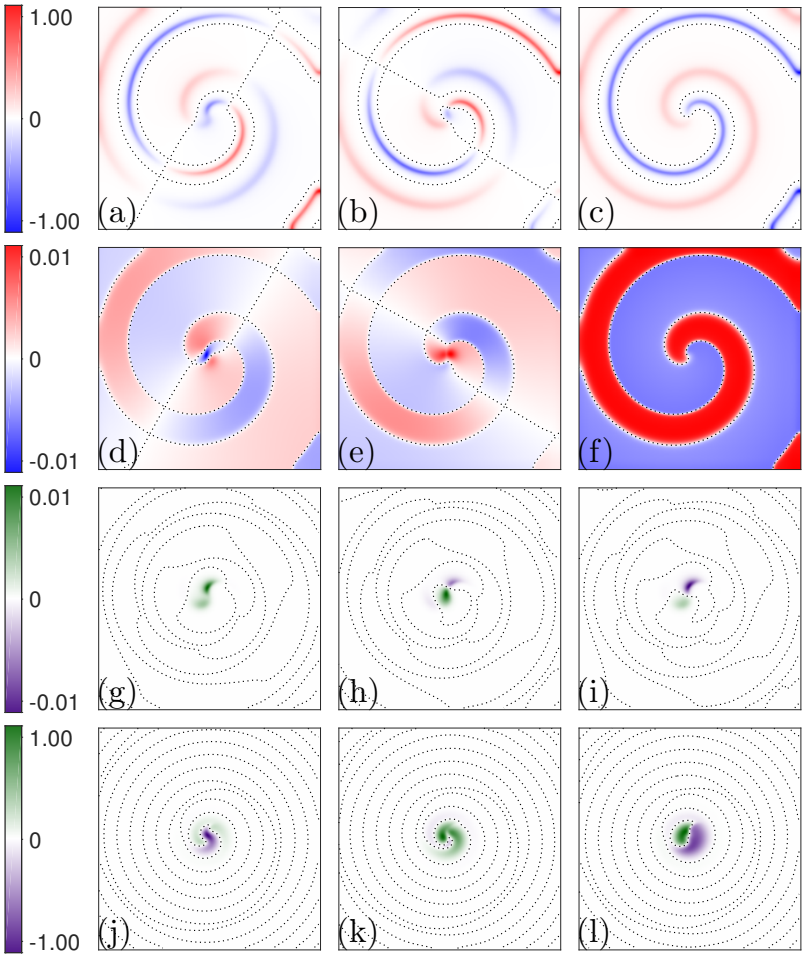

Figure 23: Goldstone modes (a-f) and response functions (g-l). The left two columns show the modes associated with spatial translation and the right column – the modes associated with temporal translations. The first (a-c) and second (d-f) rows show, respectively, the first and second components v_1^i and v_2^i of the Goldstone modes. The third (h-i) and fourth (j-l) rows show, respectively, the first and second components w_1^i and w_2^i of the response functions. The dotted curves denote nodal lines. Here and below the snapshots of eigenfunctions are shown at the same time instant ($t = 0$) as the spiral wave solution in Fig. 22.

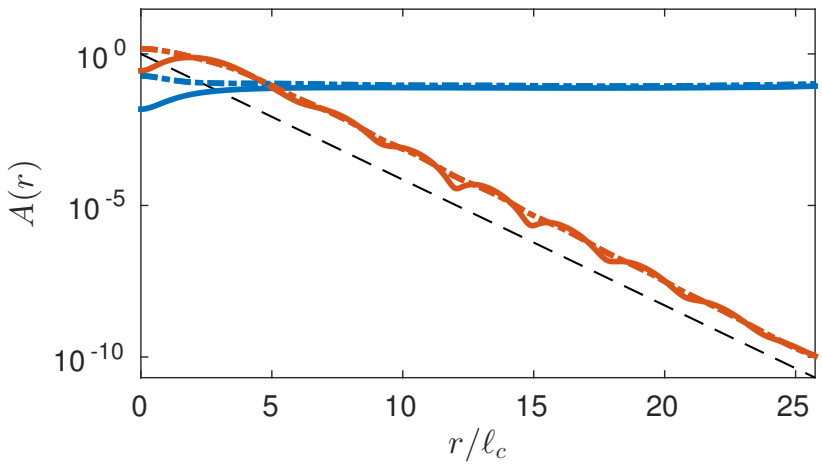

Figure 24: Amplitude of the left (red) and right (blue) eigenfunctions corresponding to spatial translations (solid), and temporal translations (dashed). Numerically determined scaling for the response functions $\ell_c^{\text{num}} = \lambda/20$ (black, dashed).

As Fig. 23 illustrates, for the Karma model the second component (gating variable) of the right eigenfunctions is very small compared to the first component (voltage variable), $\|v_2^i\| = O(10^{-2}\|v_1^i\|)$, while for the left eigenfunctions the opposite is true, $\|w_1^i\| = O(10^{-2}\|w_2^i\|)$. This disparity is due to the difference in the time scales of cellular kinetics described by the nonlinear functions $\mathbf{f} = (\tilde{f}_1, \epsilon\tilde{f}_2)$, where $\epsilon = 0.01$ is a fixed parameter and both functions $\tilde{f}_1$ and $\tilde{f}_2$ and their partial derivatives are all $O(1)$. For instance, if we rescale the two components of the right eigenfunction as $\mathbf{v}^i = (\tilde{v}_1^i, \epsilon\tilde{v}_2^i)$, then the evolution equation (34) can be rewritten as

$$\begin{aligned}
\partial_t \tilde{v}_1^i &= D_{11}\nabla^2\tilde{v}_1^i + \frac{\partial\tilde{f}_1}{\partial u_1}\tilde{v}_1^i + \epsilon\frac{\partial\tilde{f}_1}{\partial u_2}\tilde{v}_2^i, \\
\partial_t \tilde{v}_2^i &= D_{22}\nabla^2\tilde{v}_2^i + \frac{\partial\tilde{f}_2}{\partial u_1}\tilde{v}_1^i + \epsilon\frac{\partial\tilde{f}_2}{\partial u_2}\tilde{v}_2^i,
\end{aligned} \tag{45}$$

where $\partial\tilde{f}_i/\partial u_j = O(1)$ for all i and j. Similarly, rescaling the components of the left eigenfunctions $\mathbf{w} = (\epsilon\tilde{w}_1^i, \tilde{w}_2^i)$, we can rewrite the evolution equation (35) as

$$\begin{aligned}
-\partial_t \tilde{w}_1^i &= D_{11}\nabla^2\tilde{w}_1^i + \frac{\partial\tilde{f}_1}{\partial u_1}\tilde{w}_1^i + \frac{\partial\tilde{f}_2}{\partial u_1}\tilde{w}_2^i, \\
-\partial_t \tilde{w}_2^i &= D_{22}\nabla^2\tilde{w}_2^i + \epsilon\frac{\partial\tilde{f}_1}{\partial u_2}\tilde{w}_1^i + \epsilon\frac{\partial\tilde{f}_2}{\partial u_2}\tilde{w}_2^i.
\end{aligned} \tag{46}$$

Equations (45) and (46) have solutions both components of which are of the same order of magnitude, so we should indeed expect $\|v_2^i\| = O(\epsilon)\|v_1^i\|$ and $\|w_1^i\| = O(\epsilon)\|w_2^i\|$ for all eigenfunctions. Hence, in the remainder of the paper we will focus mostly on their dominant (unscaled) components v_1^i and w_2^i.

The most salient feature of the response functions in the Karma model is that they are very strongly localized near the core of the spiral, just like in most other excitable systems and the CGLE. To quantify this spatial localization we defined the amplitude following Ref. [30],

$$A(r) = \left(\frac{1}{2\pi} \int_0^{2\pi} |\mathbf{w}(r,\theta)|^2 \, \mathrm{d}\theta \right)^{1/2}, \tag{47}$$

where r is the distance from $\mathbf{x}_o$. The amplitude can be defined in a similar manner for all eigenfunctions, both left and right. As Fig. 24 shows, the response functions decay exponentially with r, while the amplitude of the Goldstone Modes, as expected, remains a constant outside of the core region. For comparison, the dashed line shows the exponential decay $A \propto e^{-r/\ell_c}$ predicted numerically Ch. 3 based on the scaling results for the spatial drift $\mathbf{h}$ and the period T of the spiral wave, where $\ell_c \approx \lambda/20$ for the value of s used here. The spatial decay rate determined directly from the response functions gives a very close value $\ell_c = 0.0478\lambda \approx \lambda/21$, which confirms the conjecture Ch. 3 that the scaling of $\mathbf{h}$ and T is indeed controlled by the spatial structure of the response functions corresponding, respectively, to the spatial and temporal Goldstone modes.

The response functions do not decay with r monotonically. Instead, the dominant component w_2 displays pronounced oscillations, with roughly the same distance ($\Delta r \approx 3.04\ell_c$) between the nodal lines for all three response functions. For the temporal response function the nodal lines form closed loops in the plane. In contrast, the nodal lines of the translational response functions form spirals (they are not closed curves). Correspondingly, the angular averaging destroys the underlying oscillation of the amplitude $A(r)$ in the latter case, while in the former case the amplitude clearly

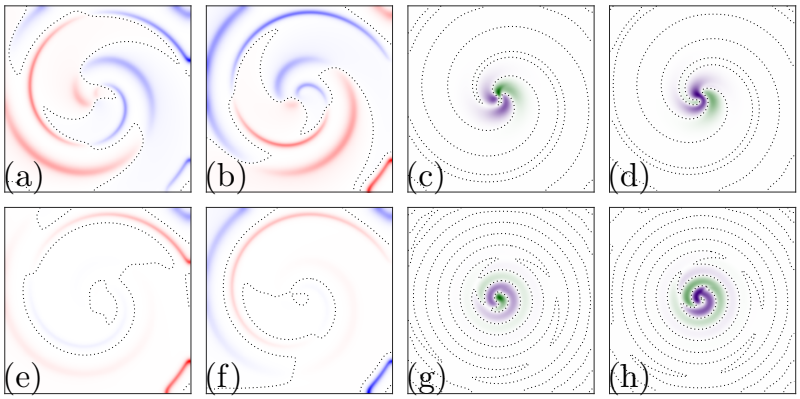

Figure 25: Snapshots of the unstable right (a-b) and corresponding left (c-d) eigenfunctions from the discrete spectrum with Floquet multiplier $\Lambda_\pm = -0.7893 \pm 1.0286\mathrm{i}$. Snapshots of the stable right (e-f) and corresponding left (g-h) eigenfunctions from the discrete spectrum with Floquet multiplier $\Lambda_\pm = -0.0315 \pm 0.2803\mathrm{i}$.

shows the modulation superimposed on top of the exponential profile.

The method introduced here allowed us to compute not only the marginal eigenfunctions, but an entire spectrum of leading modes. In particular, two pairs of complex conjugate modes – the most unstable pair and a stable pair from the discrete part of the spectrum – are shown in Figure 25 and the corresponding angle-averaged amplitudes are plotted in Fig. 26. Again we find that the adjoint eigenfunctions are strongly localized in the core region. Their amplitude *decreases* exponentially, $A(r) \propto e^{-r/\ell_-}$, just as it does for the response functions, albeit more slowly: the corresponding length scales are $\ell_- = 1.72\ell_c$ and $\ell_- = 2.20\ell_c$ for the unstable and stable modes, respectively. The right eigenfunctions show the opposite trend, their amplitude *increases* exponentially, $A(r) \propto e^{r/\ell_+}$. In particular, the stable mode is localized near the boundary, with amplitude growing on the length scale $\ell_+ = 7.04\ell_c$.

The length scale $\ell_+ \approx 5\lambda$ for the unstable modes is extremely large, so they appear to be evenly distributed throughout the entire domain (cf. Fig. 25(a-b)). The shape of the modes clearly indicates that they describe the alternans instability which is characterized by the variation in the width of the excitation wave. This particular pair of modes describes *discordant* alternans: as Fig. 25 (a) illustrates, at $t = 0$ the

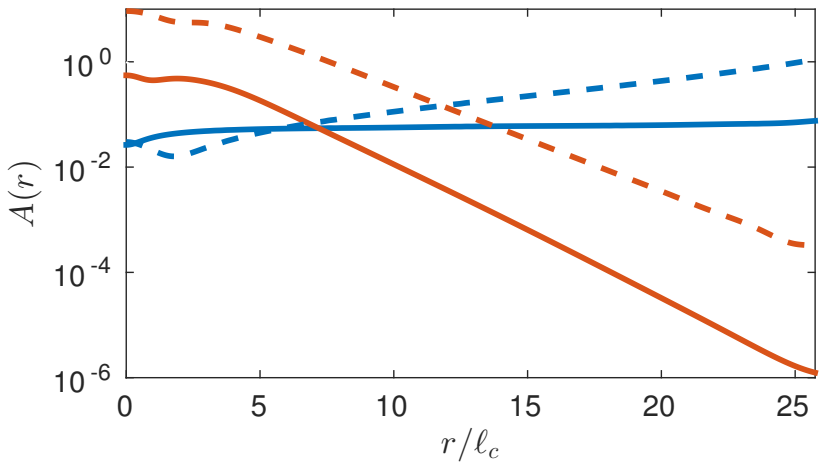

Figure 26: The amplitude of the left (red) and right (blue) unstable (solid) and stable (dashed) eigenfunctions shown in Figure 25(a-b) & (e-f) and Figure 25 (c-d) & (g-h), respectively.

thickness of the excitation wave increases in some regions (positive values of $\mathrm{Re}(v_1)$) and decreases in others (negative values of $\mathrm{Re}(v_1)$), which corresponds to an increase (respectively, descrease) in the action potential duration (APD). The corresponding Floquet multipliers are complex ($\arg(\Lambda) \approx \pm 2\pi/3$), rather than real and negative, as would be the case for a period-doubling bifurcation.

4.1.1 Convective instability

This is, however, not the only unstable mode. There are both *absolutely* unstable modes (characterized by $|\Lambda| > 1$ or $\mathrm{Re}(\sigma) > 0$) and *convectively* unstable modes (for which $\mathrm{Re}(\sigma) < 0$) in the continuous part of the spectrum. A right eigenfunction with amplitude $A(r) > Ce^{r/\ell_+}$, where C and ℓ_+ are some positive constants, describes a convectively unstable mode, if $-c/\ell_+ < \mathrm{Re}(\sigma) < 0$, where $c = \lambda/T$ is the asymptotic conductive velocity of the spiral wave. Equivalently, the temporal decay $\mathrm{Re}(\sigma)T$ must overwhelm the spatial growth λ/ℓ_+ in time T and length λ for the mode to be convectively stable. Convectively unstable modes would produce a noticeable distortion of the spiral wave on sufficiently large domains. Unexpectedly, most of the absolutely stable modes computed for the solution shown in Fig. 22 grow with radial

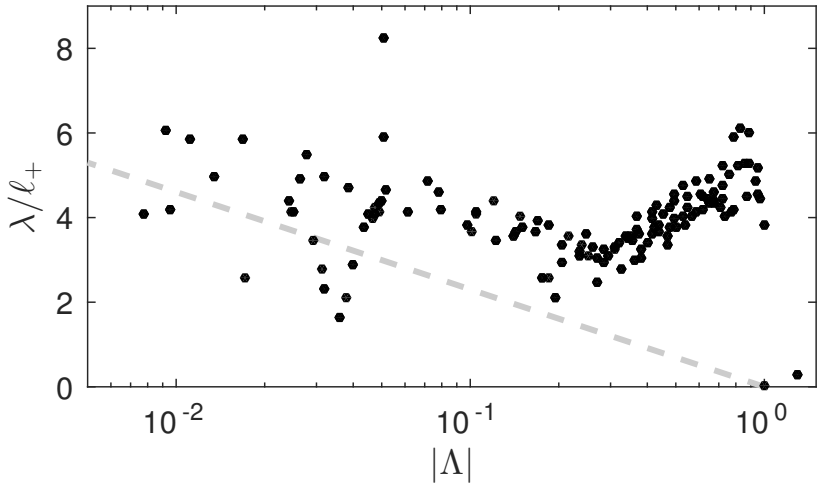

Figure 27: The spatial growth rates of the right eigenfunctions. Convectively unstable modes lie above the dashed line ($\lambda/\ell_+ = -\mathrm{Re}(\sigma)T$) and to the left of $|\Lambda| = 1$.

distance from the core so quickly that they are convectively unstable. As Fig. 27 illustrates, it is only a subset of the strongly contracting modes ($|\Lambda| < O(10^{-1})$) associated with relatively featureless eigenfunctions (i.e., for which $\ell_+ = O(\lambda)$) which are both convectively and absolutely stable. Convective instabilities and exponential growth of eigenfunctions for defect-modulated waves in reaction-diffusion systems have been investigated previously in one [152] and two [149, 169] spatial dimensions, and their role is reasonably well-understood.

As Fig. 22 shows, the continuous spectrum crosses the unit circle near $\Lambda = e^{\pm 5\pi i/6}$, indicating that on $\mathbb{R}^2$, one would expect to find an infinite number of modes close to the boundary of absolute instability. For the relatively small domain size considered here ($L = 2.46\lambda$), only a single complex pair of modes from the continuous spectrum is absolutely unstable (cf. Fig. 28 (a-d)). However, the continuous spectrum contains a large number of modes that are convectively unstable (two examples are shown in Fig. 28 (e-l)). Figures 28 and 29 show the eigenfunctions of three leading modes from the continuous spectrum and their amplitude.

The leading modes in the continuous spectrum exhibit spatial localization trends

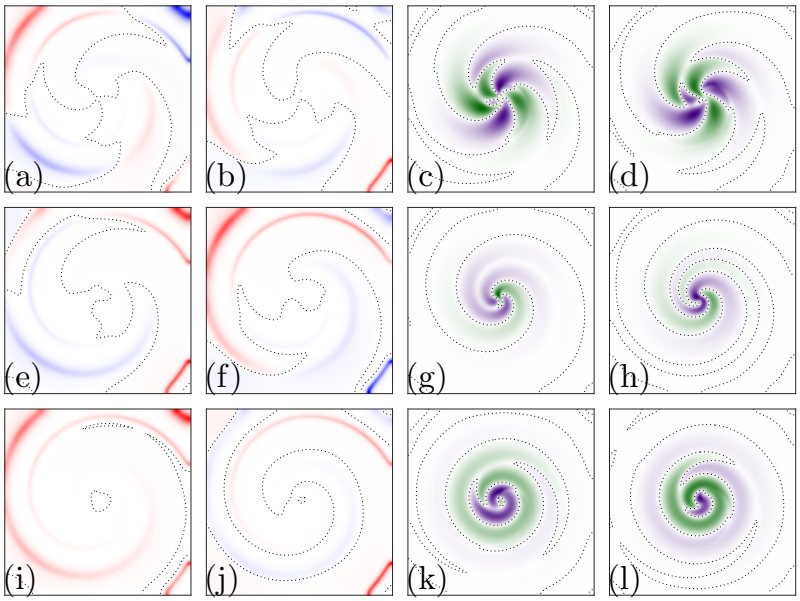

Figure 28: Snapshots of representative complex pairs of right eigenfunctions (a-b), $\Lambda = -0.8838 \pm 0.4753$i; (e-f), $\Lambda = -0.8327 \pm 0.4944$i; (i-j), $\Lambda = -0.8061 \pm 0.4986$i) from the continuous spectrum near the unit circle, and their respective adjoint eigenfunctions (c-d), (g-h), and (k-l).

similar to those from the discrete spectrum. In particular, the left eigenfunctions are localized in the core region, while the right eigenfunctions are localized near the boundaries (cf. Fig. 28). The mode amplitudes, however, are not given by pure exponentials, but rather a product of an exponential and a power, i.e.,

$$A(r) \propto (r/\ell_{\pm})^{\alpha} e^{\pm r/\ell_{\pm}} \tag{48}$$

with $\alpha \approx 2$ and $\ell_{-} \approx 2.5\ell_c$ for the left modes, and $\ell_{+} \approx 16\ell_c$ for the right modes, with $\Lambda_{\pm} = -0.88 \pm 0.48$i, -0.83 ± 0.50i, and -0.81 ± 0.50i. The spatial structure of the right eigenfunctions suggests that these modes are also related to alternans, although the width variation is mixed with bending of the excitation wave (in some regions both the leading and the trailing shock are displaced in the same direction, rather than in the opposite directions, as would be the case for alternans).

To sum up, for the domain size considered here, there are several alternans modes in the Karma model. Classical alternans (cf. Fig. 25(a-b)), the dominant mode of

instability, lacks spatial localization, while there is another unstable alternans mode that is localized near the boundary (cf. Fig. 28 (a-b)). The adjoints of these modes are all strongly localized near the core. In comparison, in the three-variable Fenton-Karma model [69], the alternans modes of an unstable spiral wave computed on a disk of comparable size [2] are characterized by adjoint eigenfunctions that show almost no attenuation with r. Our results show that, unlike the Fenton-Karma model where the development of alternans appears to be sensitive to perturbations over the entire domain, in the Karma model the development of alternans is only sensitive to perturbations near the spiral core.

In the conclusion of this section, we discuss the structure of some of the (absolutely) stable modes from the continuous part of the spectrum. The dominant components of the modes with Floquet multipliers $0.4 < |\Lambda| < 0.6$ are shown in Fig. 30. Similar to the unstable and weakly stable modes, the left eigenfunctions are found to be localized near the core of the spiral and the right eigenfunctions near the domain boundary, although the localization is weaker than for the modes with larger $|\Lambda|$. The amplitudes (cf. Fig. 31) are again found to increase/decrease exponentially (aside from some weak modulation) with r on length scales $\ell_{\pm} = O(6\ell_c)$.

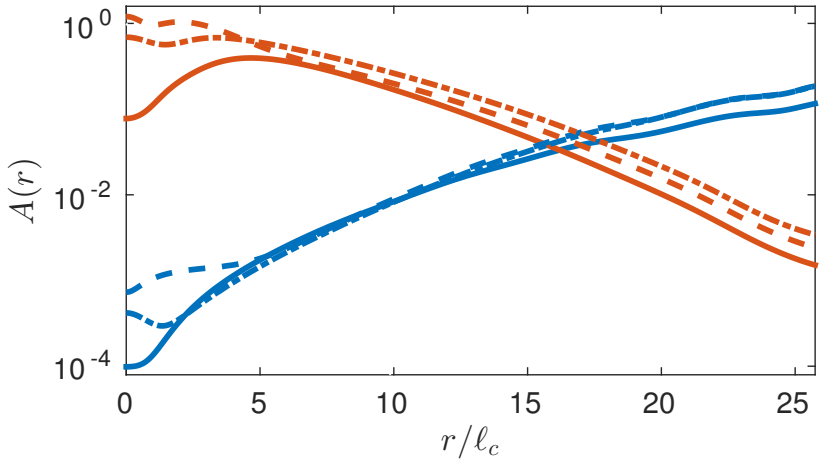

Figure 29: The radial amplitudes of the left (red) and right (blue) eigenfunctions for the modes shown in Figure 28(a-d, solid), (e-h, dashed), (i-l, dotted).

4.2 Asymptotic analysis

Although spatial localization of adjoint eigenfunctions appears to be an almost universal property of spiral wave solutions, it has only been understood for the response functions associated with a spiral wave solution in the CGLE [35, 31]. Extending these results for generic excitable systems has proved difficult due to the strong nonlinearity of the evolution equations. However, we can make progress in certain limits. Although the spiral wave solution investigated here formally corresponds to a relative periodic orbit, it is nearly indistinguishable from a rigidly rotating spiral wave (i.e., relative equilibrium) inside a circle of radius $L/2$. On an infinite domain, far from the origin, the Archimedian approximation applies

$$\mathbf{u}(r,\theta,t) \approx \mathbf{u}_0(\xi), \tag{49}$$

where $\xi = r + l\theta - ct$, $l = \lambda/(2\pi)$, $c = \lambda/T$, and $\mathbf{u}_0(\xi)$ is periodic with period λ. The adjoints can then be written in the form $\tilde{\mathbf{w}}(r,\theta,t) = \bar{\mathbf{w}}(\xi)e^{\mathrm{i}m\theta}e^{\gamma t}$ and the second of the two equations in (46) becomes

$$-\gamma\bar{w}_2^i = D_{22}\left(\partial_\xi^2\bar{w}_2^i + r^{-1}\partial_\xi\bar{w}_2^i - m^2r^{-2}\bar{w}_2^i\right) - c\partial_\xi\bar{w}_2^i + \epsilon\frac{\partial\tilde{f}_1}{\partial u_2}\bar{w}_1^i + \epsilon\frac{\partial\tilde{f}_2}{\partial u_2}\bar{w}_2^i. \tag{50}$$

For $r \gg \lambda$, the curvature of the spiral wave can be ignored, and (50) simplifies, yielding

$$-\gamma\bar{w}_2^i = D_{22}\partial_\xi^2\bar{w}_2^i - c\partial_\xi\bar{w}_2^i + \epsilon\frac{\partial\tilde{f}_1}{\partial u_2}\bar{w}_1^i + \epsilon\frac{\partial\tilde{f}_2}{\partial u_2}\bar{w}_2^i. \tag{51}$$

Since the partial derivatives $\partial\tilde{f}_i/\partial u_j$ depend only on $\mathbf{u}_0$, they are periodic in ξ and, according to the Floquet theorem, equation (51) has solutions in the form $\bar{w}_2^i(\xi) = \hat{w}_2^i(\xi)e^{k_i\xi}$, where $\hat{w}_2^i(\xi+\lambda) = \hat{w}_2^i(\xi)$. We therefore should expect the adjoints to grow or decay exponentially with ξ or r as long as $\mathrm{Re}(k_i) \neq 0$. This result generalizes the prediction of exponential far-field dependence of left eigenfunctions in one spatial dimension [149, 153]. Note that $\gamma = \sigma_i^* + ck_i$, where

$$\sigma_i = \frac{1}{T}\ln\Lambda_i = \frac{1}{T}\ln|\Lambda_i| + \frac{1}{T}\arg(\Lambda_i) \tag{52}$$

is the corresponding Floquet exponent.

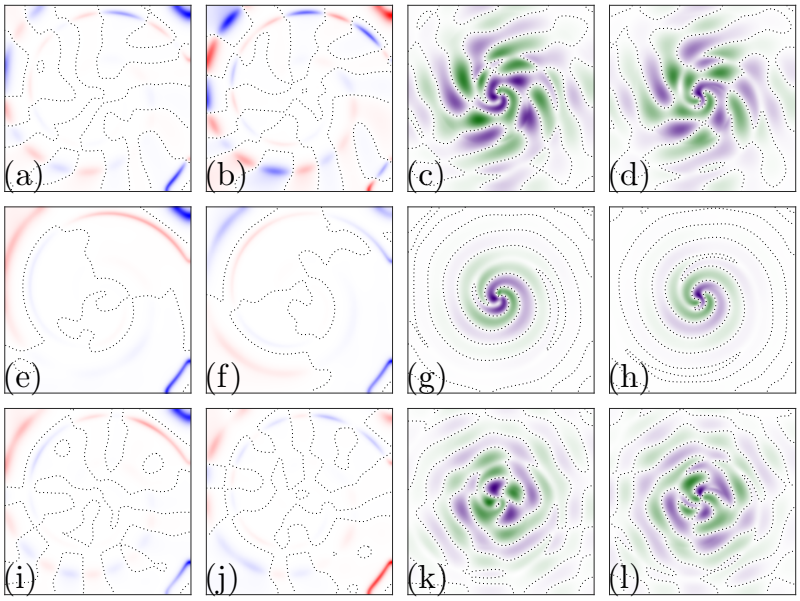

Figure 30: Strongly stable right (a,b,e,f,i,j) and left (c,d,g,h,k,l) eigenfunctions with multipliers $0.4 < |\Lambda| < 0.6$ (ordered by decreasing modulus).

We can make further progress in various special cases. For instance, when $\epsilon \ll |\sigma_i|$ (e.g., for strongly stable modes), we have $\hat{w}_2^i = \text{const}$ and $\sigma_i^* = -D_{22}k_i^2$ with solutions $k_i = |k_i|e^{i\chi_i}$, where

$$|k_i| = \sqrt{\frac{|\sigma_i|}{D_{22}}}, \qquad \chi_i = \frac{\arg(\sigma_i) - \pi}{2} + \pi n_i, \tag{53}$$

and n_i is an integer. Therefore solutions w_2^i can both decay and grow exponentially with r on finite domains. On an infinite domain, however, only solutions that decay exponentially with r are allowed ($\text{Re}(k_i) < 0$), which explains exponential localization of the adjoints with a length scale $\ell_- = \text{Re}(k_i)^{-1} \sim \sqrt{D_{22}/|\sigma_i|}$.

In the limit $D_{22} \to 0$ (which is the typical case considered in models of cardiac tissue), D_{11} becomes the only parameter in equation (35) with the dimension of length. Hence the localization length scale for all slow (unstable, marginal, and weakly stable) modes characterized by the time scale ω^{-1} can be found using dimensional analysis, which yields $\ell_- \sim \sqrt{D_{11}/\omega} = 5.90$. This is fairly close to the numerical value found

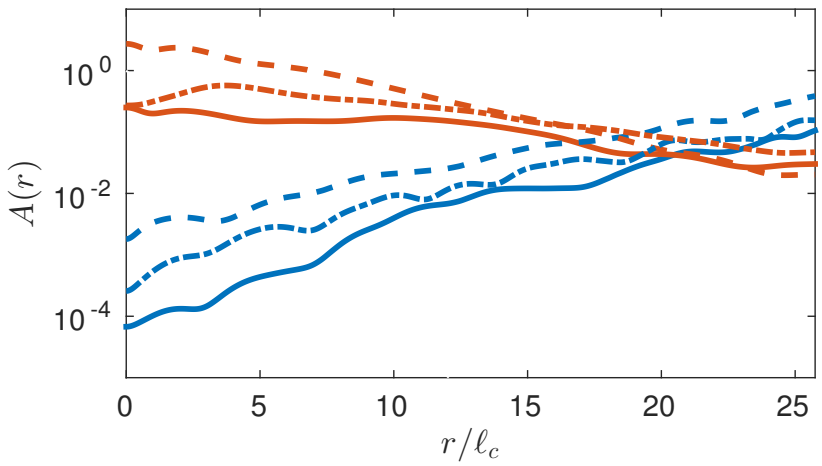

Figure 31: The radial amplitudes for the right (blue) and left (red) eigenfunctions shown in Fig. 30 (a,d) solid, (b,e) dashed, (c,f) dash-dotted.

for the response functions, $\ell_c \approx 3.72$, for $D_{22}/D_{11} = 0.05$. Indeed, this is not entirely unexpected: as Fig. 32 illustrates, the localization length scales for the amplitude of all three marginal adjoint eigenfunctions ($\mathbf{w}^x$, $\mathbf{w}^y$, $\mathbf{w}^t$) depends rather weakly on D_{22}.

For strongly stable modes the relevant time scale can be quite different, although this difference may only become apparent for very quickly decaying modes that are not resolved in the numerics. For instance, for $|\Lambda| = 0.01$ we have $|\sigma_i| \sim -\ln|\Lambda_i|/T = 0.08$ and therefore $\ell_- \sim \sqrt{D_{22}/|\sigma_i|} = 1.6$, which is of the same order of magnitude as the value we found for the marginal modes. The similarity of the length scales predicted for slow modes and the strongly contracting modes explains the relatively small variation in the localization between adjoint eigenfunctions throughout most of the spectrum.

It is also instructive to compare the structure of the response functions adjoint to the Goldstone modes associated with spatial translations with the structure of the shift map that defines how interaction with a no-flux boundary affects the drift of relative periodic solutions. We have shown previously Ch. 3 that the distance ζ_n between the spiral core and the (planar) boundary after n periods of the revolution

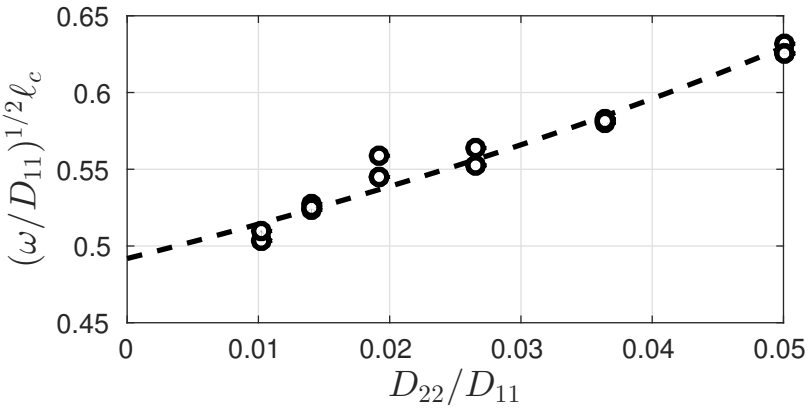

Figure 32: Dependence of the localization length scales ℓ_c for each response function on D_{22}. The dashed line corresponds to a linear fit of ℓ_c and a quadratic fit of ω with D_{22}.

can be described by a map

$$\zeta^{n+1} = \zeta^n + h_n(\zeta^n). \tag{54}$$

The roots $0 < \zeta_0 < \zeta_1 < \cdots$ of the shift function $h_n(\zeta)$ define the equilibrium separation values. When the distance between the origin $\mathbf{x}_o$ of the spiral and the closest boundary is equal to one of these equilibrium values, the spiral wave will drift tangentially to the boundary. An equilibrium ζ_k is stable provided $|1 + h_n'(\zeta_k)| < 1$ and unstable otherwise. Since $|h_n'(\zeta)| \ll 1$, this inequality is equivalent to $h_n'(\zeta_k) < 0$. In particular, $\zeta_0 = 5.36\ell_c$ is a stable fixed point, while $\zeta_1 = 7.85\ell_c$ is unstable. The existence of stable equilibria suggests the presence of bound states, where a spiral would drift along a planar no-flux boundary forever. Similar bound states were found for resonantly driven spirals next to effective boundaries [115, 116].

The drift of spiral waves caused by interaction with the boundaries can be understood by considering the relation between solutions of (13) on bounded domain and on $\mathbb{R}^2$. Consider the flux $\mathbf{j} = \sigma\nabla\mathbf{u}$, where the diffusion tensor $\sigma = D$ inside a bounded domain Ω and $\sigma = 0$ outside. In this case, the no-flux boundary condition

(15) is equivalent to the inclusion of an additional term,

$$\delta\mathbf{F}(\mathbf{u}) = \nabla\sigma(\mathbf{x}) \cdot \nabla\mathbf{u} = -D\delta_{\partial\Omega}(\mathbf{x})(\mathbf{n} \cdot \nabla)\mathbf{u}, \tag{55}$$

on the right-hand-side of (13) defined on $\mathbb{R}^2$. Here $\delta_{\partial\Omega}$ denotes a one-dimensional delta function localized at $\partial\Omega$, such that in a small neighborhood of every point $\mathbf{x}_b \in \partial\Omega$,

$$\delta_{\partial\Omega}(\mathbf{x}) = \delta(\mathbf{n} \cdot (\mathbf{x} - \mathbf{x}_b)). \tag{56}$$

In the absence of this additional term, (13) possesses a spiral wave solution rigidly rotating around the tip $\mathbf{x}_o$, which corresponds to the relative equilibrium on $\mathbb{R}^2$. The introduction of this term generates a perturbation to the dynamics of *all* the modes of this solution. In particular, the perturbation along the Goldstone modes $\mathbf{v}^x$, $\mathbf{v}^y$, and $\mathbf{v}^t$ will generate, respectively, the drift of the spiral core in the $\hat{x}$ and $\hat{y}$ directions and a phase shift (rotation). It will be convenient for us to define $\mathbf{v}^q(t, \mathbf{x})$ satisfying (34) such that

$$\mathbf{v}^q(0, \mathbf{x}) = \mathbf{v}^q(T, \mathbf{x}) = \partial_q\mathbf{u}(0, \mathbf{x}), \tag{57}$$

where $q = \{x, y, t\}$ and

$$\mathbf{w}^q(t, \mathbf{x}) = \sum_{\Lambda_j=1} \alpha_{qj}\mathbf{w}^j(t, \mathbf{x}), \tag{58}$$

where the coefficients α_{qj} are chosen such that the orthogonality condition $\langle\mathbf{w}^p|\mathbf{v}^q\rangle = \delta_{pq}$ is satisfied at $t = T$. Thus defined, $\mathbf{w}^q(t, \mathbf{x})$ will satisfy (35) and be orthogonal with respect to $\mathbf{v}^q(t, \mathbf{x})$ at all t. The spatial drift is then given by [33],

$$\dot{\mathbf{x}}_o(t) = \sum_{q=x,y} \hat{q}\,\langle\mathbf{w}^q(t)|\delta\mathbf{F}(\mathbf{u}(t))\rangle. \tag{59}$$

It should be stressed that this relation is only exact for infinitesimal perturbations, while (55) is not infinitesimal. Nonetheless, (59) provides a fairly accurate description of the drift, as we will see below.

We can make further progress assuming the boundary $\partial\Omega$ is a smooth curve. With the help of (55) the components of (59) can be rewritten as

$$\dot{q}_o(t) = -\int_{\partial\Omega} \mathrm{d}l[\mathbf{w}^q(t,\mathbf{x})]^\dagger D(\mathbf{n}\cdot\nabla)\mathbf{u}(t,\mathbf{x}), \tag{60}$$

where $\mathrm{d}l$ is the arclength element along the boundary. Placing the origin of the coordinate system at the tip of the spiral wave, we can write $\mathbf{w}^q(t,\mathbf{x}) = \hat{\mathbf{w}}^q(t,\mathbf{x})e^{-r/\ell_c}$, where $r = \sqrt{x^2+y^2}$ and $\hat{\mathbf{w}}^q(t,\mathbf{x}) = O(1)$. Since $(\mathbf{n}\cdot\nabla)\mathbf{u}(t,\mathbf{x}) = O(1)$ as well, the integral is dominated by the region of the contour around the point $\mathbf{x}_b$ closest point to origin. Let us orient the coordinate axes such that $\mathbf{x}_b = (\zeta, 0)$ and $\mathbf{n} = \hat{x}$. Since on the contour of integration

$$e^{-r/\ell_c} \approx e^{-\zeta/\ell_c}e^{-y^2/(2\zeta\ell_c)}, \tag{61}$$

the integral can be evaluated using the saddle point method yielding

$$\dot{q}_o(t) \approx -\sqrt{2\pi\zeta\ell_c}e^{-\zeta/\ell_c}[\hat{\mathbf{w}}^q(t,\mathbf{x}_b)]^\dagger D\partial_x\mathbf{u}(t,\mathbf{x}_b). \tag{62}$$

Higher order corrections can be easily generated and scale as $(\zeta\ell_c/\lambda^2)^m$ relative to (62) with integer $m \geq 1$, where $\lambda^2 \gg \zeta\ell_c$, for this spiral wave solution. Outside of the core, the Archimedian approximation (49) can be used to evaluate the spatial derivative in (62):

$$\partial_x\mathbf{u}(t,\mathbf{x}_b) = \mathbf{u}_0'(\xi_b), \tag{63}$$

where $\xi_b = \zeta - ct$, if we choose $\theta = 0$ on the x axis.

The displacement $\mathbf{h} = [h_x, h_y]$ can be found by integrating (62), where $\mathbf{x}_b$ will be a function of $\mathbf{x}_o$. For a boundary with low curvature ($\kappa \ll \zeta^{-1}$), we only need to keep track of the change in the distance ζ which satisfies

$$\dot{\zeta} = -\dot{x}_o. \tag{64}$$

In particular, when $\zeta \gg \ell_c$ we can neglect the change in ζ, so that the normal component of the shift $h_n = \mathbf{n}\cdot\mathbf{h} = h_x$ is given by

$$h_n(\zeta) \approx -\sqrt{2\pi\zeta\ell_c}e^{-\zeta/\ell_c}\int_0^T \mathrm{d}t\,[\hat{\mathbf{w}}^x(t,\mathbf{x}_b)]^\dagger D\mathbf{u}_0'(\xi_b). \tag{65}$$

The dependence of the drift function on the parameters ϵ, D_{11}, and D_{22} can be made more explicit by factoring out the dependence of the components of the solution and the response function on the small parameter ϵ: $\hat{\mathbf{w}}^x = (\epsilon\tilde{\mathbf{w}}_1^x, \tilde{\mathbf{w}}_2^x)$ and $\mathbf{u}_0' = (\tilde{\mathbf{u}}_{0,1}', \epsilon\tilde{\mathbf{u}}_{0,2}')$. Then (65) can be rewritten as

$$h_n(\zeta) \approx \ell_d \bar{h}_n(\zeta) e^{-\zeta/\ell_c}, \tag{66}$$

where

$$\bar{h}_n(\zeta) \equiv -\frac{c\ell_r}{\mathrm{tr}D}\sqrt{\frac{\zeta}{\ell_c}}\int_0^T \mathrm{d}t\,[\tilde{\mathbf{w}}^x(t,\mathbf{x}_b)]^\dagger D\tilde{\mathbf{u}}_0'(\zeta - ct) \tag{67}$$

is a non-dimensional function,

$$\ell_d \equiv \sqrt{2\pi}\frac{\epsilon\ell_c}{\ell_r}\frac{\mathrm{tr}D}{c}, \tag{68}$$

and ℓ_r are characteristic length scales that represents the dependence of the amplitude of the response function $\mathbf{w}^x$ on parameters.

Rather predictably, we find that the dominant contribution to the drift is determined by the component of the state which has the largest diffusion constant. In the Karma model considered here $D_{11} \gg D_{22}$, and so it is the first component (which corresponds to the voltage variable) that controls the drift. For the inner product generally, where the contributions from the first and second components are unweighted, it is the contribution of the second component which dominates. Hence the normalization condition for $\mathbf{w}^x$ dictates that $\tilde{w}^x \propto \ell_f/\ell_c^2$, where ℓ_f is the length scale on which the second component of $\mathbf{u}_0$ varies. Using the Karma model (13) it is straightforward to show that $\ell_f = \lambda/(2\epsilon)$ (cf. the spatial Goldstone modes in Fig. 23(d-e) and the second component of the solution shown in Fig. 22(a)). Therefore, we can define $\ell_r = \ell_c^2/\ell_f = 2\epsilon\ell_c^2/\lambda$ and

$$\ell_d \equiv \sqrt{\frac{\pi}{2}}\frac{\lambda}{\ell_c}\frac{\mathrm{tr}D}{c}. \tag{69}$$

This length scale is quite different from a naïve guess $\ell_d \sim \ell_c$ based solely on the scaling of the response functions.

Table 3: Fitting parameters for Eq. (70).

	A	$\Delta\zeta/\Delta r$	ℓ_c
Direct numerical simulation	-0.430	0.873	3.72
Integrated drift equation	-0.580	0.905	3.80
Saddle point approximation	-0.724	0.922	3.80

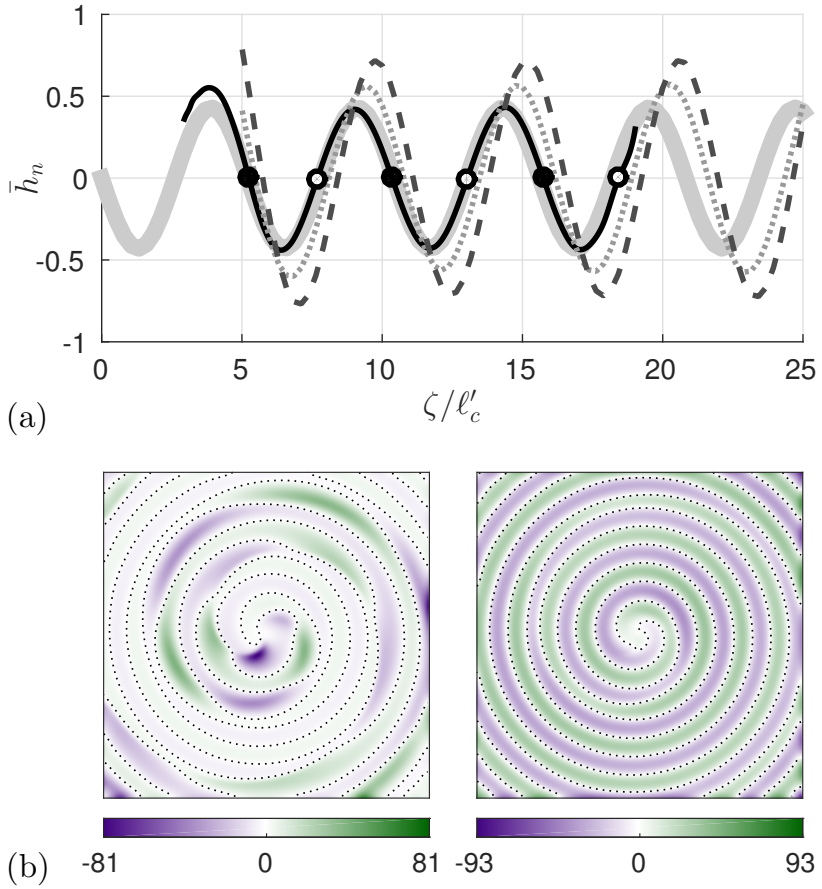

Figure 33: (a) The scaled shift function $\bar{h}_n = (h_n/\ell_d)e^{\zeta/\ell_c'}$ obtained by direct numerical simulation (black line) and its fit $A\sin(\pi\zeta/\Delta\zeta)$ (gray). The roots ζ_k are denoted by circles (filled stable, open unstable). The dotted and dashed lines corresponds to the integral of (59) over one temporal period and its saddle point approximation (65), respectively. (b) Snapshots of the first and second component of the scaled response function $\tilde{\mathbf{w}}^x(t,\mathbf{x})$ at time $t = T/2$ with nodal lines denoted by dotted curves.

As Fig. 33(b) shows, both components of $\tilde{\mathbf{w}}^x$ exhibit pronounced oscillatory dependence on the distance r from the origin. The scaled shift function $\bar{h}_n(\zeta)$ inherits this oscillatory dependence: the expression (67) is shown as the dashed line in Fig. 33(a). The amplitude of the oscillation is nearly constant for $\zeta/\ell_c \gg 1$, and to a high accuracy we can fit $\bar{h}_n(\zeta) = A\sin(\pi\zeta/\Delta\zeta)$ with constant A and $\Delta\zeta$. The corresponding scaling for the shift function

$$h_n(\zeta) = \ell_d A \sin(\pi\zeta/\Delta\zeta)e^{-\zeta/\ell_c}. \tag{70}$$

yields a prediction which is in good agreement with both our previous numerical results Ch. 3 and with the drift equation (60) integrated over one temporal period (cf. Fig. 33(a)). The fitting parameters for all three cases are given in Table 3. In particular, we find that the values of A are $O(1)$, which supports our choice of the length scale ℓ_r. The values of ℓ_c found by fitting the shifts correspond reasonably closely to the localization length scale of the response function. Moreover, the spacing $\Delta\zeta$ between the roots of the shift function corresponds well to the distance Δr between the nodal lines of the response function. This confirms our conjecture Ch. 3 that the interaction of spiral waves with a physical no-flux boundary is controlled by the response functions, just as in the case of resonantly driven spirals interacting with effective boundaries formed by a step-wise change in the excitability of the medium [115, 116].

The saddle point approximation noticeably overestimates the magnitude of the shift due to interaction of the spiral wave with the boundary, while integrating (60) directly produces an estimate that is in reasonable quantitative agreement with the result of direct numerical simulations. While the saddle point approximation can be easily improved at larger ζ/ℓ_c by retaining higher order terms in ζ, its main value is in uncovering the explicit dependence of the drift on various parameters of the problem. In practice, it is only the first root of the drift map, ζ_0, which is likely to play any role in the dynamics of spiral waves. The rest of the equilibria are essentially marginally

stable, and the shift becomes exponentially small. The saddle point approximation produces a reasonably good prediction for the value of ζ_0. Even the prediction of the spacing $\Delta\zeta$ between the equilibria is in fairly good agreement: the error is only about $0.05\zeta_0$.

Qualitatively similar results were obtained for spiral interaction in CGLE using the amplitude equation formalism [6] and for spiral interaction with domain boundaries and defects in excitable systems using the kinematic theory [5]. In the latter case, however, the interaction strength was predicted to decay super-exponentially fast (i.e., as $\exp(-\zeta^3)$), a scaling our results do not support.

4.3 Summary and discussion

On domains of arbitrary shape, pinned and drifting spiral wave solutions of excitable systems are described, respectively, by temporally periodic and generalized relative periodic solutions. We have developed a general numerical procedure that allows computation of the leading adjoint eigenfunctions for unstable spiral wave solutions of such types. In particular, we computed hundreds of the dominant adjoint eigenfunctions for (slowly) drifting single-spiral wave solutions of the Karma model.

Just like for spiral wave solutions described by relative equilibria on circular domains, we found that the response functions, or adjoint eigenfunctions that correspond to marginal degrees of freedom, are exponentially localized in the vicinity of the spiral tip. The localization length scale of the response functions found numerically is in good agreement with the order-of-magnitude estimate $\ell_c \sim \sqrt{D_{11}/\omega}$ based on dimensional analysis, where D_{11} is the diffusion constant associated with the *fast* variable and ω is the angular frequency of the underlying spiral wave solution.

Adjoint eigenfunctions associated with other leading modes, both stable and unstable ones, were also found to be exponentially localized in the vicinity of the spiral tip, with the corresponding localization length scale ℓ_- larger than ℓ_c. For strongly

stable modes it can be shown more rigorously that $\ell_- \sim \sqrt{D_{22}/|\sigma|}$, where D_{22} is the diffusion constant associated with the *slow* variable and σ is the corresponding Floquet exponent.

The significance of response functions for the dynamics of isolated spiral waves on $\mathbb{R}^2$ is well understood [36, 30, 31]. The spatial and temporal response functions determine the effect of small perturbations in the initial conditions or the evolution equations on, respectively, the drift of the spiral and its rotation speed [33, 34]. In particular, the response functions have been used to describe the interaction of spiral waves with tissue heterogeneties [24, 25, 38]. Our results further show that the spatial response functions also determine the interaction of spiral waves with physical no-flux boundaries and, by extension, the interaction with neighboring spirals through tile boundaries with effective no-flux boundary conditions, cf. Ch 3 and 5. Specifically, the spatial response functions $\mathbf{w}^x$ and $\mathbf{w}^y$ define the shift function $\mathbf{h}(\zeta)$ which describes the displacement of the spiral wave origin due to the interaction with the boundary over one temporal period.

The rest of the adjoint eigenfunctions have received very little attention in the literature dealing with excitable systems in general and the dynamics of cardiac tissue in particular. The spatiotemporal structure of unstable and weakly stable adjoints, however, is critically important for understanding spiral wave breakup and chaotic dynamics featuring multiple interacting unstable spiral waves. For instance, it is well known that stable spirals whose cores are sufficiently well separated can be considered effectively independent. The same is also true of unstable spirals Ch. 3. The spirals begin to interact at smaller separations, with interaction that can be conveniently described with the help of the adjoint eigenfunctions. Our results show that not only the position of the core and the phase of a spiral wave, but also its stability should be affected by neighboring spirals.

Furthermore, adjoints associated with slow modes play a crucial role in the design

of feedback control methods aimed at suppressing spiral wave instabilities (such as alternans) [2]. The spatial localization of the adjoints associated with unstable modes indicates that feedback is most effective when it is applied close to the core of a spiral wave. Furthermore, the spatial alternation of the phase of the adjoints associated with all slow modes (unstable, marginal, and weakly stable) in the core region significantly attenuates the effectiveness of spatially uniform perturbations [1, 28, 115] on the dynamics of spiral waves. This suggests that spatially localized perturbation, e.g., those due to virtual electrodes [64, 73] should be much more effective for control of spatiotemporally chaotic regimes, such as fibrillation.

CHAPTER V

TILING

We have previously described the symmetry of the evolution equations (13) with respect to the Euclidean group in space, and temporal translations. We have also introduced and defined the (relative) equilibria which correspond to some of these symmetries, i.e. uniform states (19), traveling waves (26), and rotating waves (42). In addition, we have shown examples of the complicated states the fully time-dependent dynamics can yield in two spatial dimensions.

Stable and unstable uniform states, plane and spiral excitation waves discussed previously illustrate some of the types of solutions (equilibria, periodic orbits, relative equilibria, and relative periodic orbits) to be found in models of cardiac tissue excitation. However, none of the solutions shown represent arrhythmic dynamics typical of fibrillation , i.e., they do not correspond to global exact coherent structures (ECS) – unstable non-chaotic solutions embedded within the chaotic set, in this case, fibrillation. For instance, while locally the excitation waves almost always take the shape of small spirals during fibrillation, they never organize – even transiently – into a single large spiral wave. This difficulty illustrates the central problem with the use of *global* exact coherent structures to describe sustained spiral chaos. In fluid turbulence, spatial correlations are relatively strong and the features of a turbulent flow are oftentimes representative of global ECS [170, 57]. In sustained spiral chaos, this approach was found to be an insufficient description of the dynamical configurations of spirals seen in numerical simulations.

In order to find global unstable non-chaotic solutions embedded in the chaotic set, we used the method of close returns [11] which has been used successfully in the

context of fluid turbulence [57]. The procedure involves finding near-recurrences in the *chaotic* solutions, which become initial conditions that are subsequently refined into exact *non-chaotic* solutions using a Newton-Krylov solver, A.4. In the presence of global symmetry, initial guesses for relative equilibria, periodic orbits, as well as relative periodic orbits can be found as the minima of the recurrence function

$$E(t,\tau) \equiv \min_{\mathcal{G}_a \in G, \tau > 0} \left(\frac{\int \mathrm{d}^2\mathbf{x}\, |\mathbf{F}(\mathbf{u}(t,\mathbf{x}), a, \tau)|^2}{\int \mathrm{d}^2\mathbf{x}\, |\mathbf{u}(t,\mathbf{x})|^2} \right)^{1/2}, \tag{71}$$

where $\mathbf{F}(\mathbf{u}, a, \tau)$ denotes the relative periodic condition (43), the group G describes the action of symmetry transformations $\mathcal{G}_a$ in the presence of boundaries, and τ represents a delay or recurrence time. However, we found that the minima of (71) are always achieved for $\mathcal{G}_a \approx \mathbf{1}$, even for periodic boundary conditions, and in practice we can set $G = \{\mathbf{1}\}$.

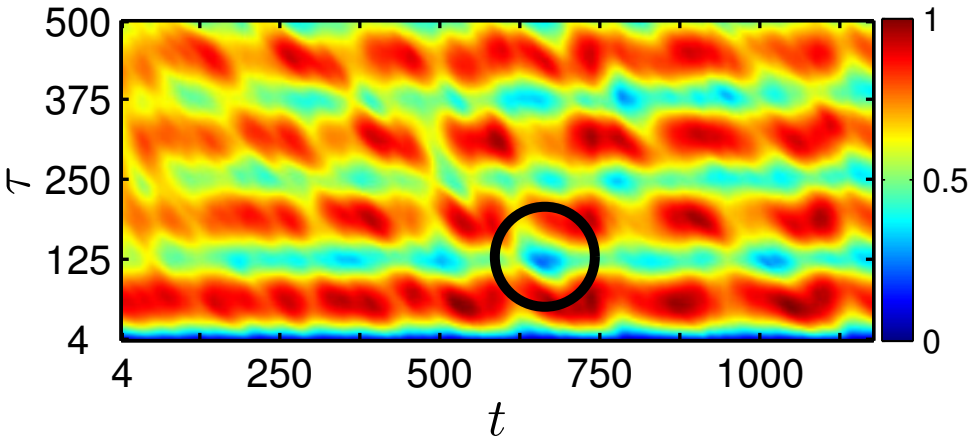

Figure 34: A fragment of the normalized recurrence function $E(t,\tau)$, where t and τ are in units of ms. The black circle identifies a minimum associated with a close return of a chaotic solution. Minima such as this one are used to identify initial conditions for refinement into ECS using the Newton-Krylov solver.

It should be noted that setting $G = \{\mathbf{1}\}$ in (71) does not constrain the exact solutions to absolute equilibria and absolute periodic orbits. For instance, a slowly drifting or rotating solution described by a relative periodic orbit or relative equilibrium, such that $\mathcal{G}_a\mathbf{u}(t,\mathbf{x}) = \mathbf{u}(t-T,\mathbf{x})$ with $\mathcal{G}_a \approx \mathbf{1}$, will generate a minimum of (71)

with $\tau \approx T$ when $G = \{\mathbf{1}\}$. Solutions that are characterized by fast global rotation or translation (e.g. spiral or plane waves), and for which $\mathcal{G}_a$ is significantly different from $\mathbf{1}$, are characterized by a high degree of spatial coherence. The lack of global spatial coherence is a distinguishing feature of fibrillation, and therefore we should not expect to find any solutions that exhibit fast global rotation or drift.

A fragment of the recurrence plot for a chaotic solution computed on a square domain Ω with side $L = 192$ (50.3 mm) and periodic boundary conditions is shown in Fig. 34. For this domain size, periodic boundary conditions lead to chaotic dynamics that are qualitatively identical to those in the presence of no-flux boundary conditions even on relatively long time scales. However, for periodic boundary conditions fibrillation persists indefinitely (at least, it does not disappear after 4.5 minutes $\approx 2000T$), while for no-flux boundary conditions it can terminate spontaneously due to the spiral cores colliding with the boundaries and disappearing. Once a sufficiently low minimum (circled) of the recurrence function $E(t, \tau)$ is identified, the corresponding state $\mathbf{u}(t - \tau, \mathbf{x})$ is used as the initial guess for a solution with period close to τ.

Rather surprisingly, none of the initial guesses we tried converged to either relative equilibria, periodic orbits, or to relative periodic orbits. We did not search for equilibria, since $\|\partial_t \mathbf{u}\|$ never becomes small for chaotic solutions. Figs. 35(a) and 35(b) show the voltage component u for two typical examples of the numerous multi-spiral states identified using the recurrence analysis. They nearly recur after $\tau = 251.94$ ms and $\tau = 251.83$ ms, respectively. These values of τ correspond to approximately double the temporal period of a single spiral shown in Fig. 9(a), $2T = 251.96$ ms. Newton iterations stagnate at the values of relative residual $\|\mathbf{u}(\tau) - \mathbf{u}(0)\|_2 / \|\mathbf{u}(0)\|_2$ equal to 9×10^{-3} for the state shown in Fig. 35(a) and 10^{-2} for the state shown in Fig. 35(b), compared to $O(10^{-13})$ for the converged single-spiral state shown in Fig. 9(a). The voltage components $u_1(t) - u_1(t - \tau)$ of the corresponding residual are

shown in Figs. 35(c-d). They are spatially localized in the regions where $|\nabla u_1(t)|$ has the largest magnitude (cf. Figs. 35(e-f)), or near the front and back of the excitation wave. In order to interpret these findings, next we consider multi-spiral solutions that are constructed artificially and do not lie on the chaotic set on which fibrillation takes place.

The results of Ch. 3 and 4 imply that invariant multi-spiral solutions exist for sufficiently large values of s and sufficiently large domains. When local continuous symmetry is broken by the presence of unresolved length or time scales within the solution, the discreteness of the underlying mesh can effectively pin each spiral wave. We expect that this feature similarly manifests in tissues for which the cellular scale is comparable to the width of the wavefront. Then, for sufficiently well-separated waves, this pinning can suppress the exponentially weak interactions between the spirals. Using this as a guideline, we can construct two-spiral, asymmetric periodic orbits satisfying (43) with $\mathbf{h} = \mathbf{0}$, identically, to a precision only limited by the accuracy of the time-stepping. Fig. 36 shows several examples of this type of solution, for different offsets $\delta\theta$ in the phase of the spirals and distinct chirality. This is a manifestation of a peculiar effect of weakly-broken local symmetry: exact solutions which are explicitly forbidden for the model with continuous symmetries are now trivially constructed.

5.1 Area computation

We now introduce a method of domain decomposition – *tiling* – which qualitatively isolates spiral waves in a complicated multi-spiral trajectory into irregular subdomains. The concept of domain tiling was introduced by Bohr *et al.* [40, 41] to describe frozen spiral waves, sometimes referred to as vortex glasses, in the complex Ginzburg-Landau equation (CGLE)

$$\partial_t A = A + (1 + i\alpha)\nabla^2 A - (1 + i\beta)|A|^2 A, \tag{72}$$

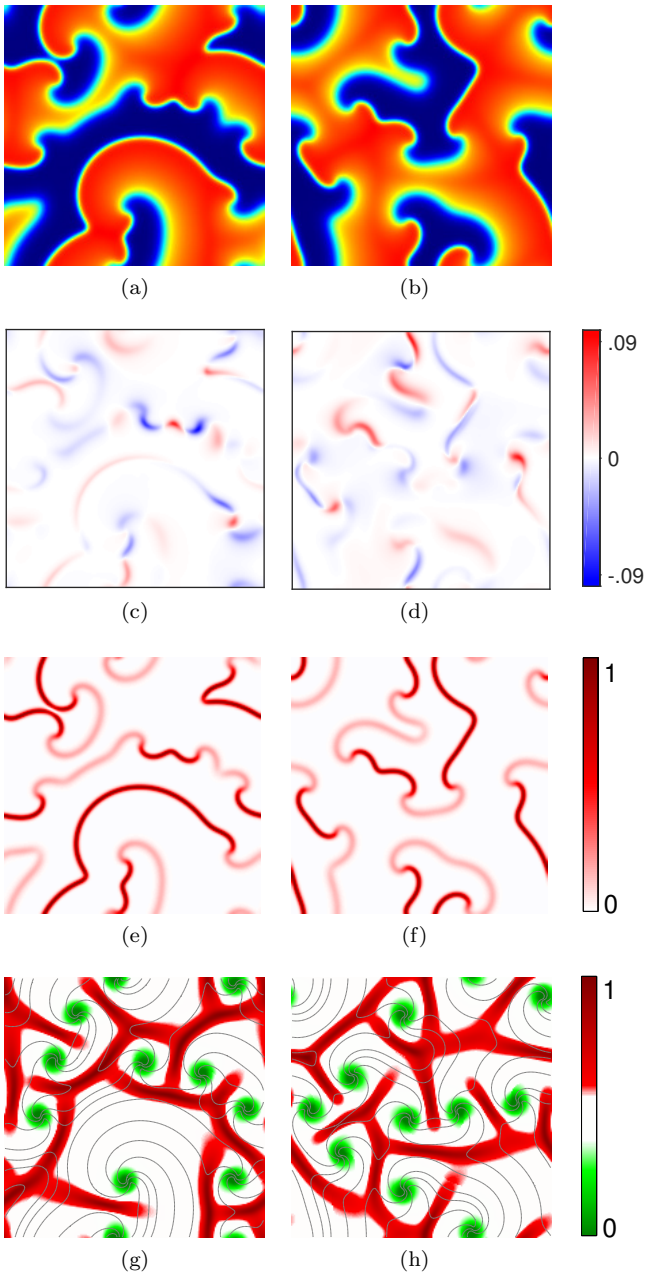

Figure 35: (a-b) Snapshots of the voltage $u_1(t)$ for two initial guesses which correspond to minima of $E(t, \tau)$. (c-d) The relative residual $[u_1(t) - u_1(t - \tau)]/\|u_1(t)\|_\infty$. (e-f) The normalized magnitude of the voltage gradient $|\nabla u_1(t)|$. (g-h) The cycle area I_1 (defined in Section 5.1). Level sets of u_2 are shown as thin gray curves, the shocks correspond to the red, and the cores to the green. The domain is a square of side $L = 50.3$ mm with periodic boundary conditions.

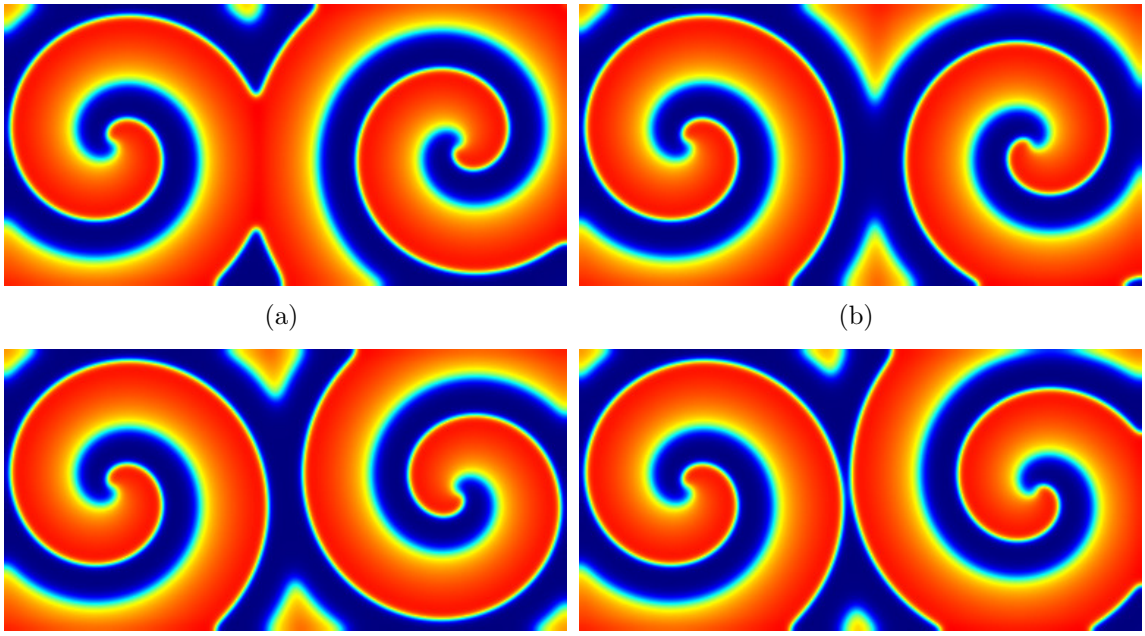

Figure 36: Snapshots of the voltage $u_1(0, \mathbf{x})$ for co- (a-b) and counter-rotating (c-d) two-spiral solutions on a rectangular domain with phase-offsets.

where A is a complex field and α and β are control parameters. Each tile contains exactly one spiral core and the dynamics on each tile is controlled almost entirely by that core. The boundaries of individual tiles were identified with the ridges (or shocks) of the field $|A|$ which describes the local amplitude of oscillation ρ, cf. (73). Fig. 37(a) shows the real part of a representative solution $A = \rho e^{i\phi}$ which can be used to identify individual spirals. In most of the domain the phase ϕ of the oscillation varies slowly in space, so according to the amplitude equation [4]

$$\partial_t \rho = [\nabla^2 - (\nabla\phi)^2]\rho - \alpha(2\nabla\phi \cdot \nabla\rho + \rho\nabla^2\phi) + (1 - \rho^2)\rho, \tag{73}$$

the amplitude of oscillation is essentially constant, $\rho \approx 1$, which corresponds to the middle cycle in the complex-A plane shown in Fig. 37(b). The spiral cores are associated with phase singularities and are characterized by small values of the amplitude ($\rho \ll 1$, small cycle). Similarly, the phase changes quickly at the boundaries of the tiles, where the amplitude increases ($\rho \gtrsim 1$, large cycle). Hence, the maxima and

minima of $|A|$ shown in Fig. 37(c) can be used to identify, respectively, the spatial locations of the tile boundaries and spiral cores.

For excitable media characterized by strongly nonlinear oscillations, a different representation has to be used, since the phase and amplitude of the oscillations can be difficult to define, let alone compute. In this case the local amplitude of oscillation can be characterized instead by the area $I(x, y)$ of the cycle C that is traced out by the solution in an appropriate state space. For CGLE the area in the complex-A plane is given by

$$I(x, y) = \oint_C \frac{\rho^2}{2}\, d\phi = \int_0^T \frac{\rho^2}{2}\dot{\phi}\, dt, \tag{74}$$

with the result shown in Fig. 37(d). For frozen spirals $\dot{\phi} = 2\pi/T$, so that $I(x, y) = \pi|A(x, y, t)|^2$ and the cycle area representation is equivalent to the amplitude representation.

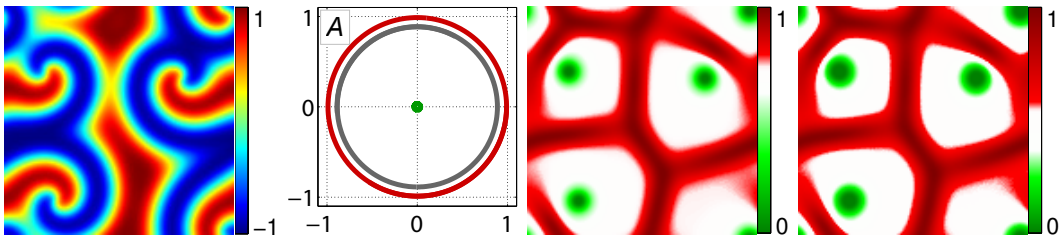

(a) (b) (c) (d)

Figure 37: A spiral wave solution of the complex Ginzburg-Landau equation with $\alpha = 0$ and $\beta = 1.2$. (a) Snapshot of $\mathrm{Re}(A)$. (b) The cycles in the complex plane for three representative spatial locations: spiral core (green), interior of a tile (gray), and a shock separating two tiles (red). The amplitude of the gray cycle is slightly less than unity because the tiles are small (the size is comparable to the wavelength λ). (c) The normalized amplitude $|A|$. (d) The normalized cycle area I.

A similar approach can be used to identify the tile boundaries for the modified Karma model. The easiest way to characterize the amplitude of the strongly nonlinear oscillations is by computing the area I_1 of the cycle C in the $\mathbf{u}$ plane,

$$I_1(x, y) = \left| \oint_C u_2\, \mathrm{d}u_1 \right| = \left| \int_0^T u_2 \dot{u}_1\, \mathrm{d}t \right|. \tag{75}$$

Several representative cycles C computed for the co-rotating two-spiral solution depicted in Fig. 36(a) are shown in Figure 38(a) and the corresponding spatial distribution $I_1(x, y)$ is shown in Figure 38(b). The two spirals are separated by a shock which corresponds to the local maximum of $I_1(x, y)$. In addition, we also find shocks that form along the outer boundary, where no-flux boundary condition is imposed. Taken together, the shocks form a closed boundary for each of the spiral domains, defining the tiles on which the dynamics is controlled by one or the other core.

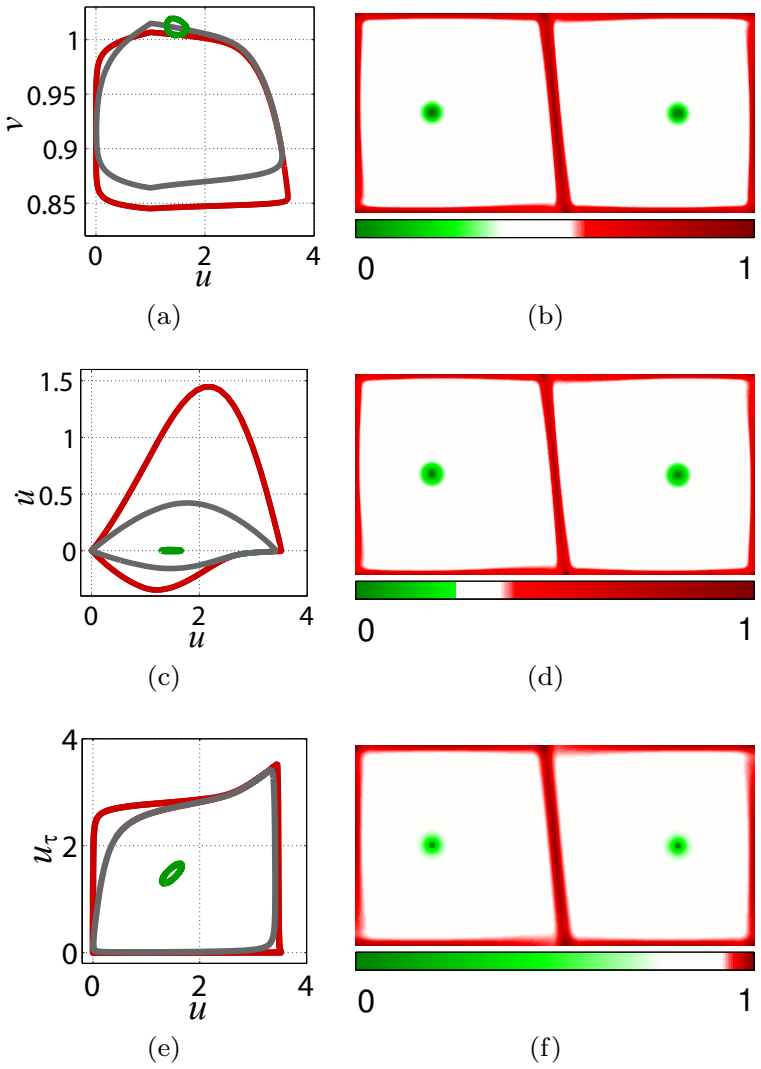

Figure 38: The cycles in the (a) $\mathbf{u}$ plane, (c) $(u_1, \dot{u}_1)$ plane, and (e) $(u_1(t), u_1(t-\tau))$ plane. The corresponding cycle areas I_1 (b), I_2 (d), and I_3 (f) for the two-spiral solution shown in Fig. 36(a). The color correspondence is the same as in Fig. 37.

While computing cycle areas in the **u** plane is convenient in the models where all variables are accessible, in experiment this is rarely the case. Most typically only one variable is easily accessible experimentally (e.g., voltage or calcium, if voltage- or calcium-sensitive dye is used). In this case cycle areas can also be computed using alternative planar representations of the cellular dynamics based solely on one variable, e.g. the voltage u. One possibility is to use a $(u_1, \dot{u}_1)$ plane, with the cycle area defined as

$$I_2(x,y) = \oint_C \dot{u}_1 \, \mathrm{d}u_1 = \int_0^T \dot{u}_1^2 \, \mathrm{d}t. \tag{76}$$

Some representative cycles and the cycle area distribution are shown in Figs. 38(c) and (d), respectively.

The expression for I_2, however, involves a derivative of u_1. Since experimental measurements are typically noisy, derivatives obtained using finite-differencing of a time series can be very inaccurate. To reduce the influence of noise, a time-delay embedding can be used instead, with the cycles defined in the plane spanned by u_1 evaluated at times t and $t - \tau$. The corresponding cycle area

$$I_3(x,y) = \left| \oint_C u_1(t-\tau) \, \mathrm{d}u_1 \right| \tag{77}$$

can be computed without evaluating derivatives of any field. The choice of the time delay τ is not unique. We chose the value $\tau = 13.5$ ms which corresponds to the first minimum of the mutual information function [105]. The corresponding representative cycles in the $[u_1(t), u_1(t-\tau)]$ plane and the cycle area distribution are shown in Figs. 38(e) and (f), respectively. Comparison of Figs. 38(b), (d), and (f) shows that all three cycle area representations are consistent and accurately capture the shock line separating the two spirals, as well as the shock lines along the domain boundaries.

In the rest of this study we use the cycle areas I_1 computed in the **u** plane to identify tiles in the computational domain. In particular, Figs. 35(g) and (h) show the shocks that separate the tiles that form for the nearly-recurrent multi-spiral solutions.

For time-periodic solutions (e.g., single- or two-spiral solutions of the Karma model) the period T is well-defined and the cycles close perfectly. For non-periodic solutions such as those shown in Figs. 35 the integration is instead performed between crossings of a convenient Poincaré section (we used $u_1 = 1.5$).

If the phase of the spiral solution is well-described by the Archimedian approximation, the tile boundaries can also be constructed analytically. Generally, the Archimedian approximation, and hence the analytic solutions for the tile boundaries, is only valid when the distance from each spiral core to the tile boundary is sufficiently large. Bohr *et al.* [40, 41] showed that for CGLE the tile boundaries are segments of hyperbolas with the two nearest spiral cores serving as foci and that the approximation is valid even when the separation between the cores is as small as one wavelength λ. The hyperbolic solution, however, only applies to spirals of opposite chirality (i.e., counter-rotating spiral waves).

A more general equation for the tile boundary between spirals of any chirality was derived by Zhan *et al.* [173]. Let the origins of the two spirals be $\mathbf{x}$ and $\mathbf{x}'$, their chiralities σ, $\sigma' = \pm 1$, $\mathbf{R} = \mathbf{x}' - \mathbf{x}$, and let $\mathbf{x} + \mathbf{r}$ define a point on the boundary. Then the boundary is given by the solution to the differential equation

$$\frac{\mathrm{d}r}{\mathrm{d}\varphi} = \frac{-\sigma r'^2 - \sigma' r(R\cos\varphi - r) + 2\pi m r' r \sin\varphi}{\sigma' R^2 \sin\varphi + m\left(r'^2 - r'(r - R\cos\varphi)\right)}, \tag{78}$$

where $m = R/\lambda$, $r' = \sqrt{R^2 + r^2 - 2rR\cos\varphi}$, and φ is the angle between $\mathbf{r}$ and $\mathbf{R}$. This equation can be solved numerically given an initial condition that lies on the line connecting the origins of the two spirals. Equation (78) was shown to accurately capture the tile boundaries not only for weakly nonlinear oscillations found in CGLE, but also for the Barkley model [18] which, like the Karma model, describes an excitable medium supporting strongly nonlinear oscillations [120].

We checked the validity of this equation for the modified Karma model by comparing the analytic solutions to those computed using the cycle area method for the

co- and counter-rotating phase-shifted solutions from Figs. 36, for which $m = 3.18$. Excellent agreement was found in all cases. Four examples with the analytic solutions superimposed on the cycle area plots are shown in Fig. 39.

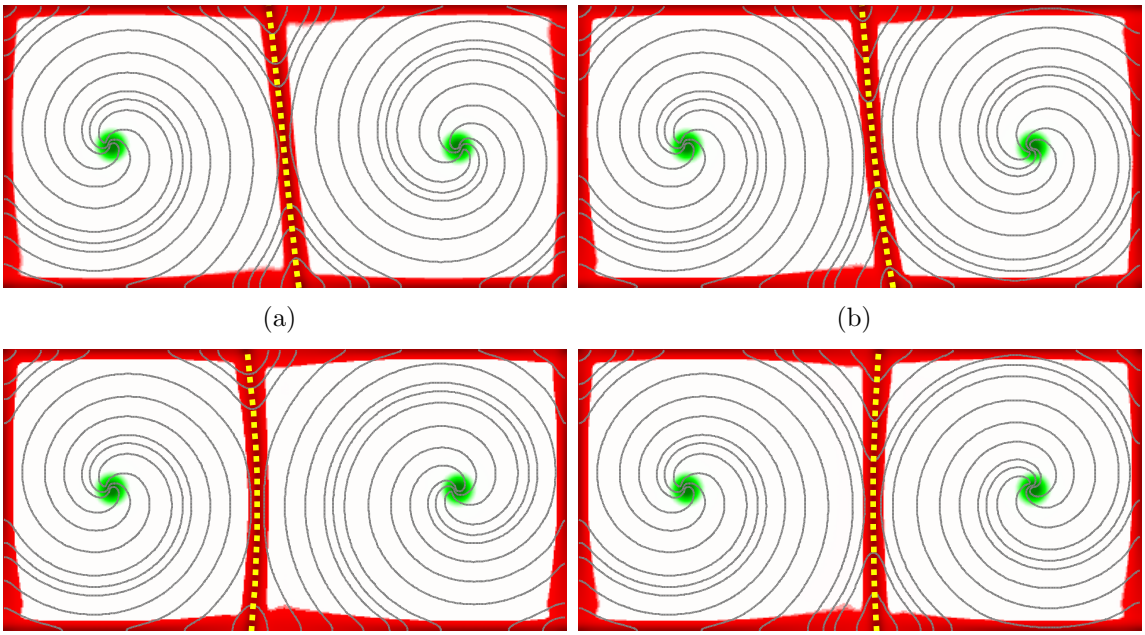

Figure 39: The cycle areas I_1 for the unstable two-spiral states shown in Fig. 36. Also shown are the analytic solutions for the (internal) tile boundaries as dashed yellow curves and level sets of $u_2(0, \mathbf{x})$ as thin gray lines. The color bar from Fig. 38(b) is used in all panels.

It should be noted that both methods of computing the tile boundaries have advantages and drawbacks. Numerical solutions based on cycle areas do not require any assumptions (e.g., the Archimedean approximation for the phase) and can be computed in real time. On the other hand, they are only updated once per period (i.e., upon crossing of the Poincaré section), which may not be adequate for quickly drifting spirals. Furthermore, the shocks often do not entirely enclose each spiral (cf. Fig. 35(g-h)); an additional construction is needed to form a closed boundary or determine the precise position of the boundary based on the transverse profile of the shock. Analytical solutions form closed boundaries, but require identification of

the position of the cores and the initial condition (e.g., the point where the boundary crosses the straight line connecting the two cores). Analytical construction also requires an algorithm for determining the endpoints of each smooth segment of the boundary where three (or more) different tiles meet.

5.1.1 Assembling a global solution

For computational domains with no-flux boundary conditions, shocks form naturally along the boundaries. Additionally, empirical observations for states with tile boundaries evolving slowly compared with the spiral rotation demonstrate that the level sets of both u_2 (cf. Figs. 35(g-h) and 39) and u_1 (not shown) are orthogonal to the shocks. Hence, the single-spiral solution on each of the tiles satisfies the no-flux boundary conditions on its entire boundary, whether it is external or internal with respect to the computational domain. We can therefore reduce the interaction between different spirals to the effect of boundary conditions, which only affects the solution in the interior of the tile through its shape (and the dynamics of the tile boundaries, if any). The effect of the boundaries on the enclosed spiral wave should be qualitatively the same regardless of the tile geometry. In particular, the temporal period of each spiral wave should depend on the size of the tile. For example, the period of unstable single-spiral wave solutions decreases from the asymptotic value T_0 as the domain size L decreases for the Karma model on square domains, cf. Fig. 21. For domains of size comparable to the smallest tiles in Figs. 35(g-h) the period is estimated to decrease by $O(10^{-2}T_0)$. Such differences in the periods of different spirals would lead to a relative residual of $O(10^{-1})$, which is consistent with the residuals reported in Figs. 35(c-d).

It is well known [100, 113] that if the frequencies ω_1 and ω_2 of two neighboring spirals differ, the boundary between them moves with velocity

$$\mathbf{c} = (\omega_1 - \omega_2)\frac{\mathbf{k}_1 - \mathbf{k}_2}{|\mathbf{k}_1 - \mathbf{k}_2|^2}, \tag{79}$$

where $\mathbf{k}_1$ and $\mathbf{k}_2$ are the wave vectors the two spirals would have on an unbounded domain at the location of the tile boundary. This is a consequence of the phase continuity at the tile boundaries: the frequencies of the two spirals become equal in a reference frame moving with velocity $\mathbf{c}$. In particular, small differences in the frequencies (equivalently, periods) of two neighboring spirals lead to a slow motion of the boundary. This is especially relevant for compositions of spiral waves on different size tiles, or even spiral waves positioned differently on equivalent tiles Ch. 3 & Ch. 4. These waves will, generically, have slightly different rotational periods even when the stiffness parameter s is large and their cores are pinned. Thus, we should expect the composition of multiple spiral wave solutions to have moving tile boundaries, except in very specific circumstances where the interaction is perfectly balanced.

Similarly, the results outlined in Ch. 3 and Ch. 4 indicated that the interaction of a spiral core with the boundary is, at closest approach ($x_o < \zeta_0$), repulsive. This appears to be a general result, as repulsive interaction with a no-flux boundary was also found in other excitable systems [115, 116]. Hence, when the distance between a spiral core and the nearest tile boundary decreases beyond ζ_0, the spiral core starts to drift away from the boundary. For pinned solutions, this mechanism will disrupt the relative stasis of the initial positions of the spiral origins, requiring movement of the spiral wave to enforce temporal periodicity. One immediate consequence of this result we have already seen in Fig. 36: there exist periodic multi-spiral solutions on sufficiently large domains which do not persist for smaller values of s, where the cores become unpinned.

The tile-based decomposition suggests a natural approach to constructing global multi-spiral solutions from single-spiral segments satisfying local Euclidean symmetries. The results obtained for single-spiral solutions (cf. Ch. 3) suggest that the solution on each tile would be defined either by a periodic solution or a generalized relative periodic solution. If the tile boundaries do not move significantly during a

typical period T_0, we can compute the solutions locally on each tile using the weighted Newton-Krylov method described in A.4. The algorithm, however, will need to be generalized in such a way that updates of the initial condition at each step of Newton iteration preserve the spatial continuity of the state $\mathbf{u}(t, \mathbf{x})$ (or equivalently the phase and amplitude) on the tile boundaries. This constraint, however, presents only computational – as opposed to conceptual – difficulties.

5.2 Summary and discussion

To summarize, we have applied numerical methods originally developed for fluid turbulence to search for the exact coherent structures that may form a skeleton for the spatiotemporally chaotic dynamics produced by a prototypical monodomain model of cardiac tissue. We showed that these methods, designed to identify recurrent solutions in the presence of global symmetries, fail rather spectacularly for an excitable reaction-diffusion system whose dynamics is characterized by local, rather than global Euclidean symmetries. The origin of the failure was traced to the weak correlation between the dynamics of individual spirals which underpin spiral turbulence, which arises due to the exponential localization of the adjoint eigenfunctions to the spiral core, cf. Ch. 4. As a result of this weak correlation, typical multi-spiral states display recurrent dynamics locally, but not globally. Locally the dynamics can be represented, to numerical accuracy, by periodic or relative periodic solutions, but globally neither periodic nor relative periodic solutions play a dynamically important role. Non-chaotic unstable solutions embedded in the chaotic set would have a more complicated nature and require development of novel computational approaches.

One such approach based on the decomposition of the computational domain into sub-domains, or tiles, that each support one spiral wave. Over short time scales (before individual spiral waves are destroyed by local instabilities) the dynamics for each near-recurrent multi-spiral state can be decomposed into the dynamics *of the tiles*

(relative motion of tiles and changes in their shape associated with the differences in the spiral frequencies) and the dynamics of individual spiral waves *on the tiles* subject to no-flux boundary conditions at the tile boundaries. In particular, the dynamics of spiral waves on the tiles would be described by periodic or relative periodic solutions which correspond, respectively, to pinned and drifting cores. This can be considered in terms of the of the dynamics in the vicinity of relative solutions induced by local symmetries [75, 76, 150, 151], as the flow primarily along the manifold spanned by local symmetry.

It should be emphasized that the formalism based on decomposition into tiles is only expected to describe spiral turbulence during relatively quiescent intervals when and where no breakups or mergers of spiral waves occur. Breakups and mergers are driven, respectively, by the alternans and meandering instabilities of individual spiral waves [108] and involve the birth or annihilation of pairs of spiral cores with opposite chirality and the associated changes in the number of tiles, cf. Ch. 3. During such events, (79) suggests that the boundaries of the tiles and the speed of the spiral cores is comparable, such that the assumptions underlying the construction based on the area computation is not reliable. These relatively active intervals should not be described using the proposed formalism.

The definition of locality is, of course, relative. In the model considered here, local symmetries survive on domains, or tiles, whose dimensions significantly exceed the characteristic correlation length ℓ_c defined by the spatial extent of the adjoint eigenmodes for spiral wave solutions [30, 33]. For excitable systems, such as the FitzHugh-Nagumo, Barkley, and Karma models, these eigenmodes decay exponentially, reflecting the lack of any long-range correlations. Short-range correlations, however, may not describe all cardiac tissue models. For instance, bidomain models [155] also include an additional Poisson equation for the extracellular potential, generating long-range correlations. Similarly, long-range correlations can arise as a result

of stretch-activated feedback [3]. Investigation of the relation between symmetries and the structure of exact coherent structures in bidomain models is of particular interest both because they provide a more realistic description of cardiac tissue, compared with the monodomain models, and because of the analogy with fluid dynamics where long-range coupling is due to the pressure field, which also satisfies a Poisson equation.

There are direct implications of our results so far for the problem of fibrillation. Unstable spiral wave solutions can only be found for sufficiently large domains, $L \geq L_0$, with the smallest domain size corresponding to the strongly-interacting regime $L_0 \approx 4\ell_c$ in the present model, cf. Ch. 3 and Ch. 4. On domains smaller than this size, spiral waves do not persist for a complete rotation. Small spirals cannot simply disappear due to topological charge conservation [58, 175], thus meander and core-pair (or core-boundary on no-flux domains) annihilation is the only reduction available. This length scale L_0 determines – in both limits of the stiffness parameter s considered here – the minimal spacing between spiral cores in the state of fibrillation. As L varies between L_0 and $\lambda/2$, the period of the spiral wave varies as much as 20%, with the smaller spirals rotating faster than the larger ones. Hence, even if we were to ignore the instabilities on time scales of order a few periods, multi-spiral states with spirals of different size should exhibit dynamics that are very complicated, i.e., at least quasiperiodic. Quasiperiodicity has been suggested as a possible dynamical mechanism for transition to fibrillation [81].

We have previously established (Ch. 3) that, for $L < L_b$ meander is the leading instability mechanism, so spirals of size $L_0 < L < L_b$ will tend to merge with neighboring spirals of opposite chirality in the same size range. This mechanism reduces the number of spirals and increases the sizes of remaining spirals, as smaller spirals rotate more quickly and invade the tiles of slower, larger ones [100, 113]. On the other hand, spirals of size $L > L_b$ are unstable towards alternans and will break up. This

mechanism increases the number of spirals by splitting large spirals into smaller ones (ranging in size down to L_0). The interaction of these two instability mechanisms alone can lead to a dynamic self-sustaining process, which would maintain the state of spiral chaos featuring multiple interacting spirals ranging in size from L_0 to L_b.

CHAPTER VI

MULTI-SPIRAL SOLUTIONS

Sustained spiral chaos features isolated spiral waves only transiently; the asymptotic dynamics involves multiple spiral waves strongly interacting and undergoing spatiotemporally local topological transitions. The simplest of these transitions is the creation or annihilation of a new pair of spiral cores through the interaction of excitation waves and refractory tissue through conduction block, cf. Ch. 2. We investigate multi-spiral solutions – including topologically stable trajectories and orbits featuring topological transitions from a long turbulent trajectory – in the remainder of this chapter.

6.1 Spiral cores and Wave anatomy

To quantitatively discuss the creation or annihilation of spiral waves through conduction block we must first define what we mean by refractory tissue, the wavefront, the waveback, and the spiral origins, with some precision. This Section is devoted to making these constructions explicit.

6.1.1 Refractory tissue

Refractoriness is typically [124] defined using the phenomenology of perturbed individual excitable cells, i.e., whether a voltage perturbation δu_1 applied to the quiescent state of the cell will trigger a depolarization-repolarization cycle – if it is defined explicitly at all – as this has a natural implementation for experimental systems. This can be interpreted using the nullclines of the present model in two distinct regimes for excitable systems with an intrinsic separation of temporal scales in the dynamics of the cellular kinetics. When the voltage perturbation is increased sufficiently quickly,

the dynamics of the slow variable can be ignored. The minimal value necessary to trigger the depolarization cycle is determined by the difference between the rest voltage ($[\mathrm{EQ}_1]_1$) and the value of the voltage on the excitability nullcline at the resting gating variable value, $f_1([u_1, [\mathrm{EQ}_1]_2]) = 0$. For the present model the voltage nullcline is approximately singular for $u_2 \approx 0$ (i.e., $\partial f_1(\mathbf{u})/\partial u_2 \to \infty$) and we should expect that minimal voltage perturbation is comparable to $[\mathrm{EQ}_2]_1 - [\mathrm{EQ}_1]_1 = [\mathrm{EQ}_2]_1$. For the parameters chosen, this value can be computed numerically, $\delta u_1^{\mathrm{fast}} \approx 0.655$. When the perturbation is increased slowly, then the value of the gating variable will change and generally it depends on the dynamics of the perturbation, $\delta \dot{u}_1(t)$, which can in principle be very complicated. We can simplify this perturbation path by asserting that the path follows the nullcline of the gating variable, and thus that the second equilibrium is reachable from the first [163]. With this assumption, the minimal voltage perturbation is the difference between the extremal points on this path, i.e., between EQ_2 and EQ_1. Therefore, the minimal perturbation necessary to trigger depolarization for slowly applied external potential is approximately $\delta u_1^{\mathrm{slow}} = [\mathrm{EQ}_2]_1 \approx 0.658$.

In the context of spatially-extended states, these values can be used to construct an approximation $\tilde{R}(t, \mathbf{x})$ to the refractory region $R(t, \mathbf{x})$,

$$\tilde{R}(t, \mathbf{x}) = \{\mathbf{x}(t) : f_1(\mathbf{u}(t, \mathbf{x}) + [\delta u_1(t), 0]) < 0\}, \tag{80}$$

for a chosen perturbation value δu_1, i.e. $\delta u_1^{\mathrm{fast}}$ or $\delta u_1^{\mathrm{slow}}$, in the fast or slow case. This defines the set of positions for a particular configuration of the state for which *each uncoupled cell* is resistant to immediate excitation due to finite-size perturbations in the amplitude.

This construction discards information associated with the coupling of the tissue, and so does not account for the interaction of the diffusion of the voltage with the dynamics of the gating variable [159]. In particular, this construction will predict no refractory behavior for equilibria (i.e., $\partial_t \mathbf{u}(t, \mathbf{x}) = \mathbf{0}$) of (13) with spatial variation, which does not capture the essential (lack of) dynamics of these states. Analogously

to the relationship between the uniform steady states and more general kinds of equilibria, we can consider (80) as a limiting case.

More generally, we can interpret the refractory boundary by considering a one-dimensional pulse train in a co-moving frame. In the frame moving with velocity c matching the propagation of the fronts, the evolution equation for the voltage variable $u_1 = u_1(x - ct)$ is

$$D_{11}u_1'' + cu_1' + f_1(\mathbf{u}) = 0, \tag{81}$$

where $u_1' = \partial_\xi u_1(\xi)$, $u_1'' = \partial_\xi^2 u_1(\xi)$, and $\xi = x - ct$. Recall that for traveling wave solutions, the diastolic interval can be written explicitly in terms of the speed of the pulse, the wavelength and the action potential duration, DI $= \lambda/c -$ APD, cf. the discussion immediately following (29). For sufficiently small DI (wavelengths) the propagation speed of the second pulse decreases monotonically and the speed vanishes identically at finite DI [108]. Thus, the advective term in (81) vanishes, $cu_1' = 0$, and we see that $D_{11}u_1'' + f_1(\mathbf{u}) = 0$ delineates the time and position of conduction block – where and when the pulse fails to propagate. Thus, the boundary of the refractory region can be described by $\partial_t u_1(t, \mathbf{x}) = 0$.

This immediately leads to a more robust definition of the refractory boundary, one which accounts for the essentially diffusive effects of the PDE model,

$$R(t, \mathbf{x}) = \{\mathbf{x}(t) : D_{11}\nabla^2 u_1(t, \mathbf{x}) + f_1(\mathbf{u}(t, \mathbf{x}) < 0\}. \tag{82}$$

Figure 42 illustrates the effectiveness of the definition of $R(t, \mathbf{x})$ over (80) for a critical excitation state on a small one-dimensional domain. This is an equilibrium solution of (13) with non-trivial spatial variation, such that $\partial_x \mathbf{u}(x) \neq \mathbf{0}$ and $\partial_t \mathbf{u}(x) = \mathbf{0}$. This state represents an edge state for the triggering of an excitation, and is thus interpreted as a one-dimensional analogue of the cellular states which lie on the $f_1(\mathbf{u}) = 0$ nullcline. In Fig. 42(b) the definition of the refractory region is shown. Throughout the domain $R(x) = 0$ (solid) reflecting the solution of the boundary value problem,

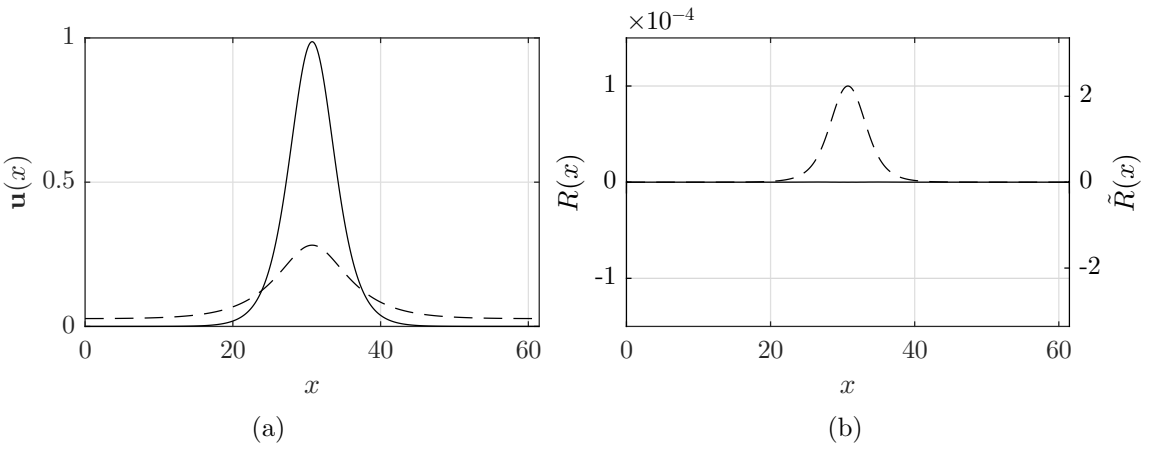

Figure 40: (a) Critical 'bump' equilibrium solution with $u_1(x)$ (solid) and $u_2(x)$ (dashed). (b) The refractory approximation (80) (dashed) and refractory region (82) (solid) on the left and right y-axes, respectively.

while $\tilde{R}(x) > 0$ (dashed) indicating that this solution will trigger an excitation if perturbed appropriately. These edge states illustrate the fundamental difference between the interpretation of $\tilde{R}(t, \mathbf{x})$ and $R(t, \mathbf{x})$: the former describes the effects of perturbations, while the latter describes the future dynamics of an *autonomous* system. Equation (82) is thus the relevant description for the work presented in this thesis.

6.1.2 Wavefront & waveback

The wavefront and waveback are, fundamentally, a region over which the voltage variable changes rapidly, whose boundaries can be made mathematically formal (e.g., by consideration of the boundary value problem corresponding to a heteroclinic connection) but are phenomenologically ambiguous. We can make these features precise by reducing their width and treating each as curves, leading to a simpler framework in which to consider wave collisions. One of the simpler definitions of the wavefront uses the level-sets of the voltage variable, $u_1(t, \mathbf{x}) = \bar{u}_1$, constrained to be increasing in time, $\partial_t u_1(t, \mathbf{x}) > 0$. The choice of level-set value $\bar{u}_1$ must distinguish between decaying excitations – those too small to generate a sustained excitation wave – and

developed excitation wave fronts, and is typically taken as a percentage of the voltage repolarization, i.e., between the minimum voltage attained and the rest state, distinguishing the action potential duration (APD) and diastolic interval (DI) [72]. Typical voltage minima during DI are -90 mV and typical voltage maxima during the APD are $+40$ mV for cardiac models [70] and typical values of the proportionality parameter are between 0.7 and 0.9, corresponding to APD definitions APD_{70} and APD_{90}, respectively. The choice of level set value $\bar{u}_1$ is arbitrary and model-specific, and different values can lead to inconsistent quantities for sufficiently complicated states, e.g., number of spiral cores which is inconsistent with the boundary conditions [175].

A definition which completely bisects the solution space of the cellular kinetics can guarantee an unambiguous construction of the excited and unexcited regions, and thus, of the wavefront and waveback. It remains, then, to define a curve through the **u**-plane which distinguishes between excited and unexcited regions. We define this curve as the segment of the nullcline $f_1(\mathbf{u}) = 0$ where $\mathrm{d}u_2/\mathrm{d}u_1 \geq 0$, extending through $u_2 \geq 1$ at the peak of $f_1(\mathbf{u}) = 0$, i.e., $\mathrm{d}u_2/\mathrm{d}u_1 = 0$ and $\mathrm{d}^2u_2/\mathrm{d}u_1^2 < 0$. To the left of this curve, we consider the state unexcited, and to the right, excited. This curve, extending along the segment of the nullcline, to the peak, and then through all $u_2 \geq 1$, we denote by $q(\mathbf{u}) = 0$. This definition distinguishes between the wavefront and the waveback,

$$0 = q(\mathbf{u}), \quad \partial_t u_1(t, \mathbf{x}) \gtrless 0, \tag{83}$$

using the sign of $\partial_t u_1(t, \mathbf{x})$. Fig. 41 shows the $f_1(\mathbf{u}) = 0$ nullcline (blue) and the excited region (shaded), along with the oscillation cycle of a traveling wave solution (black).

A construction of the wavefront and waveback utilizing a bisecting definition is, in principle, applicable to cardiac models with arbitrary numbers of gating variables or ionic concentrations, though it very quickly becomes inscrutable as higher-dimensional spaces need to be specified, segmented, and the trajectories through them

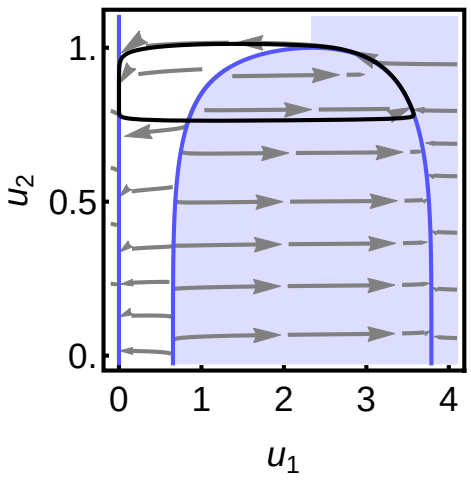

Figure 41: The $f_1(\mathbf{u}) = 0$ nullcline (blue) and the excited region $q(\mathbf{u}) > 0$ (shaded) against the flow (gray), and the oscillation of the traveling wave solution (black).

reasoned about. Additionally, as the one-dimensional curve is a result of an entirely point-wise evaluation, it is only guaranteed spatially continuous if the kinetics of all the state variables are, which is atypical for both simplified and stochastic ionic models of cardiac dynamics [70]. Alternatively, we present a method which utilizes all the information provided by the continuum model,

$$0 = A \cdot \partial_t \mathbf{u}(t, \mathbf{x}), \quad \partial_t u_1(t, \mathbf{x}) \gtrless 0, \tag{84}$$

where $A = [A_1, A_2]$ is a row vector which can be tuned, and the sign of $\partial_t u_1(t, \mathbf{x})$ selects between the wavefront ($\partial_t u_1(t, \mathbf{x}) > 0$) and the waveback ($\partial_t u_1(t, \mathbf{x}) < 0$). Choosing $A_2 = 1$ and $A_1 = O(\epsilon)$ gives extremely good agreement with (83) for both the wavefront and the waveback, cf. Fig. 42(a-b). Intuitively, the relative scales of A can be thought as normalizing the disparate scales of the components Ch. 4 of the right-hand-side of (13), as $|\partial_t \mathbf{u}| \sim [O(1), O(\epsilon)]$. For the sake of clarity, we shall drop the $O(\epsilon)$ contribution altogether (as its presence has little effect on the shape or position of the waveback of the excitation and it does not change the interpretation of the results) and use this definition from now on.

Briefly, it is tempting to define the waveback and wavefront in terms of the leading

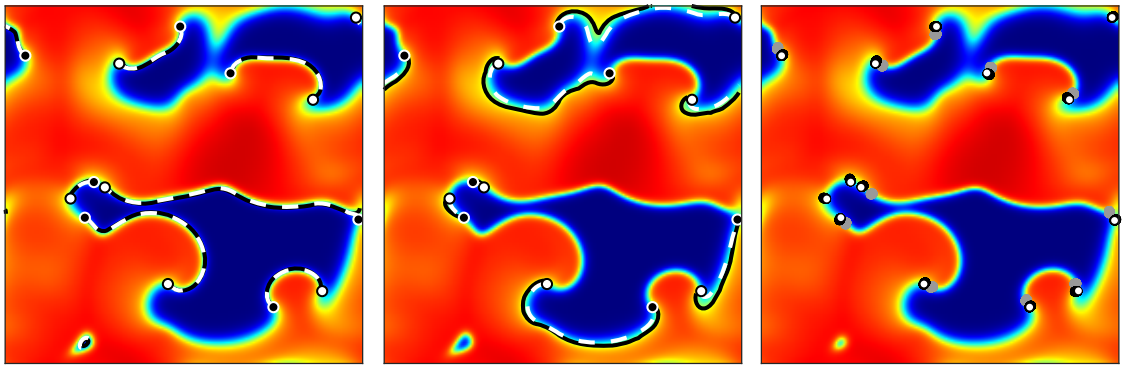

(a) (b) (c)

Figure 42: Comparison of the definition of the wavefront (a) and waveback (b) for a complicated multi-spiral state $u_1(t, \mathbf{x})$, using definitions (83) (white, solid) and (84) (black, dashed). (c) Comparison between different spiral origin definitions ZNV (white), LSI (gray), and eq. (88) (black).

and trailing boundaries of the refractory region. We believe, however, that the wavefront and waveback have merit as distinguishable features of the dynamics, while the refractory region need not be a recognizable feature within a complete representation of $\mathbf{u}(t, \mathbf{x})$. Refractoriness, in the sense defined by (80) and (82), is a consequence of the evolution of a state and not the state in isolation. For example, the critical bump solution shown in 42(a) is not obviously refractory if the reader does not know that the flow is autonomous and that it is an equilibrium solution. Defining both $R(t, \mathbf{x})$ and the wavefront and waveback independently gives a way to segment the domain into not only excited and unexcited, but excitable and unexcitable. We believe this distinction is conceptually useful.

6.1.3 Spiral origins

In order to discuss topological transitions, a reliable way to compute the positions of the spiral origins is needed. A proper description of the organizing center of a spiral wave is the phase singularity [102], computed from the original model via transformation to an amplitude-phase representation. Strictly speaking, however, this construction is only consistent when the dynamics are recurrent and may be

thought of as a weakly nonlinear oscillator cf. Ch. 5. As topological transitions – the creation or annihilation of spiral cores – are essentially non-recurrent, a more robust construction is needed.

Several definitions of the wave tip and spiral origin have been introduced in the literature (cf., Ref. [72]), including the zero normal velocity (ZNV) [69] and level-set intersection (LSI) [18]. Both ZNV and LSI define the spiral origin as the intersection of two level sets,

$$\text{LSI}: \quad u_1(t,\mathbf{x}) = \bar{u}_1, \quad u_2(t,\mathbf{x}) = \bar{u}_2, \tag{85}$$

$$\text{ZNV}: \quad u_1(t,\mathbf{x}) = \bar{u}_1,\, \partial_t u_1(t,\mathbf{x}) = 0, \tag{86}$$

where $\bar{u}_1$ and $\bar{u}_2$ are convenient numerical parameters. The intersections are compared in Fig. 42(c), where $\bar{u}_2 = 0.935$, and shows the variation in the position in the spiral origin over $1.68 \leq \bar{u}_1 \leq 2.11$, corresponding to the definitions of the voltage defining APD_{70} and APD_{90} rescaled for the present model, respectively [72]. We've focused on these constructions for being both simple and instructive, as well as being computationally convenient.

For trajectories of the state $\mathbf{u}(t)$ in which the number of cores is not fixed – precisely the kind of dynamics we wish to better understand – spatial and temporal locality is a computationally useful metric to organize the various constructions of the spiral origin. Formally, we define spatial and temporal locality by the constraint that the position of the spiral origin can be verified with only the information about the state and its derivatives at the time and position of the spiral origin, i.e.,

$$0 = J\left[\mathbf{u}, \partial_t \mathbf{u}, \nabla \mathbf{u}\right](t, \mathbf{x}_o(t)), \tag{87}$$

for some functional $J(\cdot)$, while validations which require information from disparate locations, or different times, violate spatial or temporal locality, respectively. As stated above, both LSI and ZNW constructions preserve both spatial and temporal locality. Still other methods preserve locality in both space and time [29, 18, 174, 18,

103, 69], locality in space but not in time [29, 97, 89] (and the local minima within the tiles shown in Ch. 5), locality in time but not in space [78, 13, 19, 103, 104] or dispense with locality in both space and in time altogether [102], with varying degrees of success.

We define the spiral origins $\mathbf{x}_o(t)$ as the point where the wavefront transitions into the waveback according to (84),

$$\partial_t \mathbf{u}(t, \mathbf{x}_o) = \mathbf{0}, \tag{88}$$

or the intersection of the curves defined by $0 = A \cdot \partial_t \mathbf{u}(t, \mathbf{x})$ and $0 = \partial_t u_1(t, \mathbf{x})$. Briefly, the construction in Ref. [78] asserts that the spiral origin is the point within the domain for which the state variables are time-independent in the symmetry-reduced frame, considering both rotations and translations. However, while global symmetry reduction fails for multi-spiral states, (88) is robust even when the co-moving frame can not be consistently defined. In fact, (88) has an exceedingly simple interpretation for highly symmetric non-trivial solutions of (13), in particular, rotating waves. This is a state $\tilde{\mathbf{u}}(t, \mathbf{x})$ for which temporal evolution is precisely aligned with rotation about an axis $\mathbf{x}'$,

$$\partial_t \tilde{\mathbf{u}}(t, \mathbf{x}) - \omega \partial_\theta \tilde{\mathbf{u}}(t, \mathbf{x}) = \mathbf{0}, \tag{89}$$

such that $\partial_\theta = \hat{\mathbf{z}} \cdot (\mathbf{x} - \mathbf{x}') \times \nabla$. At the axis of rotation, $\mathbf{x} = \mathbf{x}'$, and we may assert $\partial_\theta \tilde{\mathbf{u}}(t, \mathbf{x}') = \mathbf{0}$, such that $\partial_t \tilde{\mathbf{u}}(t, \mathbf{x}) = \mathbf{0}$, and immediately recognize that $\mathbf{x}' \equiv \mathbf{x}_o$ for this solution. This approximation is a simplification of the symmetry-reduction argument which assumes that each core moves slowly compared to the local propagation speed of the excitation wavefront, $|\dot{\mathbf{x}}_o| \ll |\mathbf{c}(\mathbf{x}_o)|$, and thus may be interpreted as an assumption that the dynamics near spiral cores is predominantly rotational. This assumption is certainly justified for well-developed spiral waves such as those investigated in Ch. 3 and Ch. 4, but the approximation breaks down for locally oblique wavefront collisions for which the collision point moves arbitrarily fast, i.e., during

conduction block. However, this construction of the spiral wave origin has the nice mathematical property that these positions sit precisely on the intersection of the wavefront and the boundary of the refractory region, and as we shall see below, the accuracy with which it detects phenomenological features of the state, even when the assumption of low core speed is explicitly violated, is exceedingly good.

6.1.3.1 Spiral chirality

In addition, the interpretation of $\mathbf{x}_o(t)$ as the local origin of rotation leads to a simple construction of the chirality of the wave associated with that origin. To reliably identify the chirality of the spiral wave, we compute the set of positions $\mathbf{x}_{o,j}$ following (88) and then solve for the pseudo-chirality ($\tilde{c}_j$) of each spiral wave by minimizing the functional

$$\min_{\tilde{c}_j \in \mathbb{R}} \int_\Omega \mathrm{d}^2\mathbf{x}\, w\left(r_j/d_j\right) \left|\partial_t \mathbf{u}(t,\mathbf{x}) - \tilde{c}_j \partial_\theta \mathbf{u}(t,\mathbf{x})\right|^2, \tag{90}$$

for each spiral origin, where $w(r_j/d_j)$ is an emphasis function which decreases monotonically with distance $r_j \equiv |\mathbf{x} - \mathbf{x}_{o,j}|$,

$$w(r_j(\mathbf{x})/d_j) = \exp(-|\mathbf{x} - \mathbf{x}_{o,j}|/d_j), \tag{91}$$

with the decay scale $d_j \equiv \min_{k \neq j} |\mathbf{x}_{o,j} - \mathbf{x}_{o,k}|$ given by the distance to the nearest distinct spiral origin. The chirality of rigidly rotating spiral waves (née relative equilibria) is precisely $c = \pm 1$, and using this definition we compute approximate chirality $\tilde{c}/\omega = \pm 1 + O(10^{-2})$, where $\omega \equiv 2\pi/T$ is the angular frequency of the wave. Throughout this work we shall treat the chirality c_j and the pseudo-chirality $\tilde{c}_j$ interchangeably where the distinction leads to no quantitative difference.

6.1.3.2 Application to a more complicated model

This construction of the wavefront, waveback, and spiral origins is sufficiently general to be extended to much more complicated models. At first glance, (84) works only for two-variable systems. However, for an l-variable ionic model this method trivially

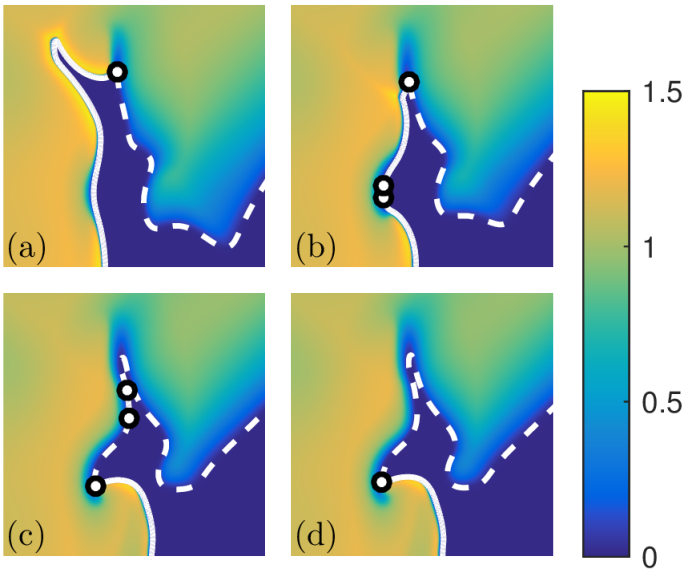

Figure 43: Snapshots of sub-regions in the non-dimensional voltage variable $u_1(t, \mathbf{x})$ from the four-variable model [43] with the wavefronts (white, solid), wavebacks (white, dashed), and spiral origins (circles) showing wave breakup and core merger.

generalizes by extending the functional for $A = [A_1, \ldots, A_l]$, with appropriately chosen weightings. For example, in Fig. 43, we used the four variable minimal model [43] and $A = [0, 0, 1, 0]$, considering only the contribution from a single slow variable as a first approximation. The only apparent shortcoming for the method applied to this model is when the diffusion coefficients for the slow variables are identically zero, which can lead to subtle artifacts when discontinuities of the kinetics, e.g. in the switching between on and off states, combine with the high spatial gradients near the wavefront. However, this issue is not a fault of the method per se, rather, the method of describing the wavefront reflects the underlying discontinuous dynamics. It is fair to conclude that the continuity of the wavefront construction in (84), then, presumes the continuity of all the variables of the right-hand-side, while the construction detailed in (83) only requires that the voltage variable be strictly continuous in space.

6.2 Singular spectrum

For closed periodic or relative periodic trajectories, the tangent propagator $\mathcal{V}_t$ may be factored using two sets of collocated eigenfunctions – the canonical and adjoint sets – which coincide with the Floquet modes, cf. (38). For open trajectories, the proper factorization of the tangent propagator is in terms of the singular triplets, i.e. using the singular value decomposition (SVD),

$$\mathcal{V}_t V = US, \qquad \mathcal{V}_t^\dagger U = VS, \tag{92}$$

where S is a diagonal matrix of singular values, V forms a real orthogonal basis ($V^\top V = \mathbf{1}$) at the temporal origin ($t = 0$) of the orbit fragment, and U forms a real orthogonal basis ($U^\top U = \mathbf{1}$) at the termination ($t = t$) of the orbit fragment. In fact, this decomposition can be consistently defined for all time intervals within an orbit fragment with the same temporal origin [44]. In practical terms, the leading right singular vector V_1 is the fastest growing perturbation to the initial state $\mathbf{u}(0, \mathbf{x})$ in time t. Similarly, the leading left singular vector U_1 represents the shape of the fastest growing perturbation at the termination of the orbit fragment. The amplification factor of the k-th right singular vector is $\sigma_k \equiv S_{kk}$ (analogous to the Floquet multiplier), ordered such that $\sigma_k \leq \cdots \leq \sigma_1$. The k-dimensional trunctation of (92) is determined by the Golub-Kahan-Lanczos algorithm [88] which applies the action of $\mathcal{V}_t$ and $\mathcal{V}_t^\dagger$ to an initial vector to iteratively construct a basis for the left and right singular vectors, repectively, cf. A.3.2. The leading singular values at time t were verified with the eigenvalues of $\mathcal{V}_t^\dagger \mathcal{V}_t$ by Arnoldi iterations. On a technical note, as the left singular vectors arise from the evaluation of $\mathcal{V}_t$ and the right singular vectors from the evaluation of $\mathcal{V}_t^\dagger$, their components exhibit the same scaling as the right and left eigenfunctions (45) & (46), so we present only the dominant components, i.e., $U_k^{(1)}$ and $V_k^{(2)}$, respectively.

The leading singular spectrum is a probe of the structure of the linear neighborhood of the trajectory about which it is computed, just as the Floquet spectrum probes the structure of the linear neighborhood of periodic orbits. This can be seen most clearly when the singular triplets are interpreted as the deformation of a hypersphere centered on an equilibrium solution of a low-dimensional system: over time, it deforms to a hyperellipse whose principle axes are determined by the singular vectors with their lengths determined by the singular values. When the underlying state is linearly unstable, then the leading singular values computed using (92) reflect this fact: indeed, as the eigenvalues of $\mathcal{V}_t^\dagger \mathcal{V}_t$ are equal to the singular values of $\mathcal{V}_t$, the leading singular spectrum offers the same interpretation of growth as the Floquet spectrum, i.e. $\sigma_k > 1$. When the underlying state is marginal, such that all $|\Lambda_k| \leq 1$, then we can expect that this will be similarly reflected in the singular spectrum, but making this expectation explicit is non-trivial. We can show this by considering the evolution of a generic perturbation $\mathbf{v}$ using the left and right Floquet modes of $\mathcal{V}_T$,

$$\begin{aligned}\mathcal{V}_T^\dagger \mathcal{V}_T \mathbf{v} &= \left(\sum_i |\mathbf{w}^i\rangle \Lambda_i^* \langle \mathbf{v}^i|\right)\left(\sum_j |\mathbf{v}^j\rangle \Lambda_j \langle \mathbf{w}^j|\right)\left(\sum_k a_k |\mathbf{v}^k\rangle\right), \\ &= \sum_{i,j} a_j \Lambda_i^* \Lambda_j \langle \mathbf{v}^i|\mathbf{v}^j\rangle |\mathbf{w}^i\rangle. \end{aligned} \tag{93}$$

The simplest interpretation of this equation is that the singular vectors (i.e., let $\mathbf{v} = V_1$) will involve coupling between different eigenmodes of the operator $\mathcal{V}_T$.

6.3 Topologically stable dynamics

Sustained spiral chaos is characterized by recurrent dynamics punctuated by fast transitions between topologically distinct multi-spiral configurations, i.e., distinct sets of spiral cores. On unbounded domains or domains with periodic boundary conditions, constraints on the net chirality of the state (i.e., the total chirality must vanish) permits only certain topological transitions: pairwise creation or annihilation of spiral origins with opposite chirality. On bounded domains – specifically with no-flux

boundary conditions – no such constraint exists and more varied kinds of transitions are observed. Numerical observations suggest that there exist effective boundaries between interacting spiral wave solutions which are approximately no-flux (cf. Ch. 5). Therefore, a qualitative characterization of some aspects of spiral chaos is inextricable from a consideration of boundary effects on spiral waves.

In Ch. 3 and Ch. 4 we discussed the effect of no-flux boundaries on single-spiral solutions of (13) in terms of their stability and drift. The single-spiral solution drifts normally to the boundary over the course of a rotation, and the spiral tip position under successive revolutions is described by the map, $\mathbf{x}_o^{n+1} = \mathbf{x}_o^n + \mathbf{h}(\mathbf{x}_o^n)$. Furthermore, the normal component of this map has several distinct roots, e.g. $\hat{\mathbf{n}} \cdot \mathbf{h}(\zeta_k) = 0$. The smallest root, ζ_0, is stable and corresponds to no drift of the spiral normal to the boundary. The localization of the response functions, and the existence of these stable core positions, has immediate consequences for multi-spiral solutions.

Figure 44(a) shows a snapshot of a temporally recurrent multi-spiral solution on a square domain of side length $L = 192$ (5.03 cm) with no-flux boundary conditions ($\hat{\mathbf{n}} \cdot \nabla \mathbf{u}(t, \mathbf{x}) = \mathbf{0}$). The solution recurs with a relative difference in Euclidean norm of $\|\mathbf{u}(T) - \mathbf{u}(0)\| / \|\mathbf{u}(0)\| = 3 \times 10^{-3}$ after time $T = 49.64$ (124.05 ms). Additionally, the net chirality of this configuration is the sum of the chirality of each spiral wave (90), $C = \sum_k c_k = 0$ (defined analogously to the winding number [55]), which is not guaranteed by the no-flux boundary conditions. The closest pairwise spirals are connected by solid white lines between chirality-coordinated markers at each spiral origin. Pairs of spiral waves in this solution are predominately spaced by $d_i \equiv \min_{j \neq i} |\mathbf{x}_{o,i} - \mathbf{x}_{o,j}| \approx 2\zeta_0$. These inter-core separations are $d = 0.99(2\zeta_0)$, $d = 1.01(2\zeta_0)$, $d = 1.01(2\zeta_0)$, $d = 1.02(2\zeta_0)$, $d = 1.04(2\zeta_0)$, $d = 1.07(2\zeta_0)$, $d = 1.28(2\zeta_0)$, $d = 0.94(2\zeta_2)$, where the scale of the last value is given by the *second* stable root of the shift map ($\hat{\mathbf{n}} \cdot \mathbf{h}(\zeta_2) = 0$). Provided that the closest tile boundaries sit at the midpoint of the lines connecting each pair (inspection of the state says this is true for

nearly all of the pairs) this local configuration corresponds to approximately static cores according to the normal component of the drift map. The instantaneous tile boundaries (inferred from the ridges of the area of the local oscillation over $0 \leq t \leq 2T$) are overlaid as black curves.

The state shown in Figure 44(a) is highly atypical: it persists without any mergers or breakups for extraordinarily long times. The dynamics is dominated by slow deformation of the state where each spiral core drifts, but does not meander. Direct numerical simulation sets the lower bound for the persistence of these cores at 4096 revolutions, equivalently 8 minutes. This initial condition was refined using the Newton-Krylov solver described in A.4 from a weakly recurrent segment within a long simulation of sustained spiral chaos.

The Floquet spectrum of the multi-spiral solution shown in Figure 44(b) is dramatically different from that for the single-spiral solution, cf. Fig. 22(c); it includes a multiplicity of eigenvalues (24) which lie near the intersection of the real axis and the unit circle. We identify this set of modes as "near-marginal", signifying their relationship to the marginal modes of exact solutions, in particular those associated with continuous symmetries. There is a total of 24 near-marginal modes – 3 for each of the 8 cores in the solution. The near-degeneracy of these near-marginal modes makes the determination of unique spatially- or temporally-aligned eigenfunctions impossible. Indeed, the projections of the Goldstone modes $\{\partial_x \mathbf{u}, \partial_y \mathbf{u}, \partial_t \mathbf{u}\}$ onto the adjoint eigenfunctions show significant components in all 24 near-marginal modes. In Figure 44(c-e) three near-marginal eigenfunctions with significant projections onto the temporal eigenfunction are presented. The corresponding adjoints are localized around the positions of the spiral tips, c.f. Figure 44(f-h), as in the single-spiral solution. Of essential importance is the fact that each adjoint eigenfunction is not strictly a superposition of the same single-spiral response function, but rather, each adjoint eigenfunction is a superposition of multiple single-spiral response functions,

with distinct phases.

Comparison of the multi-spiral spectrum with that of the drifting single-spiral solution indicates that the dominant instability is stabilized by the presence of nearby spiral cores. This is not entirely unexpected, for sufficiently small domains, the Floquet multiplier for the meander mode of a single-spiral solutions decreases and the Goldstone modes destabilize, cf. Fig. 21(a). For decreasing domain sizes the translational Goldstone modes destabilize as the spiral core-boundary interaction dominates the meander instability ($L/\lambda \lesssim 0.4$). For the present solution, this result can be interpreted as the stabilization of isolated spiral waves on small tiles.

This multi-spiral trajectory is only approximately periodic and so the Floquet multipliers of $\mathcal{V}_T$ do not accurately describe the stability of the trajectory over times $t \gg T$. Rather, the growth of perturbations to this state is described most conveniently using the singular values which require no assumption of periodicity. Figure 45(a) depicts the leading 512 singular values of $\mathcal{V}_T$, 220 of which describe growth ($\sigma > 1$) for the base recurrence interval T. The singular values of $\mathcal{V}_t$ depicted in Figure 45(b) are computed for times $0 \leq t \leq 10T$. The leading singular value reaches a local maximum for $t = 3.5T$ due to transient growth, after which the marginal dynamics dominate ($t \gtrsim 5T$).

The leading singular vector pair, computed for the multi-spiral solution shown in Figure 44 over time $t = T$, is shown in Figure 46(a-b). The mode is localized to the spiral on the largest tile, and corresponds to local translation of the spiral toward its closest neighbor. When the singular vectors are computed over a longer time period, $t = 10T$, the leading singular vector U_1 recruits more of the domain, cf., Figure 46(c-d). The leading singular vector V_1 exhibits similar time-dependent localization properties. As the tiles are different sizes their boundaries move (79), and in increasing time (since the state is strictly not periodic) this movement is cumulative. Eventually the displacement of the tile boundaries effects the drift and rotation of

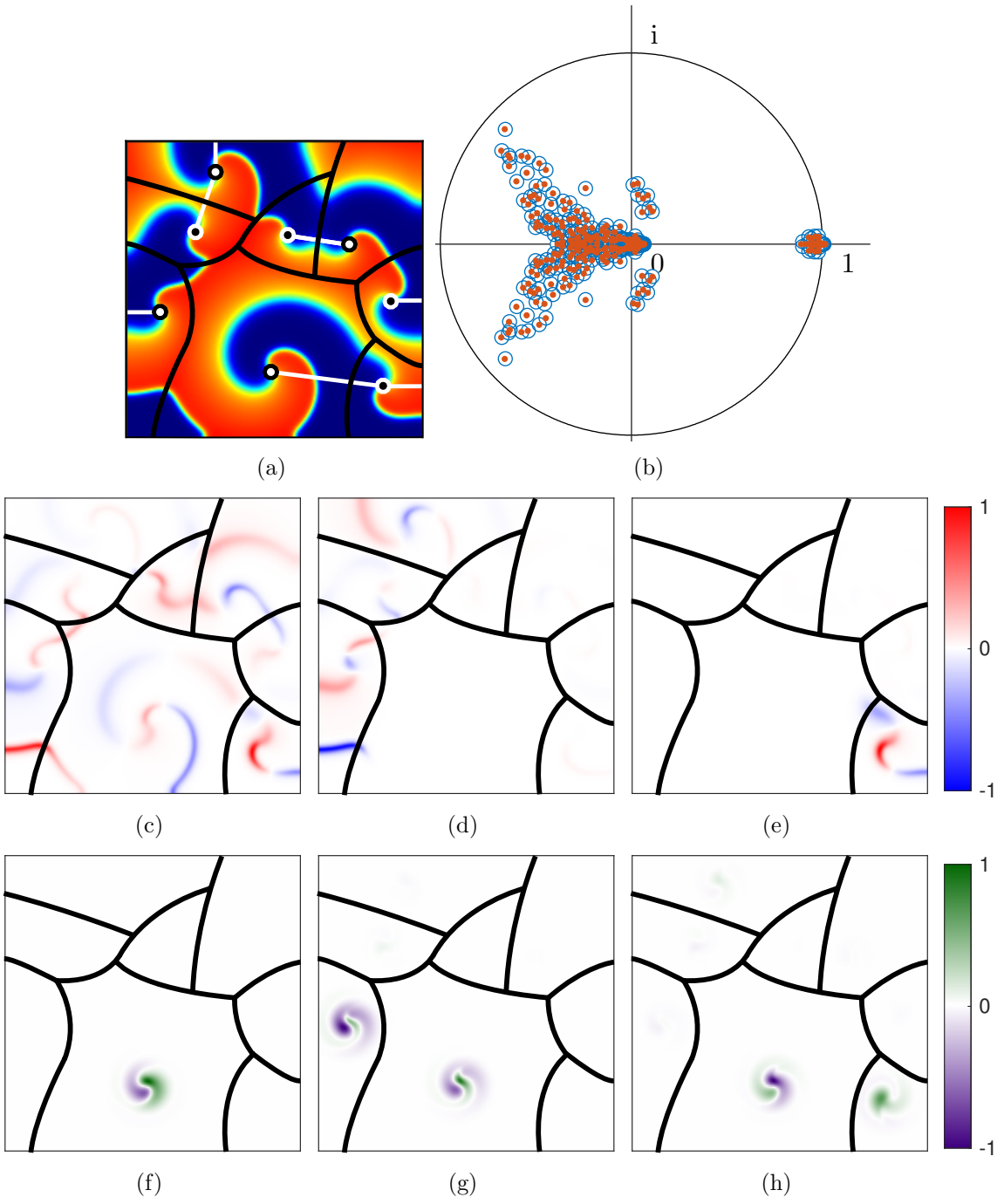

Figure 44: (a) Snapshot of $u_1(0, \mathbf{x})$ the unstable recurrent multi-spiral solution with recurrence time $T = 49.64$, chirally-coordinated spiral cores marked with nearest neighbors linked by solid white lines, and approximate tile boundaries overlaid as solid black curves. (b) Approximate spectrum of the recurrent solution over the recurrence time. (c-e) Snapshots of $v_1(0, \mathbf{x})$ the quasi-Goldstone Modes of the solution ($\Lambda \approx 1$). (f-g) Snapshots of $w_2(T, \mathbf{x})$ the response functions adjoint to (d-f).

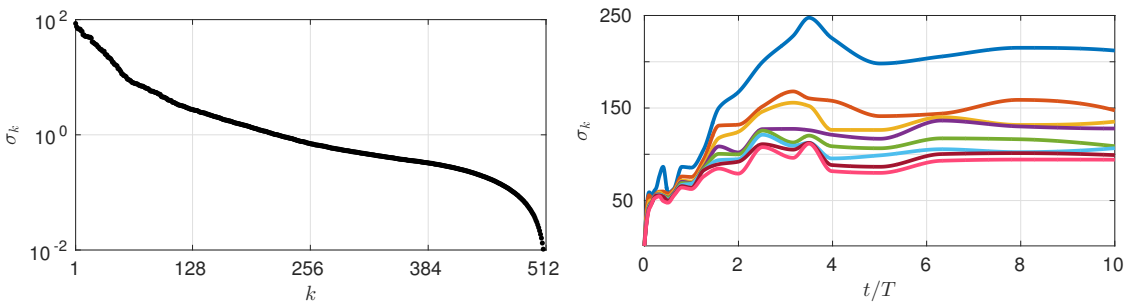

(a) (b)

Figure 45: (a) Singular spectrum for the multi-spiral solution shown in Fig. 44(a), over recurrence time $t = T$. (b) Leading singular values σ_k of $\mathcal{V}_t$ over recurrence times $0 \leq t \leq 10T$, $1 \leq k \leq 8$.

the spirals on the adjacent tiles. This leads to extraordinarily weak coupling between different spiral cores on sufficiently long time-scales.

The leading singular vectors for a recurrent solution describe the shape of the fastest growing perturbations in the forward and adjoint tangent spaces. Qualitatively, the leading modes localize to spirals on particular tiles, before extending across the domain (signifying inter-spiral coordination), which reaffirms our expectation that the spirals in recurrent multi-spiral solutions are dominantly independent. However, global recurrence is the coordination of local recurrence – both temporally and spatially. Over time scales comparable to the rotational period of a spiral wave and over distances comparable to the wavelength, a fully-formed spiral wave is expected to recur approximately. For globally defined multi-spiral states, this means that while each spiral may recur on an individually relevant time scale, the whole solution may not recur on a uniform time scale because the spiral waves are typically different sizes and thus rotate at different rates, cf. Fig. 21.

In this sense, the multi-spiral solution is highly unexpected: it has aperiodic temporal dynamics, is spatially complex, and it is topologically stable. These properties imply that the state can *not* be responsible for sustaining spiral chaos as it is colloquially defined. Indeed, while the long-term dynamics of recurrent multi-spiral states

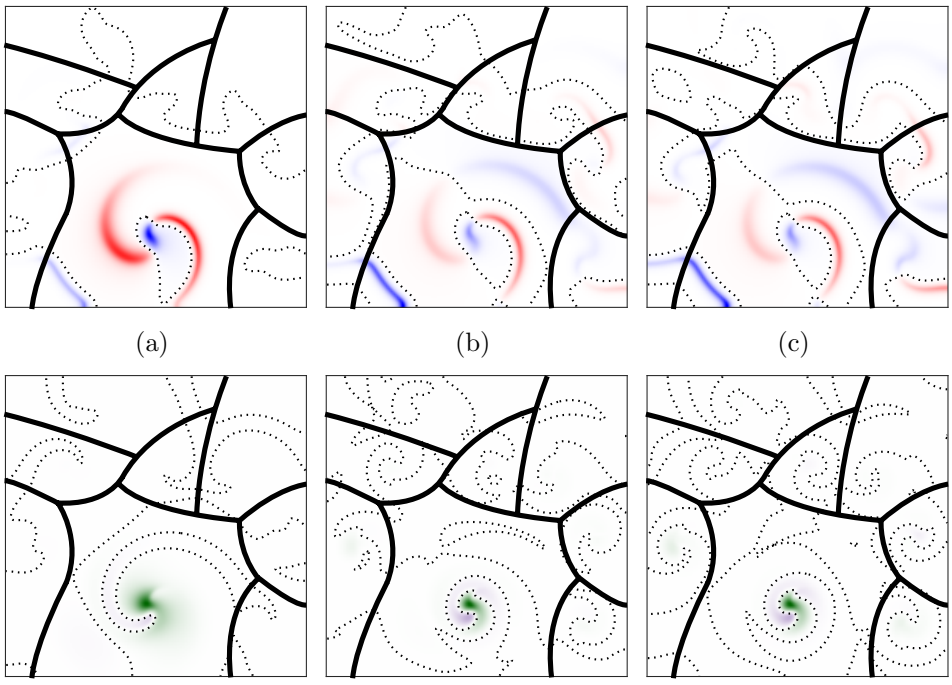

Figure 46: (a) Dominant component of the leading singular vectors ($U_1^{(1)}$ and $V_1^{(2)}$) computed over optimization times $t = T$ (a & d), $t = 5T$ (b & e) and $t = 10T$ (c & f). Nodal lines are denoted by the dotted curves.

is probably weakly chaotic, the observed exponential divergence of nearby trajectories is not due to topologically stable states whose dynamics is dominated on longer time-scales by the near-marginal degrees of freedom. This suggests that it is the topological transitions of a multi-spiral chaos – the creation and destruction of spiral cores – which generate the observed exponential separation of nearby trajectories.

6.4 Topologically nontrivial orbits

While there exist topologically stable trajectories embedded within the chaotic attractor of sustained spiral chaos, these are atypical. Rather, trajectories featuring multiple spiral mergers and wave breakups are the generic case, and such dynamics require consideration in their own right. Additionally, the presence of no-flux boundaries makes new topological transitions possible: most notably the collision of a spiral core with the boundary. Extending the bounded domain by symmetric mirroring across the no-flux boundary, we immediately see that this event can be equivalently understood as the collision of a spiral core with a flip-symmetric partner. As this collision between a spiral core and the boundary is a highly-symmetric configuration between a spiral core and its mirror-symmetric virtual partner, these types of collisions are not generic for sustained spiral chaos away from the boundary. To remove the possibility of core-boundary collisions altogether, we have chosen periodic boundary conditions to investigate breakup and merger events.

6.4.1 Spiral breakup

Spiral wave breakup is due to the development of linear instability, specifically alternans, leading to variation in the width and timing of excitation waves and eventually conduction block. For highly regular solutions, e.g. single-spiral relative periodic orbits, this is an accurate depiction of the breakup of the wave. The mechanism is essentially due to absolute instability, and the cumulative effect of variations in the refractory region in the train of pulses propagating radially. When the dynamics

is highly irregular and features multiple spiral waves which can not be isolated by the tiling decomposition of the state, this identification is non-trivial. Effectively in the absence of well-defined tiles, different excitation frequencies combine to create irregular refractory regions, which further complicates the dynamics through further interaction with the wavefronts.

From a long chaotic trajectory we monitor the set of spiral origins over time, and select instances of temporally isolated topological transitions. In particular, we select an event from the sequence which corresponds to the creation of two new spiral cores, through the breakup of a wavefront due to conduction block. Four snapshots from a time-T trajectory segment featuring this event are shown in Fig. 47(a-d), including immediately pre- and post-breakup. The solution begins with 8 spiral cores with net chirality zero (as required by the boundary conditions), which transitions to a 10-core state within a single rotation period, $T \approx 56$ (140 ms).

During this trajectory, a wave breaks due to the collision between the wavefront and the trailing boundary of the refractory region, identically with the canonical representation of conduction block. In this example, the trailing boundary of the refractory region (white curve) lies between the wavefront (black curve) and the phenomenological waveback at the moment of breakup, leading to the illusion that the impinging of the wavefront on the waveback is responsible, cf. Fig. 47(a-d). Rather, the proper interpretation is that the slowly receding waveback causes a similarly slowly receding refractory region, while the incoming wavefront is unaffected until the boundary is reached – i.e. conduction block. The distinction between the waveback and the trailing boundary of the refractory region, though occasionally subtle, proves to be essential for explaining conduction block in the present model.

Iterating the tangent evolution propagator for this trajectory generates the leading singular spectrum of the solution as a function of time. For short times, depending

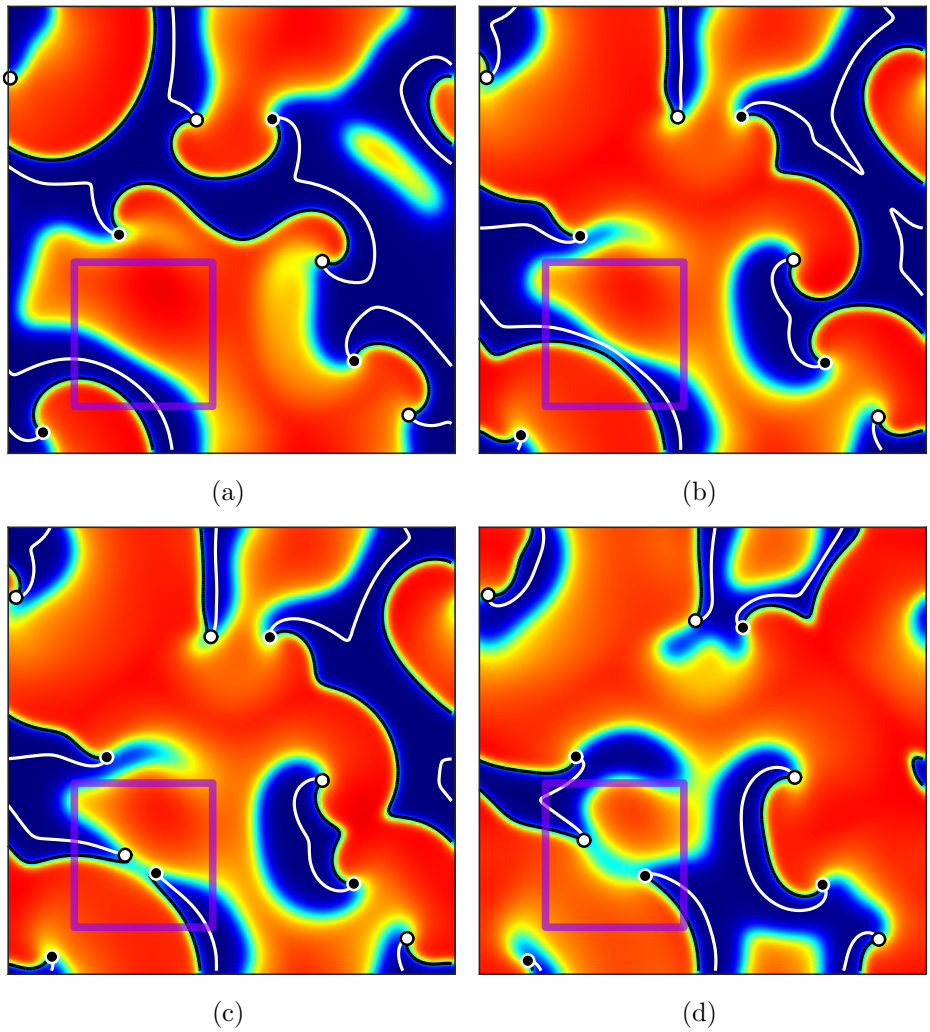

Figure 47: Snapshots of $u_1(t, \mathbf{x})$ at times $t = 0.375T$, $t = 0.583T$ (immediately pre-breakup), $t = 0.625T$ (immediately post-breakup), and $t = 0.813T$ featuring the breakup of a wavefront (black curve) into two new spiral origins (black & white dots) due to collision with the trailing boundary of the refractory region (white curve) in a chaotic multi-spiral state around $t \approx 0.6T$.

on the spectral norm of the Jacobian, the leading singular values do not appreciably separate. For longer times, the leading singular values are distinct, and we can correlate temporal features of the singular spectrum with the dynamics of the underlying nonlinear state. In particular, around $t \approx 0.6T$, the wavefront collides with the boundary of the refractory region and generates two new opposite-chirality spiral cores.

The first four singular values $\sigma_k(t)$, $k = 1 \ldots 4$, are shown in Fig. 48(a) over a time-span including the topological transition. The scale of the leading singular value depends on the choice of temporal origin, and is thus not a universal measure of all topological transitions. Rather, it is the dynamics of the leading singular value, $\dot{\sigma}_1(t)$, which describes the nature of the linear neighborhood of the underlying state, as this reflects the spectral norm of the instantaneous Jacobian, $\mathcal{L}[\mathbf{u}(t, \mathbf{x})]$.

We can interpret these leading singular value dynamics in the context of this particular instance of wave breakup. The leading singular value grows steadily until the topological transition at time $t = t_c \approx 0.6T$ reaching a peak of $\sigma_1(t_c) \approx 400$, which is comparable to the norm of the state, $\|\mathbf{u}(t_c)\|$. The simplest interpretation of this observation is that $O(\sigma_1^{-1}(t_c)\|\mathbf{u}(t_c)\|) \sim O(1)$ perturbations at time $t = 0$ will grow to deviations comparable to the state at that time – a global reconfiguration of the dynamics from the growth of small perturbations over time-scales comparable to half of the period of a single spiral wave.

The leading right singular vector $U_1^{(1)}(t)$ is shown in Fig. 48(b-e). In general the leading singular values reflect the sensitivity of the state as a whole to global perturbations in the shape of the corresponding singular vectors. If, rather, the value of the leading singular value is transiently determined by the sensitivity of the evolution to the presence of a topological transition *in particular*, then the shape of the leading singular vector must similarly reflect the spatial coherence of the topological transition. Plainly, should the sensitivity to the topological transition dominate the

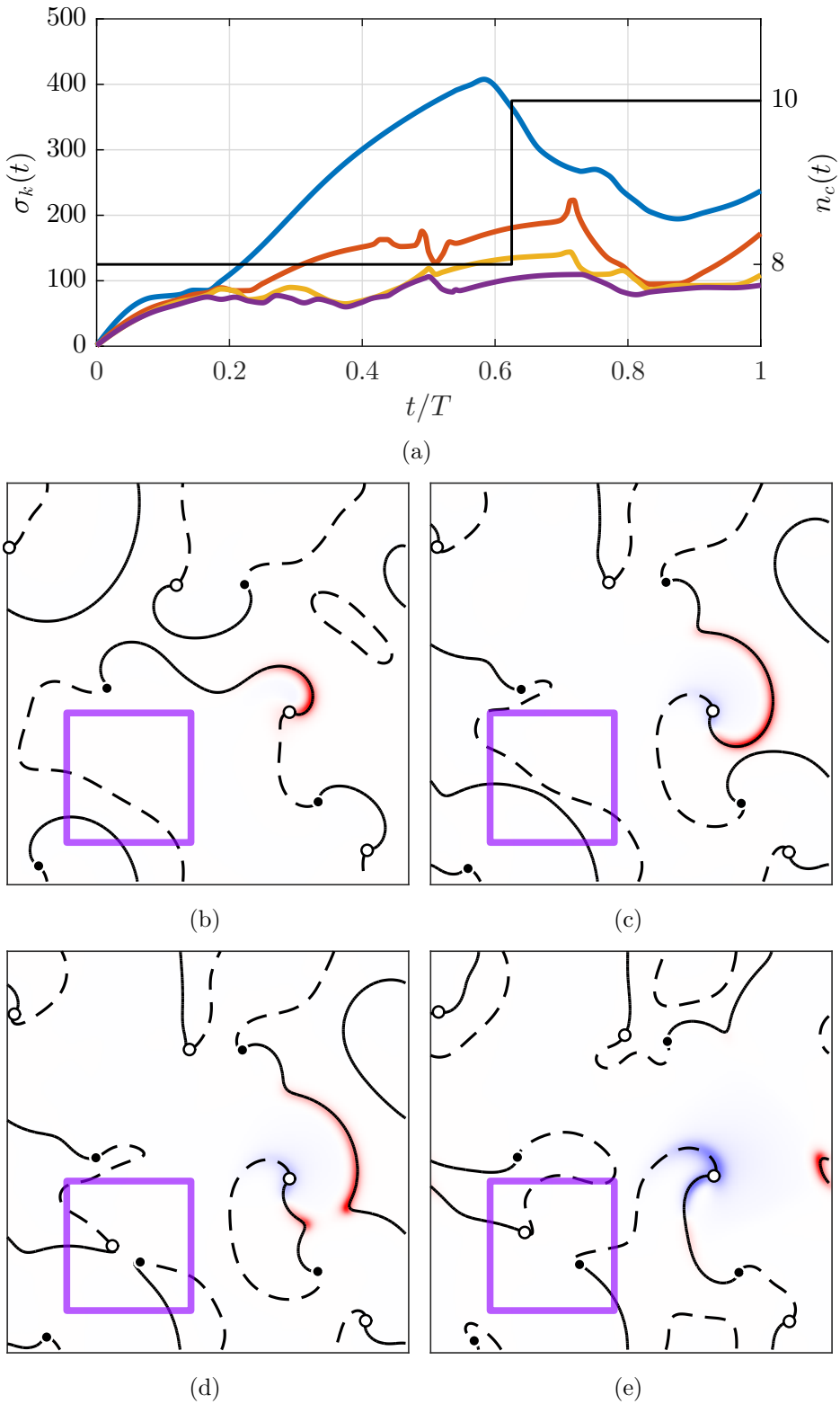

Figure 48: Leading singular values $\sigma_k(t)$ (a) over the time-span including the topological transition. The leading left singular vector $U_1^{(1)}(t)$ (b-d) at the same times as Fig. 47, with the wavefront (solid) and waveback (dashed), and the spiral origins (dots).

sensitivity of the rest of the state, then the leading singular vectors should localize to the feature; the singular vectors shown in Figs. 48(b-e), however, do not. The leading singular vector for this trajectory localizes to the wavefront and waveback of one spiral wave which is $O(\lambda)$ away from and thus has no apparent effect on the breakup event. The shape of the singular vector suggests that a perturbation along this direction would locally enhance the rotation of this wave, while shifting slightly to the right. As both these effects belong to the marginal set, specifically the action of local symmetries, the dominant stretching of the linear neighborhood is due to the presence of small deformations in the position of the spiral waves. Thus, we must conclude, that the presence of topological transitions alone does not guarantee the exponential growth in the leading singular value. Rather, the identification of stretching of the linear neighborhood of a trajectory with the time-dependent features of the state requires more information than the number of cores

6.4.2 Spiral merger

The intuition from isolated spiral solutions provides a simple mechanism for core-pair annihilation. On sufficiently small tiles, the leading instability develops into core meander – the growth of the movement of the spiral origin from a fixed position cf. Fig. 20(a) – to form a complicated path in the plane. Eventually the movement of the core leads to significant deformation of the spiral wave, reinforcing the meander. The meander of the spiral origin grows until the wavefront reaches a boundary – whether refractory, of the tile, or physically no-flux – at which point the propagation of the wavefront is halted, i.e. conduction block.

We can illustrate the development of conduction block for a flip-symmetric configuration of two spiral waves with opposite chirality. In this case there is always a continuous curve connecting the spiral origins extending along the wavefront, and similarly a continuous curve connecting them along the boundary of the refractory

region. The excitable region is bounded by these two curves, and as the meander develops over a time-scale much longer than the rotation time of the spiral waves, the state deforms and the region bounded by these curves not only oscillates with the period of the spiral waves, but deforms on the longer time-scale as well. The excitable region can, in principle, contract and eventually vanish, or it can break into disjoint regions due to the irregularity of fully-developed meander. In the former case, conduction block reduces the number of cores through merger of the spiral cores, while in the latter case conduction block leads to local breakup of the wave, increasing the number of cores, and beginning the meander process again.

Similar to the example of wave break-up, from a long turbulent trajectory we select an isolated topological transition corresponding to the merging of two spiral cores. As before, conduction block is the primary mechanism for this development, this time due to the movement of spiral cores along the boundary of the refractory region. This corresponds to the close-pair case outlined above: the excitable region bounded by the refractory boundary and the wavefront shrinks to zero, annihilating the cores which sit on the intersection of the boundary. As in the case of wave breakup, the identification of the saturation of linear instability resulting in conduction block for irregular multi-spiral states non-trivial. More typically for multi-spiral states is the situation depicted in Fig. 49(a-d), in which movement of the spiral cores is constrained by the refractory boundary, and this region of excitable tissue is slowly eroded by incoming waves until it is fully recruited by the external dynamics, and the pair of cores annihilates.

Qualitatively, the excitable region bounded by the wavefront and the trailing boundary of the refractory region contracts, changing shape from a crescent, to an ellipse, and finally vanishing altogether. As the boundaries move, the spiral origins (which define their endpoints) are similarly driven by the dynamics of the local configuration of the state. As observed in the breakup example, Fig. 47, we compute

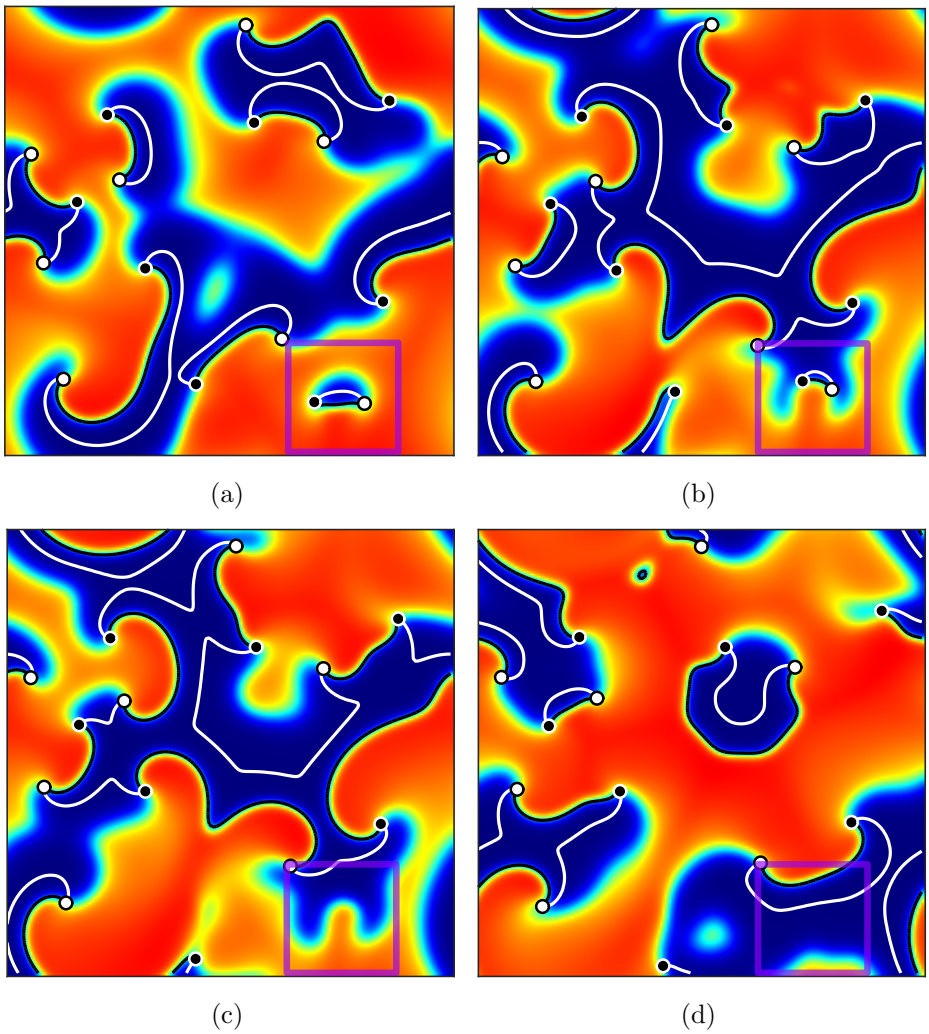

Figure 49: Snapshots of $u_1(t, \mathbf{x})$ at times $t = 0.206T$, $t = 0.427T$ (immediately pre-merger), $t = 0.500T$ (immediately post-merger), and $t = 0.720T$, featuring the merging of two spiral cores (black & white dots) in a chaotic multi-spiral state around $t \approx 0.5T$ due to local coalescence of the wavefront (black curve) and the trailing boundary of the refractory region (white curve).

the time-dependent singular spectrum for this orbit fragment. The leading singular values are shown as functions of time in Fig. 50(a).

The dynamics of the leading singular value for the merger over this time-interval Fig. 50(a) is qualitatively similar to the same quantity for the breakup, Fig. 48(a). However, the correlation between the dynamics of the leading singular value $\sigma_1(t)$ and the number of spiral origins $n_c(t)$ for this example of spiral merger is technically significant ($|r_{\text{corr}}^{\text{merger}}| = 0.5556$ and $p = 0.0001$), while for the example of wave breakup is not ($|r_{\text{corr}}^{\text{breakup}}| = 0.0921$ and $p = 0.5038$). This further reinforces that the leading singular value captures the global sensitivity of the state to specific perturbations, and not merely the presence of topological transitions. The significance of the result for the merger also suggests an explanation for the relevance of topological transitions in the generation of sensitivity of initial conditions in sustained spiral chaos – the importance of curvature in the determination of the dynamics of the refractory region, equivalent in the dynamics of the spiral origins.

6.4.3 Transition sequences

Both Fig. 47 and 49 exhibit isolated topological transitions between distinct multi-spiral configurations. Sustained spiral chaos, however, exhibits sequences of topological transitions within comparably short time-intervals. This system exhibits very short spatial correlations, and is practically guaranteed that multiple transitions will occur within an arbitrarily small time-frame for sufficiently large domains. It behooves us to consider, then, trajectories with sequences of transitions in addition to the temporally isolated topological transitions considered already and in particular how trajectories with multiple distinct transitions differ qualitatively from those with isolated transitions over the same time-span.

Fig. 51 shows a sequence of snapshots $u_1(t, \mathbf{x})$ from a trajectory of length T which exhibits multiple mergers and breakups, in frames (a-f). This trajectory features

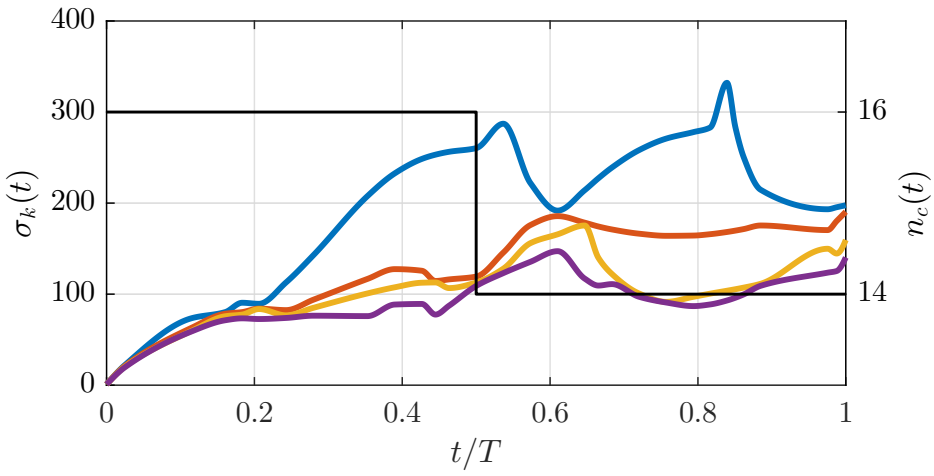

(a)

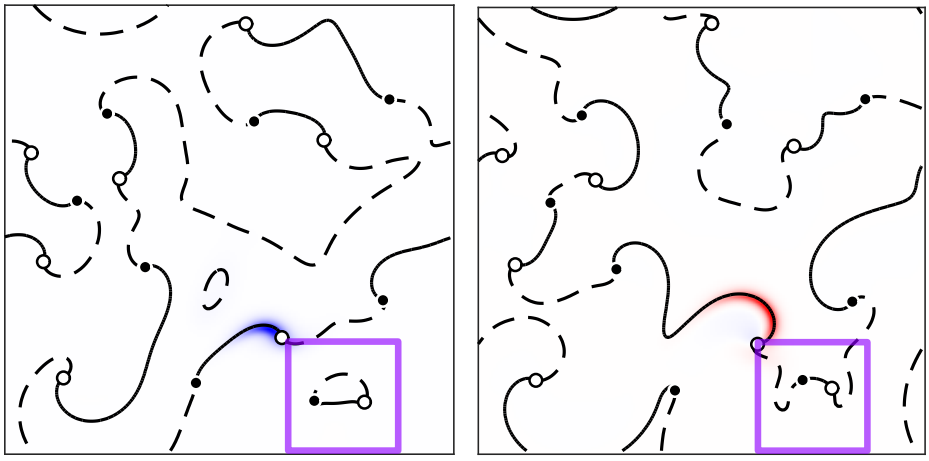

(b) (c)

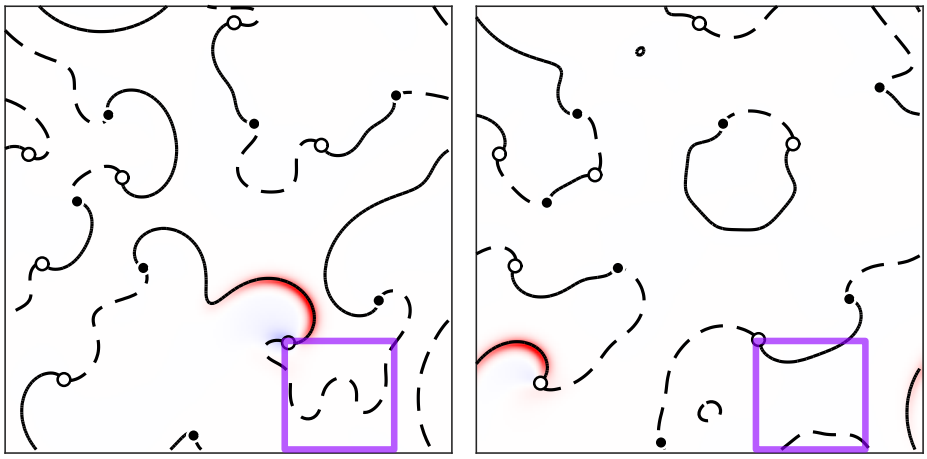

(d) (e)

Figure 50: Leading singular values $\sigma_k(t)$ (a) over the time-span including the topological transition. The leading left singular vector $U_1^{(1)}(t)$ (b-d), at the same times as in Fig. 49, with the wavefront (solid) and waveback (dashed).

multiple breakups and mergers in the same time-span as the isolated examples shown in Figs. 47 and 49. The structure of the state is significantly more complicated than either of the previous examples.

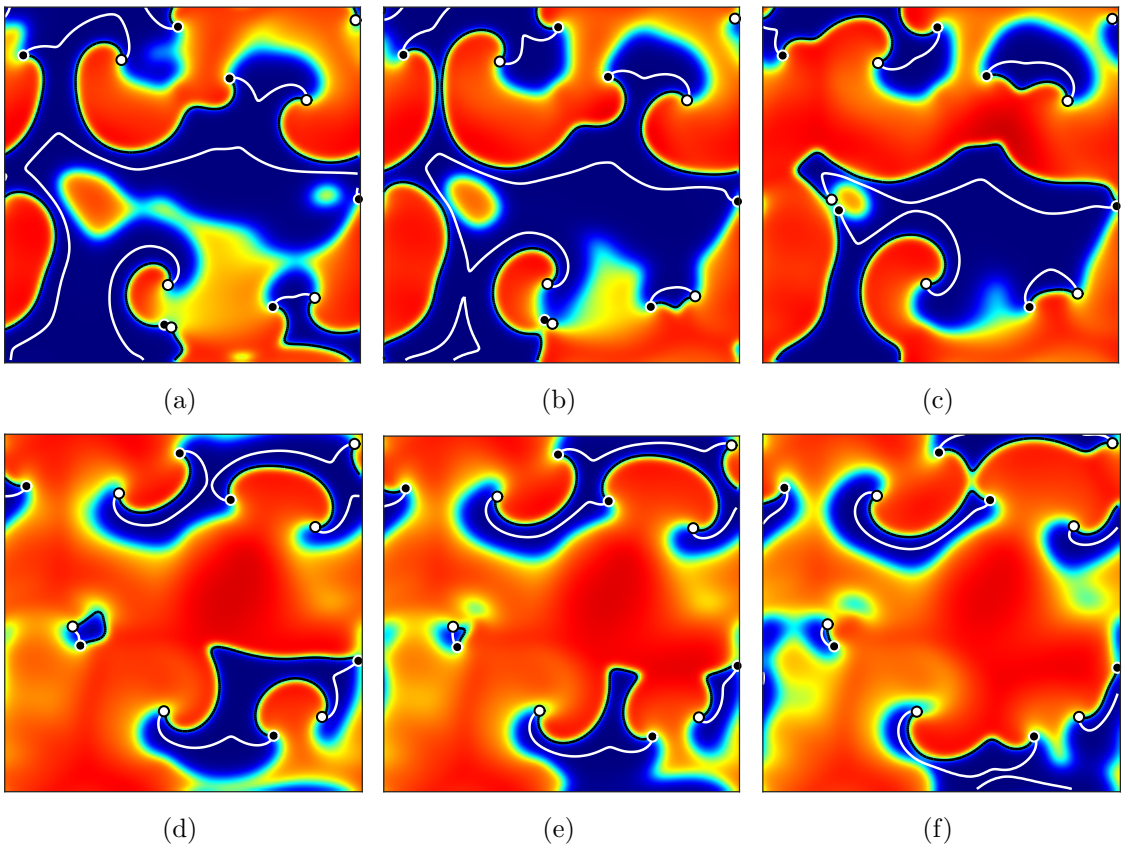

Figure 51: Sequence of snapshots $u_1(t, \mathbf{x})$ for $t/T = 0.2, 0.3, 0.4, 0.7, 0.8, 0.9$ (a-f), with the wavefronts (black curve) and the trailing boundary of the refractory region (white curve) terminating in the spiral origins (black & white dots).

In Fig. 52(a) we show the leading singular values associated with the trajectory shown in Fig. 51, which goes through several transitions in rapid succession, cf. the number of cores $n_c(t)$ (black curve). Note that at times $t/T = 0.2, 0.7$, the value of the first singular value is almost indistinct from the value of the second, $\sigma_1(t) \approx \sigma_2(t)$, and that the singular vectors are *strongly delocalized*. The leading singular value grows exponentially in two temporal regions, around $t \approx 0.3T$ and $t \approx 0.8T$, which has no apparent correlation with the transitions between $10 \leq n_c \leq 14$. However, the

apparent competition between the leading singular values around $t = 0.8T$ suggests that multiple transitions reorient the leading singular vectors. Indeed, the correlation of the leading singular value $\sigma_1(t)$ with the number of cores $n_c(t)$ is not statistically significant ($|r_{\text{corr}}^{\text{noniso}}| = 0.1468$ and $p = 0.1909$).

The two spikes in the leading singular value have right singular vectors which localize to regions representing regions of high curvature at that time, cf. Fig. 52(b-f). Shortly after $t = 0.3T$, the region in the bottom center of frame (c) lies in a critical state whereby the front propagates, but a perturbation which locally reduces the value of the voltage (i.e., $U_1^{(1)}(t)$) will significantly effect the dynamics of the state. This is the proper statement of the growth of the leading singular value: small perturbations at the temporal origin lead to qualitatively distinct outcomes in finite time. In the instance of the spike at $t = 0.8T$, we have an analogous situation, whereby the pair of spiral origins annihilate, due predominantly to the effects of curvature. The interpretation of this localization is that small perturbations can suppress or enhance the breakups or mergers near high-curvature regions of the state. Effectively, when the singular spectrum can not differentiate between dominant growth rates ($\sigma_1 \approx \sigma_2$), the entire state is effected weakly, while strongly dominant perturbations ($\sigma_1 \gg \sigma_2$) have localized effects.

6.4.4 Critical curvature states

The importance of curvature in the regions surrounding mergers and breakups for both temporally isolated and continuous sequences of topological transitions suggests an interpretation for the existence of exponential growth in the leading singular spectrum. Effectively, the transient halting of the propagation of the wavefront – conduction block – can be understood as the approach of the *local configuration* of the extended state to a critical solution of (13), i.e., $\partial_t \mathbf{u} \approx \mathbf{0}$.

We seeks equilibrium solutions of (13) with appropriate boundary conditions

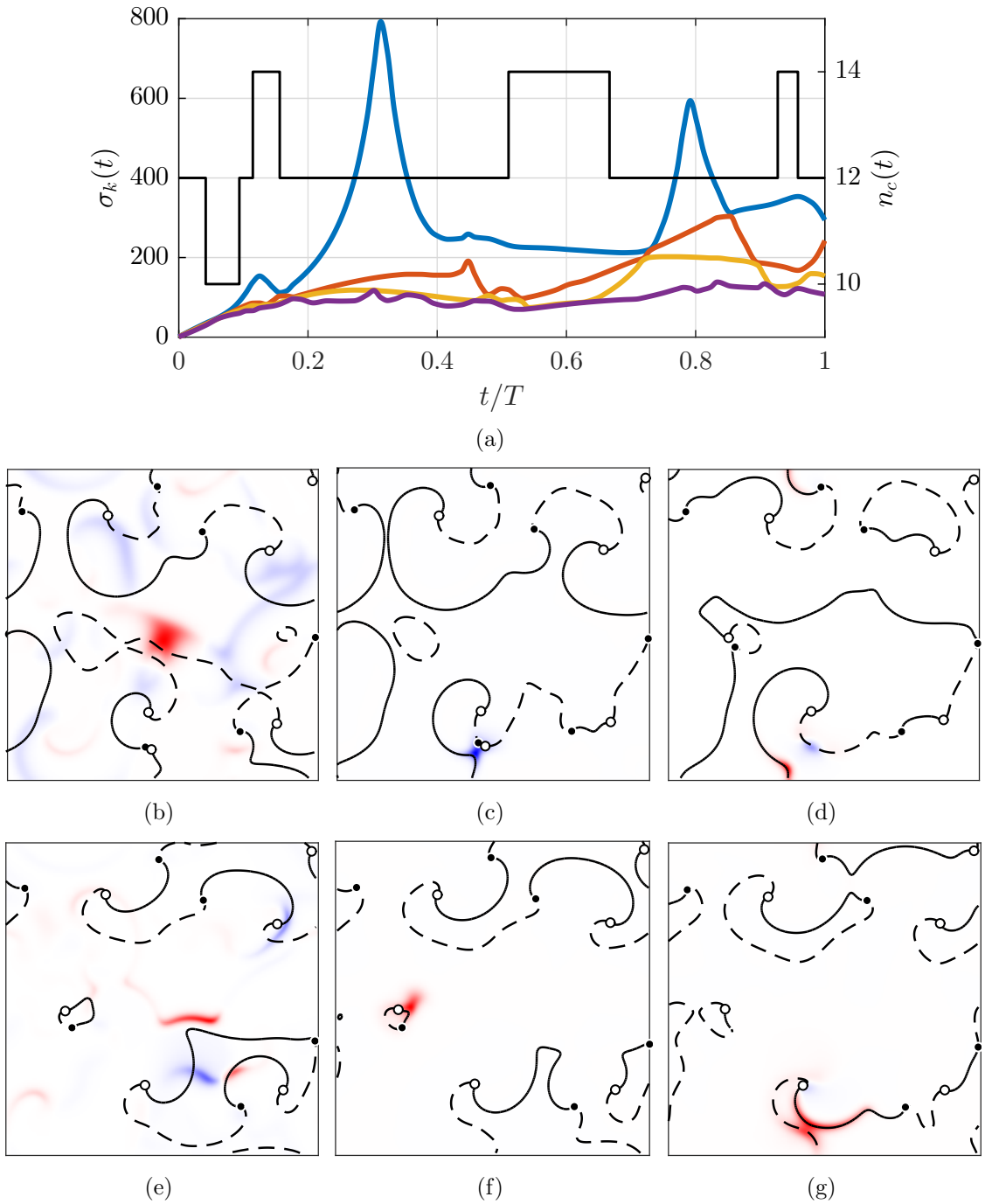

Figure 52: Leading singular values from a chaotic trajectory with many topological transitions and the number of cores (a). Panels (b-g) show the corresponding leading right singular vectors $U_1^{(1)}(t)$ at the same instants as the snapshots shown in Fig. 51, with the wavefront (solid) and the waveback (dashed) and the spiral origins (black and white dots).

which capture the behavior of the high-curvature regions of a complicated multi-spiral state, preferably including multiple spiral origins. The merger and collapse of spiral origins, and of the interaction of curvature on the propagation of the wave more generally, is an essentially two-dimensional process. However, we can make progress by considering a simplified model of the effects of curvature and foregoing any explicit constraints on the position of the spiral origins. For $\nu \to 0$, this relationship is summarized by the eikonal relation, $c = c_n - D_{11}\kappa$ [111], where c is the propagation speed of a wavefront, c_n is the normal velocity of a flat wavefront, and κ denotes the curvature of the wave. When the propagation speed is zero $c = 0$, the normal velocity intrinsic to the one-dimensional structure of the wave is balanced exactly by the curvature. In particular, we can identify a simpler state which is subject to the maximal curvature supported by the medium – the two-dimensional realization of the solution shown in Fig. 42(a) – and refer to this solution as the critical bump solution for this model in two spatial dimensions.

The appropriate boundary conditions for the critical bump solution are no-flux, applied at the origin and at infinity. Interpreted in the context of the states shown in Fig. 51, we are considering the features of the state in the absence of external forcing. Explicitly, the critical bump solution is an equilibrium solution of (13) satisfying

$$\mathbf{0} = D\partial_r^2\mathbf{u} + Dr^{-1}\partial_r\mathbf{u} + Dr^{-2}\partial_\theta^2\mathbf{u} + \mathbf{f}(\mathbf{u}), \tag{94}$$

written in polar coordinates for $\mathbf{u} = \mathbf{u}(r, \theta)$. Solving (94) with no-flux boundary conditions at $r = 0$ and $r \to L$ (L taken to be merely large) in full generality is non-trivial, and for the type of dynamics we are trying to explain, it is unclear that the full system is a helpful model. In particular, while we can immediately identify the term $Dr^{-1}\partial_r\mathbf{u}$ with the contribution of curvature, the harmonic term $Dr^{-2}\partial_\theta^2\mathbf{u}$ is related to the angular variation of the state and identifies the position of the spiral origins. Since we should not expect static solutions *with spiral origins in close proximity*, we shall drop the contribution from this term.

Consider the simplified system, rescaled with $x = r/L$ for finite L,

$$0 = (D_{11}/L^2)u_1'' + x^{-1}(D_{11}/L^2)u_1' + f_1(\mathbf{u}), \tag{95}$$

$$0 = (\nu D_{11}/L^2)u_2'' + x^{-1}(\nu D_{11}/L^2)u_2' + f_2(\mathbf{u}), \tag{96}$$

where $u' = \mathrm{d}u(x)/\mathrm{d}x$. It is easy to show that, for $L \sim \epsilon^{-1/2}$, $|f_2(\mathbf{u})| \sim O(\epsilon) \gg \nu D_{11}/L^2$, which suggests neglecting the spatial variation of the slow variable entirely. We reduce the slow variable conditions to an additional boundary condition, $f_2(\mathbf{u}) = 0$. In this moment, there are several undetermined parameters which are related by the nonlinear solution of the BVP: the position of the wavefront (r_c, the value of the gating variable u_2, and the radial domain length L. We choose to prescribe the value of u_2 – based on our experience with both traveling wave solutions and sustained spiral chaos in general – to the value at the third steady state solution, $u_2 = [\mathrm{EQ}_3]_2$. This constraint implicitly defines the position of the wavefront by the shape of $u_1(r)$, which itself depends on the domain size L, through the additional boundary condition derived above from the reduction of the gating variable equation.

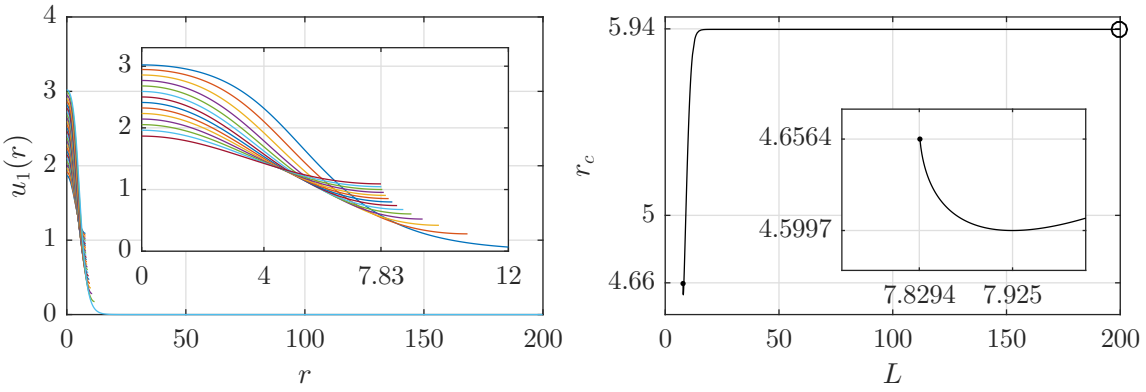

Figure 53: Continuation of the critical bump branch of solutions on successively smaller domains, showing $u_1(r)$ (a), and the position of the wavefront as a function of domain size $r_c(L)$ (b).

The critical radius $r_c(L)$ in this continuation can be estimated by computing the position of the wavefront, defined by $0 = f_2(\mathbf{u}(r_c))$, giving $4.60 \leq r_c \leq 5.94$, cf.

Fig. 53(b). This gives an estimate more consistent with the numerical results than the simpler method using the eikonal approximation, $0 = c_n - D_{11}/r_c$, for which $r_c \approx 2.8$ when using the normal velocity of a very large spiral wave ($c_n \approx 1.44$), which is quite small and is even smaller if instead the speed of large traveling wave solutions is used, cf. Fig. 7(b). From two-dimensional simulations, the minimal inter-core spacing determines the upper bound for the critical radius, which is $r_c \leq \bar{r}_c = 8$, very similar to the result from the continuation.

Checking the assumption, $\nu D_{11}/L_c^2 \approx 0.32\epsilon$, so we are confident in the simplification made to the fully realized system for $L \geq 12$, and less so for the smallest domain sizes considered here. It is important to recognize that the solutions of (95) (with or without r-dependence of u_2) can not capture the presence of spiral origins, since these require the intersection of curves in a two-dimensional space. We have attempted the numerical solution of the more complete boundary value problem (95) including the spatial variation of the gating variable, $u_2 \to u_2(r)$, but the results could not be made to converge. In principle, the original formulation (94) can capture high-curvature dynamics and the interaction with spiral origins in more realistic scenarios through the harmonic term.

6.5 Chaotic spacing

Finally, the shape of the adjoint eigenfunctions of single-spiral solutions has implications for the distribution of spirals in multi-spiral chaotic dynamics. Given two structurally coherent spirals on a large domain, their interaction is determined primarily by the inter-core distance, d, through the decay of their adjoint eigenfunctions, cf. Ch. 4. When these two spirals are far apart (compared to the decay scale of the most unstable adjoint eigenfunctions) then they may be considered as essentially independent. The extremes of spiral core density within a domain are neatly delineated by the first stable root of the drift map ζ_0, or pairwise distances of $d = 2\zeta_0$.

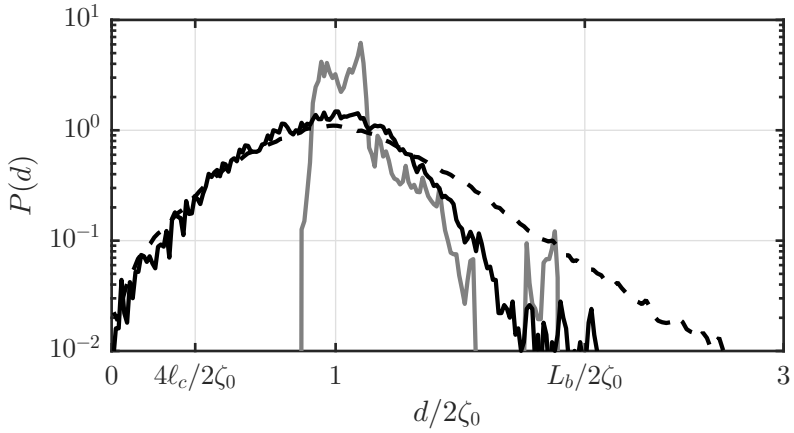

Figure 54: Probability distribution of pairwise distances $P(d)$ from a long trajectory of spiral chaos with no-flux boundary conditions (dashed), periodic boundary conditions (solid), and from a long topologically stable trajectory (grey), with minimal tile size $L_0 \approx 4\ell_c$ and meander-alternans transition tile size $L_b \approx \lambda$.

Given an unbounded multi-spiral state, the set of inter-core distances is defined by $d_{ij}(t) = |\mathbf{x}_{o,i}(t) - \mathbf{x}_{o,j}(t)|$ for all $i \neq j$. Over time-scales much longer than the periodicity of the multi-spiral state, the configuration of spirals changes and the inter-core distances similarly adapt. For a representative set of states (i.e., a long trajectory exhibiting sustained spiral chaos), the distribution of relative distances of spiral cores can be computed. This describes the probability of detecting at any given instant a spiral core within a finite distance d of another by the probability distribution function, $P(d)$, such that $\int_0^\infty \mathrm{d}d\, P(d) \equiv 1$. Approximating this distribution numerically is, implicitly, dependent on the size of the domain on which the sampling states were computed.

Tracking the closest pairwise distances between spiral tips in a long trajectory exhibiting sustained spiral chaos indicates that the asymptotic dynamics favor spacings $d \approx 2\zeta_0$, c.f., Figure 54 (dashed black curve) for domains with side-length $L \gg 2\zeta_0$. The probability distribution function $P(d)$ falls off exponentially for larger and smaller distances than $d = 2\zeta_0$ indicating that this peak is strong over a range of dynamically relevant multi-spiral configurations. The turbulent trajectory was

simulated on a bounded domain of side-length $L = 192$ with no-flux boundary conditions $\hat{\mathbf{n}} \cdot D\nabla\mathbf{u} = \mathbf{0}$. The same domain and boundary conditions are used for a very long ($\tau > 2^{12}T$) topologically stable trajectory (grey curve). The effect of the boundary conditions on the shape of the distribution is somewhat subtle: on a periodic domain the long tail ($d \gg 2\zeta_0$) is suppressed. The suppression of very distant nearest-neighbors is because the largest accessible inter-core spacing on the same length-L periodic domain is smaller than the largest accessible inter-core spacing on a no-flux domain due to the topological constraint. Effectively, as there must always be a chirally-matched pair on the periodic domain, the furthest these cores may be is $d = L/\sqrt{2}$, as opposed to an isolated spiral matched with it's mirror image across the boundary, which corresponds to maximal distance $d = \sqrt{2}L$. Thus, on a periodic domain, the maximal accessible distance is precisely $1/2$ the maximal distance available on a no-flux domain of the same size (solid black curve).

However, pairs of opposing-chirality phase-locked spirals at a separation distance d correspond to the case of a single-spiral interacting with its image across a no-flux boundary, and is analogous to a single-spiral centered on a domain of side-length $L = d$. As $\zeta_0 \approx \lambda/4$, the domain size for a position-stable, centered, single-spiral is $L \approx \lambda/2$. For domains of these sizes, the leading unstable mode generates a growing meander of the spiral origin, distinguished from alternans when $L \gtrsim \lambda$. Interestingly, the leading right eigenfunction does not modify its shape significantly in the transition from alternans ($L > \lambda$) to core meander ($L < \lambda$). This suggests that the core meander and alternans instabilities in this cardiac model are largely distinguished by the saturation of the instability mode. For domains $L \approx 2\zeta_1$, direct numerical simulation indicates that the centered single-spiral state ultimately returns to quiescence due to the growth of core meander, cf. Ch. 3.

Roots of the forcing function describing radial drift – essentially the projection of a localized heterogeneity onto the response functions – were used to explain the orbiting

behavior of stable spirals in Ref. [24]. Orbits of different radii and alternating stability were predicted from the forcing functions and observed numerically. Furthermore, Ref. [6] gives an analytical prediction for the equilibrium distance between two bound vortex cores in the complex Ginzburg-Landau equation (CGLE) – for which small vortices are stable, unlike the present model – which correspond to roots of a periodic function, which agrees qualitatively with the structure of the roots of the drift map in our results, c.f. Fig. 33(b). The interaction strength was found to scale exponentially (again, similarly to the present model) in both the oscillatory and monotonic regimes of the CGLE. It was shown that in one dimension, the equilibrium distances between sources and sinks of the CGLE is similarly fixed [156].

6.6 Summary and discussion

We have investigated the construction of one-dimensional representations of the wavefront and waveback in a simple model of excitable tissue which reproduces the qualitative instabilities thought to be responsible for fibrillation. This naturally leads to a simple construction of the spiral origin, which gives an exact computation of the rotational origin for relative equilibria, and robustly detects the topological features of even highly complicated multi-spiral states. From the spiral origins, we are able to characterize topological transitions in chaotic trajectories. Choosing representative examples of isolated transitions, both breakups and mergers, we are able to compute the local stretching of linear neighborhoods of trajectories making use of a finite-dimensional truncation of the tangent evolution.

We found that topological transitions, the breakup and merger of spiral cores, are not the dominant generative source of chaotic stretching in sustained spiral chaos, in isolation. Rather, transitions may or may not show temporally localized exponential growth, and the presence of high-curvature dynamics is a likely candidate for the underlying feature leading to these spikes in sensitivity. We illustrated the impact

high-curvature regions have on the propagation of excitation by computing equilibria of a simplified boundary value problem, and showed that it gives predictions for the critical radius of curvature for which the propagation halts which is consistent with both the direct numerical simulation and eikonal prediction. More detailed models of the shape of critically-curved states requires further exploration. That said, we expect the techniques presented in this work to be an effective toolset for further study of these kinds of dynamics.

CHAPTER VII

CONCLUSION

The central motivation of this thesis is a better understanding of sustained spiral chaos, especially in the context of atrial fibrillation, and a description of this regime using the language of dynamical systems. Particularly, we sought to understand the transition from simple arrhythmias (i.e., tachycardia) to complex arrhythmias (fibrillation), and the mechanisms which sustain spatiotemporal chaos in cardiac systems and specifically the state of fibrillation. Of principle curiosity, at least from the perspective of dynamical systems and specifically similar efforts in instances of fluid turbulence, is what kinds of non-chaotic solutions underlie the state of spiral chaos.

The identification of single-spiral states with tachycardia demands that we understand the composition of spirals into sustained spiral chaos, alternatively the decomposition of sustained spiral chaos into single-spiral states. The expression and persistence of local Euclidean symmetry is the key to such a transformation – it enables, on the one hand, the interpretation of the dynamics of sustained spiral chaos in terms of the individual interactions of the coherent structures of the state, and contextualizes the detailed properties of the isolated structures to the asymptotic regime of spatiotemporal chaos. It is well known that smaller spirals rotate more frequently than larger ones, as is essential for their growth, but the mere fact that the periods are different with the persistence of local symmetry immediately suggests that the fundamental structure underlying recurrent multi-spiral states corresponds to dynamical tori – quasi-periodic solutions. In particular, the composition of multiple interacting spiral waves to describe spiral wave chaos leads to a natural interpretation of the regime itself: sustained spiral wave chaos is the extensive dynamics of several

competing routes between exact solutions.

The instabilities of single-spiral solutions can be used to understand the sustaining mechanisms of spiral chaos. Specifically, single-spiral states are absolutely unstable and in finite time perturbations to the spiral will develop into variations in the width and timing of the excitation wave, eventually causing the propagation to fail. Unexpectedly, the same instability manifests differently for spirals of different sizes, such that large spiral waves generates new spiral waves, while small spiral waves lead to the termination of the excitation. Once the dynamics has progressed to atrial fibrillation – nominally featuring continual breakups and mergers of excitation waves – what can be said about this regime form our detailed understanding of single-spiral states? We found that the combination of breakup and mergers for differently sized spirals leads to a self-sustaining process which maintains the state of spiral chaos, and in particular, this naturally features spiral waves of sizes ranging from a minimal size (determined by the scaling of the adjoint eigenfunctions) up to a width of approximately one wavelength.

The sensitivities of individual spiral waves can be interpreted for the state of sustained spiral chaos, and in particular, be used to understand the interactions between the spiral waves within that state – taking the wave-particle duality of the spiral wave features to the natural conclusion. The adjoint eigenfunctions of single-spiral solutions not only describe the persistence of local Euclidean symmetry, but provide a framework to predict the effect of weakly breaking those symmetries through the presence of boundaries. In the context of sustained spiral chaos this framework naturally encompasses more general interactions, and predicts the relative structure of features within the asymptotic regime of sustained spiral chaos.

One significant development arising from the work in this thesis is the development of numerical codes relating to the simulation of cardiac models and to the solution of exact solutions of these models in the presence of symmetry. Some of these codes

efficiently and accurately solve time-dependent highly stiff reaction-diffusion models of cardiac excitation using massively parallel graphics processing units (GPU) with a variety of boundary conditions. These codes are distinguished from the usual methods used predominantly in the field in that the parallelism of the GPU was exploited to speed up exceptionally accurate evaluation of the evolution equations, rather than aim for real-time computation at the expense of accuracy. We similarly implemented highly accurate methods to explicitly compute the forward and adjoint linearization of these models. The forward linearization in particular was used in the development of a specially adapted Newton-Krylov solver designed to compute exact solutions (i.e., relative equilibria, periodic orbits, and relative periodic orbits) of the underlying PDE model in the presence of multiple symmetries – whether discrete or continuous – and in particular, when those symmetries are weakly broken by the presence of boundaries. The same linearization codes were used to accurately determine the leading hundred or so Floquet eigenfunctions and Floquet multipliers of the time-dependent exact solutions.

Symmetries, and more precisely the manifestation of local symmetries, played a central role throughout our investigations. We have used the computational tools above to perform detailed continuations of unstable spiral wave solutions, characterize their stability, investigate their sensitivities, and synthesize these solutions into more complicated states. More importantly than these detailed calculations, however, are the shortcomings of the transference of this program from fluid turbulence to spatiotemporal chaos exhibited by excitable systems. In particular, local symmetry destroys the correlations of disparate physical regions featuring distinct coherent structures within a state, and this similarly destroys irregular exact solutions featuring multiple coherent structures.

This work has not exhaustively addressed the existence of non-chaotic multi-spiral solutions in this simple model of atrial fibrillation. Indeed, while all periodic solutions

featuring more than one spiral core only exists within a specific parameter range for which the spiral cores are pinned to the underlying lattice. Pinning the spiral cores to the underlying lattice breaks the local translational degrees of freedom for each spiral core, and thus prevents all relative motion of the set of cores. While pinning of the spiral cores to the lattice is of potential relevance for physical tissue, it is clearly not a justifiable prerequisite for nominally continuous models of atrial excitation, and thus these simple exact multi-spiral states are of limited relevance for a description of spatiotemporal chaos based on exactly periodic solutions. Furthermore, these solutions either feature densely spaced spirals in a highly symmetric configuration, or sparsely spaced spirals in an asymmetric configuration. The specificity of discrete symmetries for these exact solutions is non-generic for sustained spiral chaos – as is sparse configurations of multiple spirals as this definitionally suppresses spiral core interactions. We have, however, found a very weakly unstable multi-spiral state which persists indefinitely, features multiple spiral waves in an asymmetric configuration, and showed that solutions in the neighborhood are not strongly repulsed on time-scales comparable to multiples of the periodicity of the state. Fundamentally, this state is interesting in its own right but ultimately says very little about sustained spiral chaos as an unending sequence of topological transitions. Why this state persists for so long – indeed, why any topologically stable states should persist for long times – remains an open question.

The fundamental conclusions of this research program concern the persistence of Euclidean symmetries on bounded domains, and the importance of these symmetries for exact solutions of cardiac-centric excitation models exhibiting spiral chaos. We have explored their relevance and persistence for single-spiral solutions, and similarly shown their catastrophic influence on temporally recurrent multi-spiral states. We have not, however, explained why similar configurations of coherent structures in fluid turbulence do not exhibit the phenomenon of persistent local symmetry. One

theory suggests that this is simply a matter of disparate scales. Spiral cores are much smaller than the equilibrium spacing of spiral waves, and thus multi-spiral dynamics should scale rather differently than fluid turbulence, for which no such "particle-wave" description exists. Alternatively, it may be a feature of the idealized formulation of the monodomain model as distinct from mathematical descriptions of fluids. Namely the incompressibility condition, equivalently the pressure field, in fluid dynamics evolution equations which correlates spatially disparate features of the fluid has no analogue in the monodomain equation. The natural question is this: can a similar constraint be formulated for cardiac-oriented reaction-diffusion systems, to augment equation (13), and effectively suppress persistent local symmetries?

The most natural analogy is with the constraint equation of the bidomain formulation of cardiac excitation dynamics. Superficially, the correspondence is complete: a constraint on the values of the transmembrane potential via the extracellular potential is similar to a constraint on the values of the fluid velocity via the pressure supported by the fluid material.

To address this correspondence numerically, we developed a reduced set of equations to solve the bidomain equations under fairly conservative assumptions. Using this set of integro-differential equations for the transmembrane potential and the ion channel gating variables, we parametrically continue from single-spiral relative periodic orbits through a singular perturbation of (13). Preliminary results (cf. A.5) from this continuation suggests that single-spiral solutions of the reduced bidomain equations still exhibit local Euclidean symmetry, distinguishing whether this phenomenon is essential, rather than an artifact from the reduced formulation, requires further consideration.

The conditions under which local Euclidean symmetry persists is not the only open topic. The dynamics of strongly interacting spiral cores, e.g. in sustained spiral chaos governed by the monodomain model, is still poorly understood. The adjoint

eigenfunctions of single-spiral solutions have helped to explain the far-field effect of perturbations on spiral waves, but the linearization is valid for inter-core distances larger than approximately twice the first stable fixed point of the shift map, the dynamically selected distance for inter-spiral spacings in turbulent states. Clearly, for two cores to approach significantly closer than this distance, the underlying state must deform significantly from the spatial composition of two regular spiral waves very near the relative periodic orbit solution. Thus the predictions computed using the adjoint eigenfunctions of an exact solution are inaccurate at best. To properly describe the dynamics of topological transitions we must consider topologically relevant orbit segments, i.e., not exact coherent structures but trajectories in their *nonlinear* neighorhood(s). We have begun this work in Ch. 6, but much remains.

Throughout this work we have utilized a Newton-Krylov solver based on Arnoldi iterations for the resolution of temporally recurrent open trajectories into exact coherent structures such as (relative) equilibria and (relative) periodic orbits. Fundamentally, this decomposition is sub-optimal because the Arnoldi algorithm assumes collocation of the tangent spaces – that the tangent space at the beginning of the trajectory coincides with the tangent space at the end of the trajectory. As temporally recurrent open trajectories have distinct states at the beginning and end points, this assumption is explicitly violated. Aesthetically, if not mathematically, it is better to use a method for constructing the truncated tangent evolution which does not assume closure under the action of the propagator, e.g., Golub-Kahan-Lanczos outlined in A.3.2. An inexact Newton solver based on this factorization is can be formulated provided both the forward- and adjoint-tangent evolution maps and indeed, several iterative linear solver methods exist which exploit both the matrix and its transpose (née adjoint) e.g., QMR [147] or adjoint-flow minimization [67]. An exhaustive consideration of different iterative methods, utilizing either the Arnoldi algorithm or a different factorization, was simply beyond the scope of this work. In A.4 we briefly

outline the construction of an iterative solver based on the singular value decomposition (SVD) which utilizes two finite-dimensional bases at the beginning and endpoints of an open trajectory corresponding to the left and right singular vectors, describe its use for refining recurrent orbit segments from direct numerical simulation into temporally periodic solutions, and discuss the potential for computing connecting orbits between two infinite-dimensional solutions with well-resolved spectra.

APPENDIX A

NUMERICAL METHODS

For arbitrary initial data, the solution of time-dependent nonlinear partial differential equations is only tractable numerically. In this section we detail the numerical methods used to compute exact coherent structures of (13), as well as those used in the construction of the time-dependent canonical and adjoint tangent propagators. This includes a description of the spatial and temporal discretizations, the implementation of the boundary conditions, and the methods used in the time-stepping of the solution defined on the discrete grid. The inexact Newton solver – in all its gory glory – is detailed in the remainder of this section, including operator factorization methods (Arnoldi and Golub-Kahan-Lanczos), globalization techniques (line-search iteration), and heuristic optimizations to the state correction arising from the solution of a small linear problem. Throughout the section, we have included relevant measures of the accuracy of these methods including the time-stepping convergence, resolution of solutions by the Newton solver, and eigenvalue iteration accuracy, and the relevance of their interplay for constructing exact coherent structures.

A.1 Discretization

For exact solutions of nonlinear evolution equations the symmetry properties of the equations are of paramount importance. As discretization generally breaks all the continuous symmetries of a system, the discretization of (13) demands careful consideration. A priori, the optimal spatial discretization of excitation waves is far from obvious. Spectral methods possess simple physical interpretation and enable efficient and accurate numerical derivatives, but suffer from slow convergence when the spatial

scales involved differ significantly, requiring a large number of modes. Finite element methods nicely abstract the discrete numerical space in favor of function spaces, but require both large investments in infrastructure to solve, and suffer from efficiency limitations in stiff systems. In this work we have settled on a finite-difference discretization of the spatial derivatives, with isotropic spatial discretization scale, ξ. In particular, we utilize a nine-point stencil in two spatial dimensions for the discrete approximation of the Laplacian operator,

$$\tilde{\nabla}^2 u(x,y) \equiv \sum_{i=-1}^{+1} \sum_{j=-1}^{+1} a_{ij}\, u(x+i\xi, y+j\xi) = \nabla^2 u(x,y) + O(\xi^2), \tag{97}$$

where $a_{0,\pm 1} = a_{\pm 1,0} = \eta$, $a_{\pm 1,\pm 1} = (1-\eta)/2$, and $a_{0,0} = -2(1+\eta)$, where η is a numerical parameter which corresponds to the mixing of the classical "quincunx" ($\eta = 1$) and "cross" ($\eta = 0$) stencils. For $\eta = 2/3$, this discretization represents the most isotropic formulation of the nine-point finite-difference stencil on a two-dimensional uniform grid [117], and is thus expected to most faithfully recover the rotational and translational symmetry of the original system. Additionally we utilize a five-point stencil for the first-order spatial derivatives when appropriate,

$$\tilde{\partial}_x u(x) \equiv \frac{1}{12}(u(x-2\xi) - u(x+2\xi)) + \frac{2}{3}(u(x+\xi) - u(x-\xi)) = \partial_x u(x) + O(\xi^4). \tag{98}$$

On the boundaries, we utilize the "ghost-point" method, and map samples outside the numerical domain to mirrored positions within the domain.

The finite-difference discretization is additionally justified by the underlying structure of the cardiac tissue itself. Cardiac tissue is made up of muscle fibers which are, in turn, made up of cardiomyocytes. This structure breaks, perhaps weakly, the rotational symmetry of the system. Hence, even though the choice of coordinate directions in the original PDE (13) is arbitrary, the structure of the tissue imposes a natural choice on the coordinate directions. To be specific, we will assume that the x and y axes are oriented along and transverse to the fibers, respectively.

Table 4: Butcher tableau for a general fully-explicit N-th order Runge-Kutta method with N function evaluations.

0				
c_2	a_{21}			
c_3	0	a_{32}		
$\vdots$	$\vdots$	$\vdots$	$\ddots$	
c_N	0	0	$\dots$	$a_{N,N-1}$
	b_1	b_2	$\dots$	b_N

A.2 Time-stepping

The general form of any Runge-Kutta time-stepping method for a state y with fixed time-step h subject to dynamical law $\mathrm{d}y/\mathrm{d}t = f(t, y)$ is given by,

$$y_{n+1} = y_n + h \sum_{i=1}^{N} b_i k_i, \tag{99}$$

$$k_i = f\left(t_n + c_i h, y_n + h \sum_{j=1}^{i-1} a_{i,j} k_j\right), \tag{100}$$

for the solution at discrete times $y_n \equiv y(t_0 + nh)$, $t_0 \in \mathbb{R}$ arbitrary and $n \geq 0$ an integer. As this numerical method is to be applied to a PDE, Equation (13), we introduce the additional requirement that the prefactors be strictly non-negative, $a_{ij} \geq 0$. This effectively guarantees that the diffusive term in (13) always has a positive prefactor, and never drives the system. Additionally, as the PDEs are large systems, solving an implicit method on every time-step is infeasible, thus we restrict ourselves to fully explicit methods, whose general Butcher tableau are shown in Table 4.

Some minimal values for the number of function evaluations N for a $O(h^{p+1})$ local truncation error method are known [45]. In particular, for $p > 5$, $N > p$, while for $p < 5$, $N \geq p$, so for sufficiently high-order methods, Runge-Kutta methods become less efficient. In this work we are restricted to four particular methods, summarized in Table 5, with global truncation errors of $O(h^1)$, $O(h^2)$, $O(h^3)$, and $O(h^4)$, for fixed time-step $h = T/n$, $T \in \mathbb{R}$ and $n \in \mathbb{N}$,

Table 5: Butcher Tableau for explicit non-negative Runge-Kutta methods of global orders $O(h^1)$, $O(h^2)$, $O(h^3)$, and $O(h^4)$.

Euler:

0	
	1

Heun:

0		
1	1	
	1/2	1/2

Bogacki-Shampine:

0			
1/2	1/2		
3/4	0	3/4	
	2/9	3/9	4/9

RK4:

0				
1/2	1/2			
1/2	0	1/2		
1	0	0	1	
	1/6	1/3	1/3	1/6

A.2.1 Interpolation for Runge-Kutta methods

While the forward nonlinear model and the forward tangent linearization are temporally collocated, in that the map for both sets of functions at time t_{n+1} requires only knowledge of their values at time t_n, computing the adjoint tangent linearization is more subtle. The right eigenfunctions of the time-evolution operator $\mathcal{V}_T$ have been computed via Arnoldi iteration [8] which involves time-integration of the linearized equations (34). It should be pointed out that, since the instantaneous Jacobian $\mathcal{L}$ is a function of the reference state $\mathbf{u}(t)$, both (13) and (34) are time-integrated simultaneously to avoid storing and retrieving the reference solution. The same spatial (2nd order finite difference on a square mesh) and temporal (4th order fully explicit Runge-Kutta) discretization scheme is used for both equations Ch. 3.

However, the same approach cannot be used to compute the left eigenfunctions, since (49) should be integrated backwards in time and (13) cannot be time-integrated in the reverse direction. Furthermore, as the evolution equation is quite stiff, fairly small time steps have to be used ($O(10^4)$ time steps per period). One period of a fully resolved solution corresponds to about 8 GB of data, which may not fit in RAM. Hence, the entire reference solution $\mathbf{u}(t)$ must be pre-computed, stored, and

then retrieved during the time-integration of (49).

The spatial discretization and the time-stepping of the adjoint tangent evolution (35) are the same as those for (13) and (34). This choice was made out of necessity: the discrete adjoint of an explicit Runge-Kutta method is at least semi-implicit [92, 154]. For a partial-differential equation, this requires solution of an infeasibly large linear system at every time step. Furthermore, the discretization of (35) is sufficiently precise that the solution of the large linear system is unnecessary.

Runge-Kutta integrators for (35) require evaluation of $\mathbf{u}(t)$ at intermediate points between the time steps, while the solution $\mathbf{u}^n = \mathbf{u}(t_n)$ is only known at discrete times $t_n = n\Delta t$. To preserve the accuracy of time-integration of (35), we use a high-order interpolation of $\mathbf{u}(t)$. That is, for an integrator of order $O(\Delta t^p)$, we use an interpolant uniformly accurate on the interval $t \in [t_n, t_{n+1}]$ to order $O(\Delta t^q)$, with $q \geq p$. Following the methodology of Enright *et. al.* [66], the $O(\Delta t^4)$ interpolant for the classical Runge-Kutta method used in this work is

$$\begin{aligned} \mathbf{u}_4(t+\tau\Delta t) = {} & d_{4,0}(\tau)\mathbf{u}^n + d_{4,1}(\tau)\mathbf{u}^{n+1} \\ & + d_{4,2}(\tau)\partial_t\mathbf{u}^n\Delta t + d_{4,3}(\tau)\partial_t\mathbf{u}^{n+1}\Delta t \\ & + d_{4,4}(\tau)\partial_t\mathbf{u}_3(t+\eta\Delta t)\Delta t \ + O(\Delta t^5), \end{aligned} \tag{101}$$

where $\mathbf{u}_3(t+\eta\Delta t)$ is the value of the $O(\Delta t^3)$ interpolated state at time $t_n + \eta\Delta t$, which has $\eta = 1/3$. The coefficients for the fourth order interpolant are

$$\begin{aligned} d_{4,0}(\tau) &= 1 + 6\tau^2 - 16\tau^3 + 9\tau^4, \\ d_{4,2}(\tau) &= \tau - 2\tau^2 + \tau^3, \\ d_{4,3}(\tau) &= \left(5\tau^2 - 14\tau^3 + 9\tau^4\right)/4, \\ d_{4,4}(\tau) &= 27\left(\tau^2 - 2\tau^3 + \tau^4\right)/4, \end{aligned} \tag{102}$$

where $d_{4,1}(\tau) = 1 - d_{4,0}(\tau)$. Due to interpolation, it takes roughly twice as long to integrate the adjoint evolution equation (35) compared with the tangent evolution

equation (34) (e.g., 31 hours vs. 70 hours to compute the spectra shown in Fig. 55 on a single NVIDIA Tesla K20 GPU).

While the accuracy of the nonlinear map $\mathcal{U}_T$ and forward-tangent evolution map $\mathcal{V}_T$ can be assessed using the typical methods of convergence analysis, the tools available to verify the accuracy of the adjoint tangent evolution $\mathcal{V}_T^\dagger$ are limited. The accuracy of the backwards time integration can not be assessed in the typical way by increasing the temporal and spatial resolution of the discretization of (35) since these are set by the discretization of the nonlinear equation (13), and thus can not be modified independently of the forward-time solution. However, there are two independent parameters which we can vary: the order p of the interpolation method and the order q of the integration scheme used for the adjoint time-stepping. Our results suggest that the error in computing the adjoints is dominated by the interpolation order when $q \leq 3$, with significant increases in accuracy when both $q = 4$ and $p = 4$. As discussed below, the reliability of the adjoint tangent evolution may be indirectly measured either by the magnitude of the inner product (36) for $i \neq j$ or by the difference between the eigenvalues Λ_i of H_k and the eigenvalues Λ'_i of H'_k. As Fig. 55 illustrates, a 256-dimensional Krylov subspace allows computing $\sim$130 leading modes with high accuracy. More generally, a k-dimensional Krylov subspace allows accurate determination of up to $k/2$ modes with the relative error $|\Lambda' - \Lambda|/|\Lambda| = O(10^{-10})$.

As the computation of the left and right eigenfunctions involves two distinct matrices representing compact truncations of the formally infinite-dimensional evolution operator and its adjoint, there is some ambiguity in matching these two sets of eigenfunctions. The eigenfunctions can be matched based on the closeness of the associated eigenvalues, which is the choice made in the present paper. The right eigenvalues are ordered by their absolute value, from the largest to the smallest $|\Lambda_1| \geq |\Lambda_2| \geq \cdots \geq |\Lambda_k|$. Each right eigenvalue Λ_i and the corresponding eigenfunction $\mathbf{v}^i$ is then paired with the left eigenvalue Λ'_j and eigenfunction $\mathbf{w}^j$, such that

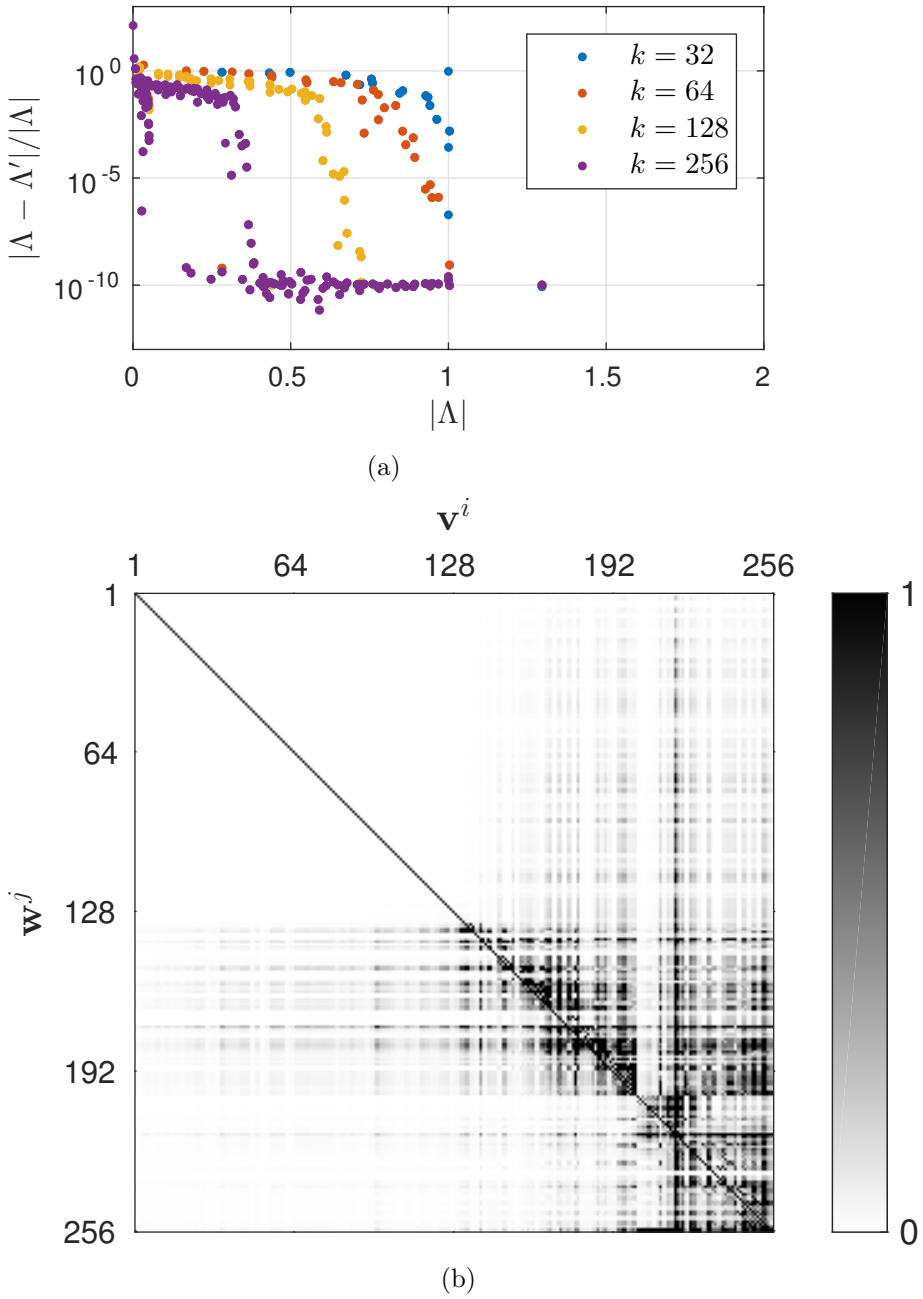

Figure 55: (a) Relative eigenvalue deviations $|\Lambda - \Lambda'|/|\Lambda|$ from the leading k-dimensional Krylov subspace. (b) The inner product of the leading set of left ($\mathbf{w}^j$) and right ($\mathbf{v}^i$) eigenfunctions.

$j \geq i$ corresponds to the smallest value of $|\Lambda'_j - \Lambda_i|$. This matching procedure makes no assumption regarding the orthogonality between the two eigenfunction sets, so the condition (36) can be used to check the accuracy with which the eigenfunctions have been computed.

Alternatively, the eigenfunctions can be matched based on the orthogonality relation (36). In this case each left eigenfunction $\mathbf{w}^i$ and the corresponding left eigenvalue Λ'_i is matched with the right eigenfunction $\mathbf{v}^j$ and eigenvalue Λ_j, such that $j \geq i$ corresponds to the largest value of the inner product $\langle \mathbf{w}^i | \mathbf{v}^j \rangle$, where both sets have been independently normalized to unity, beforehand. This procedure has the benefit of most closely reproducing the orthogonality condition (36). The differences $|\Lambda_i - \Lambda'_i|$ can be used to assess the accuracy with which the eigenvalues have been computed. Both methods of matching the right and left sets yield the same results for the resolved eigenmodes (that is, those which are effectively captured by a sufficiently large Krylov space, or the leading $k/2$ modes in the $k = 256$-dimensional space).

A.2.2 Operator-splitting methods

The generic form of Equation (13) is rather simple,

$$\partial_t \mathbf{u}(t, \mathbf{x}) = \mathcal{L}\mathbf{u}(t, \mathbf{x}) + \mathcal{N}[\mathbf{u}(t, \mathbf{x})], \tag{103}$$

where $\mathcal{L}$ is a linear differential operator of the spatial coordinates and $\mathcal{N}$ is a nonlinear operator of the field itself. This class of equations naturally lends themselves to operator-splitting methods. These methods entail solving a series of coupled subproblems in which each only involves a subset of the full complexity of the original equation. The simplest method of this type is referred to as Lie splitting [9], and has recombination error of $O(h^1)$, where h is the time-step. Provided an initial condition $\mathbf{u}(0, \mathbf{x}) = \mathbf{u}_0$,

$$\mathbf{u}_{n+1/2} = (1 + h\mathcal{L})\mathbf{u}_n, \quad \mathbf{u}_{n+1} = \mathbf{u}_{n+1/2} + h\mathcal{N}[\mathbf{u}_{n+1/2}]. \tag{104}$$

A second order method $O(h^2)$ is known as Strang splitting [160],

$$\mathbf{u}_{n+1/3} = (1 + h\mathcal{L}/2)\mathbf{u}_n, \tag{105}$$

$$\mathbf{u}_{n+2/3} = \mathbf{u}_{n+1/3} + h\mathcal{F}\left\{\mathcal{N}[\mathbf{u}_{1/3}]\right\}, \tag{106}$$

$$\mathbf{u}_{n+1} = (1 + h\mathcal{L}/2)\mathbf{u}_{n+2/3}, \tag{107}$$

assuming $\mathcal{F}\{\cdot\}$ is at least second-order, the entire method will have global truncation error $O(h^2)$, as well. As written, neither the Lie- nor Strang-splitting methods are competitive with the explicit Runge-Kutta methods of order $O(h^1)$ or $O(h^2)$. Typically, these methods are used in conjunction with a spectral representation of the fields, especially Fourier, $\mathbf{u}(t, \mathbf{x}) = \int \mathrm{d}\mathbf{q}\, \mathrm{e}^{\mathrm{i}\mathbf{q}\cdot\mathbf{x}}\, \mathbf{U}(t, \mathbf{q})$. As the differential operator $\mathcal{L}$ diagonalizes in the Fourier basis, it is trivial to solve the linear part of Equation (103) exactly using exponentiation.

A.3 Operator factorization

Given a particular orbit, it is not feasible to form the finite-time Jacobian, $\mathcal{V}_T$ explicitly. In practice, it is better to work with a finite-dimensional truncation by iteratively constructing a factorization of the operator. We make use of one of two factorizations of a generic operator $\mathcal{A}$ (e.g., $\mathcal{V}_T$ or $\mathcal{V}_T^\dagger$, in practice), depending on the structure of the underlying solution. For periodic or relative periodic solutions, the beginning and end points of the orbit are collocated, and the natural decomposition uses a single basis shared for the beginning and end tangent spaces,

$$\mathcal{A}V_k = V_{k+1}E_{k+1}\Lambda_{k+1}. \tag{108}$$

The matrix V_k denotes the $N \times k$ Krylov orthonormal basis, E_k denotes the $k \times k$ matrix of eigenvectors expressed in the Krylov basis, and Λ_k is the diagonal matrix of complex-valued eigenvalues associated with the eigenfunctions of the operator $\mathcal{A}$. The parameter N reflects the dimensionality of the underlying system, whether $N = \infty$ in the case of an infinite-dimensional dynamical system or N merely large, as results

from the discretization of a set of partial differential equations. When the beginning and end points of an orbit are not collocated, the proper description is in terms of the singular triplets,

$$\mathcal{A}V_k = U_{k+1}S_k, \quad \mathcal{A}^\dagger U_{k+1} = V_k S_k. \tag{109}$$

The matrices V_k, U_k and S_k are the usual singular triplet pairs, with the orthonormal left $V_k^\top V_k = \mathbf{1}_k$, and orthonormal right $U_k^\top U_k = \mathbf{1}_k$ singular vectors, and S_k is the diagonal matrix of non-negative real-valued singular values $S_{jj} \geq 0$.

A.3.1 Arnoldi algorithm

For (relative) periodic orbits the stability of the solution is encoded by the eigenvalues of the tangent evolution operator, $\mathcal{V}_T$, or $\mathcal{G}_\theta\mathcal{V}_T$, respectively. In either case, the beginning and end points of the orbit can be made to coincide. This algorithm describes a simple implementation of the Arnoldi method for a general operator $\mathcal{A}$. This procedure generates a linearly independent set of vectors which span the leading subspace of $\mathcal{A}$, $V_k \in \{V_1, \mathcal{A}V_1, \ldots, \mathcal{A}^{k-1}V_1\}$. Factoring $\mathcal{A}$ into the product of an $N \times (k+1)$ basis V_{k+1} and the finite-dimensional truncation of the operator in that basis, the upper-Hessenberg $(k+1) \times k$ matrix H_{k+1}, this presents a simple method for computing the eigenvalues and eigenvectors of the operator $\mathcal{A}$.

Given $\hat{\mathbf{v}}_1$, $k = 1$;
while $k \geq 1$ *and* $|h_{k+1,k}| > \epsilon$ **do**
  $\mathbf{v}_{k+1} = \mathcal{A}\hat{\mathbf{v}}_k$.
  for $j = 1 \ldots k$, **do**
    $h_{j,k} = \hat{\mathbf{v}}_j^\dagger \mathbf{v}_k$;
    $\mathbf{v}_k = \mathbf{v}_k - h_{j,k}\hat{\mathbf{v}}_j$;
  end
  $h_{k+1,k} = \|\mathbf{v}_k\|$;
  $\hat{\mathbf{v}}_{k+1} = \mathbf{v}_{k+1}/h_{k+1,k}$;
end

Algorithm 1: A simple implementation of the Arnoldi method for constructing a spectral factorization of an operator $\mathcal{A}$.

By computing the eigenvalues (Λ) and eigenvectors ($\tilde{E}$) of the comparatively

smaller matrix $H_{k+1} = \tilde{E}\Lambda$, the leading eigenfunctions (E) of the operator $\mathcal{A}$ can be approximated by projection onto the Arnoldi basis,

$$\mathcal{A}E = \mathcal{A}V_k\tilde{E} = V_{k+1}\tilde{E}\Lambda = E\Lambda. \tag{110}$$

Applying the Arnoldi algorithm to the tangent evolution operator, $\mathcal{V}_T$, for a periodic solution generates the Floquet multipliers Λ and Floquet eigenfunctions $\mathbf{v}(t, \mathbf{x})$, which satisfy,

$$\mathcal{V}_T\mathbf{v}^i(0, \mathbf{x}) = \Lambda_i\mathbf{v}^i(0, \mathbf{x}) = \mathbf{v}^i(T, \mathbf{x}). \tag{111}$$

A.3.2 Golub-Kahan-Lanczos algorithm

For open trajectories the beginning and end points do not coincide, and thus it is natural to construct bases at both the origin and termination points. More generally, we construct a right and left basis set for the factorization of the operator, $\mathcal{A}$.

Given $\hat{\mathbf{q}}_1$, $k = 1$;
while $k \geq 1$ *and* $|\beta_k| > \epsilon$ *and* $|\alpha_k| > \epsilon$ **do**
  $\mathbf{p}_k = \mathcal{A}\hat{\mathbf{q}}_k - \beta_{k-1}\hat{\mathbf{p}}_{k-1}$.
  $\alpha_k = \|\mathbf{p}_k\|$;
  $\hat{\mathbf{p}}_k = \mathbf{p}_k/\alpha_k$;
  $\mathbf{q}_{k+1} = \mathcal{A}^\dagger\hat{\mathbf{p}}_k - \alpha_k\hat{\mathbf{q}}_k$;
  $\beta_k = \|\mathbf{q}_{k+1}\|$;
  $\hat{\mathbf{q}}_{k+1} = \mathbf{q}_{k+1}/\beta_k$;
end

Algorithm 2: A simple implementation of the Golub-Kahan-Lanczos method for constructing a factorization of an operator $\mathcal{A}$.

A.4 Newton-Krylov solver

We are primarily interested in temporally recurrent solutions of Equation (13), up to symmetry transformations $g \in G = E^+ \times E(d)$, for a d-dimensional space. These are relative periodic solutions $\mathbf{z} = (\mathbf{u}, \mathbf{h}, T) \in \mathbb{R}^{N+d+1}$, which corresponds to roots of the function $\mathbf{F}(\mathbf{z}) : \mathbb{R}^{N+d+1} \to \mathbb{R}^N$ where,

$$\mathbf{F}(\mathbf{z}) = g\mathcal{U}_T\mathbf{u}(t, \mathbf{x}) - \mathbf{u}(t, \mathbf{x}) = \mathbf{u}(t + T, \mathbf{x} + \mathbf{h}) - \mathbf{u}(t, \mathbf{x}). \tag{112}$$

The symmetry transformations g correspond to translations and rotations of $\mathbb{R}^d$, additionally the evolution is invariant under positive shifts in time,

$$g : (t, \mathbf{x}) \to (t', \mathbf{x}') = (t + \tau, R_\phi \mathbf{x} + \mathbf{h}), \tag{113}$$

for $\tau \geq 0$. This makes the temporal origin arbitrary, and so we shall denote it by $t_0 = 0$ in the following. Expanding about an initial guess $\mathbf{z} = \mathbf{z}_0 + \delta\mathbf{z}_0$,

$$\mathbf{F}(\mathbf{z}) = \mathbf{F}(\mathbf{z}_0) + \partial_{\mathbf{z}}\mathbf{F}(\mathbf{z}_0) \cdot \delta\mathbf{z}_0 + O(\delta\mathbf{z}_0^\dagger \delta\mathbf{z}_0), \tag{114}$$

where $\partial_{\mathbf{z}}\mathbf{F}(\mathbf{z}_0) = [\partial_{\mathbf{u}}\mathbf{F}(\mathbf{z}_0), \partial_{\mathbf{h}}\mathbf{F}(\mathbf{z}_0), \partial_T\mathbf{F}(\mathbf{z}_0)]$. Evaluating the derivatives according to the form of Equation (112),

$$\partial_{\mathbf{u}}\mathbf{F}(\mathbf{z}_0) = \mathcal{V}_T - \mathbf{1}, \tag{115}$$

$$\partial_{\mathbf{h}}\mathbf{F}(\mathbf{z}_0) = \nabla\mathbf{u}(T, \mathbf{x}), \tag{116}$$

$$\partial_T\mathbf{F}(\mathbf{z}_0) = \partial_t\mathbf{u}(T, \mathbf{x}). \tag{117}$$

Equation (114) is an $(N + d + 1) \times N$ linear system for the update of the solution,

$$\partial_{\mathbf{z}}\mathbf{F}(\mathbf{z}_0) \cdot \delta\mathbf{z}_0 = -\mathbf{F}(\mathbf{z}_0), \tag{118}$$

where $\partial_{\mathbf{z}}\mathbf{F}(\mathbf{z}_0) = \mathcal{V}_T - \mathbf{1} \in \mathbb{R}^N \times \mathbb{R}^{N+d+1}$ is related to the Jacobian of the system evaluated on the state $\mathbf{z}_0$, $\mathcal{V}_T$. This requires the addition of $d+1$ additional constraints to fix origins of the symmetries, $\Phi = [\phi_{\mathbf{x}}, \phi_t]$,

$$\begin{pmatrix} \mathcal{J}(\mathbf{z}) & \nabla\mathbf{u}(T, \mathbf{x}) & \partial_t\mathbf{u}(T, \mathbf{x}) \\ \phi_{\mathbf{x}}^\dagger(\mathbf{u}) & \mathbf{0} & \mathbf{0} \\ \phi_t^\dagger(\mathbf{u}) & \mathbf{0} & 0 \end{pmatrix} \begin{pmatrix} \delta\mathbf{u} \\ \delta\mathbf{h} \\ \delta T \end{pmatrix} = - \begin{pmatrix} g\mathcal{U}_T\mathbf{u} - \mathbf{u} \\ \mathbf{0} \\ 0 \end{pmatrix}. \tag{119}$$

When the Arnoldi process is used to decompose the tangent evolution operator, $\mathcal{V}_T = \mathcal{J}(\mathbf{z}) + \mathbf{1}$, the system simplifies to the smaller $(k + d + 1) \times (k + d + 1)$ - system,

$$\begin{pmatrix} H_k & \mathbf{a}_{\mathbf{q}} \\ \mathbf{c}_{\mathbf{q}}^\dagger & 0 \end{pmatrix} \begin{pmatrix} \delta\mathbf{y} \\ \delta\mathbf{q} \end{pmatrix} = - \begin{pmatrix} \mathbf{b} \\ \mathbf{0} \end{pmatrix}, \tag{120}$$

where $\mathcal{J}(\mathbf{z})V_k = V_{k+1}H_{k+1}$, $\mathbf{c_q} = V_{k+1}^{\dagger}[\phi_{\mathbf{x}}(\mathbf{u}), \phi_t(\mathbf{u})]$, $\mathbf{a_q} = V_{k+1}^{\dagger}[\nabla\mathbf{u}(T,\mathbf{x}), \partial_t\mathbf{u}(T,\mathbf{x})]$, and $\mathbf{b} = V_{k+1}^{\dagger}\mathbf{F}(\mathbf{z})$.

In principle, one needs as many constraints as one has continuous symmetries, and so the inclusion of a rotational gauge, e.g.,

$$\Phi(\mathbf{u}) = [\phi_{\mathbf{x}}(\mathbf{u}), \phi_\theta(\mathbf{u}), \phi_t(\mathbf{u})], \tag{121}$$

where $\phi_\theta(\mathbf{u})$ sets the rotational origin, is necessary for sufficiently complex solutions (those for which temporal evolution is not aligned with local rotation dynamics). Throughout this work, we assert the origin-fixing conditions to simply be the corresponding derivatives of the state,

$$\Phi(\mathbf{u}) = [\partial_x\mathbf{u}, \partial_y\mathbf{u}, \partial_\theta\mathbf{u}, \partial_t\mathbf{u}]\,. \tag{122}$$

The solution update is similarly constructed from the Arnoldi basis, $\delta\mathbf{u} = V_{k+1}\delta\mathbf{y}$. Additionally, we define the corrections to the shift and period of the solution $\delta\mathbf{q} = [\delta\mathbf{h}, \delta T]$. The updated solution $\mathbf{z}_{n+1} = \mathbf{z}_n + \delta\mathbf{z}_n$, improves the periodicity of the solution by reducing the norm of the residual function, $\|\mathbf{F}(\mathbf{z}_{n+1})\| < \|\mathbf{F}(\mathbf{z}_n)\|$, for a sufficiently well-chosen initial solution, $\mathbf{z}_0$.

A.4.1 Globalization techniques

For a sufficiently well-chosen initial estimate $\mathbf{z}_0$, the following Newton iterates $\mathbf{z}_n$ converge quadratically. That is, under ideal circumstances for $\mathbf{z}_\infty - \mathbf{z}_n \equiv \mathbf{e}_n$ and $\mathbf{F}(\mathbf{z}_\infty) = \mathbf{0}$,

$$\begin{aligned}
\mathbf{e}_{n+1} &= \mathbf{z}_\infty - \mathbf{z}_{n+1}, && (123)\\
&= \mathbf{z}_\infty - (\mathbf{z}_n - D\mathbf{F}^{-1}(\mathbf{z}_n)\mathbf{F}(\mathbf{z}_n)), && (124)\\
&= \mathbf{e}_n - (\mathbf{e}_n + \frac{1}{2}\mathbf{e}_n^{\top}\, D\mathbf{F}^{-1}(\mathbf{z}_n) D^2\mathbf{F}(\mathbf{z}_n)\,\mathbf{e}_n + O(\mathbf{e}_n^3)), && (125)\\
\mathbf{e}_{n+1} &= -\frac{1}{2}\mathbf{e}_n^{\top}\, D\mathbf{F}(\mathbf{z}_n)^{-1} D^2\mathbf{F}(\mathbf{z}_n)\,\mathbf{e}_n + O(\mathbf{e}_n^3). && (126)
\end{aligned}$$

That is, asymptotically, the convergence of the solution is iteratively quadratic, $O(\|\mathbf{e}_{n+1}\|) \approx O(\|\mathbf{e}_n\|^2)$.

These are hardly ideal circumstances, in that we compute iterative updates using a truncation of the tangent evolution operator $\mathcal{V}_T \approx Q_k H_k Q_k^\top$. To extend the basin of attraction for the inexact Newton method, we add globalization methods which modify the update $\delta\mathbf{z}_n$.

A.4.1.1 Line search

The first of these globalization methods is the simplest: this uses the shape of the update, $\delta\mathbf{z}_n$, but modifies the magnitude of the contribution by a multiplier η_n:

$$\mathbf{z}_{n+1} = \mathbf{z}_n + \eta_n \delta\mathbf{z}_n. \tag{127}$$

The value of η_n is determined by a minimization procedure assuming a locally quadratic model, using the points $(\eta_n, f(\eta_n)) = (0, \|\mathbf{F}(\mathbf{z}_n)\|)$, and $(1, \|\mathbf{F}(\mathbf{z}_n + \delta\mathbf{z}_n)\|)$, and additionally computing the point $(1/2, \|\mathbf{F}(\mathbf{z}_n + \delta\mathbf{z}_n/2)\|)$ if the reduction for $\eta_n = 1$ is not sufficient. Fitting a quadratic polynomial through $(\eta_n, f(\eta_n))$ makes it trivial to estimate an optimal magnitude for the perturbation provided standard constraints on the minimization of a function,

$$f'(0) < 0, \quad f''(0) > 0, \tag{128}$$

the optimal perturbation magnitude is $\eta_n^* = -f'(0)/f''(0)$, where $f(\eta)$ is the quadratic polynomial which passes through the points mentioned prior. This new point is then the preferred update test point, and if it is similarly insufficient, then the process repeats for the value of $\eta_n' \in (0, \eta_n^*)$, until either a sufficient reduction is found or $\eta_n < \epsilon_{\text{MACH}} \|\delta\mathbf{z}_n\|$.

A.4.1.2 Windowing

Modifying the magnitude of the update $\delta\mathbf{z}_n$ is the simplest modification to the Newton iteration, but more generally, any preconditioning method which applies a transformation of $\delta\mathbf{z}_n$ is allowable. In particular, we developed a method aimed at preserving the continuous symmetries of the underlying evolution equations by suppressing the effects of the boundaries.

Boundary conditions do not merely break the translational and rotational symmetries. Finite rotations $\mathcal{R}_\phi = \exp(\phi\partial_\theta)$ on a bounded domain Ω are not injective: some points are mapped out of the domain and others into (Fig. 56a). A similar situation is encountered for finite translations $\mathcal{T}_{-\mathbf{h}}$ on a bounded domain (Fig. 56b). Consider, for example, a meandering spiral wave for which $\mathcal{R}_\phi\mathcal{U}_T\mathbf{u} = \mathbf{u}$ on an unbounded domain. On a bounded domain the residual $\mathbf{F} = \mathcal{R}_\phi\mathcal{U}_T\mathbf{u} - \mathbf{u}$ will not vanish (we set $\mathbf{u} \equiv 0$ outside of Ω to make the residual well-defined). If one places the origin of rotation near the tip of the spiral wave, the residual $\mathbf{F}$ will decompose into two easily identifiable contributions. Inside $\Omega \cap \mathcal{R}_\phi\Omega$ (the octagonal overlap region in Fig. 56a), the residual is small and lies near the group manifold,

$$\mathbf{F} \approx \delta\mathbf{q} \cdot \nabla_{\mathbf{q}}\mathbf{u}, \tag{129}$$

where $\delta\mathbf{q}$ describes the magnitudes of rotations or shifts accounting for the arbitrary choice of the origin and the frequency dependence on the domain size. Outside the overlap region $(\Omega \cup \mathcal{R}_\phi\Omega) \setminus (\Omega \cap \mathcal{R}_\phi\Omega)$ (the eight triangular regions in Fig. 56a), the residual is large, $\mathbf{F} = O(1)$.

Figure 56b describes the effect of boundaries on drifting spiral waves described by relative periodic orbits for which $\mathcal{T}_{-\mathbf{h}}\mathcal{U}_T\mathbf{u} = \mathbf{u}$ on an unbounded domain. On a bounded domain we find a decomposition of the residual $\mathbf{F} = \mathcal{T}_{-\mathbf{h}}\mathcal{U}_T\mathbf{u} - \mathbf{u}$ analogous to the case of meandering waves. In the overlap region $\Omega \cap \mathcal{T}_{\mathbf{h}}\Omega$ (the rectangular region in Fig. 56b), the residual again can be represented in the form (129), where the small

shifts and rotations account for the dependence of the drift velocity and rotation frequency on the domain size. Outside of the overlap region, again the residual is large, $\mathbf{F} = O(1)$. Therefore, our objective is to minimize the residual inside the overlap region and suppress it everywhere else.

Generalized relative periodic orbits on bounded domains can be found using a modification of the traditional Newton-Krylov method which introduces an auxiliary weighting (or windowing) of the residual,

$$A'\delta\mathbf{w} = -\rho\mathbf{F}', \tag{130}$$

where ρ is a diagonal matrix with elements $0 \leq \rho_{ii} \leq 1$. The first $2N^2$ diagonal elements correspond to the weights associated with the dynamical field variables u_1 and u_2; they correspond to the values of the windowing function

$$W_d(\mathbf{x}) = \frac{1}{2}\left[1 - \tanh\left(\sigma\frac{2|\mathbf{x} - \mathbf{x}_c| - dL}{2L}\right)\right], \tag{131}$$

where $\mathbf{x}_c$ denotes the center of the window region and d determines the diameter of the (circular) "window" in units of L (we set $d = 0.7$ and $\sigma = 32$, unless specified otherwise). Specifically, $\rho_{ii} = W_d(\mathbf{x}_i)$. The remaining diagonal elements correspond to the spatial displacements (if applicable) and the period of the spiral wave and are all set to unity. The effect of windowing on the residual is illustrated for the cases of a meandering and a drifting spiral in Fig. 56c and Fig. 56d, respectively. We should point out that the weighting approach is not limited to square domains and rectangular grids and can be easily applied to domains of any shape with any grids, including unstructured ones.

We should also point out the closely related applications of weighting functions in numerical methods for PDEs such as the phase-field boundary method [42], domain decomposition [39, 171], and the damping filter method [162]. Alternatively, the weighting may by interpreted as an ad-hoc Jacobi-type preconditioning method for solving linear problems [164]. Even though the use of weighting is not a novel

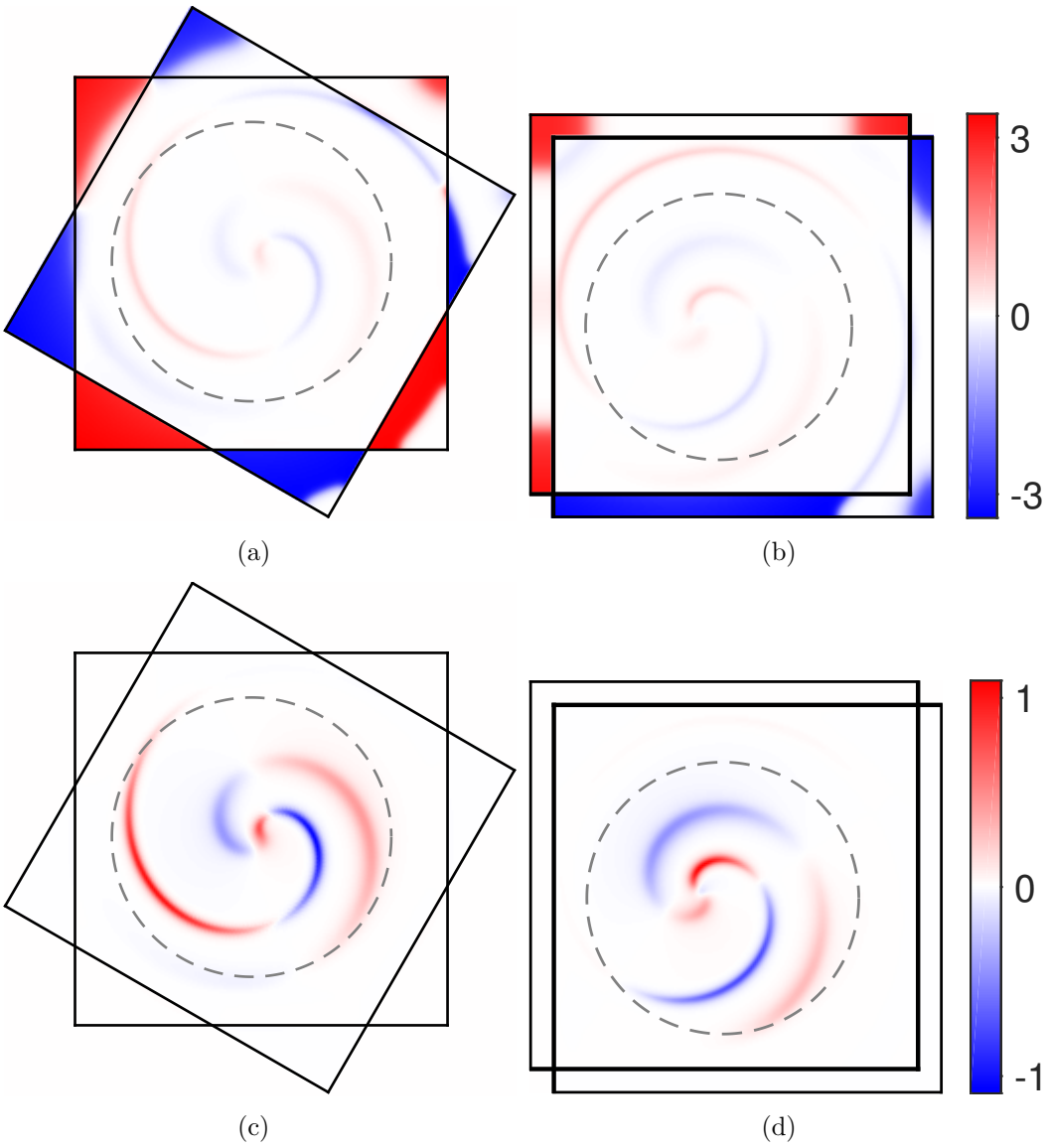

Figure 56: The residuals for spiral waves described by relative periodic orbits. The unweighted residual for a meandering spiral (a) and a drifting spiral (b). The corresponding weighted residuals are shown, respectively, in panels (c) and (d). The first component of the solution u_1 is shown in all the panels. The dashed line corresponds to $r = 0.35L$, which defines the spatial extent of the weighting function.

numerical approach *per se*, to the best of our knowledge, it has never been used either for restoring broken symmetries or for computing unstable traveling wave solutions.

The linear system (130) can be solved in the same way as (120). We found that the use of weighting dramatically improves the robustness of the Newton-Krylov method, not only allowing computation of generalized relative periodic orbits, but also substantially improving convergence speed for (absolute) periodic orbits. In practice, the convergence properties of the weighted Newton-Krylov solver were found to be fairly insensitive to the shape of the function $W_d(\mathbf{x})$, provided that it vanishes near all the boundaries. In particular, solutions which satisfy (120) can be computed using (130) combined with the relaxation process in which $\rho \to \mathbf{1}$ (or $d \to \infty$). This idea is similar to the damping filter method [162].

Whether weighting is used or not, the Newton-Krylov solver generates the Floquet multipliers Λ_i and Floquet modes $\mathbf{e}_i$ of the computed solution, i.e, eigenvalues and eigenmodes of the full Jacobian $\mathcal{J} = \mathcal{V}_T$,

$$\mathcal{J}\mathbf{e}_i = \Lambda_i \mathbf{e}_i \tag{132}$$

as a matter of course. Indeed, the spectrum of the Krylov-subspace Jacobian H_k yields a good approximation to the leading eigenvalues and eigenmodes of $\mathcal{J}$, while $\mathcal{J} = g^{-1}(A+\mathbf{1})$. Of particular importance are the unstable modes (which correspond to $|\Lambda_i| > 1$) and the Goldstone modes (which correspond to $|\Lambda_i| = 1$) that characterize the symmetries of the system.

A.4.1.3 Additional symmetry effects

The Floquet spectrum of the multi-spiral solution shown in Fig. 44 suggests an explanation for the difficulty of refining recurrent segments of aperiodic spiral chaos into exactly periodic solutions using, e.g., the Newton-Krylov solver detailed in A.4. For a state with n_c cores in a model with n_g continuous symmetries, some states will have $n_g n_c$ near-marginal Floquet modes. Since only n_g symmetry constraints are

guaranteed by the evolution equations, it is only when $n_c = 1$ that the segment may be refined into a (relative) periodic orbit.

Exceptional cases do arise, specifically when additional constraints exist which increase the symmetry of state, and constrain the symmetry of each spiral wave – a rare phenomenon. An example is when the state is highly symmetric, and equivalent under a flip-symmetry. While a naïve count of this state would indicate n_c distinct spiral cores, the additional flip symmetry reduces this to $n_c/2$ in practice – equivalently a single spiral on a halved domain. Thus, for example, dual-spiral states with flip symmetry invariance may be refined into a relative periodic orbit using established techniques. This does not contradict the solutions shown in Fig. 36, rather it explains them; with the continuous symmetry broken by the stiffness of the evolution equation ($s \gg 1$), the effective accessible symmetry of the state is reduced from 2×3 to 2×1, and since the two spirals are very far apart their rotational speeds match exponentially well.

These special solutions essentially rely on the strict correlation of disparate spatial regions, and in particular, on the organizing features of the state. This is a potential path toward dealing with systems which exhibit local symmetry.

A.4.1.4 Correction Heuristics

Stepping back, we may generalize the inexact Newton system into the solution of a blocked linear equation. The canonical Newton step is determined by solving the square $(k + d + 1)$-dimensional linear system,

$$\begin{pmatrix} A & B \\ C^\dagger & 0 \end{pmatrix} \begin{pmatrix} \delta\mathbf{y}_i \\ \delta\mathbf{q}_i \end{pmatrix} = - \begin{pmatrix} D \\ \mathbf{0} \end{pmatrix}. \tag{133}$$

The update to the state is composed from the solution of this linear system, $\delta\mathbf{z} = [V_k\,\delta\mathbf{y}, \delta\mathbf{q}]$, before further transformations such as the line-search. We may similarly compose distinct updates $\delta\mathbf{y}_i$ which are not aligned with the canonical Newton step,

and indeed, these alternative steps are frequently significantly better optimizations. I have implemented seven – occasionally approximately linearly dependent – updates, and allow the solver to iterate through them until a satisfactory update direction has been found.

Several features vary in the construction of these additional update directions. To begin, while $A = H_k$ for the canonical Newton step, this is a truncation not only of the linearized dynamics but a truncation of the current Arnoldi factorization of the tangent linear operator. Several updates make use of the complete set of orthogonal Krylov basis vectors and the ragged Hessenberg Arnoldi matrix, V_{k+1} and H_{k+1}, respectively. Similarly, the residual is projected onto the subspace of appropriate size, $D = V_{k+1}^{\dagger}\mathbf{F}(\mathbf{z})$. Additionally, the construction of the symmetry-related derivative terms and constraints are projected onto the subspace of appropriate size, e.g., $B = V_{k+1}^{\dagger}\Phi(\mathbf{u}(T,\mathbf{x}))$ and $C^{\dagger} = \Phi(\mathbf{u}(0,\mathbf{x}))^{\dagger}V_{k+1}$, for a shiftless state $\mathcal{T}_h \equiv \mathbf{1}$. Indeed, allowing the solution of the linear system to vary provides further variation. The classical Newton step uses the standard linear solve methods available to the overloaded backslash operator in Matlab. Alternatively, one may directly compute the inverse or pseudo-inverse of the matrix on the left hand size and use this matrix to multiply the projected residual. We additionally construct the trust-region-model Cauchy point [119], the "GMRES point", and the result of the iterative SVD-hookstep method used in Channelflow [86] due to Dennis & Schnabel [61]. The most controversial method is motivated by the persistence of local symmetries and a concession to the iterative approximation of the corresponding eigenmodes. This method computes the eigenvalues and eigenfunctions of matrix $A + \mathbf{1}$, and uses a preset tolerance to designate a subset as 'near-marginal'. The set of near-marginal modes are used as projection constraints (matrix $C^{\dagger}$ in (133)), and the linear solve is computed using the explicit Moore-Penrose pseudo-inverse, as generically this linear system may be arbitrarily ill-conditioned. The complete set of update directions are enumerated in

the code on my github [122].

A.4.1.5 Alternative factorization

The Arnoldi algorithm utilizes computations of the form $\mathcal{V}_T \mathbf{v}_{k+1} \rightarrow \sum_{i=1}^{k} h_{i,k}\mathbf{v}_i + h_{k+1,k}\mathbf{v}_k$, resolving the action of the forward tangent propagator for arbitrary inputs in a k-dimensional subspace. This factorization after k iterations is usually written as a matrix equation, $\mathcal{V}_T V_k = V_{k+1} H_{k+1}$, where V_k and H_k are matrices of size $N \times k+1$ and $k+1 \times k$, where $N \gg k$. In general, this method is sub-optimal because the propagator maps an initial disturbance relative to a state at time $t = 0$ to a disturbance relative to a state at time $t = T$. Thus, for states which evolve aperiodically in that temporal interval – as is every state selected from direct numerical simulation before resolving into a periodic solution – the tangent spaces at the beginning and end points are not collocated. Ideally, the solver would construct a truncation of the operator using both the forward and adjoint tangent propagators. In this light, the proper factorization is likely the Golub-Kahan-Lanczos procedure described in the algorithm below. Several properties of the resulting linear system thus change, most importantly the projections.

Beginning from the full Newton method (without projection onto the basis constructed from Arnoldi iteration) the update to the state is generated from the full (nominally infinite-dimensional) finite-time Jacobian operator,

$$\begin{pmatrix} \mathcal{G}_a \mathcal{V}_T - \mathbf{1} & \Phi(\mathcal{G}_a \mathcal{U}_T \mathbf{u}) \\ \Phi^\dagger(\mathbf{u}) & 0 \end{pmatrix} \begin{pmatrix} \delta\mathbf{u} \\ \delta\mathbf{a} \end{pmatrix} = - \begin{pmatrix} \mathcal{G}_a \mathcal{U}_T \mathbf{u} - \mathbf{u} \\ \mathbf{0} \end{pmatrix}, \tag{134}$$

where we have absorbed T into $\mathbf{a} = [a, T]$ for concision. Rewriting the operator $\mathcal{G}_a \mathcal{V}_T = USV^\dagger$, we immediately see the path forward: factoring out the left and right singular vectors. One way to do this is to write each element in the appropriate basis. As we have not yet truncated the singular spectrum, we can express both $\Phi(\mathcal{G}_a \mathcal{U}_T \mathbf{u})$ and $\Phi^\dagger(\mathbf{u})$ in the basis of singular vectors, as $\Phi(\mathcal{G}_a \mathcal{U}_T \mathbf{u}) = UB$ and $\Phi^\dagger(\mathbf{u}) = C^\dagger V^\dagger$.

Using the identities $VV^\dagger = UU^\dagger = \mathbf{1}$, it can easily be shown that $USV^\dagger - \mathbf{1} = U(S - U^\dagger V)V^\dagger$, again provided completeness. We rewrite the update in the temporal-origin singular basis $\delta\mathbf{u} = V\delta\mathbf{y}$ likewise,

$$\begin{pmatrix} USV^\dagger - \mathbf{1} & UB \\ C^\dagger V^\dagger & 0 \end{pmatrix} \begin{pmatrix} V\delta\mathbf{y} \\ \delta\mathbf{q} \end{pmatrix} = \begin{pmatrix} -\mathcal{G}_a\mathcal{U}_T\mathbf{u} - \mathbf{u} \\ \mathbf{0} \end{pmatrix}. \tag{135}$$

The system, as of now, is not simplified, merely obfuscated by the introduction of distinct bases at the temporal origin and termination of the orbit. In particular, it is ambiguous *a priori* whether the residual on the right-hand-side should be constructed in the origin or termination basis, as it is essentially the collocation of the two. It can be trivially shown that the system is equivalent to

$$\begin{pmatrix} S - U^\dagger V & B \\ C^\dagger & 0 \end{pmatrix} \begin{pmatrix} \delta\mathbf{y} \\ \mathbf{0} \end{pmatrix} = - \begin{pmatrix} D \\ \mathbf{0} \end{pmatrix}, \tag{136}$$

where $D = U^\dagger(\mathcal{G}_a\mathcal{U}_T\mathbf{u} - \mathbf{u})$. At this point, one should construct finite-dimensional approximations of the singular factorization $S \to S_k$, $U \to U_k$, and $V \to V_k$. With these substitutions, it is suggestive that the limiting effectiveness of this formulation is due to the resolution of unity in the identities used above. Indeed, as $U^\dagger V$ is generically dense, one should expect that this methods convergence is related to the spectral norm of the leading k-by$k$ block of the matrix $U^\dagger V$ on iteration k. This solver was not utilized for the present work, as the singular spectrum is convenient for the study of time-dependent aperiodic orbits, which was prioritized, but there is potentially much to be gained from its application. In several numerical experiments this factorization, if not (136) proper, generated effective corrections to unresolved recurrent multi-spiral states for which the Newton-Krylov solver using the Arnoldi factorization had stagnated.

While the preceding discussion has been specific to relative periodic orbits, there is little in principle to forbid the application to more interesting orbits whose endpoints

are not collocated in the state space, i.e., heteroclinic connections. The condition for a connection from the linear neighborhood of state $\mathbf{u}_0$ to the neighborhood of state $\mathbf{u}_1$ can be written,

$$\mathbf{0} = \mathcal{G}_a \mathcal{U}_T(\mathbf{u}_0 + \mathbf{u}) - \mathbf{u}_1, \tag{137}$$

with appropriate constraints on the form of $\mathbf{u}$, i.e., $\mathbf{u}$ is orthogonal to the stable subspace of $\mathbf{u}_0$, $\mathbf{u} = \sum_k |\mathbf{v}^k\rangle H(|\Lambda_k| - 1)\langle \mathbf{w}^k|\mathbf{u}\rangle$. In principle, the same factorization can be applied to the linearization and the system can be solved iteratively – though expensively – through the flexibility afforded by dislocated tangent spaces. The presence of continuous symmetry is the main complication to this application; it is presently unclear how to properly quotient this for arbitrary initial and final configurations (e.g., between two relative periodic orbits). We do not attempt to address this very difficult problem in the appendix.

A.5 Bidomain model reduction

Upon rescaling and including explicitly the dependence of the ionic currents the bidomain equations (4) take the generic form,

$$\begin{aligned} \partial_\tau u &= \nabla \cdot (\sigma_i \nabla)(u + w) + f(u, \mathbf{v}), \\ \partial_\tau v_\mu &= \nu_\mu \nabla \cdot (\sigma_i \nabla) v_\mu + g_\mu(u, \mathbf{v}), \\ 0 &= \nabla \cdot [(\sigma_e + \sigma_i)\nabla] w + \nabla \cdot (\sigma_i \nabla) u, \end{aligned} \tag{138}$$

with σ_i and σ_e denoting the intra- and extracellular conductivity tensors, respectively, and u, $\mathbf{v} = [v_\mu]_\mu$, and w represent the (non-dimensionalized) transmembrane potential, a vector of gating variables, and the extra-cellular potential, respectively.

For the reduction we require that the constraint in (138) be satisfied identically,

$$(\mathcal{L}_i + \mathcal{L}_e) w = -\mathcal{L}_i u, \tag{139}$$

where operators $\mathcal{L}_i = \nabla \cdot (\sigma_i \nabla)$ and $\mathcal{L}_e = \nabla \cdot (\sigma_e \nabla)$, for concision. As the operator on

the left has vanishing eigenvalues, we impose a solvability condition that the right-hand-side not drive the null eigenfunctions of the adjoint operator, $(\mathcal{L}_i + \mathcal{L}_e)^\dagger w_0 = 0$. The Fredholm alternative theorem states that this is a necessary and sufficient condition [56]. This constraint can be stated $(w_0, \mathcal{L}_i u) = 0$, and requires the solution of the null eigenfunctions of $(\mathcal{L}_i + \mathcal{L}_e)^\dagger = \nabla \cdot [(\sigma_i + \sigma_e)^\dagger \nabla]$.

The constrained bidomain evolution equations then simplify through the elimination of the extracellular potential in favor of an implicit constraint. The reduced equations take the form of an implicit integro-differential equation

$$\begin{aligned} \partial_\tau u &= \left[\mathbf{1} - \mathcal{L}_i \left(\mathcal{L}_i + \mathcal{L}_e\right)^{-1}\right] \mathcal{L}_i u + f(u, \mathbf{v}), \\ \partial_\tau v_\mu &= \nu_\mu \mathcal{L}_i v_\mu + g_\mu(u, \mathbf{v}). \end{aligned} \tag{140}$$

Additionally, the bidomain formulation of cardiac tissue dynamics recovers, in the limit of equally anisotropic conductivity tensors $\sigma_e = \lambda \sigma_i$, the structure of the monodomain model equations with modified diffusion factor $(1+\lambda)/\lambda$. Similarly, the singular limit $(\lambda \to -1)$ is forbidden by the physical interpretation of the variable σ_e. This formulation of the effective bidomain system reduces the number of boundary conditions from six to four, involving only the intracellular potential, gating variables, and intracellular conductivity tensor.

The system of reduced bidomain equations (140) takes the form of the abstract dynamical system,

$$\dot{\mathbf{z}} = \mathcal{L}[\mathbf{z}] + \mathcal{N}[\mathbf{z}],$$

where $\mathbf{z} = [u, \mathbf{v}] \in \mathcal{M}$ denotes a point in the state-space, and $\mathcal{L}$, $\mathcal{N}$ are linear and nonlinear operators, respectively. Similarly we define the Fourier transform of the state vector $\hat{\mathbf{z}} = [\mathcal{F}[u], \mathcal{F}[\mathbf{v}]]$. Further, the clear delineation between differential and polynomial terms suggests a solution method which exploits this structure, namely operator splitting.

From this point on, we shall make several assumptions. We fix the nonlinear

model to a modified Karma model Ch. 3 and we assume spatially-homogeneous tissue properties, i.e., $\nabla\sigma_i = \mathbf{0} = \nabla\sigma_e$. This assumption diagonalizes the differential operator $\mathcal{L}$ in Fourier space,

$$\dot{\hat{\mathbf{z}}}_{\mathbf{q}} = \begin{pmatrix} \left[1 - \mathcal{L}_{i,\mathbf{q}} \left(\mathcal{L}_{i,\mathbf{q}} + \mathcal{L}_{e,\mathbf{q}}\right)^{-1}\right] & 0 \\ 0 & \nu \end{pmatrix} \mathcal{L}_{i,\mathbf{q}} \hat{\mathbf{z}}_{\mathbf{q}} + \hat{\mathcal{N}}_{\mathbf{q}}[\mathbf{z}] \tag{141}$$

where $\hat{\mathcal{N}}_{\mathbf{q}}$ is the complex-valued amplitude of the Fourier mode of $\hat{\mathcal{N}}[\mathbf{z}] = \mathcal{F}[\mathcal{N}[\mathbf{z}]]$ at $\mathbf{q} = [q_1 \; q_2]$. In Fourier space, the elements of the differential operator $\mathcal{L}_i$ acting on the $\mathbf{q}$th Fourier mode of u, $\hat{u}_{\mathbf{q}} \exp(\mathrm{i}\mathbf{q}\mathbf{x})$, are given by

$$\mathcal{L}_{i,\mathbf{q}} \hat{u}_{\mathbf{q}} = -\left[\sigma_i^{1,1} q_1^2 + \sigma_i^{2,2} q_2^2 + (\sigma_i^{1,2} + \sigma_i^{2,1}) q_1 q_2\right] \hat{u}_{\mathbf{q}}, \tag{142}$$

and so the evolution of $\hat{\mathbf{z}}_{\mathbf{q}}$ obeys

$$\dot{\hat{\mathbf{z}}}_{\mathbf{q}} = -\begin{pmatrix} \left[1 - \frac{\mathbf{q}\sigma_i\mathbf{q}^\top}{\mathbf{q}(\sigma_i+\sigma_e)\mathbf{q}^\top}\right] & 0 \\ 0 & \nu \end{pmatrix} \left[\mathbf{q}\sigma_i\mathbf{q}^\top\right] \hat{\mathbf{z}}_{\mathbf{q}} + \hat{\mathcal{N}}_{\mathbf{q}}[\mathbf{z}]. \tag{143}$$

The system is integrated using the symmetric Strang splitting method. The sequence begins with a half-step ($\Delta t/2$) according to the linear terms, followed by full steps (Δt) in the nonlinear terms and linear terms sequentially, repeating until the last time-step, in which the linear terms are again taken as a half-step ($\Delta t/2$). The linear terms are solved exactly, using the exponential form of the solution, in Fourier space. This exploits the semi-group property of the exponential to reduce the computational workload of the symmetric splitting method. The nonlinear terms are solved using an explicit Runge-Kutta method, of order $p \geq 2$, within an inner loop. This maintains a large time-step for the linear terms while resolving the short time-scales of the cellular dynamics. Using this method, the single-step recombination term – proportional to $([\mathcal{N}[\mathcal{N}, \mathcal{L}]] - [\mathcal{L}, [\mathcal{L}, \mathcal{N}]]/2)\Delta t^3$ where $[\cdot, \cdot]$ denotes the commutator – is the dominant contribution to the error of the method, which is $O(\Delta t^2)$ over the finite timescales of the present investigation. There exist several methods which improve the convergence rates of simple splitting methods [84], and several high-order

methods of much greater complexity [109], but for the present purposes these were deemed unnecessary.

As the evolution is written in terms of the Fourier modes of the expansion of $\mathbf{z}$, these enforce periodic boundary conditions unilaterally. To instead assert no-flux conditions, we double the spatial domain in both Cartesian dimensions (a four-fold increase in the discrete number of points) and define the Fourier-space differential operators in the usual space for this domain. In the transformation step, instead of a straight-forward Fourier transform, the solution is mirrored across the physical no-flux boundary to three additional 'images' on the quadrupled periodic domain. Formally, this is the action of an operator $M : \mathbb{R}^N \to \mathbb{R}^{4N}$. This has the advantage of maintaining the diagonality of the differential operators (on the mirror-extended domain), preserving the simple inverse (again, on the mirror-extended domain), while requiring only $2.5\times$ to compute compared to the original periodic domain at the grid sizes considered here. The application of the linear operator, including transform, is a relatively small contribution to the overall computation time. We acknowledge the applicability of various other methods (esp., Ref. [42]) for applying general boundary conditions to Fourier domains, numerically. These were not considered as they couple differential operators to spatial dependence through convective terms (i.e., $\mathbf{p}(t, \mathbf{x})\cdot\nabla\mathbf{z}$) and would thus require changing the integration method to a more sophisticated one.

The linearization of this method can be computed trivially in forward time, and so we shall not detail the methods here. However, this method also possesses a simple discrete adjoint, provided the nonlinear iterations are sufficiently low-order (i.e., second). We use the discrete forward and adjoint methods to compute the right and left eigenfunctions, respectively, of the Jacobian about an unstable single-spiral generalized relative periodic orbit Ch. 3. These solutions satisfy the relative periodic orbit condition (43),

$$\mathbf{0} = \mathcal{T}_{-\mathbf{h}}\mathcal{U}_T\mathbf{z}(t, \mathbf{x}) - \mathbf{z}(t, \mathbf{x}), \tag{144}$$

where the group transformation is explicitly $\mathcal{T}_{\mathbf{h}}$ (the translation operator) and $\mathcal{U}_T$ is the finite-time evolution map according to (140). This solution corresponds to a spiral wave with a small displacement over the course of a rotation which we identify with the net movement of the spiral core $\mathbf{h}$ over the course of one revolution, in time T.

A generalized relative periodic solution corresponding to a single spiral wave roughly centered in a square domain with no-flux boundary conditions was found from a nearby direct numerical simulation using an iterative Newton-Krylov solver to determine the optimal shape, displacement, and rotational period. The conductivity tensors used in the solution were diagonal and proportional, and correspond to the values in the monodomain limit, and we denote this solution $\mathbf{z}_0$, and will treat it as our origin in the parameter space. By making small changes to the conductivity tensors, we can make the simulation correspond *essentially* to the bidomain system, and this perturbation to the conductivity forms the basis of our continuation from the monodomain to the bidomain model. Unexpectedly, this continuation (essentially monodomain to essentially bidomain) stabilizes the spiral wave; this phenomenon is not yet understood. For the moment, we only assert the ground truth of a stable solution, as the instability appears to be of minimal relevance for the consideration of continuous symmetries.

We define the parametrized non-dimensional conductivity tensors for the intracellular and extracellular tissues

$$\sigma_e = \mathbf{1}, \quad \sigma_i = \alpha \begin{pmatrix} 1 & 0 \\ 0 & (1-\varepsilon^2) \end{pmatrix}, \tag{145}$$

where $\varepsilon^2 = 1 - G_i^{2,2} G_e^{1,1} / G_i^{1,1} G_e^{2,2}$ is the (squared) eccentricity of the intracellular conductivity ellipse, and $\alpha = G_i^{1,1}/G_e^{1,1}$ is the characteristic non-dimensional length scale, set to unity throughout following Ref. [146]. The continuation is performed for $\varepsilon \in [0, 1]$, smoothly interpolating between the limits of equal anisotropy and

the physically relevant anisotropy ratios for the bidomain model ($\varepsilon \approx 0.9981$) [145], and maintaining the ideally-scaled monodomain limit for our origin solution, $\mathbf{z}_0 = \mathbf{z}(\varepsilon = 0)$ to clearly show the deformation as ε is varied. Exactly relative periodic solutions (to precision $\|\mathbf{F}(\mathbf{z})\|_2 \sim O(10^{-4})$) were found for values of $\varepsilon \in [0.0, 1.0)$. The characteristic deformation expected from the rescaling of the spatial coordinates is readily apparent, cf. Fig. 57.

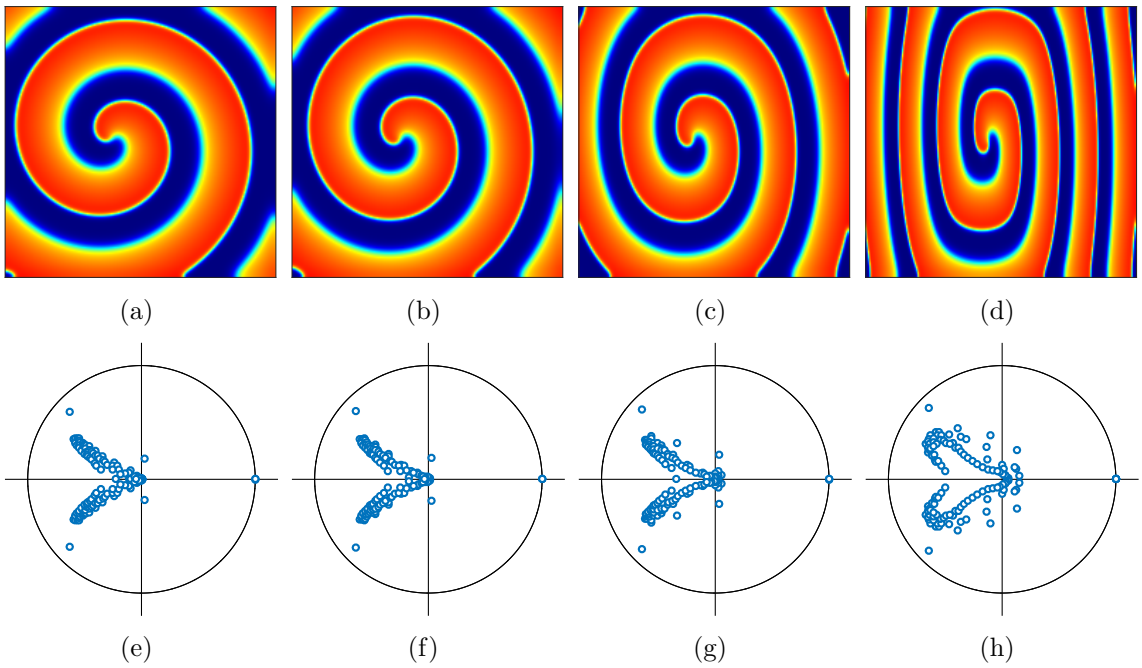

Figure 57: Solutions (a-d) $u_1^{(\varepsilon)}(0, \mathbf{x})$ and associated Floquet spectra (e-h) $\Lambda^{(\varepsilon)}$ of the reduced bidomain model (140) using Karma kinetics (14) for eccentricity $\varepsilon = 0.00, 0.51, 0.81, 0.93$, respectively.

Especially notable, however, is that the marginal eigenmodes corresponding to continuous spatial and temporal symmetries do not deviate from unity within the precision of the relative periodic solution. These results indicate that, despite global coupling through (numerically) the pseudo-spectral time-stepping and (physically) the bidomain constraint equation, local Euclidean symmetry persists for the reduced bidomain model. Were that the symmetry was violated at this step, the story would conclude, but the persistence demands additional investigation – not least of which

involving the fully realized bidomain model, without the assumptions made in the construction of (140). We expect such a program to be both computationally difficult and computationally expensive, as well as presenting new conceptual difficulties for the construction of invariant solutions in this constrained PDE model.

REFERENCES

[1] Agladze, K. I., Davydov, V. A., and Mikhailov, A. S., "An observation of resonance of spiral waves in distributed excitable medium," *JETP Lett*, vol. 45, pp. 767–770, 1987.

[2] Allexandre, D. and Otani, N. F., "Preventing alternans-induced spiral wave breakup in cardiac tissue: An ion-channel-based approach," *Phys. Rev. E*, vol. 70, p. 061903, 2004.

[3] Alvarez-Lacalle, E. and Echebarria, B., "Global coupling in excitable media provides a simplified description of mechanoelectrical feedback in cardiac tissue," *Phys. Rev. E*, vol. 79, p. 031921, 2009.

[4] Aranson, I. S. and Kramer, L., "The world of the complex Ginzburg-Landau equation," *Rev. Mod. Phys.*, vol. 74, pp. 99–143, 2002.

[5] Aranson, I., Kessler, D., and Mitkov, I., "Drift of spiral waves in excitable media," *Physica D*, vol. 85, pp. 142–155, 1995.

[6] Aranson, I. S., Kramer, L., and Weber, A., "Theory of interaction and bound states of spiral waves in oscillatory media," *Phys. Rev. E*, vol. 47, pp. 3231–3241, May 1993.

[7] Aranson, I., Kramer, L., and Weber, A., "On the interaction of spiral waves in non-equilibrium media," *Physica D*, vol. 53, no. 2, pp. 376–384, 1991.

[8] Arnoldi, W. E., "The principle of minimized iterations in the solution of the matrix eigenvalue problem," *Quart. Appl. Math.*, vol. 9, pp. 17–29, 1951.

[9] Ascher, U. M., Ruuth, S. J., and Wetton, B. T., "Implicit-explicit methods for time-dependent partial differential equations," *SIAM Journal on Numerical Analysis*, vol. 32, no. 3, pp. 797–823, 1995.

[10] Aslanidi, O. V., Stewart, P., Boyett, M. R., and Zhang, H., "Optimal velocity and safety of discontinuous conduction through the heterogeneous Purkinje-ventricular junction," *Biophys. J.*, vol. 97, pp. 20–39, 2009.

[11] Auerbach, D., Cvitanović, P., Eckmann, J.-P., Gunaratne, G., and Procaccia, I., "Exploring chaotic motion through periodic orbits," *Phys. Rev. Lett.*, vol. 58, pp. 2387–2389, 1987.

[12] Bär, M. and Eiswirth, M., "Turbulence due to spiral breakup in a continuous excitable medium," *Phys. Rev. E*, vol. 48, pp. 1635–1637, 1993.

[13] Bär, M., Gottschalk, N., Eiswirth, M., and Ertl, G., "Spiral waves in a surface reaction: model calculations," *The Journal of chemical physics*, vol. 100, no. 2, pp. 1202–1214, 1994.

[14] Barkley, D., "A model for fast computer simulation of waves in excitable media," *Physica D*, vol. 49, pp. 61–70, 1991.

[15] Barkley, D., "Linear stability analysis of rotating spiral waves in excitable media," *Phys. Rev. Lett.*, vol. 68, pp. 2090–2093, 1992.

[16] Barkley, D., "Euclidean symmetry and the dynamics of rotating spiral waves," *Phys. Rev. Lett.*, vol. 72, pp. 164–167, 1994.

[17] Barkley, D. and Kevrekidis, I. G., "A dynamical systems approach to spiral wave dynamics," *Chaos*, vol. 4, pp. 453–460, 1994.

[18] Barkley, D., Kness, M., and Tuckerman, L. S., "Spiral wave dynamics in a simple model of excitable media: Transition from simple to compound rotation," *Phys. Rev. A*, vol. 42, pp. 2489–2492, 1990.

[19] Beaumont, J., Davidenko, N., Davidenko, J. M., and Jalife, J., "Spiral waves in two-dimensional models of ventricular muscle: formation of a stationary core," *Biophysical Journal*, vol. 75, no. 1, pp. 1–14, 1998.

[20] Bernus, O., Verschelde, H., and Panfilov, A. V., "Spiral wave stability in cardiac tissue with biphasic restitution," *Phys. Rev. E*, vol. 68, p. 021917, 2003.

[21] Bevans, C. G., Kordel, M., Rhee, S. K., and Harris, A. L., "Isoform composition of connexin channels determines selectivity among second messengers and uncharged molecules," *J. Biol. Chem.*, vol. 273, pp. 2808–2816, 1998.

[22] Beyn, W.-J. and Lorenz, J., "Nonlinear stability of rotating patterns," *Dynamics of PDE*, vol. 5, pp. 349–400, 2008.

[23] Beyn, W.-J. and Thümmler, V., "Freezing solutions of equivariant evolution equations," *SIAM J. Appl. Dyn. Syst.*, vol. 3, pp. 85–116, 2004.

[24] Biktashev, V. N. and Biktasheva, I. V., "Orbital motion of spiral waves in excitable media," *Phys. Rev. Lett.*, vol. 104, p. 058302, 2010.

[25] Biktashev, V. N., Biktasheva, I. V., and Sarvazyan, N. A., "Evolution of spiral and scroll waves of excitation in a mathematical model of ischaemic border zone," *PLoS One*, vol. 6, p. e24388, 2011.

[26] Biktashev, V. N. and Holden, A. V., "Resonant drift of autowave vortices in two dimensions and the effects of boundaries and inhomogeneities," *Chaos Soliton Fract.*, vol. 5, pp. 575–622, 1995.

[27] Biktashev, V., "Causodynamics of autowave patterns," *Physical review letters*, vol. 95, no. 8, p. 084501, 2005.

[28] Biktashev, V. and Holden, A., "Resonant drift of an autowave vortex in a bounded medium," *Physics Letters A*, vol. 181, no. 3, pp. 216–224, 1993.

[29] Biktashev, V., Holden, A., and Zhang, H., "Tension of organizing filaments of scroll waves," *Philosophical Transactions of the Royal Society of London. Series A: Physical and Engineering Sciences*, vol. 347, no. 1685, pp. 611–630, 1994.

[30] Biktasheva, I. V., Barkley, D., Biktashev, V. N., Bordyugov, G. V., and Foulkes, A. J., "Computation of the response functions of spiral waves in active media," *Phys. Rev. E*, vol. 79, p. 056702, 2009.

[31] Biktasheva, I. V. and Biktashev, V. N., "Response functions of spiral wave solutions of the complex Ginzburg-Landau equation," *J. Nonlin. Math. Phys.*, vol. 8, pp. 28–34, 2001.

[32] Biktasheva, I. V. and Biktashev, V. N., "Wave-particle dualism of spiral waves dynamics," *Phys. Rev. E*, vol. 67, p. 026221, 2003.

[33] Biktasheva, I. V., Biktashev, V. N., and Foulkes, A. J., "Computation of the drift velocity of spiral waves using response functions," *Phys. Rev. E*, vol. 81, p. 066202, 2010.

[34] Biktasheva, I. V., Dierckx, H., and Biktashev, V. N., "Drift of scroll waves in thin layers caused by thickness features: Asymptotic theory and numerical simulations," *Phys. Rev. Lett.*, vol. 114, p. 068302, 2015.

[35] Biktasheva, I. V., Elkin, Y. E., and Biktashev, V. N., "Localized sensitivity of spiral waves in the complex Ginzburg-Landau equation," *Phys. Rev. E*, vol. 57, pp. 2656–2659, 1998.

[36] Biktasheva, I. V., Holden, A. V., and Biktashev, V. N., "Localization of response functions of spiral waves in the FitzHugh–Nagumo system," *Int. J. Bifur. Chaos*, vol. 16, pp. 1547–1555, 2006.

[37] Biktasheva, I. V., Elkin, Y. E., and Biktashev, V. N., "Resonant drift of spiral waves in the complex Ginzburg-Landau equation," *Journal of biological physics*, vol. 25, no. 2-3, pp. 115–127, 1999.

[38] Biktasheva, I., "Drift of spiral waves in the complex Ginzburg-Landau equation due to media inhomogeneities," *Phys. Rev. E*, vol. 62, no. 6, p. 8800, 2000.

[39] Bjorstad, P. and Gropp, W., *Domain decomposition: parallel multilevel methods for elliptic partial differential equations*. Cambridge Univ. Press, 2004.

[40] Bohr, T., Huber, G., and Ott, E., "The structure of spiral domain patterns," *Europhys. Lett.*, vol. 33, p. 589, 1996.

[41] Bohr, T., Huber, G., and Ott, E., "The structure of spiral-domain patterns and shocks in the 2D complex Ginzburg-Landau equation," *Physica D*, vol. 106, pp. 95–112, 1997.

[42] Bueno-Orovio, A., Perez-Garcia, V. M., and Fenton, F. H., "Spectral methods for partial differential equations in irregular domains: The spectral smoothed boundary method," *SIAM J. Sci. Comp.*, vol. 28, pp. 886–900, 2006.

[43] Bueno-Orovio, A., Cherry, E. M., and Fenton, F. H., "Minimal model for human ventricular action potentials in tissue," *Journal of Theoretical Biology*, vol. 253, pp. 544–560, Aug. 2008.

[44] Bunse-Gerstner, A., Byers, R., Mehrmann, V., and Nichols, N. K., "Numerical computation of an analytic singular value decomposition of a matrix valued function," *Numerische Mathematik*, vol. 60, no. 1, pp. 1–39, 1991.

[45] Butcher, J. C., "Numerical methods for ordinary differential equations in the 20th century," *Journal of Computational and Applied Mathematics*, vol. 125, no. 1-2, pp. 1–29, 2000.

[46] Chandler, G. J. and Kerswell, R. R., "Invariant recurrent solutions embedded in a turbulent two-dimensional Kolmogorov flow," *J. Fluid Mech.*, vol. 722, pp. 554–595, 2013.

[47] Cherry, E. M., Ehrlich, J. R., Nattel, S., and Fenton, F. H., "Pulmonary vein reentry-Properties and size matter: Insights from a computational analysis," *Heart Rhythm*, vol. 4, pp. 1553–1562, 2007.

[48] Cherry, E. M. and Fenton, F. H., "Suppression of alternans and conduction blocks despite steep apd restitution: Electrotonic, memory and conduction velocity restitution effects," *Am. J. Physiol. Heart Circ. Physiol.*, vol. 286, pp. 2332–2341, 2004.

[49] Cherry, E. M. and Fenton, F. H., "Visualization of spiral and scroll waves in simulated and experimental cardiac tissue," *New J. Phys.*, vol. 10, p. 125016, 2008.

[50] Cherry, E. M., Greenside, H. S., and Henriquez, C. S., "A space-time adaptive method for simulating complex cardiac dynamics," *Phys. Rev. Lett.*, vol. 84, pp. 1343–1346, 2000.

[51] Chossat, P. and Lauterbach, R., *Methods in Equivariant Bifurcations and Dynamical Systems*. Singapore: World Scientific, 2000.

[52] Christiansen, F., Cvitanović, P., and Putkaradze, V., "Hopf's last hope: Spatiotemporal chaos in terms of unstable recurrent patterns," *Nonlinearity*, vol. 10, pp. 55–70, 1997.

[53] Clayton, R. H., Bernus, O., Cherry, E. M., Dierckx, H., Fenton, F. H., Mirabella, L., Panfilov, A. V., Sachse, F. B., Seemann, G., and Zhang, H., "Models of cardiac tissue electrophysiology: Progress, challenges and open questions," *Prog. Biophys. Mol. Biol.*, vol. 104, pp. 22–48, 2011.

[54] Courtemanche, M., "Complex spiral wave dynamics in a spatially distributed ionic model of cardiac electrical activity," *Chaos*, vol. 6, p. 579, 1996.

[55] Cross, M., *Pattern Formation and Dynamics in Nonequilibrium Systems*. Cambridge, UK ; New York: Cambridge Univ. Press, 1 edition ed., 2009.

[56] Cross, M. C. and Hohenberg, P. C., "Pattern-formation outside of equilibrium," *Rev. Mod. Phys.*, vol. 65, pp. 851–1112, 1993.

[57] Cvitanović, P. and Gibson, J. F., "Geometry of turbulence in wall-bounded shear flows: Periodic orbits," *Phys. Scr. T*, vol. 142, p. 014007, 2010.

[58] Davidsen, J., Glass, L., and Kapral, R., "Topological constraints on spiral wave dynamics in spherical geometries with inhomogeneous excitability," *Phys. Rev. E*, vol. 70, p. 056203, 2004.

[59] Davydov, V. A. and Zykov, V. S., "Spiral autowaves in a round excitable medium," *J. Exp. Theor. Phys.*, vol. 76, no. 3, pp. 414–419, 1993.

[60] de Lozar, A., Mellibovsky, F., Avila, M., and Hof, B., "Edge state in pipe flow experiments," *Phys. Rev. Lett.*, vol. 108, p. 214502, 2012.

[61] Dennis Jr, J. E. and Schnabel, R. B., *Numerical Methods for Unconstrained Optimization and Nonlinear Equations*. Society for Industrial and Applied Mathematics, Jan. 1996.

[62] Dominguez, G. and Fozzard, H. A., "Effect of streach on conduction velocity and cable properties of cardiac Purkinje fibers," *Am. J. Physiol.*, vol. 237, p. C119, 1979.

[63] Eckmann, J. P. and Ruelle, D., "Ergodic theory of chaos and strange attractors," *Reviews of Modern Physics*, vol. 57, pp. 617–656, July 1985.

[64] Efimov, I. R., Gray, R. A., and Roth, B. J., "Virtual electrodes and deexcitation: new insights into fibrillation induction and defibrillation," *Journal of cardiovascular electrophysiology*, vol. 11, pp. 339–353, 2000.

[65] Eisenberg, R. S., Barcilon, V., and Mathias, R. T., "Electrical properties of spherical syncytia," *Biophysical Journal*, vol. 25, pp. 151–180, Jan. 1979.

[66] Enright, W. H., Jackson, K., Nørsett, S. P., and Thomsen, P. G., "Interpolants for runge-kutta formulas," *ACM Transactions on Mathematical Software (TOMS)*, vol. 12, no. 3, pp. 193–218, 1986.

[67] Farazmand, M., "An adjoint-based approach for finding invariant solutions of Navier–Stokes equations," *J. Fluid Mech.*, vol. 795, pp. 278–312, Apr. 2016.

[68] Fast, V. G. and Kléber, A. G., "Role of wavefront curvature in propagation of cardiac impulse," *Cardiovascular research*, vol. 33, pp. 258–271, 1997.

[69] Fenton, F. and Karma, A., "Vortex dynamics in three-dimensional continuous myocardium with fiber rotation: Filament instability and fibrillation," *Chaos*, vol. 8, pp. 20–47, 1998.

[70] Fenton, F. H. and Cherry, E. M., "Models of cardiac cell," *Scholarpedia*, vol. 3, p. 1868, 2008.

[71] Fenton, F. H., Cherry, E. M., and Glass, L., "Cardiac arrhythmia," *Scholarpedia*, vol. 3, p. 1665, 2008.

[72] Fenton, F. H., Cherry, E. M., Hastings, H. M., and Evans, S. J., "Multiple mechanisms of spiral wave breakup in a model of cardiac electrical activity," *Chaos*, vol. 12, pp. 852–892, 2002.

[73] Fenton, F. H., Luther, S., Cherry, E. M., Otani, N. F., Krinksy, V., Pumir, A., Bodenschatz, E., and Jr., R. F. G., "Termination of atrial fibrillation using pulsed low-energy far-field stimulation," *Circulation*, vol. 120, pp. 467–476, 2009.

[74] Fenton, F. and Cherry, E., "Models of cardiac cell," *Scholarpedia*, vol. 3, no. 8, p. 1868, 2008.

[75] Fiedler, B., Sandstede, B., Scheel, A., and Wulff, C., "Bifurcation from relative equilibria of noncompact group actions: Skew products, meanders, and drifts," *Doc. Math.*, vol. 141, pp. 479–505, 1996.

[76] Fiedler, B. and Turaev, D., "Normal forms, resonances, and meandering tip motions near relative equilibria of Euclidean group actions," *Arch. Rational Mech. Anal.*, vol. 145, pp. 129–159, 1998.

[77] FitzHugh, R., "Impulses and Physiological States in Theoretical Models of Nerve Membrane," *Biophysical journal*, vol. 1, pp. 445–466, Jan. 1961.

[78] Foulkes, A. J. and Biktashev, V. N., "Riding a spiral wave: Numerical simulation of spiral waves in a comoving frame of reference," *Phys. Rev. E*, vol. 81, p. 046702, 2010. `arXiv:1001.4454`.

[79] Fox, J. J., Riccio, M. L., Hua, F., Bodenschatz, E., and Gilmour, R. F., "Spatiotemporal transition to conduction block in canine ventricle," *Circulation research*, vol. 90, pp. 289–296, 2002.

[80] Garcia-Dorado, D., Rodriguez-Sinovas, A., and Ruiz-Meana, M., "Gap junction-mediated spread of cell injury and death during myocardial ischemia-reperfusion," *Cardiovasc. Res.*, vol. 61, pp. 386–401, 2004.

[81] Garfinkel, A., Chen, P. S., Walter, D. O., Karagueuzian, H. S., Kogan, B., Evans, S. J., Karpoukhin, M., Hwang, C., Uchida, T., Gotoh, M., Nwasokwa, O., Sager, P., and Weiss, J. N., "Quasiperiodicity and chaos in cardiac fibrillation," *J. Clin. Invest.*, vol. 99, pp. 305–314, 1997.

[82] Garzón, A., Grigoriev, R. O., and Fenton, F. H., "Model-based control of cardiac alternans in Purkinje fibers," *Phys. Rev. E*, vol. 84, p. 041927, 2011.

[83] Garzón, A., Grigoriev, R. O., and Fenton, F. H., "Continuous-time control of alternans in long purkinje fibers," *Chaos*, vol. 24, p. 033124, 2014.

[84] Geiser, J., "Iterative operator-splitting methods with higher-order time integration methods and applications for parabolic partial differential equations," *Journal of Computational and Applied Mathematics*, vol. 217, no. 1, pp. 227–242, 2008.

[85] Gibson, J. F., Halcrow, J., and Cvitanović, P., "Equilibrium and traveling-wave solutions of plane Couette flow," *J. Fluid Mech.*, vol. 638, pp. 243–266, 2009.

[86] Gibson, J. F., Halcrow, J., and Cvitanović, P., "Visualizing the geometry of state space in plane Couette flow," *J. Fluid Mech.*, vol. 611, pp. 107–130, 2008.

[87] Goldhirsch, I., Orszag, S. A., and Maulik, B. K., "An efficient method for computing leading eigenvalues and eigenvectors of large asymmetric matrices," *J. Sci. Comp.*, vol. 2, pp. 33–58, 1987.

[88] Golub, G. and Kahan, W., "Calculating the singular values and pseudo-inverse of a matrix," *Journal of the Society for Industrial and Applied Mathematics, Series B: Numerical Analysis*, vol. 2, no. 2, pp. 205–224, 1965.

[89] Gray, R. A., Pertsov, A. M., and Jalife, J., "Spatial and temporal organization during cardiac fibrillation," *Nature*, vol. 392, pp. 75–78, 1998.

[90] Gutzwiller, M. C., "Periodic orbits and classical quantization conditions," *J. Math. Phys.*, vol. 12, pp. 343–358, 1971.

[91] Hagberg, A. and Meron, E., "From labyrinthine patterns to spiral turbulence," *Phys. Rev. Lett.*, vol. 72, pp. 2494–2497, 1994.

[92] Hager, W. W., "Runge-kutta methods in optimal control and the transformed adjoint system," *Numerische Mathematik*, vol. 87, no. 2, pp. 247–282, 2000.

[93] Halcrow, J., Gibson, J. F., Cvitanović, P., and Viswanath, D., "Heteroclinic connections in plane Couette flow," *J. Fluid Mech.*, vol. 621, pp. 365–376, 2009.

[94] Hartmann, N., Bär, M., Kevrekidis, I., Krischer, K., and Imbihl, R., "Rotating chemical waves in small circular domains," *Physical review letters*, vol. 76, no. 8, p. 1384, 1996.

[95] Henry, H. and Hakim, V., "Linear stability of scroll waves," *Phys. Rev. Lett.*, vol. 85, pp. 5328–5331, 2000.

[96] Henry, H. and Hakim, V., "Scroll waves in isotropic excitable media: Linear instabilities, bifurcations, and restabilized states," *Phys. Rev. E*, vol. 65, p. 046235, 2002.

[97] Henze, C., Lugosi, E., and Winfree, A., "Helical organizing centers in excitable media," *Canadian Journal of Physics*, vol. 68, no. 9, pp. 683–710, 1990.

[98] Hermann, S. and Gottwald, G. A., "The large core limit of spiral waves in excitable media: A numerical approach," *SIAM J. Appl. Dyn. Sys.*, vol. 9, pp. 536–567, 2010. `arXiv:1003.5830`.

[99] Heron, M. and Tejada-Vera, B., "Deaths: leading causes for 2005.," *National vital statistics reports: from the ...*, 2009.

[100] Howard, L. N. and Kopell, N., "Slowly varying waves and shock structures in reaction-diffusion equations," *Studies Appl. Math.*, vol. 56, pp. 95–145, 1977.

[101] Ideker, R. E., Zhou, X., and Knisley, S. B., "Correlation among fibrillation, defibrillation, and cardiac pacing," *Pacing and Clinical Electrophysiology*, vol. 18, pp. 512–525, 1995.

[102] Iyer, A. N. and Gray, R. A., "An experimentalist's approach to accurate localization of phase singularities during reentry," *Annals of biomedical engineering*, vol. 29, no. 1, pp. 47–59, 2001.

[103] Jahnke, W., Skaggs, W., and Winfree, A. T., "Chemical vortex dynamics in the belousov-zhabotinskii reaction and in the two-variable oregonator model," *The Journal of Physical Chemistry*, vol. 93, no. 2, pp. 740–749, 1989.

[104] Jahnke, W. and Winfree, A. T., "A survey of spiral-wave behaviors in the oregonator model," *International Journal of Bifurcation and Chaos*, vol. 1, no. 02, pp. 445–466, 1991.

[105] Kantz, H., *Nonlinear Time Series Analysis*. Cambridge, UK: Cambridge Univ. Press, 2 edition ed., 2004.

[106] Karma, A., "Universal limit of spiral wave propagation in excitable media," *Physical Review Letters*, 1991.

[107] Karma, A., "Spiral breakup in model equations of action-potential propagation in cardiac tissue," *Phys. Rev. Lett.*, vol. 71, pp. 1103–1106, 1993.

[108] Karma, A., "Electrical alternans and spiral wave breakup in cardiac tissue," *Chaos*, vol. 4, pp. 461–472, 1994.

[109] Kassam, A.-K. and Trefethen, L. N., "Fourth-Order Time-Stepping for Stiff PDEs," *SIAM Journal on Scientific Computing*, vol. 26, pp. 1214–1233, Apr. 2005.

[110] Keener, J. P. and Tyson, J. J., "Spiral waves in the Belousov-Zhabotinskii reaction," *Physica D*, vol. 21, pp. 307–324, 1986.

[111] Keener, J. P., "A Geometrical Theory for Spiral Waves in Excitable Media," *SIAM Journal on Applied Mathematics*, vol. 46, pp. 1039–1056, Dec. 1986.

[112] Keener, J. P., "The dynamics of three-dimensional scroll waves in excitable media," *Physica D*, vol. 31, no. 2, pp. 269–276, 1988.

[113] Krinsky, V. I. and Agladze, K. I., "Interaction of rotating waves in an active chemical medium," *Physica D*, vol. 8, pp. 50–56, 1983.

[114] Lan, Y. and Cvitanović, P., "Unstable recurrent patterns in Kuramoto-Sivashinsky dynamics," *Phys. Rev. E*, vol. 78, p. 026208, 2008.

[115] Langham, J. and Barkley, D., "Non-specular reflections in a macroscopic system with wave-particle duality: Spiral waves in bounded media," *Chaos*, vol. 23, p. 013134, 2013. `arXiv:1304.0591`.

[116] Langham, J., Biktasheva, I., and Barkley, D., "Asymptotic dynamics of reflecting spiral waves," *Phys. Rev. E*, vol. 90, no. 6, p. 062902, 2014.

[117] Lindeberg, T., "Scale-space for discrete signals," *IEEE Transactions on Pattern Analysis and Machine Intelligence*, vol. 12, pp. 234–254, 1990.

[118] López, V., Boyland, P., Heath, M. T., and Moser, R. D., "Relative periodic solutions of the complex Ginzburg-Landau equation," *SIAM J. Appl. Dyn. Syst.*, vol. 4, pp. 1042–1075, 2006. `arXiv:nlin/0408018`.

[119] Lourakis, M. and Argyros, A. A., "Is Levenberg-Marquardt the most efficient optimization algorithm for implementing bundle adjustment?," *Tenth IEEE International ...*, pp. 1526–1531 Vol. 2, 2005.

[120] Luo, J., Zhang, B., and Zhan, M., "Frozen state of spiral waves in excitable media," *Chaos*, vol. 19, p. 033133, 2009.

[121] Luther, S., Fenton, F. H., Kornreich, B. G., Squires, A., Bittihn, P., Hornung, D., Zabel, M., Flanders, J., Gladuli, A., Campoy, L., Cherry, E. M., Luther, G., Hasenfuss, G., Krinsky, V. I., Pumir, A., Gilmour, R. F., and Bodenschatz, E., "Low-energy control of electrical turbulence in the heart," *Nature*, vol. 475, pp. 235–9, 2011.

[122] Marcotte, C. D., "`https://github.com/cmarcotte/thesis-codes/`," 2016.

[123] Maree, A. and Panfilov, A. V., "Spiral breakup in excitable tissue due to lateral instability," *Phys. Rev. Lett.*, vol. 78, no. 9, pp. 1819–1822, 1997.

[124] Merideth, J., Mendez, C., MUELLER, W. J., and MOE, G. K., "Electrical excitability of atrioventricular nodal cells," *Circulation Research*, vol. 23, no. 1, pp. 69–85, 1968.

[125] Meseguer, A., Mellibovsky, F., Avila, M., and Marques, F., "Families of subcritical spirals in highly counter-rotating Taylor-Couette flow," *Phys. Rev. E*, vol. 79, 2009.

[126] Miller, W. T. and Geselowitz, D. B., "Simulation studies of the electrocardiogram. I. The normal heart," *Circ. Res.*, vol. 43, pp. 301–315, Aug. 1978.

[127] Molnos, S., Löber, J., Totz, J. F., and Engel, H., "Control of transversal instabilities in reaction-diffusion systems," *arXiv.org*, Jan. 2015.

[128] Mornev, O. A., Tsyganov, I. M., Aslanidi, O. V., and Tsyganov, M. A., "Beyond the Kuramoto-Zel'dovich theory: Steadily rotating concave spiral waves and their relation to the echo phenomenon," *Journal of Experimental and Theoretical Physics Letters*, vol. 77, no. 6, pp. 270–275, 2003.

[129] Morris, S. W., Bodenschatz, E., Cannell, D. S., and Ahlers, G., "Spiral defect chaos in large aspect ratio Rayleigh-Benard convection," *Phys. Rev. Lett.*, vol. 71, pp. 2026–2029, 1993.

[130] Muler, A., "Electrical properties of anisotropic neuro-muscular syncytia. III. Steady-state shape of the excitation front," *Biofizika*, vol. 22, pp. 671–675, Jan. 1977.

[131] Muler, A., "Electrical properties of anisotropic neuromuscular syncytia. I. Distribution of electrotonic potential (Russian)," *Biofizika*, vol. 22, pp. 307–312, Jan. 1977.

[132] Muler, A., "Electrical properties of anisotropic neuromuscular syncytium. II. Propagation of flat front of excitation," *Biofizika*, vol. 22, pp. 518–522, Jan. 1977.

[133] Müller, S. C., PLESSER, T., and Hess, B., "The Structure of the Core of the Spiral Wave in the Belousov-Zhabotinskii Reaction," *Science*, vol. 230, no. 4726, pp. 661–663, 1985.

[134] Murray, J. D., Stanley, E. A., and Brown, D. L., "On the spatial spread of rabies among foxes," *Proc. R. Soc. Lond. B*, vol. 229, pp. 111–150, 1986.

[135] Noble, D., "A modification of the Hodgkin—Huxley equations applicable to Purkinje fibre action and pacemaker potentials," 1962.

[136] Ouyang, Q. and Swinney, H. L., "Transition to chemical turbulence," *Chaos*, vol. 1, 1991.

[137] Panfilov, A. V. and Hogeweg, P., "Spiral breakup in a modified FitzHugh-Nagumo model," *Phys. Lett. A*, vol. 176, pp. 295–299, 1993.

[138] Pertsov, A. M., Davidenko, J. M., Salomonsz, R., Baxter, W. T., and Jalife, J., "Spiral waves of excitation underlie reentrant activity in isolated cardiac muscle.," *Circulation Research*, vol. 72, no. 3, pp. 631–650, 1993.

[139] Peskoff, A., "Electric potential in cylindrical syncytia and muscle fibers," *Bulletin of Mathematical Biology*, vol. 41, no. 2, pp. 183–192, 1979.

[140] Peskoff, A., "Electric potential in three-dimensional electrically syncytial tissues," *Bulletin of Mathematical Biology*, vol. 41, no. 2, pp. 163–181, 1979.

[141] Pismen, L. and Nepomnyashchy, A., "Mobility of spiral waves," *Phys. Rev. A*, vol. 44, p. R2243, 1991.

[142] Pismen, L. and Nepomnyashchy, A., "On interaction of spiral waves," *Physica D*, vol. 54, no. 3, pp. 183–193, 1992.

[143] Poincaré, H., *Les Méthodes Nouvelles de la Méchanique Céleste*. Paris: Gauthier-Villars, 1899.

[144] Pringle, C. C. T., Willis, A. P., and Kerswell, R. R., "Minimal seeds for shear flow turbulence: using nonlinear transient growth to touch the edge of chaos," *J. Fluid Mech.*, vol. 702, pp. 415–443, May 2012.

[145] Roth, B., "Bidomain model," *Scholarpedia*, vol. 3, no. 4, p. 6221, 2008.

[146] Roth, B. J., "How the anisotropy of the intracellular and extracellular conductivities influences stimulation of cardiac muscle," *Journal of mathematical biology*, vol. 30, no. 6, pp. 633–646, 1992.

[147] Saad, Y., *Iterative methods for sparse linear systems*. Boston: PWS, 1996.

[148] Saad, Y. and Schultz, M. H., "GMres: A generalized minimal residual algorithm for solving nonsymmetric linear systems," *SIAM J. Sci. Stat. Comp.*, vol. 7, pp. 856–869, 1986.

[149] Sandstede, B. and Scheel, A., "Absolute versus convective instability of spiral waves," *Phys. Rev. E*, vol. 62, pp. 7708–7714, 2000.

[150] Sandstede, B., Scheel, A., and Wulff, C., "Dynamics of spiral waves on unbounded domains using center-manifold reductions," *J. Diff. Eqn.*, vol. 141, pp. 122–149, 1997.

[151] Sandstede, B., Scheel, A., and Wulff, C., "Dynamical behavior of patterns with Euclidean symmetry," in *Pattern Formation in Continuous and Coupled Systems*, pp. 249–264, New York: Springer, 1999.

[152] Sandstede, B. and Scheel, A., "Absolute and convective instabilities of waves on unbounded and large bounded domains," *Physica D*, vol. 145, pp. 233–277, Jan. 2000.

[153] Sandstede, B. and Scheel, A., "Defects in oscillatory media: toward a classification," *SIAM Journal on Applied Dynamical Systems*, vol. 3, no. 1, pp. 1–68, 2004.

[154] Sandu, A., "On the properties of runge-kutta discrete adjoints," in *Computational Science–ICCS 2006*, pp. 550–557, Springer, 2006.

[155] Sepulveda, N. G., Roth, B. J., and Wikswo Jr., J. P., "Current injection into a two-dimensional anisotropic bidomain," *Biophys. J.*, vol. 55, pp. 987–999, 1989.

[156] Sherratt, J. A., Smith, M. J., and Rademacher, J. D. M., "Patterns of sources and sinks in the complex Ginzburg-Landau equation with zero linear dispersion," *SIAM J. Appl. Dyn. Syst.*, vol. 9, pp. 883–918, 2010.

[157] Siegert, F. and Weijer, C. J., "Analysis of optical density wave propagation and cell movement in the cellular slime mold Dictyostelium discoideum," *Physica D*, vol. 49, pp. 224–232, 1991.

[158] Simitev, R. D. and Biktashev, V. N., "Conditions for propagation and block of excitation in an asymptotic model of atrial tissue," *Biophys. J.*, vol. 90, pp. 2258–2269, 2006.

[159] Starmer, C. F., Biktashev, V. N., Romashko, D. N., Stepanov, M. R., Makarova, O. N., and Krinsky, V. I., "Vulnerability in an excitable medium: analytical and numerical studies of initiating unidirectional propagation.," *Biophysical journal*, vol. 65, no. 5, p. 1775, 1993.

[160] Strang, G., "On the construction and comparison of difference schemes," *SIAM Journal on Numerical Analysis*, vol. 5, no. 3, pp. 506–517, 1968.

[161] Takeuchi, K. A., Yang, H.-l., Ginelli, F., Radons, G., and Chaté, H., "Hyperbolic decoupling of tangent space and effective dimension of dissipative systems," *Phys. Rev. E*, vol. 84, pp. 046214–19, Oct. 2011.

[162] Teramura, T. and Toh, S., "Damping filter method for obtaining spatially localized solutions," *Phys. Rev. E*, vol. 89, p. 052910, 2014.

[163] Tomlin, C. J., Mitchell, I., Bayen, A. M., and Oishi, M., "Computational techniques for the verification of hybrid systems," *Proceedings of the IEEE*, vol. 91, no. 7, pp. 986–1001, 2003.

[164] Trefethen, L. N. and Bau, D., *Numerical Linear Algebra*. SIAM, 1997.

[165] Tung, L., "A bi-domain model for describing ischemic myocardial d-c potentials.," 1978.

[166] Vasiev, B. N., Hogeweg, P., and Panfilov, A. V., "Simulation of Dictyostelium discoideum aggregation via reaction-diffusion model," *Phys. Rev. Lett.*, vol. 73, pp. 3173–3176, 1994.

[167] Viswanath, D., "Recurrent motions within plane Couette turbulence," *J. Fluid Mech.*, vol. 580, pp. 339–358, 2007. `arXiv:physics/0604062`.

[168] Walcott, G. P., Killingsworth, C. R., and Ideker, R. E., "Do clinically relevant transthoracic defibrillation energies cause myocardial damage and dysfunction?," *Resuscitation*, vol. 59, pp. 59–70, 2003.

[169] Wheeler, P. and Barkley, D., "Computation of spiral spectra," *Siam Journal on Applied Dynamical Systems*, 2006.

[170] Willis, A. P., Cvitanović, P., and Avila, M., "Revealing the state space of turbulent pipe flow by symmetry reduction," *J. Fluid Mech.*, vol. 721, pp. 514–540, 2013.

[171] Xu, J., "Iterative methods by space decomposition and subspace correction," *SIAM Review*, vol. 34, pp. 581–613, 1992.

[172] Yang, H., Takeuchi, K. A., Ginelli, F., Chaté, H., and Radons, G., "Hyperbolicity and the effective dimension of spatially extended dissipative systems," *Physical Review Letters*, 2009.

[173] Zhan, M., Luo, J., and J., G., "Chirality effect on the global structure of spiral-domain patterns in the two-dimensional complex Ginzburg-Landau equation," *Phys. Rev. E*, vol. 75, p. 016214, 2007.

[174] Zhang, H. and Holden, A., "Chaotic meander of spiral waves in the fitzhugh-nagumo system," *Chaos, Solitons & Fractals*, vol. 5, no. 3, pp. 661–670, 1995.

[175] Zhang, H., Hu, B., Li, B.-W., and Duan, Y.-S., "Topological constraints on scroll and spiral waves in excitable media," *Chinese Phys. Lett.*, vol. 24, pp. 1618–1621, 2007.

[176] Zykov, V. S. and Morozova, O. L., "Speed of spread of excitation in a two-dimensional excitable medium," *Biophysics*, vol. 24, pp. 739–744, 1979.

VITA

Christopher D. Marcotte was born in 1988 in Providence, Rhode Island. He lived in Pawtucket until the age of five when he moved to Foster, where he lived until he begrudgingly completed high school, in 2006. He then moved to North Kingston to live with his father David, and to commute to the University of Rhode Island six days a week. In 2010 he graduated with a B.S. in Physics. In August of that year he moved to Atlanta, Georgia to pursue a Ph.D. in Physics at the Georgia Institute of Technology. Apart from applied mathematics and physics, he enjoys drag shows, co-opting the language of colonial witch-hunts for the minor inconveniences of a modern era, and excessively descriptive phrases. He leaves Georgia Tech for a post-doctoral position at the University of Exeter, in the EPSRC Centre for Predictive Modelling in Healthcare.